



HAL
open science

Numerical radiative transfer using an immerse volume method

Quentin Schmid

► **To cite this version:**

Quentin Schmid. Numerical radiative transfer using an immerse volume method. Materials. Université Paris sciences et lettres, 2016. English. NNT : 2016PSLEM086 . tel-01734545

HAL Id: tel-01734545

<https://pastel.hal.science/tel-01734545>

Submitted on 14 Mar 2018

HAL is a multi-disciplinary open access archive for the deposit and dissemination of scientific research documents, whether they are published or not. The documents may come from teaching and research institutions in France or abroad, or from public or private research centers.

L'archive ouverte pluridisciplinaire **HAL**, est destinée au dépôt et à la diffusion de documents scientifiques de niveau recherche, publiés ou non, émanant des établissements d'enseignement et de recherche français ou étrangers, des laboratoires publics ou privés.

Thèse de Doctorat

Université de recherche Paris Sciences et Lettres
PSL Research University

Préparée à MINES ParisTech

Modélisation du rayonnement thermique en immersion de volume

Ecole Doctorale n°364

Sciences Fondamentales et appliquées

Spécialité Mécanique Numérique et matériaux

Soutenue par Quentin SCHMID
Le 14 Décembre 2016

Sous la Direction de
Prof. **Elie HACHEM**
Dr. **Youssef MESRI**



JURY :

Prof. Ramon CODINA
Universitat Politècnica de Catalunya,
Président du Jury
Rapporteur

Prof. Aziz HAMDOUNI
Université de la Rochelle,
Rapporteur

Dr. Kathik DURAISAMY
University of Michigan,
examineur

Prof. Vincent LEGAT
Université Catholique de Louvain,
examineur

Prof. Elie HACHEM
CEMEF Mines Paristech,
Directeur de thèse

Dr. Youssef MESRI
CEMEF Mines Paristech,
Maître de thèse

“Die ganzen Zahlen hat der liebe Gott gemacht, alles andere ist Menschenwerk.”

“God made the integers, everything else is the work of man.”

“Dieu créa les entiers, le reste est oeuvre de l’homme.”

Leopold Kronecker (1823-1891)

Acknowledgements

A french novelist wrote a book entitled " l'amour dure trois ans", which can be translated as "love lasts three years". So does a thesis, which is somehow a love story, with happy and sad times, 'for better for worse'. Theses three years were a fantastic adventure, which brought me a lot further than where I thought I would be when it started. I would like to express my gratitude to all of the people that I met during these three years, and to all those who contributed to this thesis, near and far.

I am honoured to have shared my "PhD experience" with the following people while I was in CEMEF: Laure, Jeremy, Ghina, Margaux, Gregoire, Marie-Agathe, Stephanie, Luca, Mehdi, Alban, Ghalia, Romain, Alexandre, Jerome, Valentin, Guillaume, and to the many others I haven't mentioned above.

I really appreciate all of the people that I met during my time in the 'Cote d'Azur' because they contributed to make this period of my life unforgettable : "Wednesday in Antibes" members, all the lads of RCASA rugby team, the MAPMOD students and many more...

I would like to give a special mention to both of my advisors:

Thanks to Youssef, who joined the project whilst in progress and who proved remarkable in getting up to speed. He provided me with his encyclopedic knowledge in mathematics, numerical analysis and last but not the least, his programming skills, without which this work would not be as precise as it is now.

Thanks to Elie, for his amazing and relentless energy, his positivity, his motivational skills which helped me exceed my expectations and realise results which initially I wouldn't have thought possible, and last but not the least, who introduced me to the VMS framework, something that I think I will not be done until the very end of my career.

I am glad that fate allowed me to work with these two exceptional people, and I hope that our paths will cross again one day.

I also want to thank all of the jury members: thanks to Ramon and Aziz that agreed to review this thesis, and thanks to Karthik and Vincent for their questions and remarks

during the defense.

I am eternally grateful to all of my family for their ongoing love and support in everything that I undertake. During these three years I also met my girlfriend Marie who now supports me in more ways than one; I thank my lucky stars for this relationship.

Finally, a word for everyone who will read this thesis: I hope you will find here some insight for the problems in which you are interested, some support in understanding what is not extensively explained in detail in the literature and I sincerely hope that it might help you, as was the case for me, to see a profound beauty that is hidden (sometimes extremely well) in doing research and more generally, in science.

...

Contents

Acknowledgements	ii
List of Figures	viii
List of Tables	xv
Abbreviations	xvi
Physical Constants	xvii
Symbols	xviii
1 Motivations, context and working environment	1
1.1 General Introduction	1
1.2 General Context	3
1.2.1 Industrial Context	3
1.2.2 Academic Context	4
1.3 Working environment	5
1.3.1 Computational environment	5
1.3.2 General assumptions	5
1.4 Physics of industrial furnaces	6
1.5 Outline of the thesis	9
2 Stabilized Finite Element Method for flow and heat transfer	11
2.1 Physical models	11
2.1.1 The Navier-Stokes equations	11
2.1.2 Initial and boundary conditions for the Navier-Stokes equations	14
2.1.2.1 Initial Conditions	14
2.1.2.2 Boundary Conditions	14
2.1.3 The Convection-Diffusion-Reaction equation	15
2.1.4 Different physical examples of Convection-Diffusion-Reaction equations	16
2.1.4.1 The energy equation	16
2.1.4.2 $k - \varepsilon$ Turbulence model	17
2.1.4.3 P_1 Radiation model	18
2.1.5 Fully coupled aerothermal problem	19

2.2	Formulations for numerical approximations	20
2.2.1	Classical Finite Element Formulation for the Navier-Stokes equations	21
2.2.2	Stabilization using the Variational Multiscale Method	22
2.2.2.1	The need of stabilization	22
2.2.2.2	Scale Splitting	23
2.2.2.3	Approximation for the fine scale problem	24
2.2.3	Standard Galerkin Finite Element Method for the CDR equation	26
2.2.4	Stabilization Techniques for the CDR equation	27
2.2.4.1	Streamline Upwind Petrov Galerkin (SUPG)	27
2.2.4.2	Shock Capturing Petrov Galerkin (SCPG)	27
2.2.4.3	Derivation of the stabilization parameters: a link between SUPG and VMS	28
2.3	Numerical experiments	31
2.3.1	Natural convection in an empty cavity	31
2.3.2	Natural convection in a cavity containing a plate	36
2.3.2.1	Horizontal plate	36
2.3.2.2	Vertical plate	40
3	The Monolithic approach: levelset methods, anisotropic mesh adaptation and mixing laws	45
3.1	Representing interfaces using a levelset framework	47
3.2	Error estimators, metric fields and anisotropic mesh adaptation	48
3.2.1	Error estimation	48
3.2.1.1	Motivations	48
3.2.1.2	Approximation error	50
3.2.1.3	Interpolation error	51
3.2.2	Change of geometry: metric fields	52
3.2.2.1	Metric construction by length distribution tensor	52
3.2.2.2	Metric construction using an hessian based error estimator	55
3.2.3	Mesh adaptation algorithms	56
3.3	Multidomain problems	61
3.4	Numerical experiments	64
3.4.1	Natural convection in an empty cavity	64
3.4.2	Natural convection in a cavity containing a plate	69
3.4.3	Mixed convection of a group of ingots	80
4	Monolithic Surface Radiation: The "Immersed-Surface-to-Immersed-Surface" (IS2IS) method	83
4.1	The Radiative Transfer Equation	84
4.1.1	Equation and boundary conditions	84
4.1.2	Physical meaning of the different terms	85
4.1.3	Numerical difficulties	86
4.2	Numerical formulations for the RTE	87
4.2.1	Monte Carlo Method	87
4.2.2	Finite Element Methods	87
4.2.3	S_N : Discrete Ordinates Method	87
4.2.4	P_N : Spherical Harmonics	88

4.3	The Surface-to-Surface Method: state of the art	90
4.3.1	The view factor: a geometric function	90
4.3.2	Visibility and obstructions	93
4.3.2.1	Visibility	93
4.3.2.2	Obstruction	94
4.3.3	Total exchange area, real surfaces and coupling with thermal balance	96
4.4	The <i>IS2IS</i> method	99
4.4.1	Motivations and features	99
4.4.2	Interface reconstruction	99
4.4.3	Computational aspects	103
4.4.4	"Immersed" features of the <i>IS2IS</i> method	105
4.4.5	Parallel processing aspects	106
4.5	Numerical experiments	106
4.5.1	Natural convection in a square empty cavity	106
4.5.2	Natural Convection in a cavity containing a plate	111
5	Monolithic Volume Radiation: Stabilized Finite Element Method for the Minimum Entropy closure M_1 radiation model	119
5.1	Introduction to moment models	120
5.2	Different closures	122
5.2.1	Rosseland approximation	122
5.2.2	P_1 model	123
5.2.3	Minimum entropy closure: the M_1 model	124
5.2.4	Extensions of the M_1 model	128
5.2.4.1	Method of partial moments	128
5.2.4.2	Non-gray radiative transfer	129
5.3	State of the art: existing schemes for the M_1 model	129
5.4	Mixed Finite Element formulation for the M_1 radiation model	129
5.4.1	Weak formulation	129
5.4.1.1	Time discretization and treatment of the non-linear term	130
5.4.1.2	Galerkin finite element approximation	131
5.4.2	The VMS as an abstract tool	132
5.4.3	Stabilization for the proposed formulation	132
5.4.3.1	Scale splitting within the VMS framework	132
5.4.3.2	Approximation for the Fine-scale problem	133
5.5	Numerical results	135
5.5.1	Transparent media in a square enclosure	136
5.5.2	Participating media with discontinuous coefficients: fixed temperature	137
5.5.3	Radiation of an absorbing rod in a scattering media: the Mordant Test	139
5.5.4	Radiative transfer behind an obstacle: the shadow test	140
6	Industrial Applications	145
6.1	Quenching of an hat shaped disk in various configurations	145
6.1.0.1	Cooling in open air	146
6.1.0.2	Forced convection using air blast cooler	148

6.1.0.3	Natural convection with multi-material	152
6.1.1	Conclusions about the study	155
6.2	Quenching of two ingots in an enclosure	155
6.2.1	Mesh Generation	156
6.2.2	First computations and simplifying assumptions	158
7	Conclusions and Outlook	162
7.1	Conclusions	162
7.2	Outlook	164
A	Parametrized Rayleigh and Prandtl numbers for natural convection	167
B	Double line integral for the view Factor Calculation: 8 points quadrature rule	169
C	Detailed calculations for the SFEM formulation	171
C.1	Calculation of the Jacobians	171
C.2	Calculation of spectral radii	173
C.3	Algorithm for the proposed formulation	174
C.4	Final Stabilized formulation	174
	Bibliography	177

List of Figures

1.1	Illustration of the fully coupled physics in an industrial furnace	6
1.2	Illustration of the coupled physics in an industrial furnace without combustion	6
2.1	Illustration of Eulerian and Lagrangian points of view	12
2.2	Illustration of 1d shape function modification	28
2.3	2d Empty cavity: iso temperature for $Ra = 10^2$	31
2.4	2d Empty cavity: streamlines for $Ra = 10^2$	31
2.5	2d Empty cavity: iso temperature for $Ra = 10^3$	31
2.6	2d Empty cavity: streamlines for $Ra = 10^3$	31
2.7	2d Empty cavity: iso temperature for $Ra = 10^4$	32
2.8	2d Empty cavity: streamlines for $Ra = 10^4$	32
2.9	2d Empty cavity: iso temperature for $Ra = 10^5$	32
2.10	2d Empty cavity: streamlines for $Ra = 10^5$	32
2.11	2d Empty cavity: iso temperature for $Ra = 10^6$	32
2.12	2d Empty cavity: streamlines for $Ra = 10^6$	32
2.13	2d Empty cavity: iso temperature for $Ra = 10^7$	33
2.14	2d Empty cavity: streamlines for $Ra = 10^7$	33
2.15	2d Empty cavity: iso temperature for $Ra = 10^8$	33
2.16	2d Empty cavity: streamlines for $Ra = 10^8$	33
2.17	2d Empty cavity: θ along $y = 0.5$ for the considered range of Ra	33
2.18	2d Empty cavity: u_2 along $y = 0.5$ for the considered range of Ra	33
2.19	3d Empty cavity: streamlines along l_c for $Ra = 10^3$	34
2.20	3d Empty cavity: streamlines around x_c for $Ra = 10^3$	34
2.21	3d Empty cavity: streamlines along l_c for $Ra = 10^4$	34
2.22	3d Empty cavity: streamlines around x_c for $Ra = 10^4$	34
2.23	3d Empty cavity: streamlines along l_c for $Ra = 10^5$	35
2.24	3d Empty cavity: streamlines around x_c for $Ra = 10^5$	35
2.25	3d Empty cavity: streamlines along l_c for $Ra = 10^6$	35
2.26	3d Empty cavity: streamlines around x_c for $Ra = 10^6$	35
2.27	3d Empty cavity: iso temperature surfaces for $Ra = 10^3$	35
2.28	3d Empty cavity: iso temperature surfaces for $Ra = 10^4$	35
2.29	3d Empty cavity: iso temperature surfaces for $Ra = 10^5$	35
2.30	3d Empty cavity: iso temperature surfaces for $Ra = 10^6$	35
2.31	2d Horizontal plate: iso temperature for $Ra = 10^4$	37
2.32	2d Horizontal plate: velocity for $Ra = 10^4$	37
2.33	2d Horizontal plate: iso temperature for $Ra = 10^5$	37
2.34	2d Horizontal plate: velocity for $Ra = 10^5$	37

2.35	2d Horizontal plate: iso temperature for $Ra = 10^6$	37
2.36	2d Horizontal plate: velocity for $Ra = 10^6$	37
2.37	2d Horizontal plate: θ along $y = 0.65$ for the considered range of Ra	38
2.38	2d Horizontal plate: u_2 along $y = 0.65$ for the considered range of Ra	38
2.39	2d Horizontal plate: θ along $y = 1.0$	38
2.40	3d Horizontal plate: temperature pattern in symetry planes for $Ra = 10^3$	38
2.41	3d Horizontal plate: temperature pattern in symetry planes for $Ra = 10^4$	38
2.42	3d Horizontal plate: temperature pattern in symetry planes for $Ra = 10^5$	39
2.43	3d Horizontal plate: temperature pattern in symetry planes for $Ra = 10^6$	39
2.44	3d Horizontal plate: streamlines in symetry planes for $Ra = 10^3$	39
2.45	3d Horizontal plate: streamlines in symetry planes for $Ra = 10^4$	39
2.46	3d Horizontal plate: streamlines in symetry planes for $Ra = 10^5$	39
2.47	3d Horizontal plate: streamlines in symetry planes for $Ra = 10^6$	39
2.48	3d Horizontal plate: iso temperature surfaces for $Ra = 10^3$	39
2.49	3d Horizontal plate: iso temperature surfaces for $Ra = 10^4$	39
2.50	3d Horizontal plate: iso temperature surfaces for $Ra = 10^5$	40
2.51	3d Horizontal plate: iso temperature surfaces for $Ra = 10^6$	40
2.52	2d Vertical plate: iso temperature for $Ra = 10^4$	40
2.53	2d Vertical plate: velocity for $Ra = 10^4$	40
2.54	2d Vertical plate: iso temperature for $Ra = 10^5$	40
2.55	2d Vertical plate: velocity for $Ra = 10^5$	40
2.56	2d Vertical plate: iso temperature for $Ra = 10^6$	41
2.57	2d Vertical plate: velocity for $Ra = 10^6$	41
2.58	2d Vertical plate: θ along $y = 0.8$ for the considered range of Ra	41
2.59	2d Vertical plate: u_2 along $y = 0.8$ for the considered range of Ra	41
2.60	2d Vertical plate: θ along $y = 1.0$	42
2.61	3d Vertical plate: temperature patterns for $Ra = 10^3$	42
2.62	3d Vertical plate: streamlines for $Ra = 10^3$	42
2.63	3d Vertical plate: temperature patterns for $Ra = 10^4$	42
2.64	3d Vertical plate: streamlines for $Ra = 10^4$	42
2.65	3d Vertical plate: temperature patterns for $Ra = 10^5$	43
2.66	3d Vertical plate: streamlines for $Ra = 10^5$	43
2.67	3d Vertical plate: temperature patterns for $Ra = 10^6$	43
2.68	3d Vertical plate: streamlines for $Ra = 10^6$	43
2.69	3d Vertical plate: iso temperature for $Ra = 10^3$	43
2.70	3d Vertical plate: iso temperature for $Ra = 10^4$	43
2.71	3d Vertical plate: iso temperature for $Ra = 10^5$	43
2.72	3d Vertical plate: iso temperature for $Ra = 10^6$	43
3.1	levelset Function of a circle	47
3.2	levelset Function of a square	47
3.3	Illustration of anisotropic elements	53
3.4	Mesh adaptation procedure: initial mesh	57
3.5	Mesh adaptation procedure: first remeshing	57
3.6	Mesh adaptation procedure: third remeshing	57
3.7	Mesh adaptation procedure: fifteenth remeshing	57
3.8	Zoom on the refined interface	57

3.9	3d Adapted mesh: brick	58
3.10	3d Adapted mesh: cylinder	58
3.11	View of the industrial ingot	58
3.12	Cross section along the x axis	58
3.13	Cross section along the y axis	58
3.14	Whole Facility: overview	58
3.15	Whole Facility: cross section along the xz plane	59
3.16	Whole Facility: cross section along the xy plane	59
3.17	Whole Facility: cross section along the yz plane	59
3.18	2d Empty Cavity for $Ra = 10^6$: Temperature lines	60
3.19	2d Empty Cavity for $Ra = 10^6$: adapted mesh on temperature	60
3.20	2d Empty Cavity for $Ra = 10^6$: streamlines	60
3.21	2d Empty Cavity for $Ra = 10^6$: adapted mesh on velocity	60
3.22	3d Horizontal plate: adapted mesh on temperature	60
3.23	3d Horizontal plate: adapted mesh on velocity	61
3.24	Industrial Facility: effective heat capacity	63
3.25	Industrial Facility: effective viscosity	63
3.26	2d Empty cavity: mesh for the body-fitted approach	64
3.27	2d Empty cavity: mesh for the immersed volume method	64
3.28	2d Empty cavity: velocity profile using the body-fitted approach (left) and the immersed approach (right)	65
3.29	2d Empty cavity: temperature distribution using the body-fitted approach (left) and the immersed approach (right)	65
3.30	2d Empty cavity: T for several meshes	66
3.31	2d Empty cavity: u_2 for several meshes	66
3.32	2d Empty cavity: T along $x = 0.5$	66
3.33	2d Empty cavity: u_2 along $x = 0.5$	66
3.34	2d Empty cavity: error analysis on the temperature	66
3.35	2d Empty cavity: error analysis on the velocity	66
3.36	3d Empty cavity: meshes used for the "BF" (left) and "IVM" (right) simulations	67
3.37	3d Empty cavity: temperature profiles for "BF" (left) and "IVM" (right) simulations	67
3.38	3d Empty cavity: velocity profile for "BF" (left) and "IVM" (right) simulations	68
3.39	3d Empty cavity: u_1 along l_1	68
3.40	3d Empty cavity: θ along l_1	68
3.41	3d Empty cavity: u_3 along l_1	68
3.42	3d Empty cavity: profile of u_3 for the considered line	68
3.43	3d Empty cavity: u_3 along l_2	69
3.44	3d Empty cavity: θ along l_2	69
3.45	3d Empty cavity: u_1 along l_2	69
3.46	3d Empty cavity: profile of u_1 for the considered line	69
3.47	3d Empty cavity: u_2 along l_3	70
3.48	3d Empty cavity: profile of u_2 for the considered line	70
3.49	Mesh for the 2d horizontal case	70
3.50	Mesh for the 2d vertical case	70

3.51	2d Horizontal plate: θ for IVM and BF	70
3.52	2d Horizontal plate: velocity for IVM and BF	71
3.53	2d Vertical plate: θ for IVM and BF	71
3.54	2d Vertical plate: velocity for IVM and BF	71
3.55	2d Vertical obstacle: θ along considered lines 1/2	72
3.56	2d Vertical obstacle: u_2 along considered lines 1/2	72
3.57	2d Vertical obstacle: θ along considered lines 2/2	72
3.58	2d Vertical obstacle: u_2 along considered lines 2/2	72
3.59	2d Horizontal obstacle: θ along considered lines 1/2	73
3.60	2d Horizontal obstacle: u_2 along considered lines 1/2	73
3.61	2d Horizontal obstacle: θ along considered lines 2/2	73
3.62	2d Horizontal obstacle: u_2 along considered lines 2/2	73
3.63	3d Horizontal plate: IVM mesh	74
3.64	3d Vertical plate: IVM	74
3.65	3d Horizontal plate: θ in the $z = 0.5$ plane	75
3.66	3d Horizontal plate: velocity in the $z = 0.5$ plane	75
3.67	3d Horizontal plate: θ in the $y = 0.5$ plane	75
3.68	3d Horizontal plate: velocity in the $y = 0.5$ plane	76
3.69	3d Vertical plate: θ in the $z = 0.5$ plane	76
3.70	3d Vertical plate: velocity in the $z = 0.5$ plane	76
3.71	3d Vertical plate: θ in the $y = 0.5$ plane	77
3.72	3d Vertical plate: velocity in the $y = 0.5$ plane	77
3.73	3d Horizontal plate: u_2 along l_4	77
3.74	3d Horizontal plate: θ along l_4	77
3.75	3d Horizontal plate: u_3 along l_4	78
3.76	3d Horizontal plate: corresponding velocity profile	78
3.77	3d Horizontal plate: u_2 along l_5	78
3.78	3d Horizontal plate: θ along l_5	78
3.79	3d Horizontal plate: u_1 along l_5	78
3.80	3d Horizontal plate: corresponding velocity profile	78
3.81	3d Vertical plate: u_3 along l_6	79
3.82	3d Vertical plate: θ along l_6	79
3.85	2d Mixed convection: velocity at several time steps	80
3.86	2d Mixed convection: velocity at several time steps	81
3.87	2d Mixed convection: mesh at several time steps	81
4.1	Illustration of the photon balance on an elementary volume	85
4.2	Geometric characteristics of the two surfaces	90
4.3	Illustration of the crossed strings method	92
4.4	Different possibility for surfaces relative orientations	93
4.5	Notations for visibility test	94
4.6	Two surfaces obstructed by a third	94
4.7	Notations for obstruction test	95
4.8	2d Situations	100
4.9	3d Situations	100
4.10	Test on a square brick: mesh	101
4.11	Test on a square brick: elements crossed (zoom on the corner)	101

4.12	Test on a rectangular circle: mesh	101
4.13	Test on a rectangular circle: elements crossed	101
4.14	2d Example: Mesh	102
4.15	2d Example: levelset of the square	102
4.16	2d Example: Element crossed by The levelset zero isovalue	102
4.17	2d Example: levelset zero isovalue	102
4.18	3d Example: Mesh	103
4.19	3d Example: levelset Zero isovalue and Flag field	103
4.20	3d Adapted mesh: brick	104
4.21	3d Adapted mesh: cylinder	104
4.22	2d Empty cavity: iso temperature and streamlines: $\varepsilon = 0$	107
4.23	2d Empty cavity: iso temperature and streamlines: $\varepsilon = 1$	107
4.24	2d Empty cavity: θ along $y = 0.5$	107
4.25	2d Empty cavity: temperature profile BF $\varepsilon = 1$	108
4.26	2d Empty cavity: temperature profile IMV $\varepsilon = 1$	108
4.27	2d Empty cavity: velocity profile BF $\varepsilon = 1$	108
4.28	2d Empty cavity: velocity profile IMV $\varepsilon = 1$	108
4.29	2d Empty cavity: θ along $y = 0.5$	108
4.30	2d Empty cavity: u_1 along $y = 0.5$	108
4.31	2d Empty cavity: θ along $x = 0.5$	109
4.32	2d Empty cavity: u_2 along $x = 0.5$	109
4.33	3d Empty cavity: iso Temperature: $\varepsilon = 1$ (left) and $\varepsilon = 0$ (right)	109
4.34	3d Empty cavity: iso Temperature: $\varepsilon = 1$ (left) and $\varepsilon = 0$ (right)	109
4.35	3d Empty cavity: streamlines along x : $\varepsilon = 1$ (left) and $\varepsilon = 0$ (right)	110
4.36	3d Empty cavity: streamlines along z : $\varepsilon = 1$ (left) and $\varepsilon = 0$ (right)	110
4.37	3d Empty cavity: θ along l_1	111
4.38	3d Empty cavity: u_3 along l_1	111
4.39	2d Horizontal plate: iso temperature and streamlines: $\varepsilon = 0$	112
4.40	2d Horizontal plate: iso temperature and streamlines: $\varepsilon = 1$	112
4.41	2d Horizontal plate: θ along $y = 0.15$	112
4.42	2d Horizontal plate: V_y along $y = 0.15$	112
4.43	2d Vertical plate: iso temperature and streamlines: $\varepsilon = 0$	113
4.44	2d Vertical plate: iso temperature and streamlines: $\varepsilon = 1$	113
4.45	2d Vertical plate: θ along $y = 0.15$	113
4.46	2d Vertical plate: u_2 along $y = 0.15$	113
4.47	2d Horizontal obstacle: iso temperature $\varepsilon = 1$	113
4.48	2d Horizontal obstacle: streamlines $\varepsilon = 1$	114
4.49	2d Horizontal obstacle: iso temperature $\varepsilon = 1$	114
4.50	2d Horizontal obstacle: streamlines $\varepsilon = 1$	114
4.51	2d Vertical obstacle: θ along considered lines	115
4.52	2d Vertical obstacle: u_2 along considered lines	115
4.53	2d Horizontal obstacle: θ along considered lower lines	115
4.54	2d Horizontal obstacle: u_2 along considered lower lines	115
4.55	2d Horizontal obstacle: θ along considered upper lines	115
4.56	2d Horizontal obstacle: u_2 along considered upper lines	115
4.57	3d Horizontal obstacle: iso-temperature : $\varepsilon = 1$ (left) and $\varepsilon = 0$ (right)	116
4.58	3d Horizontal obstacle: streamlines: $\varepsilon = 1$ (left) and $\varepsilon = 0$ (right)	116

4.59	3d Vertical obstacle: iso-temperature : $\varepsilon = 1$ (left) and $\varepsilon = 0$ (right)	117
4.60	3d Vertical obstacle: streamlines: $\varepsilon = 1$ (left) and $\varepsilon = 0$ (right)	117
5.1	Radiative Energy for P_1 model (left) and M_1 model (right): $t = 5\delta t$	136
5.2	Radiative Energy for P_1 model (left) and M_1 model (right): $t = 25\delta t$	136
5.3	Radiative Energy for P_1 model (left) and M_1 model (right): $t = 400\delta t$	136
5.4	Radiative Energy for P_1 model (left) and M_1 model (right): steady state	136
5.5	L^2 error with respect to the mesh size	137
5.6	Adapted mesh and levelset of the center zone	138
5.7	Patterns of the radiative energy obtained for P_1 (left) and M_1 (right) models	139
5.8	Radiative Energy along $x = 0.5$: present results	139
5.9	Radiative Energy along $x = 0.5$: reference from [274]	139
5.10	Adapted mesh and levelset of the center zone	140
5.11	Patterns obtained for M_1 model	141
5.12	Patterns obtained for P_1 model	141
5.13	Iso-lines obtained for M_1 model	141
5.14	Iso-lines obtained for P_1 model	141
5.15	Distributed absorption and adapted mesh	142
5.16	Radiative Energy for the P_1 model (bottom) and for the M_1 model (top)	142
6.1	Geometry of the hat-shaped disk	146
6.2	The obtained adapted mesh	147
6.3	Position of the different sensors inside the disk	147
6.4	Comparisons of the temperature evolution in sensor 3	147
6.5	Comparisons of the cooling speed in sensor 3	147
6.6	Comparisons of the temperature evolution in sensor 7	148
6.7	Comparisons of the cooling speed in sensor 7	148
6.8	Comparisons of the temperature evolution in sensor 14	148
6.9	Comparisons of the cooling speed in sensor 14	148
6.10	The experimental setup	149
6.11	Position of the sensors	149
6.12	Position of the different injectors	150
6.13	The obtained adapted mesh	150
6.14	Comparisons of the temperature evolution in sensor 1	150
6.15	Comparisons of the cooling speed in sensor 1	150
6.16	Comparisons of the temperature evolution in sensor 2	151
6.17	Comparisons of the cooling speed in sensor 2	151
6.18	Comparisons of the temperature evolution in sensor 3	151
6.19	Comparisons of the cooling speed in sensor 3	151
6.20	Comparisons of the temperature evolution in sensor 4	151
6.21	Comparisons of the cooling speed in sensor 4	151
6.22	Comparisons of the temperature evolution in sensor 5	152
6.23	Comparisons of the cooling speed in sensor 5	152
6.24	The immersed disk inside the chamber: experimental (left) and numerical (right)	152
6.25	The adapted obtained mesh	153
6.26	A snapshot of the streamline solution	153

6.27	Comparisons of the temperature evolution in sensor 1	153
6.28	Comparisons of the cooling speed in sensor 1	153
6.29	Comparisons of the temperature evolution in sensor 2	154
6.30	Comparisons of the cooling speed in sensor 2	154
6.31	Comparisons of the temperature evolution in sensor 3	154
6.32	Comparisons of the cooling speed in sensor 3	154
6.33	Comparisons of the temperature evolution in sensor 4	154
6.34	Comparisons of the cooling speed in sensor 4	154
6.35	Comparisons of the temperature evolution in sensor 5	155
6.36	Comparisons of the cooling speed in sensor 5	155
6.37	Cross section along the xz plane with hessian metric	156
6.38	Cross section along the xz plane with edge based metric	157
6.39	Cross section along the xy plane with hessian metric	157
6.40	Cross section along the xy plane with edge based metric	157
6.41	Cross section along the yz plane with hessian metric	157
6.42	Cross section along the yz plane with edge based metric	158
6.43	patterns of streamlines obtained for the facility	158
6.44	Conduction-radiation: temperature cross section at $t = 500s$	159
6.45	Conduction-radiation: temperature cross section at $t = 812.5s$	159
6.46	Conduction-radiation: temperature cross section at $t = 1312.5s$	160
6.47	Conduction-radiation: temperature cross section at $t = 2125s$	160
6.48	Conduction-radiation: pattern of streamlines and iso temperature surfaces	161

List of Tables

2.1	2d Empty cavity: comparisons with benchmark solutions	34
2.2	3d Empty cavity: comparisons with benchmark solutions	36
3.1	Notations for the mesh.	53
3.2	2d plates: y for the chosen lines	72
3.3	3d plates: coordinates of the chosen lines	74
4.1	Notations for the mesh.	99
4.2	Notations for faces numbers.	103
4.3	2d Meshes	104
4.4	3d Meshes	105
4.5	3d Empty cavity: comparisons with benchmark solution	110
4.6	2d Horizontal plate: comparisons with benchmark solution	111
4.7	2d Vertical plate: comparisons with benchmark solution	112
5.1	Meshes used for the error analysis	137
5.2	Thermodynamical properties of the considered case	140
6.1	Properties of materials.	146
B.1	Weights and abscissas for the considered quadrature	170

Abbreviations

PDE	P artial D ifferential E quation
FEM	F inite E lement M ethod
NS	N avier S tokes
CDR	C onvection D iffusion R eaction
VMS	V ariational M ulti S cale M ethod
SUPG	S treamline U pwind P etrov G alerkin
SCPG	S hock C apturing P etrov G alerkin
IVM	I mmersed V olume M ethod
BF	B ody F itted
RTE	R adiative T ransfer E quation
DOM	D iscrete O rdinates M ethod

Physical Constants

Speed of Light	c	$=$	$2.997\,924\,58 \times 10^8 \text{ m} \cdot \text{s}^{-1}$
Gravity acceleration	g	$=$	$9,80665 \text{ m} \cdot \text{s}^{-2}$
Planck constant	h	$=$	$6,62607004 \times 10^{-34} \text{ m}^2 \cdot \text{kg} \cdot \text{s}^{-1}$
Boltzmann constant	k	$=$	$1,38064852 \times 10^{-23} \text{ m}^2 \cdot \text{kg} \cdot \text{s}^{-2} \cdot \text{K}^{-1}$
Stefan-Boltzmann constant	$\sigma_r = \frac{2\pi^5 k^4}{15h^3 c^2}$	$=$	$5,670373.13 \times 10^{-8} \text{ kg} \cdot \text{s}^{-2} \cdot \text{K}^{-4}$

Symbols

d	space dimension	/
\mathbb{R}	set of real numbers	/
$\ \mathbf{X}\ _p$	L_p norm of a vector \mathbf{X}	/
$\nabla()$	Gradient operator	m^{-1}
$\nabla \cdot ()$	Divergence operator	m^{-1}
$\mathbf{u}(\mathbf{x}, t)$	velocity field	$\text{m} \cdot \text{s}^{-1}$
$p(\mathbf{x}, t)$	pressure field	$\text{Kg} \cdot \text{m}^{-1} \cdot \text{s}^{-2}$
$T(\mathbf{x}, t)$	temperature field	K
$I(\mathbf{x}, t, \boldsymbol{\omega})$	specific radiative intensity	$\text{Kg} \cdot \text{m}^3 \cdot \text{K}^{-3}$
$E_r(\mathbf{x}, t)$	radiative energy	$\text{Kg} \cdot \text{m}^3 \cdot \text{K}^{-3}$
$\mathbf{F}_r(\mathbf{x}, t)$	radiative flux	$\text{Kg} \cdot \text{m}^3 \cdot \text{K}^{-3}$
h	convection coefficient	$\text{W} \cdot \text{m}^{-2} \cdot \text{K}^{-1}$
ρ	density	$\text{Kg} \cdot \text{m}^{-3}$
η	dynamic viscosity	$\text{Kg} \cdot \text{m}^{-1} \cdot \text{s}^{-1}$
λ	thermal conductivity	$\text{Kg} \cdot \text{m} \cdot \text{s}^{-3} \cdot \text{K}^{-1}$
c_p	heat capacity	$\text{m}^2 \cdot \text{s}^{-2} \cdot \text{K}^{-1}$
β	thermal expansion coefficient	K^{-1}
κ	absorption opacity	m^{-1}
σ	scattering opacity	m^{-1}
$\boldsymbol{\omega}$	solid angle vector	/
ε	emissivity	/

For my family...

Chapter 1

Motivations, context and working environment

1.1 General Introduction

The engineering problems encountered today in the field of material forming processes are getting more and more complex, due to the fast evolution of technology for existing processes, the design of new materials and the need to produce more and more sophisticated devices. This leads engineers, guided by economic and quality products constraints, to try to achieve a better understanding of those processes, and therefore gain a better control of those processes. To this end, two main different approaches can be adopted to reach the required level of understanding:

- The first is to use experimental devices to monitor the process: by measuring relevant physical quantities (temperature, heat flux , velocity of the air,...) at several locations of the considered facility. This approach is widely used in many situations, and its efficiency is not to be demonstrated anymore, but, on the one hand, a particular experimental set up remains largely facility-dependant, and, on the other hand, when applied to "real" devices, that is to say the ones used for the industrial processes, the cost can easily become substantial, due to the experimenters, energy for the device and raw material.
- The second consists in the numerical modelling and simulation of the system of interest: the first step is the modelling step, when physics is used to describe the physical phenomena (flow, heat transfer, electromagnetism, material deformations, ...) formally, most of the time by means of partial differential equations

(PDE), referred to as models in the following. When different physical phenomena are at stake, a coupling strategy has to be conceived to ensure the exchange between models. Since in most cases corresponding to real situations, analytical solutions of those PDE are not available, alternative means are needed to obtain a quantitative description of system output. Hence, the second step consists in working on the model to convert it into a form where a computer can be used to get an approximation of the system output; this step, related to the field of applied mathematics, is often referred to as numerical analysis. The third step, closely related to the second one, consists in the implementation of the designed method, using softwares (MATLAB©, SciLab©) or programming languages (C++, FORTRAN) to concretely obtain the desired output. The result of this process will be referred to as a "code" in the following. Once this work has been done, one needs to ensure that the simulated result is realistic, or, in other words, one has to ensure the global model properly mimics the considered system.

If the engineers used methods, both experimental or numerical, that are well established and mastered, the diversity of industrial problems poses new problems everyday, and the duty to propose answers to those new problems belongs to researchers. Even if experimental and numerical approaches correspond to two very different (sometimes distinct) communities, the two approaches present complementary features, and a performant framework for analysis of real industrial systems should, from the author's point of view, combine the two approaches. For example, a numerical simulation tool should be at first tested on "academic" examples (i.e examples not corresponding to physical situations) in order to assess the robustness and performances of the designed tools. Once the obtained results are considered satisfactory, the tool can undergo the trial of a real industrial investigation. Then, the results can be compared to experimental data, provided by an appropriate monitoring of the facility. An analysis of the deviation between experimental and numerical datas will help to improve the code. This PhD comes within a such approach, applied to the study of heat transfer in industrial furnaces and quenching problems. Since the PhD is part in the Thost consortium, all the involved compagnies will be briefly presented. Then, the working environment will be described, with a particular focus on the computational tools used for the numerical simulations. Finally, a short description of the physics of industrial furnaces will be given, in order to highlight the critical points that will be adressed in this PhD and to recall the past and ongoing research on this topic

1.2 General Context

1.2.1 Industrial Context

The consortium Thost, created in 2006, composed of the following industrial partners:



AUBERT & DUVAL Created in 1907, Aubert & Duval is part of the Eramet group. The group employs about 4.700 collaborators and declares a turnover of 991 million euros in 2015. They are specialized in hot material forming processes for steel and aluminium alloys for various applications within the high standards requirements: aeronautics, automotive and medical among others.



SAFRAN AIRCRAFT ENGINE Formerly the national society for study and design of aircraft engines (SNECMA) founded in 1945, it is now part of the Safran group. They produce engines for the aerospace and aeronautics (both civilian and military) industry. They employ about 11.600 people over 12 different sites in France. The declared turnover in 2015 is 7.6 billions euros in 2015.



AREVA Created in 2001, AREVA is a French group in the field of Energy, the core business being the nuclear energy, with various tasks as uranium extraction, operation of nuclear plants and management of nuclear wastes. Composed of about 42.000 collaborators, the declared turnover was 8.3 billions euros in 2014.



FAURECIA Created in 1997, Faurecia produces various automotive equipments, and is the world leader of equipments for automotive interior and seating. Employing 99.000 collaborators all around the world, the declared turnover is about 18.83 billions euros in 2014.



LISI AEROSPACE Part of the LISI group, founded in 1899, Lisi Aerospace is specialized in the fabrication of clamping devices and components for the aeronautics industry. Employing about 11.000 collaborators, the declared turnover in 2015 is of 1.458 millions euros.



SCIENCE COMPUTERS CONSULTANTS Created in 2001, Science Computers Consultants is not an industrial partner, but the society that produces the software to be used by the industrial partners from the C++ code developed in the CEMEF, as well as other products as XIMEX ©, LUDOVIC © and SOLID ©. It is a SME of 5 collaborators with a declared turnover of 401.880 euros in 2015.

1.2.2 Academic Context



This PhD was conducted in the CEMEF (Center for Material Forming). Founded in 1976, it is part of Mines Paristech, a French Engineering school created in 1783. Originally specialized in the modelling of material forming processes for polymers and metallurgy, it has recently acquired an expertise in the field of computational fluid dynamics and heat transfer, with PhD's on Finite Element method for fluid flow and heat transfer [1], numerical simulation of boiling [2], Fluid Structure Interaction [3], space time adaptation [4] and NURBS for complex geometries [5].

1.3 Working environment

1.3.1 Computational environment

All the numerical methods that will be described in this PhD will have to be implemented. This will be done in the CIMLIB library [6]: it is a collaborative C++ library, developed since 15 years. It is connected with external libraries, as PETSC [7] to handle the linear algebra (vector and matrix manipulation, linear system resolution) and MPI [8] (Message passing interface) to handle the parallel processing. It is worth mentioning that we have at our disposal advanced tools for parallel meshing and remeshing [9] that will be at the heart of this work.

1.3.2 General assumptions

We detail here all the common features of the results that will be presented in this thesis, that will not be repeated again, with the exception of chapter 5 where a new formulation will be presented:

- All physical properties will be expressed in units of the international system, so the unities will not be repeated in this thesis.
- For all finite element simulations, we will make use of P_1 approximations, on meshes of tetrahedral elements (triangles in $2d$). Moreover, the objects related with discrete formulations will be denoted with a subscript h .
- All along this work, differential operators, as gradients and divergences will be manipulated: it is understood that that we use the general tensorial definition, so that those operators apply regardless the order of the considered tensor, knowing that the gradient of a n th order tensor gives a tensor of order $n + 1$, and the divergence of a tensor gives a a tensor of order $n - 1$.

- In the same vein than the previous observation, the inner products and associated norms in functional space will be used indifferently for scalar or vector valued functions, the computations being performed componentwise.

1.4 Physics of industrial furnaces

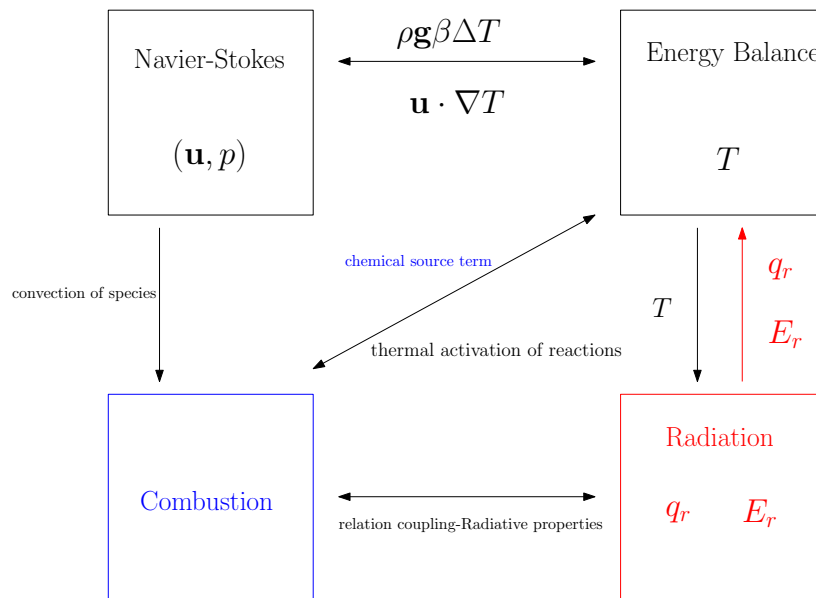


FIGURE 1.1: Illustration of the fully coupled physics in an industrial furnace

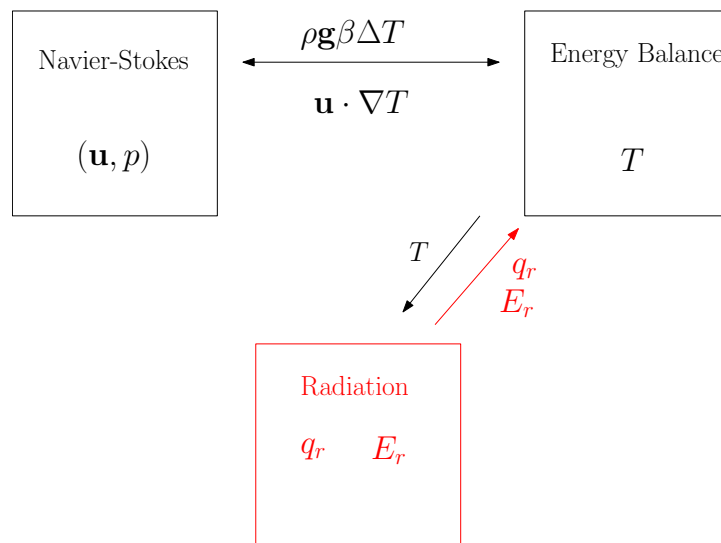


FIGURE 1.2: Illustration of the coupled physics in an industrial furnace without combustion

A lot of coupled physical phenomena are occurring in a furnace or in a quenching chamber: Burners or nozzles generate a flow that drives convective heat transfer, with heat transfer

of other types (conduction inside solid parts, radiation between walls and pieces). Some other phenomena are involved as well, but will not be touched upon in this work:

- In the case of burner, combustion is occurring. It consists in the mixing of different chemical species reacting to form a flame. Modelling this phenomenon requires to deal with a system of convection-diffusion-reaction equations coupled by stiff source terms related to the chemical reaction. It could serve as a PhD topic within itself, and increase the complexity of the full problem, since it would influence the thermal balance due to the energy generated by chemical reactions, the reaction being thermo-active itself. It could even influence the radiative transfer with a growing concentration of combustion products in the enclosure. Due to the increase of complexity it would induce, combustion will be neglected in this thesis, but appears as a promising lead for future work.
- Some metallurgic transformation could occur during the cooling or heating of solid parts. There is some expertise on this field in our laboratory [10], and a coupling with another software could be considered, but it will not be covered in this work.
- In the case of water quenching, heat transfer is caused by boiling and phase change. A PhD on this topic is actually ongoing in the laboratory [11].

Since this thesis will be focused on radiative heat transfer, one could be tempted to evaluate the importance of this phenomenon regarding others: since it is an interface phenomenon, it should be compared with convective heat transfer, so first, it is important to have a simple way to determine the order of magnitude of those transfers. We define $T_c = 20C = 293K$ and $T_h = 1000C = 1273K$ to be the operative temperature of a generic system. Those values are representative of furnaces situations ($T_{ingot} = T_c$ and $T_{enclosure} = T_h$) or quenching ($T_{ingot} = T_h$ and $T_{enclosure} = T_c$), so we will omit signs in further computations.

- The order of magnitude of the radiative heat transfer can be evaluated by $q_{rad} = \sigma_r(T_h^4 - T_c^4)$.
- The order of magnitude of the convective heat transfer can be evaluated by $q_{conv} = h_{conv}(T_h - T_c)$, h_{conv} being the convection coefficient.

Determining the value of h_{conv} for a given application is not a straightforward task. It mostly depends on the thermophysical properties of the considered fluid, and the "characteristics" of the considered situation. If thermophysical properties are temperature dependent only, the "characteristics" of the situations include various different parameters: type of convection (natural or forced), geometry of the enclosure and the object,

nature of the device that generates the flow, etc. Most of the time, it is determined by applying inverse analysis, but can be obtained by using correlations between adimensional numbers relating to the Nusselt number $Nu = \frac{h_{conv}L}{\lambda}$ that relates the *total* heat transfer to the *conductive* heat transfer (other adimensional numbers appearing here will be defined in the chapter 2).

- for forced convection, one has correlations of type

$$Nu = f(Re, Pr) \quad (1.1)$$

- for natural convection, one has correlations of type

$$Nu = g(Ra, Pr) \quad (1.2)$$

In order to set the ideas, we will consider the very simple case of a plate of characteristic dimension $L = 1m$. The thermophysical properties of the air (considered at atmospheric pressure) will be computed at the temperature $T_{av} = \frac{T_c + T_h}{2} = 510C = 783K$. If we approximate $X(T = 510C) \simeq X(T = 500C)$, some realistic values are $\rho = 0.441$, $\eta = 3.63.10^{-5}$, $c_p = 1098$, $\lambda = 0.0578$, $\beta = 1.25.10^{-3}$. We also take $g = \|\mathbf{g}\|_2 = 10$. The radiative flux will be the same value for natural and forced convection.

$$q_{rad} = 1.485.10^5 \text{ W.m}^{-2} \quad (1.3)$$

Natural Convection Those values leads to $Ra = 1.246.10^9$ and $Pr = 0.689$, so that the natural convection can be considered turbulent. Following the lines in [12], we use the following relation:

$$\sqrt{Nu} = 0.825 + \frac{0.387Ra^{\frac{1}{6}}}{(1 + (\frac{0.492}{Pr})^{\frac{9}{16}})^{\frac{8}{27}}} \quad (1.4)$$

We therefore obtain $Nu = 130.945$ and $h_{conv} = 7.568$. It follows that

$$q_{conv} = 7.417.10^3 \text{ W.m}^{-2} \quad (1.5)$$

One can see for those cases, the convective transfer does not exceed 5% of the radiative transfer.

Forced convection Here, one needs to determine a Reynolds number. It might be very dependent on the situations, but when the surrounding fluid is air, a typical value is $Re = 10^5$. Here, the Nusselt number is determined by [13] :

$$Nu = 0.036Re^{0.8}Pr^{0.43}\left(\frac{\eta_h}{\eta_c}\right)^{\frac{1}{4}} \quad (1.6)$$

With $\eta_h = \eta(T = T_h)$ and $\eta_c = \eta(T = T_c)$. We get here $Nu = 390.7$ and $h_{conv} = 22.5$, from which we deduce

$$q_{conv} = 2.21.10^4 \text{ W.m}^{-2} \quad (1.7)$$

Here again, the order of magnitude of the convection is about 15% of the radiative flux, underlining the importance of the phenomenon.

Even if the estimation just presented is not representative of a real industrial situation, it shows the crucial importance of radiative transfer in such situations. Hence, it is mandatory to have at hand performant tools for the modelling of such a phenomenon. This will be the object of this thesis, of which the outline is detailed below

1.5 Outline of the thesis

- First, we will describe the physics of interest here and the formulations used to obtain numerical solutions. This will be the object of chapter 2.
- Then, the framework to deal with complex problems involving different components will be explained in chapter 3.
- Next, we will see the main contribution of this thesis which concerns radiative transfer. To this end, the chapter 4 will give a short overview of the physics of radiation, most common models for our range of applications, and the approach we developed for modelling surface radiation.
- Formerly, we will depict the method developed for volume radiation. Since the model we chose is quite recent (the unifying publication is dated in 1999, even if there exists some previous work), so we will take the time to detail the model, its derivation and its main properties.
- In the chapter 6, we will present real problems rising from our industrials partners to illustrate how all the presented concepts work in unison.

- Finally, chapter 7 will be devoted to some concluding remarks, things that could be improved and ideas for future work.

Résumé français

Les problématiques rencontrées dans le domaine de l'ingénierie deviennent, du fait de l'émergence des nouveaux procédés et technologies, de plus en plus complexes. Dans cette perspective, il est de plus en plus fréquent de recourir à la modélisation numérique afin d'atteindre une meilleure compréhension et, par suite, une meilleure maîtrise de ces procédés. C'est dans ce contexte que s'inscrit ce travail, plus précisément pour la modélisation des transferts thermiques dans le cadre de la mise en forme des matériaux. Ce chapitre constitue une introduction générale de la problématique; on y précise les acteurs académiques et industriels impliqués dans le projet, on y détaille le cadre de travail qui sera utilisé, tant du point de vue théorique que celui de l'implémentation. On expose ensuite les différents phénomènes mis en jeu dans un four industriel, afin de démontrer que le rayonnement thermique y joue un rôle prépondérant, ce qui légitime ce travail de thèse. Enfin on y présente le plan de ce manuscrit.

Chapter 2

Stabilized Finite Element Method for flow and heat transfer

As it was stated previously, even if thermal radiation is the dominant physical phenomenon in industrial furnaces, the approach retained for modelling radiation will be detailed in further chapters. The objective of this chapter is to detail the physical models of phenomena occurring in furnaces. We will see that most of those phenomena can be cast under the form of a convection-diffusion-reaction equation, at the exception of the flow that will be modelled by the Navier Stokes equations. The outline of the chapter will be as follows: we will first give details on the equations, their physical signification and an overview on the different possibilities for the boundary conditions. Then, the stabilized finite element formulations used in this work will be described, and some illustrative benchmarks will be given to demonstrate the potential of the methods. In what follows, we will denote by $\Omega \in \mathbb{R}^d$ the computational domain, and $\partial\Omega$ its boundary, assumed to be regular. The time interval of interest is $[0; T]$

2.1 Physical models

2.1.1 The Navier-Stokes equations

The Navier-Stokes (NS) equations can be considered as the "standard" model for the fluid dynamics. The paternity for this group of equations is to be credited to Claude Navier (1785-1836), a French engineer and physicist of "Ecole Nationale Supérieure des Ponts et Chaussées" specialized in mechanics and Georges Stokes (1819-1903), physicist and mathematician of Cambridge university. The point of view differs from the classical Lagrangian mechanics point of view, where a closed system is considered for the study,

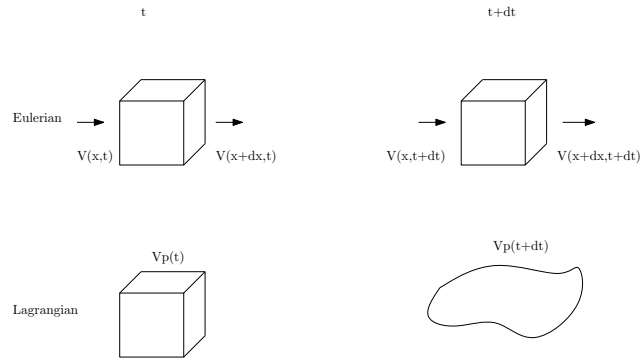


FIGURE 2.1: Illustration of Eulerian and Lagrangian points of view

and is "followed" over time. If this point of view fits for the description of motion of rigid and deformable solids, it is not well adapted for description of fluids, for the reason that it is not easy to "follow" a particle of fluid along its motion. For this problem an Eulerian approach is more adapted: it consists in considering local quantities passing through a fixed certain elementary volume (referred to as "particle of fluid" hereafter) and consider the fluid passing through it over time. This volume should be big enough to perform statistical averages, so that the local quantities of interest will be average of microscopic quantities. Here, the quantities of interest will be:

- A velocity vector $\mathbf{u}(\mathbf{x}, t)$, being an average of velocities of all discrete particles (atoms or molecules) contained in the "particle of fluid". $\mathbf{u}(\mathbf{x}, t)$ is a vector of \mathbb{R}^d , and \mathbf{x} stands for the position. For boundary conditions, it is sometimes useful to work with the components separately, as $\mathbf{u}(\mathbf{x}, t) = (u_i(\mathbf{x}, t))_{i \in \{1; d\}}$.
- A scalar pressure field $p(\mathbf{x}, t)$, representing the average effect of discrete particles on the elementary volume boundary, all contributing to a global surfacic force.

Even though modern physics provides different ways to derive the NS equations, beginning from the Boltzmann equation to the use of the continuum mechanics framework, we will derive it here in a way close to the original one given by Navier and Stokes, by evaluating the momentum balance over the particle of fluid. However, for the kinematics description of the "particle of fluid", one needs to take into account not only the time variations, but also spatial variations due to what is entering and leaving the volume of interest. The appropriate description is given by

$$\frac{D\mathbf{u}}{Dt} = \frac{\partial \mathbf{u}}{\partial t} + (\mathbf{u} \cdot \nabla)\mathbf{u} \quad (2.1)$$

This variation of momentum is balanced by all the forces applied on the volume; we can denote:

- the gravity forces, coming from the gravitation field of the earth, given by $\mathbf{F}_{grav} = \rho \mathbf{g}$. A modified form of this term can be considered to take into account natural convection, but this will be detailed when the fully coupled problem will be presented
- the viscosity forces, caused by the friction due to velocity gradients within the flow. This is given by $\mathbf{F}_{visc} = \nabla \cdot (\eta \nabla(\mathbf{u}))$. We restrain ourselves to the case of Newtonian fluids, so that η will remain constant in the whole fluid, even though temperature-dependancy could be considered.
- The pressure forces: as stated before, the pressure represents the average effect of particles acting on the border of the volume of interest. It is given by $\mathbf{F}_{press} = -\nabla(p)$.

The momentum balance can now be written, and is given by:

$$\rho \frac{D\mathbf{u}}{Dt} = \mathbf{F}_{grav} + \mathbf{F}_{visc} + \mathbf{F}_{press} \quad (2.2)$$

which can be re-arranged in

$$\rho \left(\frac{\partial \mathbf{u}}{\partial t} + (\mathbf{u} \cdot \nabla) \mathbf{u} \right) = -\nabla(p) + \nabla \cdot (\eta \nabla(\mathbf{u})) + \rho \mathbf{g} \quad (2.3)$$

It is now necessary to model the fact that we consider incompressible fluids. A fluid is said to be incompressible when its volume remains constant under the action of an external pressure. In practice, there exists no fully incompressible fluids, but it was stated that, in cases where the characteristic velocity is low compared to the velocity of the sound in the considered medium, the flow can be treated as an incompressible flow. This formally can be written under the form

$$\nabla \cdot \mathbf{u} = 0 \quad (2.4)$$

We are now able to write the NS equations, describing the incompressible flow of a Newtonian fluid.

$$\text{Find } (\mathbf{u}, p) \text{ such } \forall (\mathbf{x}, t) \in \Omega * [0; T] \quad (2.5)$$

$$\begin{cases} \rho \left(\frac{\partial \mathbf{u}}{\partial t} + (\mathbf{u} \cdot \nabla) \mathbf{u} \right) = -\nabla(p) + \nabla \cdot (\eta \nabla(\mathbf{u})) + \rho \mathbf{g} \\ \nabla \cdot \mathbf{u} = 0 \end{cases} \quad (2.6)$$

These equations have received, and are still receiving, interest from researchers, mathematicians as well as engineers, and one of the millenium problems is related to the existence and regularity of solutions in $3d$. We now turn to the the different types of boundary conditions.

2.1.2 Initial and boundary conditions for the Navier-Stokes equations

2.1.2.1 Initial Conditions

In the incompressible version presented above, since there is no transient term for the pressure, no initial condition is needed. For the velocity, one needs to specify $\mathbf{u}_0(\mathbf{x})$, so we have

$$\mathbf{u}(\mathbf{x}, 0) = \mathbf{u}_0(\mathbf{x}) \quad \forall \mathbf{x} \in \Omega \quad (2.7)$$

Note that, for the well posedness of the problem, $\mathbf{u}_0(\mathbf{x})$ should be consistent with the incompressibility constraint, that is to say, we should have $\nabla \cdot \mathbf{u}_0(\mathbf{x}) = 0$.

2.1.2.2 Boundary Conditions

As it is usually done, we make the difference between Dirichlet and Neumann boundary conditions, since the superposition of different types of boundary conditions at the same location would lead to an ill posed problem. Formally, we denote by $\partial\Omega_D$ and $\partial\Omega_N$ the location of Dirichlet (Neumann respectively) boundary conditions. They should verify:

$$\partial\Omega_D \cup \partial\Omega_N = \partial\Omega \quad (2.8)$$

$$\partial\Omega_D \cap \partial\Omega_N = \emptyset \quad (2.9)$$

For the Dirichlet type, the imposed values will be related to the "role" of the boundary or to the way friction is taken into account:

- $\mathbf{u} = \mathbf{u}_D$ with $\mathbf{u}_D \neq 0$ corresponds to the inlet (a burner for a furnace, a nozzle for quenching problems). \mathbf{u}_D can be constant or dependant on a local coordinate to obtain a parabolic profile.
- $\mathbf{u} = 0$ is used for classical solid boundaries, known as a no slip boundary condition. It is also possible to only set to zero the component normal to the boundary.

The Neumann boundary conditions are sometimes referred to as traction boundary conditions, since in the continuum mechanics framework, the stress tensor is related to the velocity gradient by the constitutive relation. Defining boundary conditions at the outlet of the domain is not straightforward, and remains an open question, so a zero Neumann boundary condition will be used for the velocity. One can see [14] for boundary condition related problem of NS equations.

The pressure boundary conditions are of primary importance in the case where $\partial\Omega_N = \emptyset$. In this case, the pressure is defined up to an arbitrary constant, and imposing a specified pressure on a part of the boundary helps to determine this constant.

There exists many ways of with dealing boundary conditions: the penalty method [15], Lagrange multipliers [16], but the Nitsche method has received a growing interest over the past years: it is a way to impose the boundary conditions weakly by remaining consistent with the original PDE, at the contrary of penalty method: it also provides a way to impose conditions on boundaries not fitting the mesh and yields to a symmetric positive definite matrices [17, 18].

2.1.3 The Convection-Diffusion-Reaction equation

If the particular structure of the Navier-Stokes requires a special analysis and treatment, most of the physical phenomena that will be encountered in our context (at the exception of radiation) can be cast in the general form of a convection-diffusion-reaction (CDR) equation that will be detailed in this subsection. An abstract form will be given, and the physical meaning and particular boundary conditions will be enumerated in the next section.

The abstract form reads:

$$\text{find } v(\mathbf{x}, t) \text{ such } \forall(\mathbf{x}, t) \in \Omega * [0; T] \quad (2.10)$$

$$\frac{\partial v}{\partial t} + \boldsymbol{\beta} \cdot \nabla(v) - \nabla \cdot (\lambda \nabla(v)) + \alpha v = f \quad (2.11)$$

the different terms in this equation will be referred to as following:

- the term $\boldsymbol{\beta} \cdot \nabla(v)$ is the convection term. $\boldsymbol{\beta}$ is the convection field, or advection velocity.
- the term $-\nabla \cdot (\lambda \nabla(v))$ is the diffusion term. λ stands for the diffusion coefficient.

- the term αv is the reaction term, α being the reaction coefficient.
- f represents the source term, or forcing term.

All the particular cases of this abstract form share the need of prescribing an initial condition of the form

$$v(\mathbf{x}, 0) = v_0(\mathbf{x}) \quad \forall \mathbf{x} \in \Omega \quad (2.12)$$

The different physical situations and associated boundary conditions are detailed below, but what was said about $\partial\Omega_D$ and $\partial\Omega_N$ holds for the CDR equation as well.

2.1.4 Different physical examples of Convection-Diffusion-Reaction equations

2.1.4.1 The energy equation

This equation, issued from the first principle of thermodynamics (energy balance) governs the variations of temperature. It is sometimes presented with the NS equations, for schemes where all equations are solved together, referred to as "strong" coupling. In all this work, a weak coupling will be used, that is to say, all equations are solved consecutively, and the quantities involved in the coupling terms are treated explicitly, as known quantities from the previous time stepping.

$$\rho c_p \left(\frac{\partial T}{\partial t} + \mathbf{u} \cdot \nabla T \right) - \nabla \cdot (\lambda \nabla T) = f \quad (2.13)$$

\mathbf{u} represents here the velocity field coming from the NS equation. For this reason, the assumption of a divergence-free velocity field is often made in the analysis of the CDR equation. f might be temperature-dependent, as it will be the case for the P_1 radiation model that will be described below, but it will always be treated in an explicit manner. For the energy equation, the following boundary conditions will be considered:

- $T = T_D$ will be used for illustrative benchmarks mostly, or at nozzles for quenching problems. However this type of boundary condition is rarely representative of real situations.
- $\nabla(T) \cdot \mathbf{n} = q_N$ will be encountered more often, a zero value corresponding to an adiabatic wall, a constant prescribed value representing the interaction between a volumic boundary and the outer environment. Modelling radiation by computing a flux involving border temperatures and geometric quantities is also a possibility, and will be the object of chapter 4.

2.1.4.2 $k - \varepsilon$ Turbulence model

It is known that, for turbulent flows (roughly speaking, with high velocities or low viscosity, but this will be detailed further) often encountered in industrial furnaces, a chaotic behaviour of the flows is observed, resulting from large structures and small structures. The large scale is responsible of the transport of the major part of the conserved quantities and the small scale is composed of whirlpools of changing characteristics being zero on average. It is in theory possible to model those effects by a direct resolution of the transient NS equations, but the computation power to perform such simulations is in practice out of range, since the grid size required is related to $Re^{\frac{9}{4}}$ (with Re to be defined later on). To circumvent this issue, modelling turbulence allows to properly model the large scale by taking into account the small structures effects. Many options are possible for modelling of turbulence, and the one retained here is to solve supplementary equations, the resulting quantities being used to include turbulence effects in physical parameters, like viscosity and thermal conductivity. The $k - \varepsilon$ model was chosen here: the idea is to introduce two equations governing the turbulent kinetic energy k and its dissipation rate ε . The more general model, derived from the NS equations [19] presents unknown constants, for which values are situation-dependent, and are available in literature [20]. There also exists a well established one equation model, the Spallart-Allmaras model [21], but on the one hand, it is more dedicated to external flows and on the other hand, the way to properly derive a turbulent conductivity has not been clearly investigated yet, so the following version of the $k - \varepsilon$ model will be used here :

$$\rho \left(\frac{\partial k}{\partial t} + \mathbf{u} \cdot \nabla(k) \right) - \nabla(\mu + \mu_t \nabla(k)) + \rho \varepsilon = P_t \quad (2.14)$$

$$\rho \left(\frac{\partial \varepsilon}{\partial t} + \mathbf{u} \cdot \nabla(\varepsilon) \right) - \nabla(\mu + \mu_t \nabla(\varepsilon)) + C_1 \rho \frac{\varepsilon^2}{k} = C_2 \frac{\varepsilon}{k} P_t \quad (2.15)$$

with $C_1 = 1.92$, $C_2 = 1.44$ and $C_3 = 0.09$. $P_t = \frac{\mu_t}{2} ((\nabla(\mathbf{u})) + \nabla(\mathbf{u})^T)$ is the turbulent production. The results are used to compute turbulent and effective viscosity as well as conductivity μ_t , λ_t and μ_{eff} , λ_{eff}

$$\mu_{eff} = \mu + \underbrace{C_3 \frac{\rho k^2}{\varepsilon}}_{=\mu_t}, \quad \lambda_{eff} = \lambda + \underbrace{\frac{c_p \mu_t}{0.85}}_{=\lambda_t} \quad (2.16)$$

where the constant $Pr_t = 0.85$ corresponds to a turbulent Prandtl number (to be defined later on). The boundary conditions are related to the ones used for NS equations. At an inlet, for a prescribed velocity u_D , one has

$$k = c_{bc} \|u_D\|_2^2 \quad (2.17)$$

$$\varepsilon = C_3 \frac{k^{\frac{3}{2}}}{L} \quad (2.18)$$

where c_{bc} is an empirical constant (set to 0.02 here) and L is a characteristic length of the model.

At the outflow boundary, zero Neumann boundary condition are usually applied.

The boundary conditions on solid walls require a more sophisticated treatment. A law wall on a layer of thickness δ is considered, with a tangential stress τ_w opposite to the local velocity, given by

$$\frac{\|\mathbf{u}\|_2}{\sqrt{\frac{\tau_w}{\rho}}} - \frac{1}{\chi} \ln\left(E \frac{\delta \rho}{\eta t} \sqrt{\frac{\tau_w}{\rho}}\right) = 0 \quad (2.19)$$

where E is related to the roughness of the wall and $\chi = 0.41$. Defining $u_* = \sqrt{\frac{\tau_w}{\rho}}$, the following values are imposed as Dirichlet boundary conditions for k and ε :

$$k = \frac{u_*^2}{\sqrt{C_3}} \quad (2.20)$$

$$\varepsilon = \frac{u_*^3}{\chi} \quad (2.21)$$

An interesting property of those turbulent models is to be noted: the results obtained with turbulence modelling should correspond to the ones obtained by direct resolution of NS equations averaged over space and time. This property is useful to check that the turbulence model is implemented correctly.

2.1.4.3 P_1 Radiation model

As we will see in further chapters, the major issue when dealing with numerical modelling of radiation is the angular dependency. Moreover to be something very unusual in the "engineering physics", it introduces a supplementary dimension to discretize, and for each point. An interesting lead is to consider models where angular dependency is eliminated. This can be done in several ways: expansion using spherical harmonics [22, 23], asymptotic expansion with respect to opacities [24, 25], or averaging over directions

[26]. The simplest model that can be obtained within this approach is given by the following equation

$$\begin{cases} \nabla \cdot \left(\frac{1}{3\kappa} \nabla(G) \right) - \kappa G = 4\kappa\sigma T^4 \\ \frac{\partial G_w}{\partial n} = \frac{3\kappa\epsilon_w}{2(2 - \epsilon_w)} (4\sigma T_w^4 - G_w) \end{cases} \quad (2.22)$$

The boundary condition used here is of Robin type, which is a combination of Dirichlet and Neumann boundary conditions. This model has well known limitations which will be detailed in a further chapter, but it will be useful to perform comparisons with the new method that will be presented in the same chapter.

2.1.5 Fully coupled aerothermal problem

As it can be seen in equation (2.13), a flow of velocity has an effect on the temperature through the term $\mathbf{u} \cdot \nabla T$; that kind of exchange is referred to as *convective* heat transfer. It is easy to understand the effect when the flow is generated independently of the heat transfer (burner, nozzle, turbines,...): this type of transfer is referred to as *forced* convection. However, some flows are generated by a temperature gradient (atmosphere wind formation, earth mantle convection, curls of smoke above hot liquids), referred to as *natural* convection. The physical cause of this phenomenon is the surrounding fluid receiving heat becomes less dense and it rises. A proper modelling would be to consider compressible flows, by modifying equation (2.4) as done in [27], but it leads to a more complex model, whereas most of the flows of interest here can be treated as weakly compressible flows. A good compromise is the Boussinesq approximation, consisting in ignoring the density variations except in the gravity term $\rho \mathbf{g}$. The Boussinesq term reads $\mathbf{F}_{grav} = \rho\beta(T(\mathbf{x}, t) - T_0)\mathbf{g}$, where T_0 is a reference temperature. Under this approximation, the fully coupled aerothermal problem can be formulated as follows:

$$\text{Find } (\mathbf{u}, p, T) \text{ such } \forall (\mathbf{x}, t) \in \Omega * [0; T] \quad (2.23)$$

$$\begin{cases} \nabla \cdot \mathbf{u} = 0 \\ \rho \left(\frac{\partial \mathbf{u}}{\partial t} + (\mathbf{u} \cdot \nabla) \mathbf{u} \right) + \nabla(p) - \nabla \cdot (\eta \nabla(\mathbf{u})) = \rho\beta(T - T_0)\mathbf{g} \\ \rho c_p \left(\frac{\partial T}{\partial t} + \mathbf{u} \cdot \nabla T \right) - \nabla \cdot (\lambda \nabla T) = f \end{cases} \quad (2.24)$$

When the situation requires it, effective viscosity and conductivity, computed by (2.16) will replace η and λ . At this point, it is interesting to introduce some adimensional

numbers characterizing the different "regimes" for this coupled problem. In the following, L is characteristic distance of the considered phenomenon, and U stands for a characteristic velocity

- The Reynolds Number $Re = \frac{\rho UL}{\eta}$. This number represents the ratio between inertial forces $\rho(\mathbf{u} \cdot \nabla)\mathbf{u}$ and viscous forces $\nabla \cdot (\eta \nabla(\mathbf{u}))$. A low value corresponds to a dominant transfer of momentum by diffusion (laminar regime), whereas a high value corresponds to a dominant transfer of momentum by convection (turbulent regime).
- The Rayleigh number $Ra = \frac{\rho^2 c_p g \beta \Delta T L^3}{\eta \lambda}$ is characteristic of the dominant mode of heat transfer within a flow: the low values corresponding to conduction, and high values corresponding to natural convection.
- The Prandtl number $Pr = \frac{\eta c_p}{\lambda}$ compares the diffusion of momentum and the thermal diffusion: the higher the value of the Prandtl number, the more the velocity profile will have an effect on the temperature distribution.
- The Grashof number $Gr = \frac{g \beta \Delta T L^3 \rho^2}{\eta}$, that characterizes the natural convection in a fluid. It can be understood as the ratio of gravity forces on viscous forces and can be related to the Rayleigh and Prandtl number by $Gr = \frac{Ra}{Pr}$.
- The Peclet number $Pe = \frac{\rho c_p LU}{\lambda}$ is the ratio of convective and conductive heat transfer. When applied to a CDR equation with an high value of Pe , the classical formulations will produce numerical solutions of poor accuracy, and justify the stabilization methods that will be exposed in latter parts.

Now all the continuous models (at the exception of radiation) that will be used in this thesis have been presented, the formulations used for the numerical approximations will be detailed.

2.2 Formulations for numerical approximations

The Finite Element Methods, since their emergence in the 1950's, have gained more attention from researchers and engineers with the evolution of computers (see [28] for a short historical review). The main features are the conversion of the initial PDE into a variational problem integrated over the computational domain, and using a piecewise approximation on a triangulation Ω_h that stands for an approximation of the original domain Ω . It permits to work only at the local level (the level of an element of the

triangulation), the assembling procedure being standard and independent of the considered PDE. Moreover, functional analysis offers a setting to predict the quality of the computed approximation (existence, regularity, error estimates). Traditionally used in the field of structural mechanics, its utilisation in other fields of physics draws the attention of many researchers (see [29] for applications to a large class of problems). However, the classical FEM fails to produce accurate solutions when applied to the type of problems described in the precedent part, justifying the design of *Stabilized FEM* that will be the topic of the next part.

2.2.1 Classical Finite Element Formulation for the Navier-Stokes equations

Let us start by defining the functional setting and the Hilbertian structures necessary for a weak formulation

$$L^2(\Omega) = \left\{ w, \text{ such } \int_{\Omega} w d\Omega < \infty \right\} \quad (2.25)$$

$$H^1(\Omega) = \left\{ w \in L^2(\Omega), \text{ such } \int_{\Omega} \|\nabla(w)\|_2 d\Omega < \infty \right\} \quad (2.26)$$

The definition of H^1 is given for scalar valued functions, but the definition straightforwardly extends for vector valued functions componentwise. The subscript 0 for those functional spaces means that the elements of the respective spaces are zero-valued on $\partial\Omega_D$. On those spaces the following form defines an inner product and an associated Hilbertian norm

$$(u, w) = \int_{\Omega} u w d\Omega \quad (2.27)$$

The functional space for p will be $P = L^2(\Omega)$, with a possible zero mean condition, since the pressure is defined up to a additional constant. For \mathbf{u} , one needs to introduce the boundary conditions in the definition of the space, the associated test functions being defined for homogeneous boundary conditions

$$U = \left\{ \mathbf{u} \in (H^1(\Omega))^d, \mathbf{u}|_{\partial\Omega_D} = \mathbf{u}_D \right\} \quad (2.28)$$

$$U_0 = \left\{ \mathbf{u} \in (H^1(\Omega))^d, \mathbf{u}|_{\partial\Omega_D} = 0 \right\} \quad (2.29)$$

U and U_0 are referred to as the trial and test spaces, respectively. The weak formulation of (2.5) is obtained by multiplying by test functions, integrating over the domain and performing integration by parts on certain terms. The weak formulation reads

$$\text{Find } (\mathbf{u}, p) \in U * P \text{ such } \forall (\mathbf{w}, q) \in U_0 * P \quad (2.30)$$

$$\begin{cases} (\rho \frac{\partial \mathbf{u}}{\partial t}, \mathbf{w}) + (\rho(\mathbf{u} \cdot \nabla) \mathbf{u}, \mathbf{w}) + (\eta \nabla(\mathbf{u}), \nabla(\mathbf{w})) + (\nabla(p), \mathbf{w}) = (\rho \mathbf{g}, \mathbf{w}) \\ (\nabla \cdot \mathbf{u}, q) = 0 \end{cases} \quad (2.31)$$

At this stage, even though the pressure was defined as a primary variable, this mixed formulation can be viewed as an augmented formulation, the pressure being a Lagrange multiplier associated to the incompressibility constraint. The Galerkin approximation consists in constructing a approximation Ω_h of Ω into a partition \mathcal{K}_h of non overlapping elements K covering the whole domain. Only triangular elements (tetrahedral in $3d$) will be used here. This partition is then used to construct approximation spaces from (2.26) and (2.25), spanned by basis polynomial functions (shape functions $(\phi_{h,K})_{K \in \mathcal{K}_h}$) on each element of the partition, the global approximated fields (\mathbf{u}_h, p_h) being continuous over the whole domain

$$U_h = \left\{ \mathbf{u}_h \in (C^0(\Omega))^d, \mathbf{u}_{h|_K} \in (P^1(K))^d, \forall K \in \mathcal{K}_h \right\} \quad (2.32)$$

$$P_h = \left\{ p_h \in (C^0(\Omega))^d, p_{h|_K} \in P^1(K), \forall K \in \mathcal{K}_h \right\} \quad (2.33)$$

Expressing (\mathbf{u}_h, p_h) on the basis of shape functions and evaluating (\mathbf{v}, q) for all the shape functions in (2.30) lead to a linear system, the unknown being the values of the fields at points of the triangulation.

2.2.2 Stabilization using the Variational Multiscale Method

2.2.2.1 The need of stabilization

The presented formulation is known to fail for two reasons:

- the theory of mixed finite elements (see [29] for a detailed analysis) state that the approximation spaces should verify an inf-sup condition (also known as Babuska-Brezzi condition), formulated as follows:

$$\exists \beta \text{ such } \inf_{\mathbf{u}_h \in U_{h,0}} \sup_{q_h \in P_h} \frac{(\nabla \cdot \mathbf{u}_h, q_h)}{\|q_h\|_{P_h} \|\mathbf{u}_h\|_{U_{h,0}}} \geq \beta > 0 \quad (2.34)$$

where β is independent of the mesh size h . It imposes a compatibility between velocity and pressure approximation spaces (roughly speaking, the velocity space has to be "bigger" than the pressure space). An option would be to use a different order of interpolation for velocity and pressure ($P_1 - P_0$ or $P_2 - P_1$), but a pressure constant is sometimes not accurate enough for drag and lift computations, and using a P_2 approximation (or higher) is prohibitive in terms of computation time when applied to $3d$ coupled problems. So equal order interpolation pair will be used in this work.

- For turbulent flows, the non-linear convective term $(\mathbf{u} \cdot \nabla)\mathbf{u}$ is the predominant one and might generate spurious oscillations, leading to a poorly accurate approximation.

2.2.2.2 Scale Splitting

Most of the stabilization methods rely on enrichment of functional spaces used in the variational formulation. An option is to add extra diffusion in the upwind direction, but this will be detailed with the variational formulation for CDR equations. For mixed variational formulation, a powerful framework to design a stabilized Finite Element method is the Variational Multiscale method (VMS): proposed by Hughes [30, 31], the idea is to model the effect of the smallest scale structures of the flows, but to numerically resolve only the large scales, so that the small scales are taken into account without an explicit resolution. Formally, it consists in splitting both unknowns and test functions into a large (resolved) part and a small (unresolved) part. This decomposition is then introduced in (2.30) leading to a large scale problem, with supplementary small scale terms that will provide the desired stabilization, and a fine scale problem, with right hand sides being some residuals of the large scale. This problem is solved in an approximate manner, and the fine scale is reintroduced in the large scale problem. The splitting for the unknowns and test functions is performed as follows:

$$U = U_h \oplus \tilde{U} \Rightarrow \mathbf{u} = \mathbf{u}_h + \tilde{\mathbf{u}} \quad (2.35)$$

$$V = V_h \oplus \tilde{V} \Rightarrow \mathbf{v} = \mathbf{v}_h + \tilde{\mathbf{v}} \quad (2.36)$$

$$P = P_h \oplus \tilde{P} \quad (2.37)$$

$$\Rightarrow p = p_h + \tilde{p} \text{ and } q = q_h + \tilde{q} \quad (2.38)$$

Introducing these decompositions in (2.30), one gets the large scale and fine scale problems:

$$\begin{cases} \left(\rho \frac{\partial(\mathbf{u}_h + \tilde{\mathbf{u}})}{\partial t}, \mathbf{v}_h \right) + (\rho(\mathbf{u}_h + \tilde{\mathbf{u}}) \cdot \nabla(\mathbf{u}_h + \tilde{\mathbf{u}}), \mathbf{v}_h) + (\nabla(p_h + \tilde{p}), \mathbf{v}_h) + (\eta \nabla(\mathbf{u}_h + \tilde{\mathbf{u}}), \nabla(\mathbf{v}_h)) = (\rho \mathbf{g}, \mathbf{v}_h) \\ (\nabla \cdot (\mathbf{u}_h + \tilde{\mathbf{u}}), q_h) = 0 \end{cases} \quad (2.39)$$

$$\begin{cases} \left(\rho \frac{\partial(\mathbf{u}_h + \tilde{\mathbf{u}})}{\partial t}, \tilde{\mathbf{v}} \right) + (\rho(\mathbf{u}_h + \tilde{\mathbf{u}}) \cdot \nabla(\mathbf{u}_h + \tilde{\mathbf{u}}), \tilde{\mathbf{v}}) + (\nabla(p_h + \tilde{p}), \tilde{\mathbf{v}}) + (\eta \nabla(\mathbf{u}_h + \tilde{\mathbf{u}}), \nabla(\tilde{\mathbf{v}})) = (\rho \mathbf{g}, \tilde{\mathbf{v}}) \\ (\nabla \cdot (\mathbf{u}_h + \tilde{\mathbf{u}}), \tilde{q}) = 0 \end{cases} \quad (2.40)$$

2.2.2.3 Approximation for the fine scale problem

The next step is to solve (2.40) to reintroduce $(\tilde{\mathbf{u}}, \tilde{p})$ into (2.39). The first step is to move all the large scale terms at the right hand side of the fine scale problem, leading us to define large scale residuals:

$$\mathcal{R}_{u,h} = \rho \mathbf{g} - \left(\frac{\rho \partial \mathbf{u}_h}{\partial t} + \rho(\mathbf{u}_h \cdot \nabla) \mathbf{u}_h + \nabla(p_h) - \nabla \cdot (\eta \nabla(\mathbf{u}_h)) \right) \quad (2.41)$$

$$\mathcal{R}_{p,h} = -\nabla \cdot \mathbf{u}_h \quad (2.42)$$

To solve the fine scale problem, some assumptions have to be made, the quality of the stabilization depending on these assumptions, leading to different features of the fine

scale problem. See [32] for a detailed description of VMS methods for incompressible flows:

- The subscales will not be tracked in time, but will remain time dependent, driven by the large scale residuals. For examples with dynamic subscales, see [33, 34] and [35]
- The non-linear convective term only retains the large scale velocity $((\mathbf{u}_h + \tilde{\mathbf{u}}) \cdot \nabla)(\mathbf{u}_h + \tilde{\mathbf{u}}) \simeq (\mathbf{u}_h \cdot \nabla)(\mathbf{u}_h + \tilde{\mathbf{u}})$. The fine scale problem is therefore linear. For non-linear subscales, see [32].
- The subscales are assumed to vanish on inter-element boundaries, leading to local contributions of each element to the global stabilization term. An extension to non-zero inter-element subscales consists in treating the subscales values with appropriate transmission conditions, see [36]

Now, the fine scale problem can be expressed, in an abstract form, as follows:

$$\mathcal{B}_u(\tilde{\mathbf{u}}, \tilde{p}) = \mathcal{R}_u \quad (2.43)$$

$$\mathcal{B}_p(\tilde{\mathbf{u}}) = \mathcal{R}_p \quad (2.44)$$

The principle is now to express the fine scale only in terms of large scale residuals. It consists in finding a "good" approximation of inverses of operators \mathcal{B}_u and \mathcal{B}_p in a spectral sense. This is done by using a Fourier analysis [37], so that one finally gets:

$$\tilde{\mathbf{u}} = \tau_u \Pi_{\tilde{U}}(\mathcal{R}_{u,h}) \quad (2.45)$$

$$\tilde{p} = \tau_p \Pi_{\tilde{P}}(\mathcal{R}_{p,h}) \quad (2.46)$$

where $\Pi_{\tilde{U}}$ and $\Pi_{\tilde{P}}$ stands for projection operator onto the spaces \tilde{U} and \tilde{P} . Taking the projection operators equal to the identity on the considered space is usually referred to as "Algebraic Subgrid Scale", and will be done in this work. It is also possible to take as orthogonal projection onto finite element spaces, known as "Orthogonal Subscales" [37]. The values of the stabilization parameters τ_u and τ_p are obtained through the Fourier analysis of the fine scale problem, leading to the following values, computed at element level

$$\tau_u = \frac{1}{\sqrt{\left(\frac{c_1 \eta}{\rho h^2}\right)^2 + \left(\frac{c_2 \|\mathbf{u}_h\|_{K,2}}{h}\right)^2}} \quad (2.47)$$

$$\tau_p = \sqrt{\left(\frac{\eta}{\rho}\right)^2 + \left(\frac{c_2 \|\mathbf{u}_h\|_{K,2} h}{c_1}\right)^2} \quad (2.48)$$

where h is the characteristic mesh size, $\|\mathbf{u}_h\|_{K,2}$ is the L^2 norm of the velocity on the element. c_1 and c_2 are algorithmic constants. An interpretation about those constants, available in [37], will be detailed for the CDR equation. It gives conditions on the values of those constants, so that we will take here $c_1 = 4$ and $c_2 = 2$.

The particular VMS approach that we presented have demonstrated its efficiency in many situations: for NS problems only [38, 39], but also for coupled problems rising from industrial applications [40–42]. However, we want to emphasize the fact the VMS framework offers flexibility to design other stabilized formulations: Codina and coworkers have proposed other formulations based on a different treatment of the fine scale problem for incompressible flows [34, 37], flows with Coriolis forces [43], and aerothermal coupled flows [33, 44]. An interesting interpretation about the dissipative structure of the VMS was also presented [45]. We can also quote the work of Jiang and coworkers [46] providing error estimates, the work of Gravemeier [47, 48] using a three-scale VMS method, and publications with special treatment for turbulence [49],[50] and compressible flows [51]. Similar techniques have also been successfully used for Stokes [52, 53] and Darcy [54, 55] [56] flows. In a forthcoming chapter, we will see that the VMS framework can be used for physical models very different of fluid dynamics.

2.2.3 Standard Galerkin Finite Element Method for the CDR equation

Since the CDR equation only involves one scalar equation, the classical Finite Element theory applies here. Even though we demonstrated that this type of equation can be encountered in various situations, the formulation and the stabilization is independent of the physics. If we define the following space:

$$V = \{v \in H^1(\Omega) \mid v|_{\partial\Omega_D} = v_D\} \quad (2.49)$$

homogeneous V_0 and discrete V_h spaces are naturally defined in the same manner than in the previous section.

Multiplying by a test function w and integrating over the domain, one gets

$$\text{Find } v \in V \text{ such } \forall w \in V_0 \quad (2.50)$$

$$\begin{cases} (\frac{\partial v}{\partial t}, w) + \mathcal{B}(v, w) = (f, w) \\ \mathcal{B}(v, w) = (\boldsymbol{\beta} \cdot \nabla(v), w) + (\lambda \nabla(v), \nabla(w)) + (\alpha v, w) \end{cases} \quad (2.51)$$

However, it can be shown that the formulation presented above fails for high Peclet numbers. The following part is then dedicated to stabilization techniques.

2.2.4 Stabilization Techniques for the CDR equation

All the stabilization techniques relies, from a theoretical point of view, on modification of the test function. That kind of Finite Element methods, where trial and test spaces are not the same, is referred to as Petrov-Galerkin methods, at the contrary of Bubnov-Galerkin method, when trial and test spaces are the same.

2.2.4.1 Streamline Upwind Petrov Galerkin (SUPG)

Historically, some numerical pollution were observed for High Peclet numbers. The instability is therefore related to the convective phenomenon. The pioneering work of Hughes [57] was based on the following idea: a one dimensional analysis with help of finite differences show that the *upwind* schemes give more accurate solutions when the Peclet number rises (this can be related to the condition number of the global matrix), that can be interpreted as the artificial diffusion coming from the numerical approximation of the derivatives. A similar term can be obtained in a finite element context by a modification of test function in the following manner:

$$\tilde{\varphi} = \varphi + \tau \boldsymbol{\beta} \cdot \nabla(\varphi) \quad (2.52)$$

2.2.4.2 Shock Capturing Petrov Galerkin (SCPG)

However, in some situations, the streamline direction is not the upwind direction (where artificial diffusion is needed to stabilize the solution). For those situations, Galeo and coworkers [58] extended the SUPG method in the direction of the gradient of the velocity. The test functions are modified accordingly

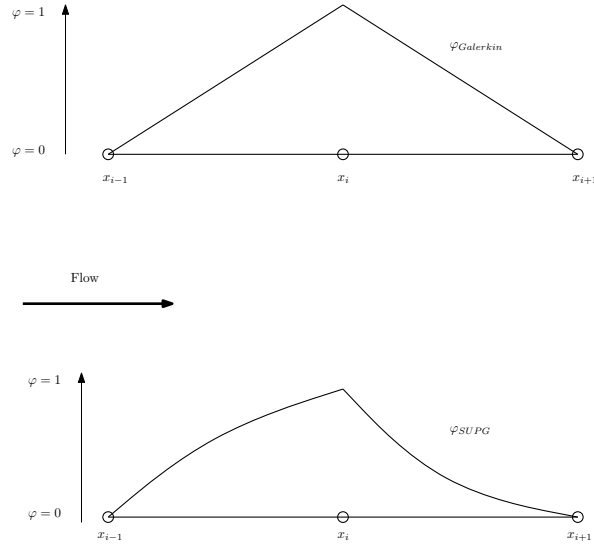


FIGURE 2.2: Illustration of 1d shape function modification

$$\tilde{\varphi} = \varphi + \tau_{SUPG} \boldsymbol{\beta} \cdot \nabla(\varphi) + \tau_{SCPG} \mathbf{w} \cdot \nabla(\varphi) \quad (2.53)$$

$$\mathbf{w} = \begin{cases} \frac{\boldsymbol{\beta} \cdot \nabla(\varphi)}{\|\nabla(\varphi)\|_2} \nabla(\varphi) & \text{if } \nabla(\varphi) \neq 0 \\ 0 & \text{if } \nabla(\varphi) = 0 \end{cases} \quad (2.54)$$

The additional velocity \mathbf{w} is nothing but an orthogonal projection of the advection field $\boldsymbol{\beta}$ onto the gradient of the shape functions.

2.2.4.3 Derivation of the stabilization parameters: a link between SUPG and VMS

The SUPG and SCPG both rely on adding artificial diffusion in a certain direction. However, adding "too much" extra diffusion can modify substantially the solution, rendering it physically irrelevant. Two parameters τ_{SUPG} and τ_{SCPG} were introduced in the previous section, in order to tune the stabilization to only add the required amount of diffusion. An appropriate choice of those parameters is therefore critical in the design of a stabilized Finite Element Method. The values for those parameters were obtained following the lines in [57–59], are:

$$\tau_{SUPG} = \frac{1}{\sqrt{(c_1 \frac{2\|\boldsymbol{\beta}\|_{K,2}}{h})^2 + (c_2 \frac{\lambda}{h^2})^2 + \alpha^2}} \quad (2.55)$$

$$\tau_{SCPG} = \frac{h}{2\|\boldsymbol{\beta}\|_{K,c}} \gamma\left(\frac{\|\boldsymbol{\beta}\|_{K,c}}{\|\boldsymbol{\beta}\|_{K,2}}\right) \quad (2.56)$$

where $\gamma(x) = 2x(1-x)$ and $\|\boldsymbol{\beta}\|_{K,c} = \begin{cases} \frac{\boldsymbol{\beta} \cdot \nabla(\varphi)}{\|\nabla(\varphi)\|_2} & \text{if } \nabla(\varphi) \neq 0 \\ 0 & \text{if } \nabla(\varphi) = 0 \end{cases}$. c_1 and c_2 being algorithmic coefficient similar to the ones evoked for NS equations.

A fully detailed derivation is available in the references quoted above. However, the VMS framework presented in the context of NS equation offers a systematic and rigorous way for deriving the SUPG parameter (The SCPG term consists just in a different computation of the upwind velocity), and such a derivation provides insight about the values of the algorithmic constants.

The first step consists in a scale splitting for both trial and test functions

$$V = V_h \oplus \tilde{V} \Rightarrow v = v_h + \tilde{v} \quad (2.57)$$

$$V_0 = V_{0,h} \oplus \tilde{V}_0 \Rightarrow w = w_h + \tilde{w} \quad (2.58)$$

Introducing (2.57) in (2.50) gives one coarse scale problem and one fine scale problem

$$\left(\frac{\partial(v_h + \tilde{v})}{\partial t}, w_h\right) + \mathcal{B}((v_h + \tilde{v}), w_h) = (f, w_h) \quad (2.59)$$

$$\left(\frac{\partial(v_h + \tilde{v})}{\partial t}, \tilde{w}\right) + \mathcal{B}((v_h + \tilde{v}), \tilde{w}) = (f, \tilde{w}) \quad (2.60)$$

The methodology is similar as before: the fine scale problem has to be approximated to be reintroduced in the coarse scale problem. To this end, we define a residual for the CDR equation, and using similar notations

$$\mathcal{R}(v_h) = f - \frac{\partial v_h}{\partial t} - \boldsymbol{\beta} \cdot \nabla(v_h) + \nabla \cdot (\lambda \nabla(v_h)) - \alpha v_h \quad (2.61)$$

under the same assumptions which detailed for the fine scale problem of NS equations, (2.60) can be re-arranged into

$$(\boldsymbol{\beta} \cdot \nabla(\tilde{v}), \tilde{w}) - (\nabla \cdot (\lambda \nabla(\tilde{v}), \tilde{w}) + (\alpha \tilde{v}, \tilde{w}) = (\Pi_{\tilde{V}}(\mathcal{R}(v_h)), \tilde{w}) \quad (2.62)$$

$$\Rightarrow (\boldsymbol{\beta} \cdot \nabla(\tilde{v}) - \nabla \cdot (\lambda \nabla(\tilde{v}) + \alpha \tilde{v} - \Pi_{\tilde{V}}(\mathcal{R}(v_h))), \tilde{w}) = 0 \quad \forall \tilde{w} \in \tilde{V} \quad (2.63)$$

The last equality says nothing other than the left term of the inner product is zero. To obtain an approximation of the fine scale $\tilde{w} = \tau \Pi_{\tilde{V}}(\mathcal{R}(v_h))$, we follow the pioneering work of [37] by introducing a Fourier transform over an element K with respect to the space dimension.

$$\widehat{v}(\mathbf{k}) = \int_K v(\mathbf{x}) \exp(-i \frac{\mathbf{x} \cdot \mathbf{k}}{h}) dK \quad (2.64)$$

applying this transform to (2.62), one gets

$$\left(\frac{i \boldsymbol{\beta} \cdot \mathbf{k}}{h} - \frac{\|\mathbf{k}\|_2 \lambda}{h^2} + \alpha \right) \widehat{v} = \Pi_{\tilde{V}}(\widehat{\mathcal{R}(v_h)}) \quad (2.65)$$

Using the Plancherel equality and the mean value theorem, the following expression for τ can be obtained

$$\tau = \frac{1}{\sqrt{\left(\frac{\|\mathbf{k}\|_{K,2} \|\boldsymbol{\beta}\|_{K,2} \cos((\boldsymbol{\beta} \cdot \mathbf{k}))}{h} \right)^2 + \left(\frac{\lambda \|\mathbf{k}\|_{K,2}^2}{h^2} \right)^2 + \alpha^2}} \quad (2.66)$$

by setting $c_1 = \|\mathbf{k}\|_{K,2} \cos((\boldsymbol{\beta} \cdot \mathbf{k}))$ and $c_2 = \|\mathbf{k}\|_{K,2}$, it is straightforward that $c_1^2 \leq c_2$, therefore $c_1 = 2$ and $c_2 = 4$ are appropriate values. Some modified parameters can be considered, to include unsteady effects or to ensure a correct asymptotic behaviour regarding the Peclet number, so that the stabilization vanishes when not needed, but we refer the reader to [1] and references therein. The choice of a characteristic mesh size is not straightforward either, and will be detailed in the next chapter.

Now that all the ingredients for the numerical approximation of the physical models presented above was detailed, the next section is devoted to several numerical examples to assess the robustness and accuracy of the presented formulations. Cases of natural convection will be presented, in $2d$ as well as in $3d$.

2.3 Numerical experiments

2.3.1 Natural convection in an empty cavity

The considered case models a square cavity of length $L = 1.0m$, with left and right walls maintained at fixed temperatures T_h and T_c , respectively. Compressibility effects are modelled using the Boussinesq approximation. The physical parameters are chosen here to obtain the desired Rayleigh and Prandtl numbers, as depicted in the appendix A. The horizontal walls are considered adiabatic. The initial condition for temperature is $T_0 = \frac{T_c + T_h}{2}$. Regarding the flow computation, classical boundary conditions are used. We plot the adimensional temperature θ , defined by $\theta = \frac{T - T_c}{T_h - T_c}$. We propose here to explain the variations of temperature and velocity patterns with varying Rayleigh numbers from 10^2 to 10^8 .

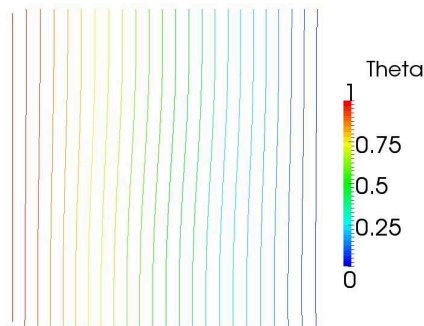


FIGURE 2.3: 2d Empty cavity: iso temperature for $Ra = 10^2$

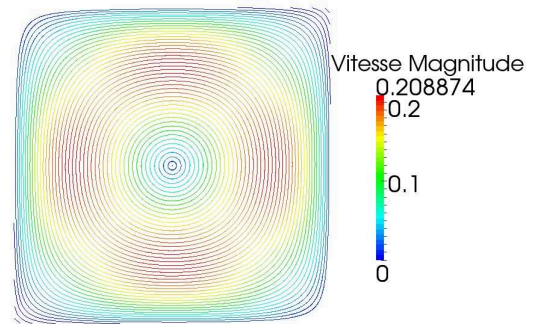


FIGURE 2.4: 2d Empty cavity: streamlines for $Ra = 10^2$

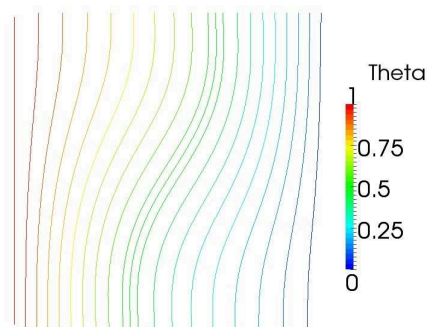


FIGURE 2.5: 2d Empty cavity: iso temperature for $Ra = 10^3$

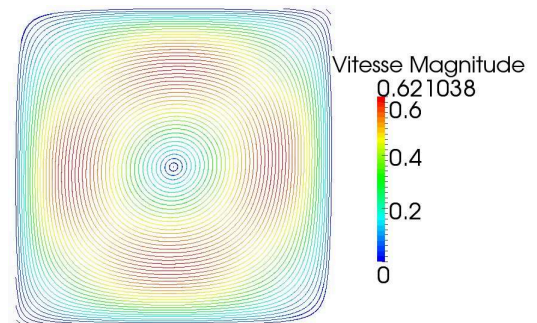


FIGURE 2.6: 2d Empty cavity: streamlines for $Ra = 10^3$

For $Ra = 10^2$ and $Ra = 10^3$, the temperature patterns correspond to almost only the diffusion, with a single recirculation zone at the center of the cavity. For Ra ranging from 10^4 to 10^7 , the iso-lines becoming closer to southwest and northeast boundaries, showing the formation of thermal boundary layers, as we can see on the curves. The

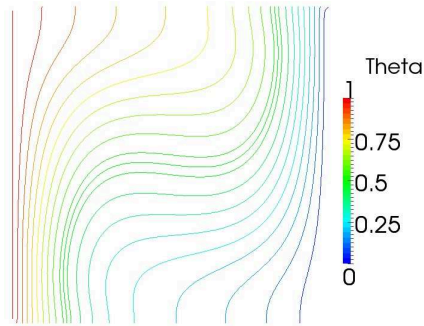


FIGURE 2.7: 2d Empty cavity: iso temperature for $Ra = 10^4$

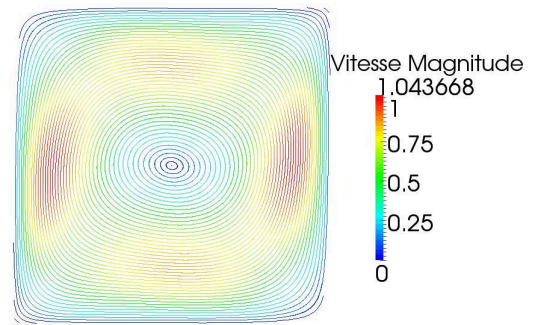


FIGURE 2.8: 2d Empty cavity: streamlines for $Ra = 10^4$

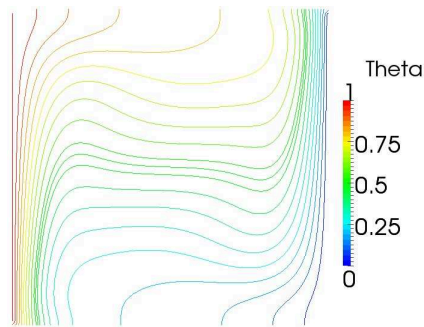


FIGURE 2.9: 2d Empty cavity: iso temperature for $Ra = 10^5$

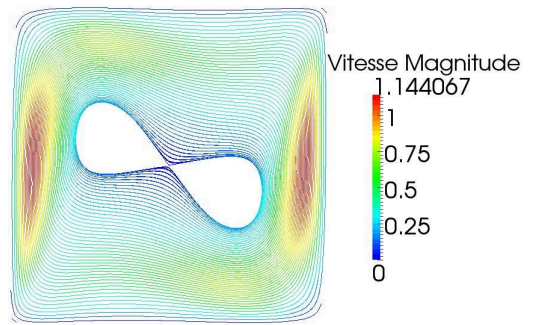


FIGURE 2.10: 2d Empty cavity: streamlines for $Ra = 10^5$

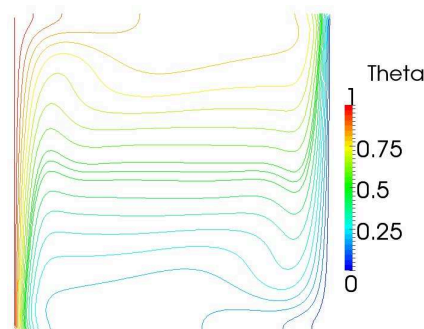


FIGURE 2.11: 2d Empty cavity: iso temperature for $Ra = 10^6$

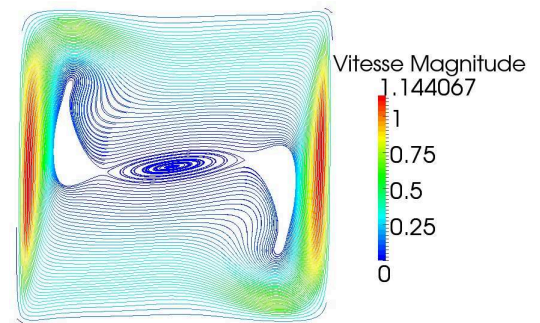


FIGURE 2.12: 2d Empty cavity: streamlines for $Ra = 10^6$

recirculation becomes more curved as Ra increases, creating secondary recirculation zones at the vicinity of the main one (2 for $Ra = 10^5$, 3 for $Ra = 10^6$ and 5 for $Ra = 10^7$). The results for $Ra = 10^8$ shows streamlines becoming chaotic, the flow becoming turbulent for those values. The use of a turbulence model would be necessary for higher values of Ra .

However, even though each value of Ra produces a curve of a certain shape, different set of parameters can lead to such a value. Hence, these curves are not a sufficient tool for

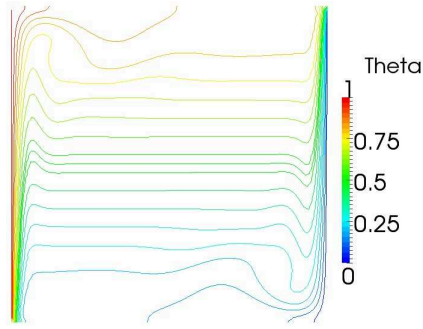


FIGURE 2.13: 2d Empty cavity: iso temperature for $Ra = 10^7$

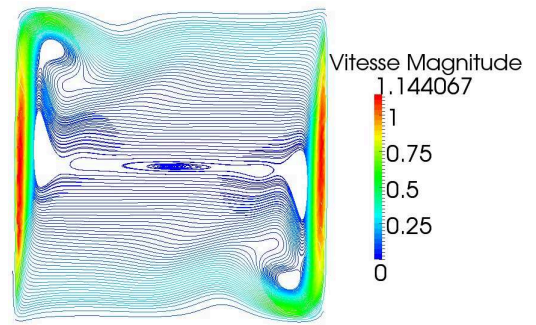


FIGURE 2.14: 2d Empty cavity: streamlines for $Ra = 10^7$

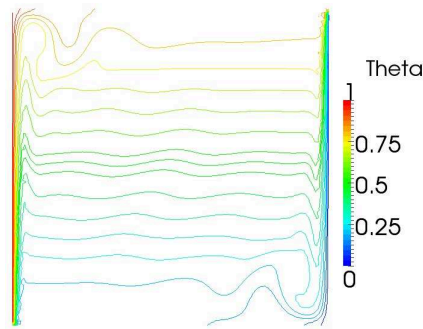


FIGURE 2.15: 2d Empty cavity: iso temperature for $Ra = 10^8$

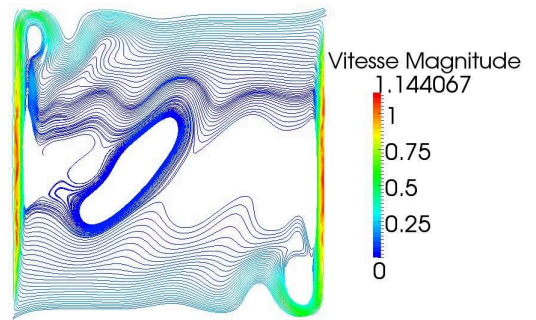


FIGURE 2.16: 2d Empty cavity: streamlines for $Ra = 10^8$

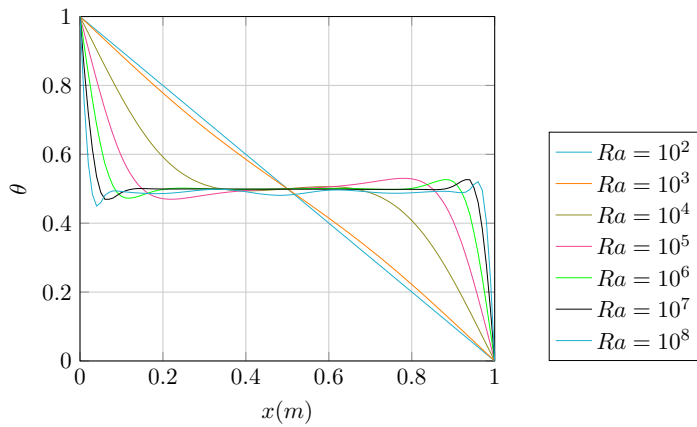


FIGURE 2.17: 2d Empty cavity: θ along $y = 0.5$ for the considered range of Ra

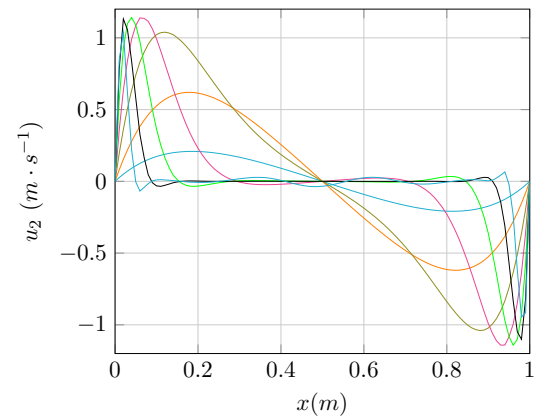


FIGURE 2.18: 2d Empty cavity: u_2 along $y = 0.5$ for the considered range of Ra

the validation of our code. The comparison will then be performed on a local version of the Nusselt number presented in the chapter 1, defined as follows:

$$\overline{Nu}_{conv} = \frac{L}{\lambda(T_h - T_c)} \int_0^1 \frac{\partial T}{\partial x}(0, y) dy \quad (2.67)$$

The obtained values are compared with some of the ones available in literature in the table below:

reference \ Ra	10^3	10^4	10^5	10^6
De Vahl [60]	1.118	2.243	4.519	8.8
Kalita and al. [61]	1.118	2.243	4.521	8.831
Dixit and al. [62]	1.118	2.286	4.5463	8.652
present work	1.13	2.445	4.661	8.446

TABLE 2.1: 2d Empty cavity: comparisons with benchmark solutions

One can see that the maximum discrepancy between the obtained results and the references does not exceed 5%. It is straightforward to extend this case into a three dimensional version by an extrusion in the z dimension. All quantities are symmetric around the point $\mathbf{x}_c = (0.5; 0.5; 0.5)$. The temperature remains invariant by translations in the z direction, since adiabatic walls have no influence on the temperature patterns, and the velocity profile is symmetric around the $z = 0.5$ plane, as it is displayed on the streamlines, plotted along the line $\mathbf{l}_c = (1; 1; 1)$ and the center point \mathbf{x}_c .

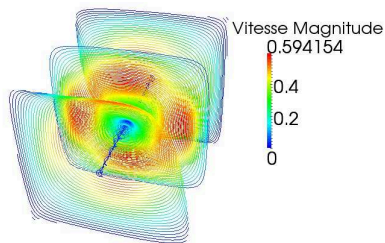


FIGURE 2.19: 3d Empty cavity: streamlines along \mathbf{l}_c for $Ra = 10^3$

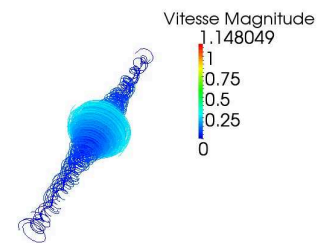


FIGURE 2.20: 3d Empty cavity: streamlines around \mathbf{x}_c for $Ra = 10^3$

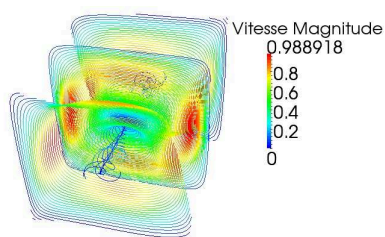


FIGURE 2.21: 3d Empty cavity: streamlines along \mathbf{l}_c for $Ra = 10^4$

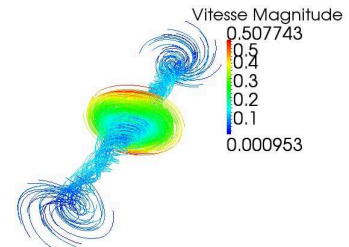


FIGURE 2.22: 3d Empty cavity: streamlines around \mathbf{x}_c for $Ra = 10^4$

For symmetry reasons exposed earlier, the profiles of temperature and velocity are similar to the ones obtained in the two dimensional case, but we will perform a similar

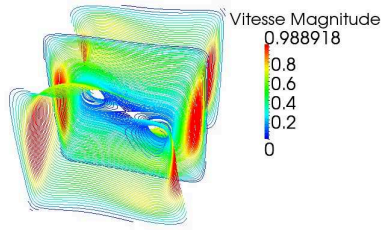


FIGURE 2.23: 3d Empty cavity: streamlines along l_c for $Ra = 10^5$

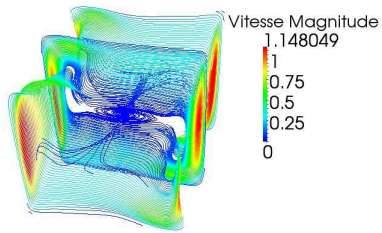


FIGURE 2.25: 3d Empty cavity: streamlines along l_c for $Ra = 10^6$

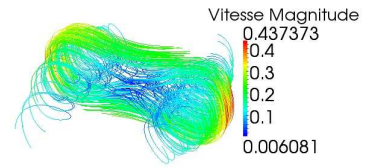


FIGURE 2.24: 3d Empty cavity: streamlines around x_c for $Ra = 10^5$

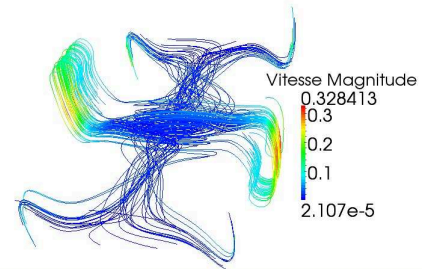


FIGURE 2.26: 3d Empty cavity: streamlines around x_c for $Ra = 10^6$

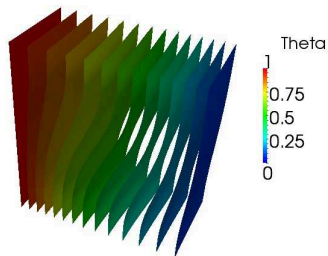


FIGURE 2.27: 3d Empty cavity: iso temperature surfaces for $Ra = 10^3$

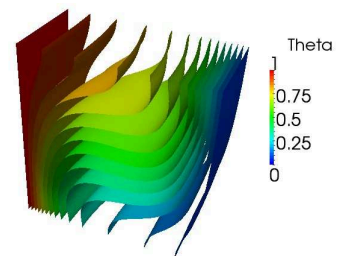


FIGURE 2.28: 3d Empty cavity: iso temperature surfaces for $Ra = 10^4$

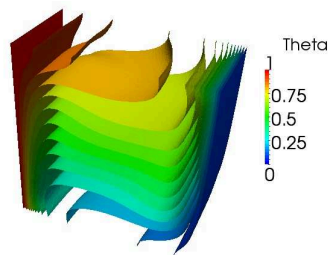


FIGURE 2.29: 3d Empty cavity: iso temperature surfaces for $Ra = 10^5$

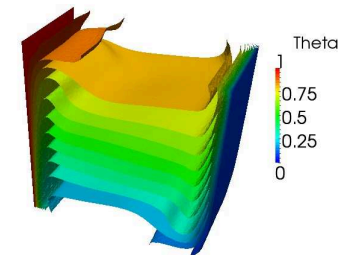


FIGURE 2.30: 3d Empty cavity: iso temperature surfaces for $Ra = 10^6$

validation than in 2d by comparing values of Nusselt numbers to the ones available in literature, even though there are less references available for the 3d case. These results are summarized in the following table

reference \ Ra	10^3	10^4	10^5	10^6
Wakashima and al. [63]	-	2.0634	4.3713	8.77
Tric and al. [64]	1.07	2.054	4.337	8.64
present work	1.09	2.188	4.76	8.22

TABLE 2.2: 3d Empty cavity: comparisons with benchmark solutions

2.3.2 Natural convection in a cavity containing a plate

The second problem, proposed in [65], is another natural convection example with a heated plate at T_h inside a cavity of length $L = 1.0m$ with horizontal walls maintained at T_c . Two configurations, with a plate at horizontal and vertical positions, are considered. No mention about the plate thickness is available in the reference, so we set a thickness of $0.02m$, corresponding approximately to one characteristic mesh size. As in the previous case, homogeneous Neumann boundary conditions are applied on horizontal walls. The following pictures represent the iso-temperature lines on the left, and velocity patterns on the right. The results, in terms of iso temperature and streamlines, are in good agreement with [65] for $Ra = 10^6$, but like in the previous case, we display the evolution of the results with increasing Rayleigh. The patterns for low Ra will not be displayed, since they are representative of diffusion only. Three dimensionnal versions of these cases will be presented, but, to the best of author's knowledge, results about such cases are not available in literature, so the validation step will not be adressed.

2.3.2.1 Horizontal plate

A similar behaviour of the aforementioned can be observed than in the previous case with boundary layers forming on the upper part of the vertical walls. The patterns in the lower part of the cavity are almost homogeneous cold temperature and low velocity, the compressibility effects making the hot fluid rise in the upper part of the cavity. The plate impacts the flows, small recirculation zone forming close to the horizontal limits of the plate and regrouping in a bigger one as the convection effect increases.

The obtained results were compared with the ones with the reference, in terms of adimensional temperature on the top horizontal wall

A small difference is observed, which can be explained by the fact that a high order finite difference method was used in the reference. In fact, in order to eliminate bias, it would be more coherent to make comparison between BF results obtained using our

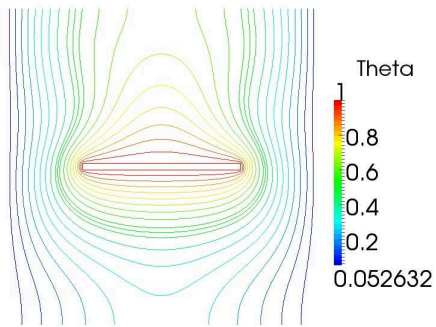


FIGURE 2.31: 2d Horizontal plate: iso temperature for $Ra = 10^4$

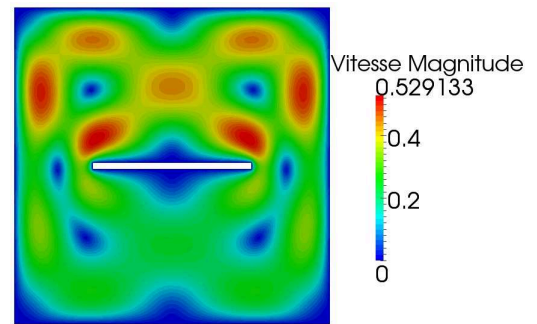


FIGURE 2.32: 2d Horizontal plate: velocity for $Ra = 10^4$

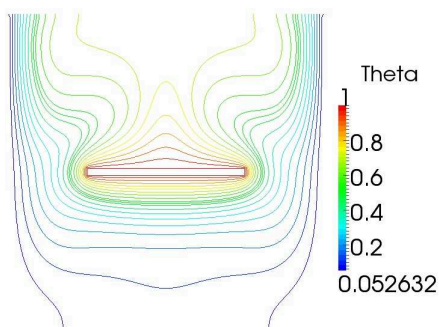


FIGURE 2.33: 2d Horizontal plate: iso temperature for $Ra = 10^5$

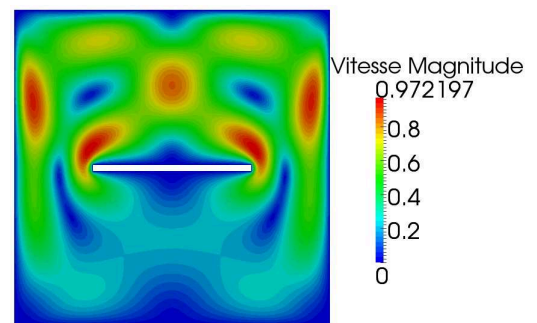


FIGURE 2.34: 2d Horizontal plate: velocity for $Ra = 10^5$

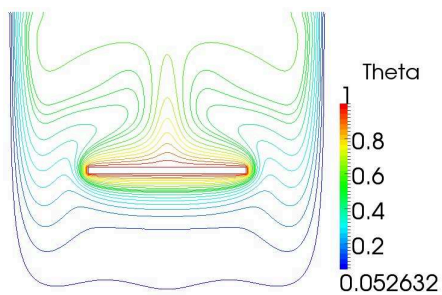


FIGURE 2.35: 2d Horizontal plate: iso temperature for $Ra = 10^6$

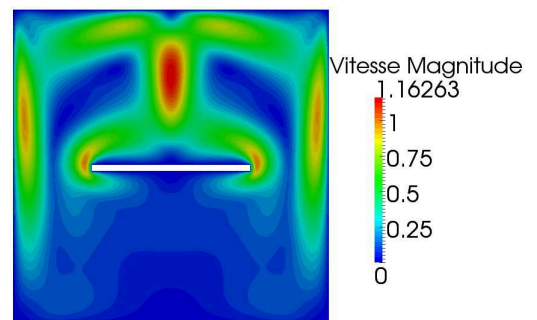


FIGURE 2.36: 2d Horizontal plate: velocity for $Ra = 10^6$

code with the same numerical formulation, and the consistency of the method which we will expose in the next chapter.

A three dimensional version of this case was considered, as an extrusion of the two-dimensional case in the z direction to consider a unit cube. The plate thickness in the z direction was set to 0.5 in order to have symmetric results in the z direction likewise in the x direction. This symmetry can be observed on the normalized temperature patterns and on streamlines.

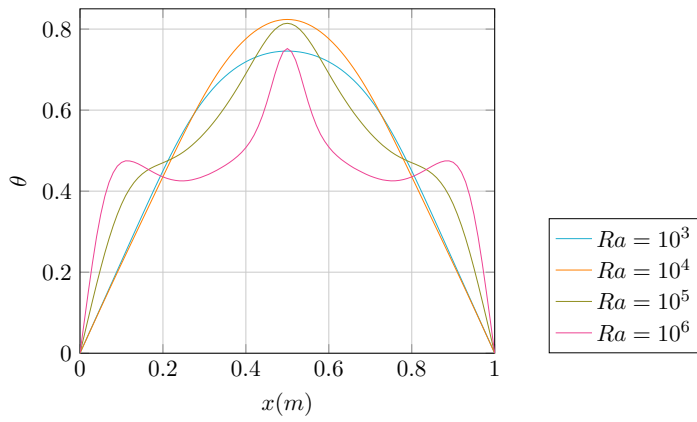


FIGURE 2.37: 2d Horizontal plate: θ along $y = 0.65$ for the considered range of Ra

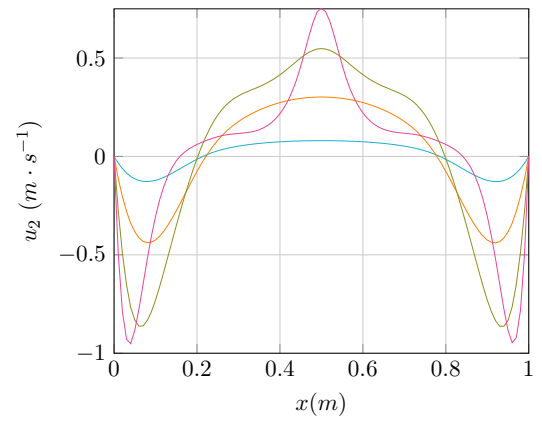


FIGURE 2.38: 2d Horizontal plate: u_2 along $y = 0.65$ for the considered range of Ra

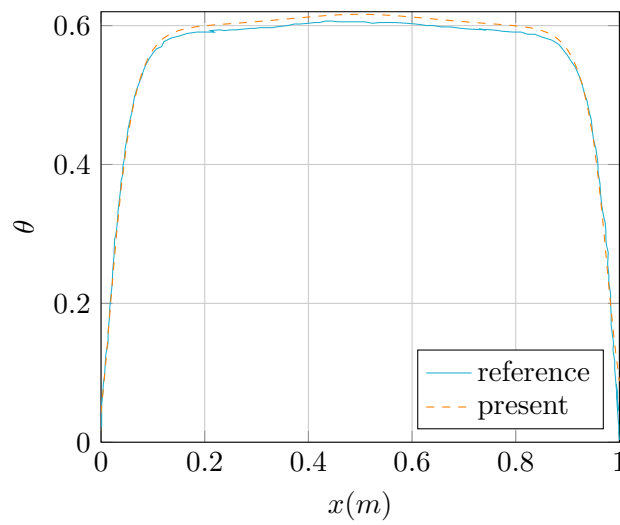


FIGURE 2.39: 2d Horizontal plate: θ along $y = 1.0$

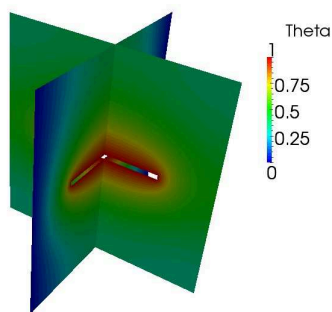


FIGURE 2.40: 3d Horizontal plate: temperature pattern in symmetry planes for $Ra = 10^3$

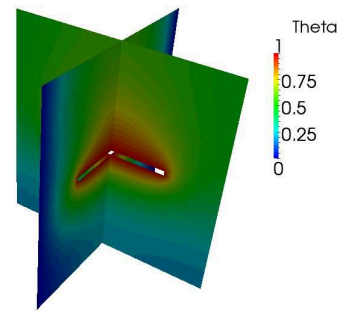


FIGURE 2.41: 3d Horizontal plate: temperature pattern in symmetry planes for $Ra = 10^4$

It would be possible to only simulate a quarter of the effective domain with appropriate boundary conditions, and deduce the whole results by symmetry, as it can be seen on

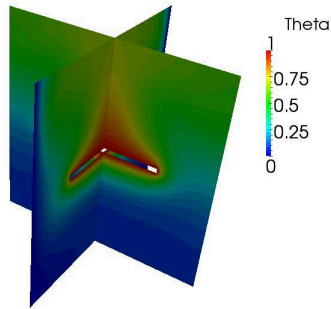


FIGURE 2.42: 3d Horizontal plate: temperature pattern in symetry planes for $Ra = 10^5$

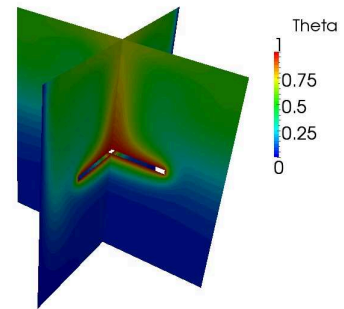


FIGURE 2.43: 3d Horizontal plate: temperature pattern in symetry planes for $Ra = 10^6$

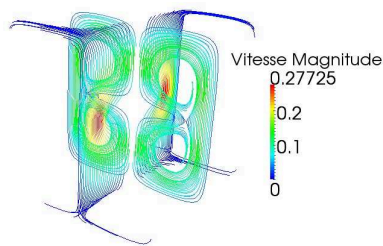


FIGURE 2.44: 3d Horizontal plate: streamlines in symetry planes for $Ra = 10^3$

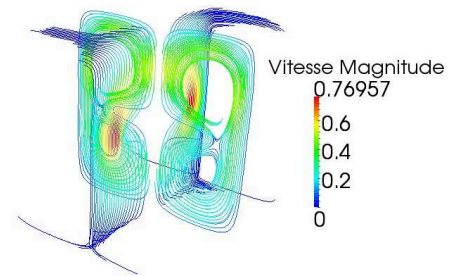


FIGURE 2.45: 3d Horizontal plate: streamlines in symetry planes for $Ra = 10^4$

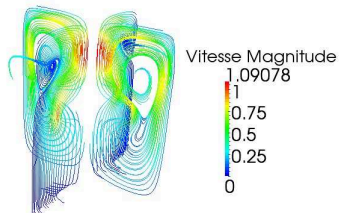


FIGURE 2.46: 3d Horizontal plate: streamlines in symetry planes for $Ra = 10^5$

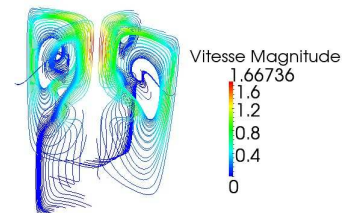


FIGURE 2.47: 3d Horizontal plate: streamlines in symetry planes for $Ra = 10^6$

the 3d isothermperature surfaces.

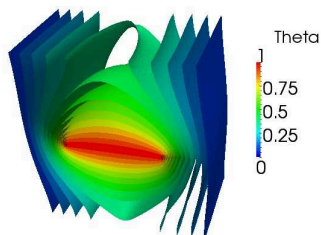


FIGURE 2.48: 3d Horizontal plate: iso temperature surfaces for $Ra = 10^3$

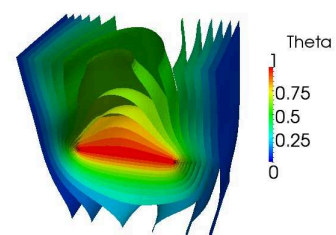


FIGURE 2.49: 3d Horizontal plate: iso temperature surfaces for $Ra = 10^4$

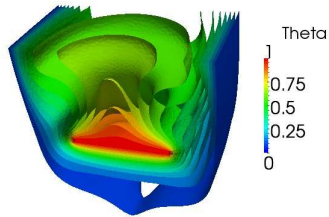


FIGURE 2.50: 3d Horizontal plate: iso temperature surfaces for $Ra = 10^5$

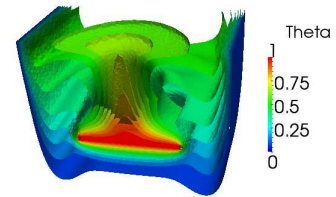


FIGURE 2.51: 3d Horizontal plate: iso temperature surfaces for $Ra = 10^6$

2.3.2.2 Vertical plate

For this case, it is interesting to remark that for $Ra = 10^5$ and $Ra = 10^6$, close to the center of the plate, the situation is similar to what happens in the empty cavity. One can note that, at this location, the iso temperature lines display the same shape as in the empty cavity. However, the velocity is different due to the absence of a solid boundary at the upper limit of the plate. We can observe two symmetric small recirculation zones between the plate and solid boundaries, in the direction of the iso-temperature lines for $Ra = 10^4$, the shape becoming more complex when convection increases.

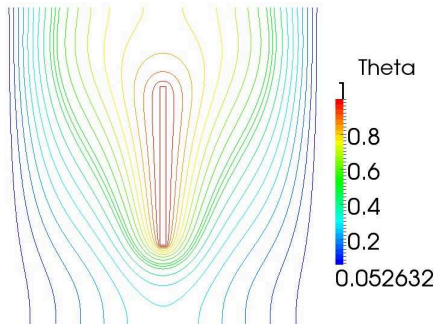


FIGURE 2.52: 2d Vertical plate: iso temperature for $Ra = 10^4$

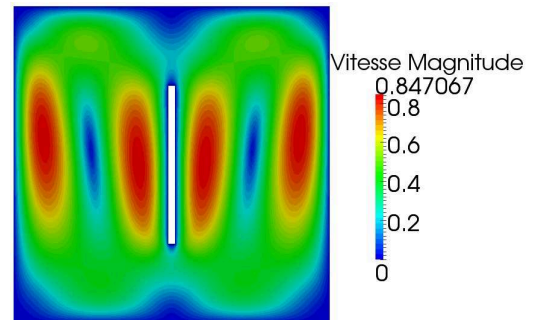


FIGURE 2.53: 2d Vertical plate: velocity for $Ra = 10^4$

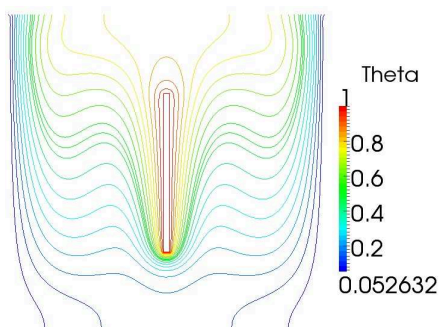


FIGURE 2.54: 2d Vertical plate: iso temperature for $Ra = 10^5$

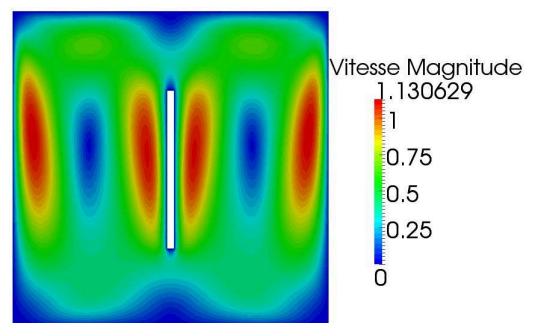


FIGURE 2.55: 2d Vertical plate: velocity for $Ra = 10^5$

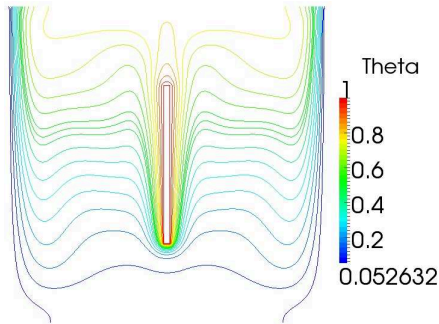


FIGURE 2.56: 2d Vertical plate: iso temperature for $Ra = 10^6$

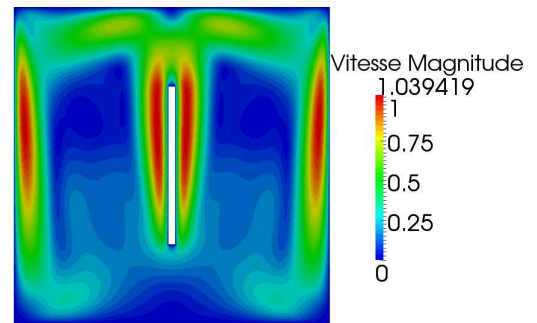


FIGURE 2.57: 2d Vertical plate: velocity for $Ra = 10^6$

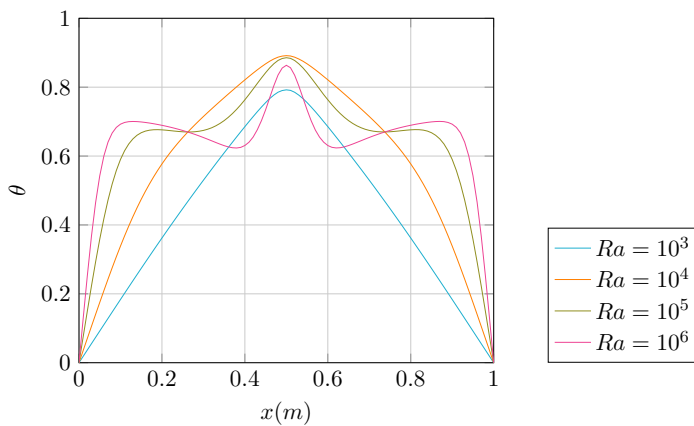


FIGURE 2.58: 2d Vertical plate: θ along $y = 0.8$ for the considered range of Ra

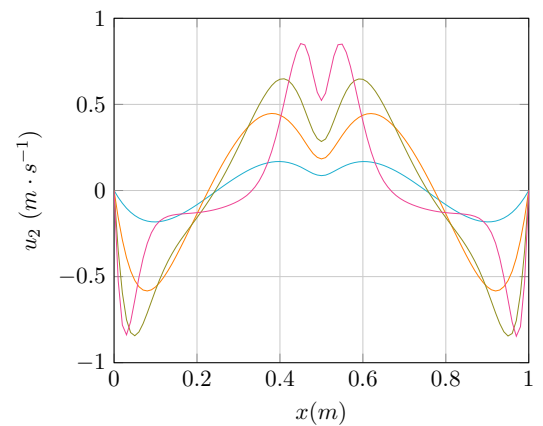
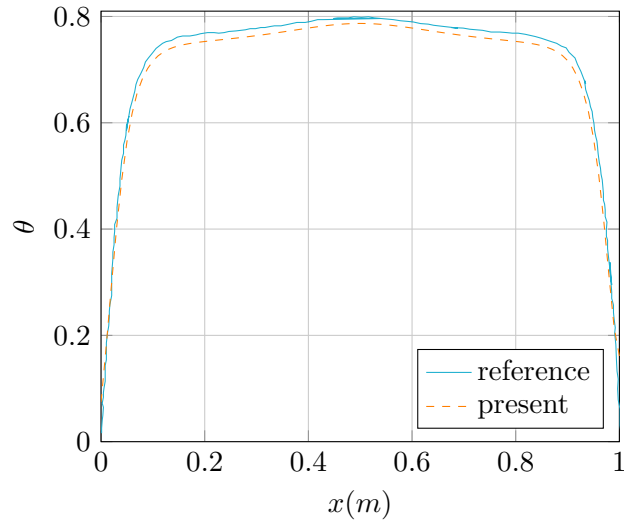
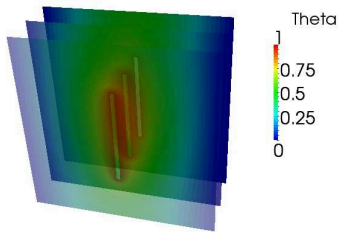
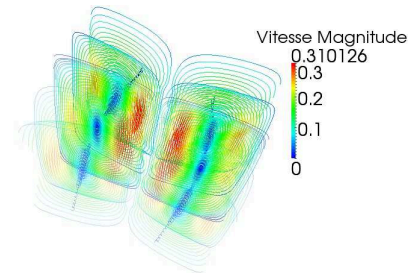
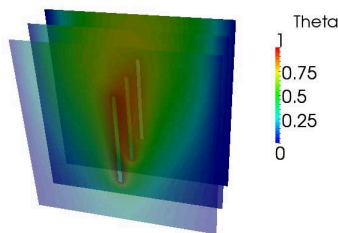
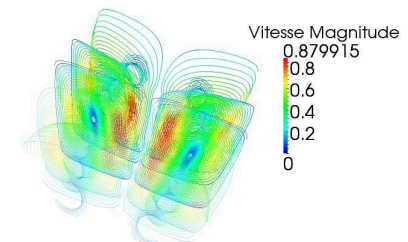


FIGURE 2.59: 2d Vertical plate: u_2 along $y = 0.8$ for the considered range of Ra

As in the previous case, we compared the obtained results in terms of temperature along the top horizontal wall. For the same reasons exposed earlier, a small difference is observed but the discrepancy remains small.

The 3d version of this problem was addressed, the extension being in the same fashion as in the two other cases. One can observe the symmetry of the temperature with respect to the plane of equation $z = 0.5$, and symmetry of the velocity streamlines with respect to \mathbf{x}_c , the above pictures presenting temperature patterns and streamlines in plane $z = 0.3$, $z = 0.5$ and $z = 0.7$, respectively.

The iso temperature surfaces display, as for the horizontal case, some artifacts can be seen at the location of thermal boundary layers. It would be possible to have more proper iso surfaces by using a finer mesh, but on the one hand, the mesh used here is made up of about 1 million elements, so using a finer mesh could seem like an exaggeration, and on the other hand, we will see in the next chapter that the monolithic methods we will make use require fine meshes.

FIGURE 2.60: 2d Vertical plate: θ along $y = 1.0$ FIGURE 2.61: 3d Vertical plate: temperature patterns for $Ra = 10^3$ FIGURE 2.62: 3d Vertical plate: streamlines for $Ra = 10^3$ FIGURE 2.63: 3d Vertical plate: temperature patterns for $Ra = 10^4$ FIGURE 2.64: 3d Vertical plate: streamlines for $Ra = 10^4$

Conclusions

This chapter has demonstrated the potential of the stabilized finite element formulations for the physical models of interest presented above. The results shown are satisfactory in the range of Ra , and were validated in terms of local quantities (temperature) as well as on global quantities (Nusselt numbers). 2d and 3d problems can be treated indifferently, even though finer meshes have to be considered for 3d simulations. The question of the

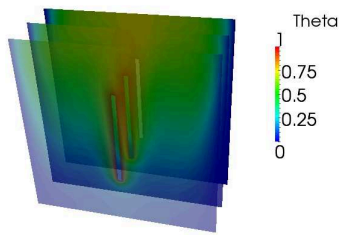


FIGURE 2.65: 3d Vertical plate: temperature patterns for $Ra = 10^5$

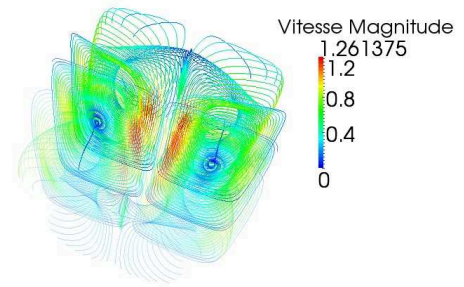


FIGURE 2.66: 3d Vertical plate: streamlines for $Ra = 10^5$

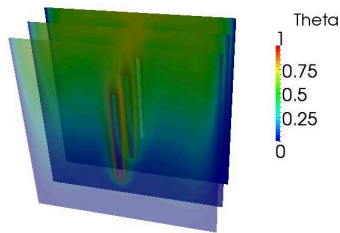


FIGURE 2.67: 3d Vertical plate: temperature patterns for $Ra = 10^6$

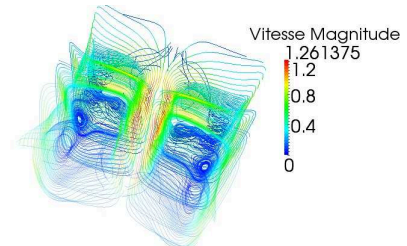


FIGURE 2.68: 3d Vertical plate: streamlines for $Ra = 10^6$

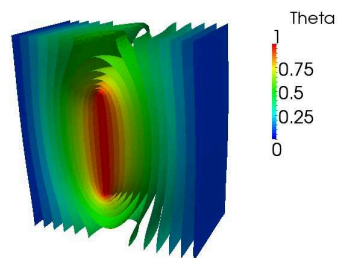


FIGURE 2.69: 3d Vertical plate: iso temperature for $Ra = 10^3$

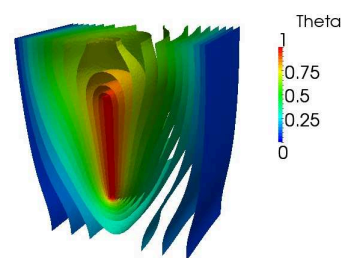


FIGURE 2.70: 3d Vertical plate: iso temperature for $Ra = 10^4$

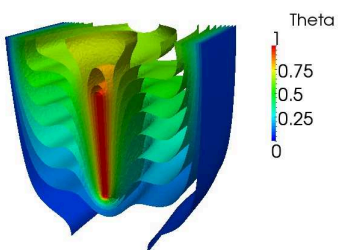


FIGURE 2.71: 3d Vertical plate: iso temperature for $Ra = 10^5$

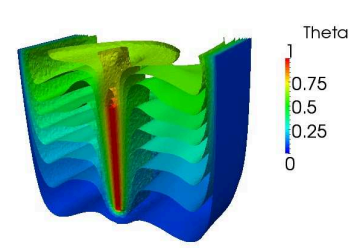


FIGURE 2.72: 3d Vertical plate: iso temperature for $Ra = 10^6$

convergence with respect to the mesh size was not addressed in this chapter, but will be in the next, along with the type of meshes that will be introduced in the next chapter.

Résumé français

Ce chapitre décrit les modèles physiques et les méthodes de résolution numérique utilisées tout au long de ce travail. On détaille pour la mécanique des fluides incompressibles, les équations de Navier-Stokes, les différents types de conditions aux limites et initiales envisagées. Le reste de la physique modélisée ici, à l'exception du rayonnement, peut être décrit au moyen d'une équation de convection-diffusion-réaction générale, ou les spécificités relatives à chaque modèle (équation de l'énergie, modèle de turbulence, modèle de rayonnement P_1) sont introduites et détaillées une par une. Le problème d'aérothermie couplée est ensuite présenté. La seconde partie de ce chapitre est consacrée aux formulations aux éléments finis utilisées: on dérive les formulations faibles à partir des problèmes continus, on y rappelle les notions nécessaires aux approximations éléments finis classiques ainsi que leurs limitations pour les problèmes considérés. On précise ensuite les méthodes de stabilisation utilisées, basé sur l'approche variationnelle multi-échelle, en terme de laquelle on peut interpréter les méthodes plus classiques, telles que la méthode SUPG. Ces méthodes sont illustrées sur des exemples illustratifs issus de la littérature en $2d$ et $3d$, où l'on observe une bonne corrélation entre les résultats obtenus et ceux présentés dans les références.

Chapter 3

The Monolithic approach: levelset methods, anisotropic mesh adaptation and mixing laws

The previous chapter was dedicated to the physical models of interest in this work, and the mathematical formulations to obtain numerical solutions of the aforementioned models. However, problems arising from industrial applications often present different components: in a furnace, not only the surrounding fluid is of interest, but also the solid boundaries that limit the enclosure, and, the most important, the ingots inside the enclosure. Let us recall that the goal of this work is the direct numerical simulation of heat transfer in material forming processes. Therefore, even though an accurate description of the flow and heat transfer inside the fluid is important to achieve a better control of the facility, the critical point is the temperature inside the ingots, since the temperature time story inside the solid parts have a strong influence on the mechanical properties of the final products, at the macroscale (yield limit, fatigue strenght) as well at the microscale (microstucture, cluster, surface roughness). The classical approach, usually referred to as the "Body-fitted" approach, is what we used in the previous chapter: the solid and the fluid computations are performed on separated meshes, the fluid domain containing a "hole" at the location of the solid part, and an appropriate coupling is required to ensure the communication at the interface between models. Even though this approach is used in many commercial softwares, it has some well-known drawbacks:

- When complex geometries for the ingots are considered, the construction of an appropriate mesh can be very time consuming. Moreover, different softwares are

based on different numerical methods, therefore the mesh requirements are different for each software, rendering more difficult the task of designing a mesh for a specific application.

- A change in the position of the ingots means redefining the whole mesh. This becomes more problematic when solids move during the process, as it is often the case, since at each change of mesh, all the boundary conditions have to be redefined, which is a tedious task for complex geometries.
- The Body fitted approach often models the convection at the interface fluid-solid with boundary conditions of type $-\lambda \nabla(T) \cdot \mathbf{n} = h_{conv}(T - T_w)$, h_{conv} being the convection coefficient. As explained in chapter 1, this convection coefficient can be obtained by different ways: correlations between adimensional numbers through the Vaschy-Buckingham or inverse problems, but such coefficients are very dependent on the configuration inside the facility (position of ingots and burner/nozzles, inlets velocities, physical properties of the fluid).

For all the reasons mentionned, as we want to design "general" numerical tools, in the sense that it should be adapted to a broad range of situations, a classical body-fitted approach does not seem well adapted. To circumvent these issues, we propose to use an immersed volume method (IVM), consisting in treating both solids and fluids on a single mesh and with a single set of equations being solved for the whole domain, that is to say, in a monolithic way. The field of immersed methods have attracted the attention of many researchers in the past few years, with applications to different types of flows, such as Stokes flows [66], incompressible viscous flows [67, 68], fluid-structure interaction with rigid [69],[70],[71] and flexible bodies [72]. Heat transfer in a monolithic context was only adressed very recently, with applications to biology [73] and phase change [74]. The immersed volume method that is going to be described was already successfully applied to different situations [38, 40, 42], but the main characteristics will be recalled in this chapter, and supplementary validation test will be performed.

The three main features of an immersed method are:

- The representation of interfaces.
- The construction of a mesh to properly capture the interface phenomena.
- The assessment of effective physical properties for different domains.

Each of the three aforementioned points will be the object of a subsection in this chapter

3.1 Representing interfaces using a levelset framework

The first issue is how to represent the interfaces between fluid and different solids. To this end, an interesting approach consists in using levelset functions (see [75] for a good review). It is used in many domains as computer vision, optimization [76] and image processing. The principle is to define a signed distance function $\alpha(\mathbf{x})$, positive inside the considered object and negative outside. Formally, it reads, Γ representing the fluid-solid interface:

$$\alpha(\mathbf{x}) = \begin{cases} d(\mathbf{x}, \Gamma) & \text{if } \mathbf{x} \in \Omega_{\text{solid}} \\ -d(\mathbf{x}, \Gamma) & \text{if } \mathbf{x} \notin \Omega_{\text{solid}} \end{cases} \quad (3.1)$$

where $d(\mathbf{x}, \Gamma)$ is given by

$$d(\mathbf{x}, \Gamma) = \min_{\mathbf{y} \in \Gamma} \|\mathbf{x} - \mathbf{y}\|_2 \quad (3.2)$$

For simple geometries, as with circles or polygons, α can be determined analytically from geometric parameters. For more complex geometries, the considered object is first modelled using CAD tools, (CATIA © for instance) and a surface mesh of the object is generated. This surface mesh is then "merged" into a background mesh, and we make use of the algorithm depicted in [77] to compute the levelset on the main mesh. Here we see displayed the levelset functions a circle and a square centered on $(0.5, 0.5)$, the computational domain being $[0, 1] * [0, 1]$.

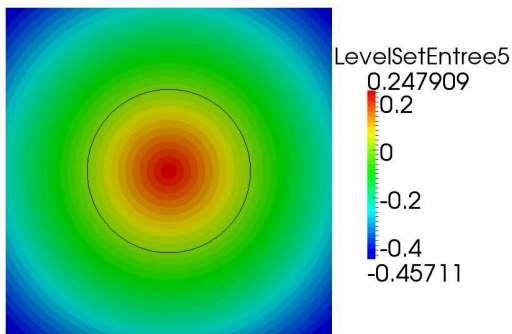


FIGURE 3.1: levelset Function of a circle

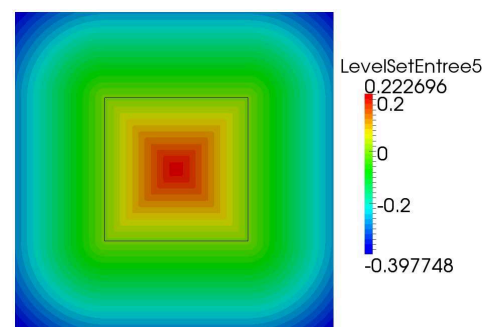


FIGURE 3.2: levelset Function of a square

It is also possible to make the levelset function "move" in the computational domain. This is achieved by introducing a supplementary equation ruling the evolution of the levelset function as follows:

$$\frac{\partial \alpha}{\partial t} + \mathbf{U} \cdot \nabla(\alpha) = 0 \quad (3.3)$$

\mathbf{U} being a transport velocity (a rigid body velocity in the case of moving objects, a convective velocity in the case of multiphase flows). Many researchers have worked on those reinitialization techniques for interface tracking [78–80], with applications for Stokes flows [81] . levelset functions can be used in a different context as well, like contact- mechanics [82] and metal microstructure modelling [10]. Some applications to Fluid-Structure interaction [83] can be noted as well. This approach, consisting in modelling the solid using levelset functions is interesting, since it provides a convenient representation of the solid , and this representation has the potential to model solids of very complex geometries [5]. However, since most of the critical phenomena occur at the interface fluid-solid (boundary layers, convective transfer, forces applied on the solid,..), it is desirable to dispose of an appropriate *discrete* representation of the interface, since the interface will, in the end, be represented on a mesh. Different options are possible to track the interface: by using another mesh or by moving on the background principal mesh as done [84], in order to track the interface, follow ”effective” nodes and edges of the mesh being representative of the interface following the lines in [85]. However, this is difficult to achieve, particularly when complex geometric forms are of interest. We will follow another approach that consists in the construction of a mesh ”adapted” to the representation of the considered levelset function, in a sense to be defined later on. The purpose of the next section is to introduce the tools necessary to the construction of such meshes

3.2 Error estimators, metric fields and anisotropic mesh adaptation

3.2.1 Error estimation

3.2.1.1 Motivations

Formally, a mesh is defined as a collection of polygons, composed of vertices, edges and faces, that defines a polyhedral object. As stated in the previous chapter, it is a natural way to construct an approximation Ω_h of the computational domain Ω . If different forms of polygons (also referred to as simplices, cells in a finite volume context, elements in a Finite Element context) can be considered (triangles, quadrangles, hexahedras), the question of building a mesh suitable for the desired application is common to all kinds of meshes. It is common to introduce more elements in the location of ”sharp”

phenomena (close to boundary for instance), but this requires an *a priori* knowledge of the considered system. Therefore, it is desirable to have at hand general tools to achieve such an understanding of the underlying model, sometimes a first calculation is necessary to have an *a posteriori* knowledge of the solution and adapt the computation afterwards. To introduce the concepts necessary to such an analysis, let us consider an abstract problem under the following form:

$$\mathcal{L}(u) = f \quad (3.4)$$

where $\mathcal{L}(\bullet)$ stands for a differential operator representing the considered PDE (including the boundary conditions, forcing terms and model parameters), f is a forcing term and u is the solution that we are looking for. Under certain assumptions (regularity, coercivity) on \mathcal{L} and f , functional analysis theory can provide information (existence, unicity, regularity regarding data) regarding the *exact* solution of this problem, that will be denoted u_{ex} in the following. Using the techniques described in the previous chapter, one can transform the problem into a weaker one, in order to be able to obtain an approximate solution u_h , so that the discrete abstract problem reads:

$$\mathcal{B}(u_h, v) = l(v) \quad \forall v \in V_h \quad (3.5)$$

Knowing this, one can define the *approximation error* e_h , as follows:

$$e_h = u_{ex} - u_h \quad (3.6)$$

e_h will be evaluated with an appropriate norm, depending on the considered problem. Two main approaches to study the behaviour of this error can be quoted:

- *A priori* error estimation: this approach consists in using the functional analysis theory to assess the order of convergence of the considered method, based on mathematical assumptions (properties of the PDE, regularity of the data, type of boundary conditions, properties of the numerical formulation). Such error estimations are often presented in the form $\|e_h\| \leq Ch^p$, where C is a constant independent of the mesh, h is the characteristic mesh size, and the exponent p is related to the order of interpolation of the chosen approximation. However, that kind of result is valid only asymptotically (i.e. when $h \rightarrow 0$), hence such an approach is impossible to use in practice.

- *A posteriori* error estimation: this approach is different in the sense that it makes use of the approximated solution to compute the approximation error e_h . This can be done by different ways, depending on the considered physics.

The following subsection is dedicated to a short overview of error estimations techniques.

3.2.1.2 Approximation error

Since the Finite Element method was originally applied to structural mechanics, the foundations of error estimation are related to such problems. One can quote at least three different approaches:

- Following the pioneering work in [86], an option is to make use of Finite Element residuals: using the Galerkin orthogonality, one can show that the error e_h is the solution of a variational problem similar to the original one, with a Finite Element residual as a right hand side. It is interesting to remark how such residual-based methods echoe with the VMS stabilization evoked in the previous chapter.
- Another option is to exploit the lack of regularity of the Finite Element solution [87–89]. The computation of the approximation error therefore consists in the construction of a smoothed approximation. Such methods are really simple and easy to implement, but they suffer from a lack of good properties, even though improved versions can be considered.
- A third option consists in defining a measure of the error with respect to the constitutive relationship [90], but with a step for the construction of a more regular solution with techniques such as flux equilibration. It offers a interesting framework but not suited for CFD, since the non linearity comes from the convective term and not from the constitutive relation.

One can see [91], [92] or [93] for reviews on error estimation for *adaptive* Finite Element formulations, but such topics are still attracting interest of many research teams, extending error estimation approaches to new problems: for linear elasticity, we can quote [94] in the context of model reduction, [95] for mixed augmented method with Lagrange multipliers and [96] for VMS formulation in elasticity. Some examples in different contexts are available as well, addressing the question of *goal oriented* estimation, when one wants to estimate not the global error of the problem, but on a quantity of interest: [97] for Poisson equation, [98] for linear transport and diffusion, [99] for diffusion-reaction systems and [100] for Maxwell equations. A great effort was also devoted to such studies

for Navier-Stokes equations, with special focus on turbulence [101] [102] [103], and some study for VMS based stabilization methods [104]. However, in our context, on the one hand we are considering multiphysic problems, so it is desirable to use an error estimation valid for all models, and on the other hand, we are looking for an estimator to adapt the mesh only. Therefore, the next subsection introduces the framework to study the *interpolation* error that will be used in this work.

3.2.1.3 Interpolation error

We start by recalling the Cea lemma that states, for linear problems:

$$\exists C \in \mathbb{R}, \forall v \in V_h, \|u_{ex} - u_h\| \leq C \|u_{ex} - v\| \quad (3.7)$$

where C is again a constant independent of the mesh. One can see that, for a suitable choice of v , it is possible to obtain a quantity that is an upper bound for the approximation error. We introduce the Clement interpolation operator, where V is the functional space where u_{ex} lies

$$\Pi_h : V \rightarrow V_h \quad (3.8)$$

Roughly speaking, Π_h can be understood as a projection operator onto the Finite element mesh. Setting $v = \Pi_h(u_{ex})$, the quantity $\|u_{ex} - \Pi_h(u_{ex})\|$, referred to as the *interpolation error* appears to be a good choice to control the approximation error. Moreover, the interpolation error only measures the error made when a function is represented on a mesh, and therefore seems a natural tool to use for mesh adaptation. The general idea of the mesh adaptation is to compute such an interpolation error once a first calculation has been done, and to construct a new mesh by equidistributing the error. However, as it was shown in the previous chapter with the SUPG and SCPG methods, some phenomena present a natural anisotropy (in the direction of the upwinding velocity). Following the same idea, an interesting lead is to consider a mesh composed of elements presenting similar characteristics, i.e. with a preferred direction aligned with the one of the gradient of the field to be represented. The purpose of the next sections is to introduce the theoretical framework necessary for the construction of such meshes using the notion of metrics.

3.2.2 Change of geometry: metric fields

It is classical to say that a geometry is defined once a scalar product and its associated norm are at hand. The usual Euclidian space considers what we refer to as the "canonical" scalar product. However, it is possible to define many other scalar products just with the help of a symmetric definite positive matrix $\mathcal{M} \in \mathbb{R}^{d \times d}$, such that the associated scalar products and norms are as follows:

$$(\mathbf{x}, \mathbf{y})_{\mathcal{M}} = \mathbf{x}^T \mathcal{M} \mathbf{y} \quad (3.9)$$

$$\|\mathbf{x}\|_{\mathcal{M}} = \sqrt{\mathbf{x}^T \mathcal{M} \mathbf{x}} \quad (3.10)$$

If we consider an element of the mesh, the definition of a single characteristic mesh size for the element (even more for the whole mesh) is not well suited for anisotropy. Hence, if we want to define characteristic mesh sizes in each direction (h_x, h_y, h_z) , a natural way to define a metric \mathcal{M}_K for the element is the following:

$$\mathcal{M} = \begin{bmatrix} \frac{1}{(h_x)^2} & 0 & 0 \\ 0 & \frac{1}{(h_y)^2} & 0 \\ 0 & 0 & \frac{1}{(h_z)^2} \end{bmatrix} \quad (3.11)$$

By doing so, each tetrahedron (triangle in $2d$) is equilateral with respect to its natural metric. For the case of an isotropic element of size h , the metric is an homothety of ratio $\frac{1}{h^2}$. Therefore, the problem of the construction of a mesh adapted to the representation of a given function is replaced by the following problem: for a given error estimate, how to build local metrics for each element, so that they will be adapted to represent a given function. We notify that the use of such elements make the definition of a characteristic length for an element even more difficult. Even if different options are possible, for the length appearing in the definition of the stabilization parameters in chapter 2, we follow the lines in [40].

Even though other alternatives are possible (see [105] and references therein), we will present two different approaches that are used in our library

3.2.2.1 Metric construction by length distribution tensor

In this case, the metric map is constructed directly at the nodes of the mesh. The construction of the metric relies on the notion of length distribution tensor and permits

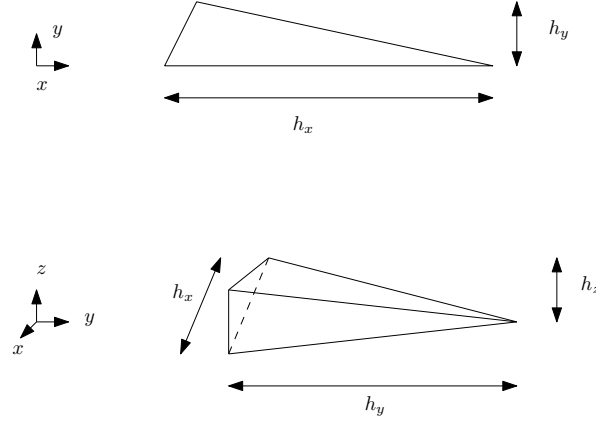


FIGURE 3.3: Illustration of anisotropic elements

to define an *edge – based* error estimator. We will recall here the main steps of the construction, but for more information, the reader can refer to [106] or [4]: let us start by introducing some useful notations:

TABLE 3.1: Notations for the mesh.

Notations	Definitions
d	dimension of space
\mathcal{K}	set of elements
\mathcal{N}	set of nodes
$K \in \mathcal{K}$	mesh element
$\mathbf{X}^i, i \in \mathcal{N}$	vector of coordinates for the i th node
$\mathbf{X}^{ij} = \mathbf{X}^i - \mathbf{X}^j$	edge vector made of nodes i and j sharing at least one element
$h_{ij} = \mathbf{X}^{ij} $	edge length
$\Gamma(i) = \{j \in \mathcal{N}, \exists K \in \mathcal{K}, \mathbf{X}^{ij} \in \mathbf{K}\}$	set of nodes connected to node i ("patch")
$ \Gamma(i) $	cardinal of the set $\Gamma(i)$

The Length Distribution Tensor is defined by

$$\mathbb{X}^i = \frac{d}{|\Gamma(i)|} \sum_{j \in \Gamma(i)} \mathbf{X}^{ij} \otimes \mathbf{X}^{ij} \quad (3.12)$$

This tensor will appear in the construction of an interpolation error that measures the accuracy of the process of building a continuous gradient from values at nodes of the mesh. This reconstructed gradient \mathbf{G}^i is defined using the following minimization problem

$$\mathbf{G}^i = \arg \min_{\mathbf{G}} \left(\sum_{j \in \Gamma(i)} |\mathbf{G} \cdot \mathbf{X}^{ij} - U^{ij}|^2 \right) \quad (3.13)$$

where U^{ij} is the nodal value of a field approximated in the interpolation space. The solution of this problem is given by:

$$\mathbf{G}^i = (\mathbb{X}^i)^{-1} \mathbf{U}^i \quad (3.14)$$

We can now turn to the definition of the interpolation error estimator e^{ij} , which is given by:

$$e_{ij} = \mathbf{G}^{ij} \cdot \mathbf{X}^{ij} \quad (3.15)$$

This estimator is then used to compute a stretching factor s^{ij} , based on a principle of equidistributed error e for all lengths, with a fixed number of nodes N , which leads to the following definition of the stretching factor

$$s_{ij} = \left(\frac{e}{e(N)} \right)^{-\frac{1}{2}} = \left(\frac{\sum_i n^i}{N} \right)^{\frac{2}{d}} e_{ij}^{-1/2}, \quad (3.16)$$

$$\text{with } n^i = \det \left(\frac{d}{|\Gamma(i)|} \sum_{j \in \Gamma(i)} s_{ij}^{-1} \frac{\mathbf{X}^{ij}}{|\mathbf{X}^{ij}|} \otimes \frac{\mathbf{X}^{ij}}{|\mathbf{X}^{ij}|} \right)$$

Then, the new metric can finally be defined:

$$\widetilde{\mathbb{M}}^i = \frac{|\Gamma(i)|}{d} \left(\widetilde{\mathbb{X}}^i \right)^{-1}, \quad (3.17)$$

where $\widetilde{\mathbb{X}}^i$ is computed by substituting \mathbf{X}^{ij} with $\widetilde{\mathbf{X}}^{ij} = s_{ij} \mathbf{X}^{ij}$. However, even though this approach is interesting in the sense that it exploits an analogy with an orientation tensor, the construction of the metric relies on geometric characteristics only. Another approach is possible, based on a different philosophy, and will be detailed in the next part.

3.2.2.2 Metric construction using an hessian based error estimator

Here again, the reader can refer to [107], but we recall here the components of the approach. This philosophy is different than the previous one in the sense that we make use of higher order derivatives. If we come back to (3.7), one can show

$$\|u_{ex} - u_h\|_p \leq C \|u_{ex} - v\|_p \leq C \left(\sum_{K \in \mathcal{K}} \|H(u_{ex})(\mathbf{x})\|_{K,p}^p \right)^{\frac{1}{p}} \quad (3.18)$$

where $H(u_{ex})(x) = D_2(u_{ex})(\mathbf{x})(x - x_K)(x - x_K)$, $D_2(u_{ex})(x)$ stands for the hessian matrix of u_{ex} and x_K being the barycenter of element K . The computation of the error estimator is based on a recovered Hessian $H_R(u_{ex})(x)$, obtained through techniques depicted in [88, 89]. Using this the following error estimates can be obtained, with $\alpha \geq 0$:

$$\|u_{ex} - u_h\|_p \leq C \|u_{ex} - v\|_p \leq \frac{C'}{\text{card}(\mathcal{K})^\alpha} \|H_R(u_{ex})(\mathbf{x})\|_p \quad (3.19)$$

The local metric is defined according to the recovered Hessian, related to its eigenvectors $(\mathbf{e}_i)_{1 \leq i \leq d}$ ($H_R(u_{ex})(\mathbf{x})$ is a real symmetric matrix due to the Schwartz theorem) and the mesh sizes in each corresponding directions $(h_i)_{1 \leq i \leq d}$, as follows:

$$\mathcal{M} = \sum_{i=1}^d \frac{1}{h_i} \mathbf{e}_i \otimes \mathbf{e}_i \quad (3.20)$$

However, even though $H(u_h)(x)$ appears as a good candidate for the recovered hessian, it cannot be used directly as a metric, since it is not guaranteed to be positive-definite. If we denote by $(\lambda_i)_{1 \leq i \leq d}$ its eigenvalues, we can define

$$\mathcal{H} = \mathcal{R} \Lambda \mathcal{R}^T \quad (3.21)$$

with \mathcal{R} being a rotation matrix formed of $(\mathbf{e}_i)_{1 \leq i \leq d}$ as column vectors (the order being re-arranged to form an orthonormal basis), and $\Lambda = \text{diag}(|\lambda_i|_{1 \leq i \leq d})$. That allows us to define an error estimator ε_K on each element K and an upper bound

$$\varepsilon_K = \left(\int_K (H(u_h)(x_K)(x - x_K)(x - x_K))^p \right)^{\frac{1}{p}} \quad (3.22)$$

$$\Rightarrow \varepsilon_K \leq \left(\int_K \sum_{i=1}^d \lambda_i(x_K) h_i^2 \right)^{\frac{1}{p}} \quad (3.23)$$

In the following, the two metrics will be referred to as "Edge-based" metric and "Hessian-based" metric, respectively. A proper comparison of the two metrics could be performed by using "exotic" analytical functions, but will not be performed in this thesis, since the two approaches lead to similar results, even though the "Hessian-based" approach is simpler to implement. Now that we exposed two approaches to compute anisotropic error estimators, it is necessary to construct a mesh with respect to those error estimators, in a way described in the next section.

3.2.3 Mesh adaptation algorithms

The construction of a mesh is, in general, not an easy task. It is easy in the case of structured mesh, but becomes more tricky for unstructured meshes, and could serve as a PhD topic on itself. Even though the principle is always to equidistribute the error on each element, some geometric considerations are of interest:

As described in [108, 109] relying on a *discrete* point of view, a mesh is a set of node and a topology. Within this view, an optimal mesh is constructed using criterions such as minimal volume for simplices, by performing "cut and paste" operations for node generation and deletion.

The mesh adaptation procedure is illustrated below on the case of a circle, where the mesh is adapted on the levelset of the circle. One can see that the mesh obtained through this procedure is gradually refined at the interface, enabling a sharp description of the interface on the one hand and ensuring an accurate description of interface quantities (Temperature, velocity), mandatory for industrial applications on the other hand. The four pictures illustrate that the static mesh adaptation is an iterative process. One could argue that such a mesh adaptation is costly in terms of computational resources, but such a mesh adaptation process is "offline", because it is done before any calculation. The procedure has also been tested on 3d examples, displayed in the following. The results show the performances of the procedure, on simple geometric forms as well as on more complicated geometries coming from our industrial partners.

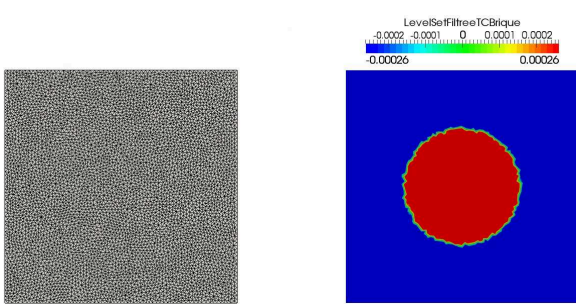


FIGURE 3.4: Mesh adaptation procedure: initial mesh

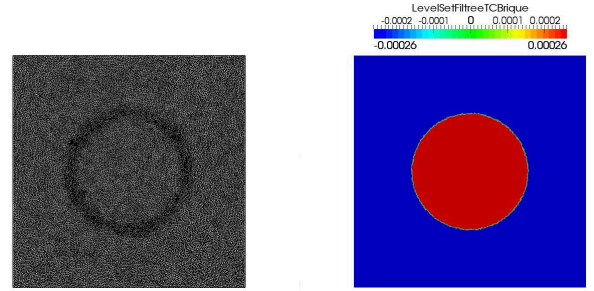


FIGURE 3.5: Mesh adaptation procedure: first remeshing

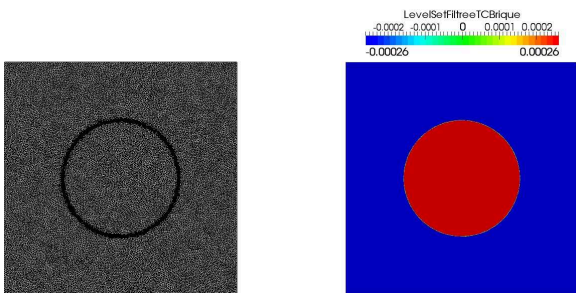


FIGURE 3.6: Mesh adaptation procedure: third remeshing

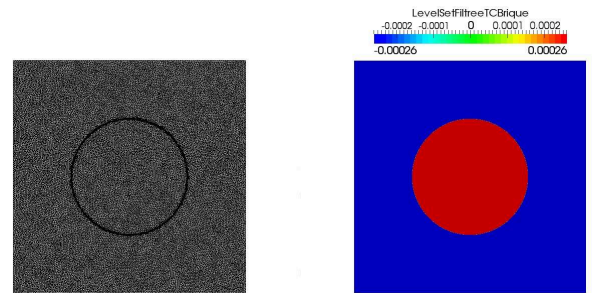


FIGURE 3.7: Mesh adaptation procedure: fifteenth remeshing

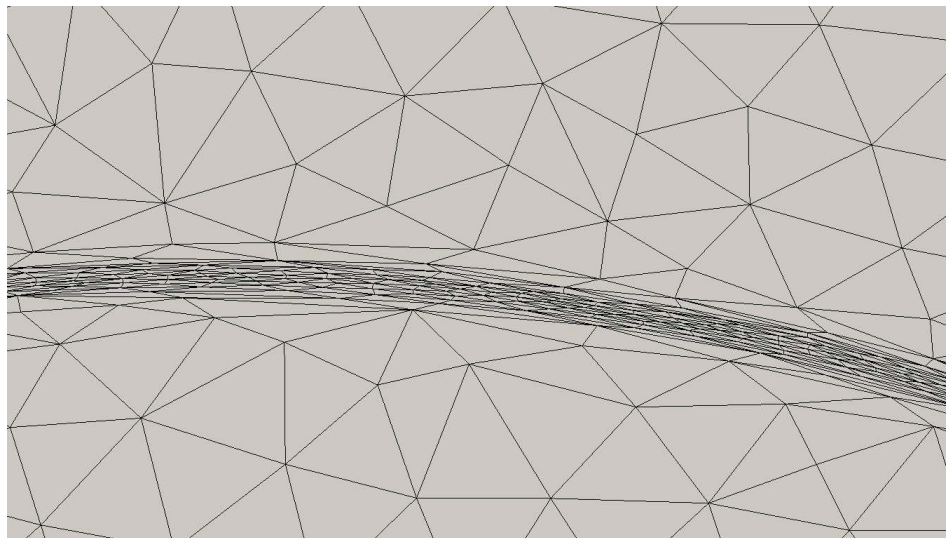


FIGURE 3.8: Zoom on the refined interface

The whole industrial facility (an overview is depicted below) was modelled as well, with an explicit description of boundaries and a sand layer, demonstrating the potential of the method to properly capture several interfaces. A special treatment is required to adapt simultaneously on ingots, walls and sand, but this will be detailed in the chapter regarding industrial applications.

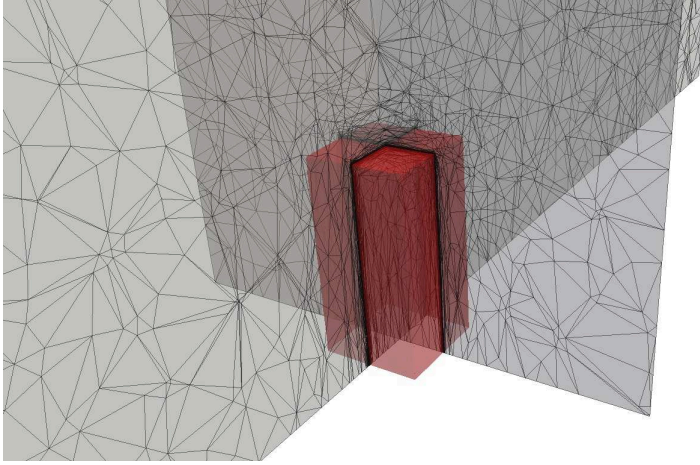


FIGURE 3.9: 3d Adapted mesh: brick

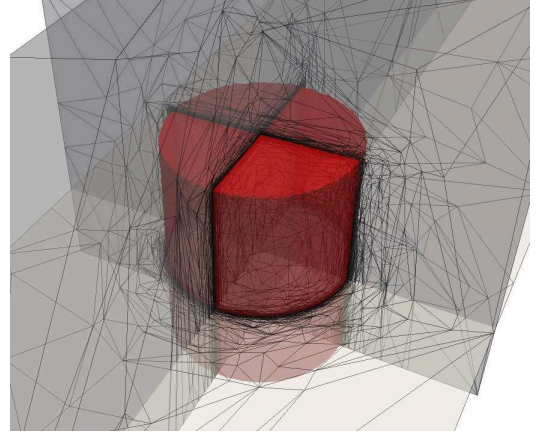


FIGURE 3.10: 3d Adapted mesh: cylinder



FIGURE 3.11: View of the industrial ingot

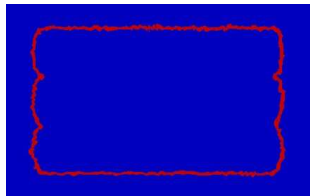
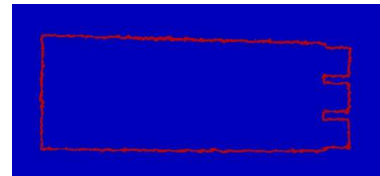
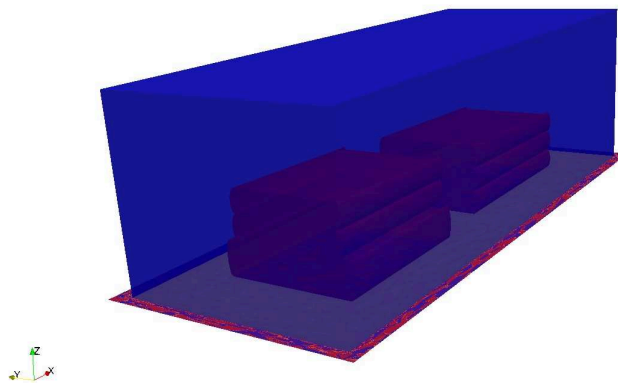
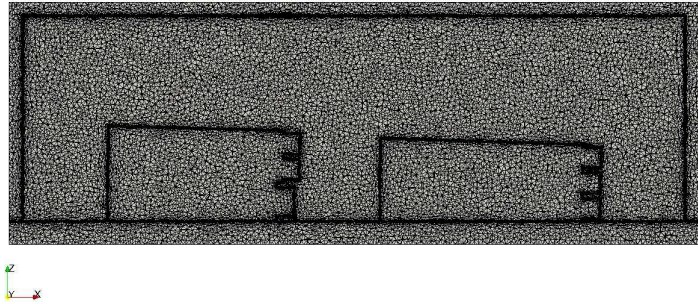
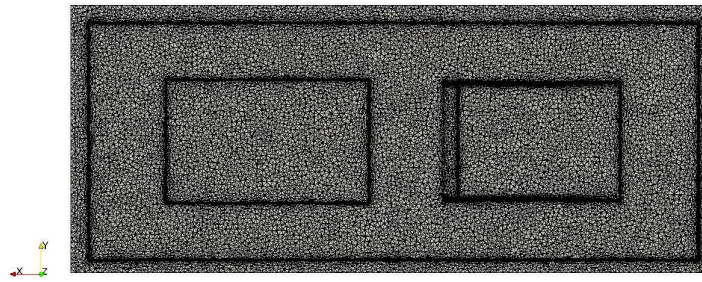
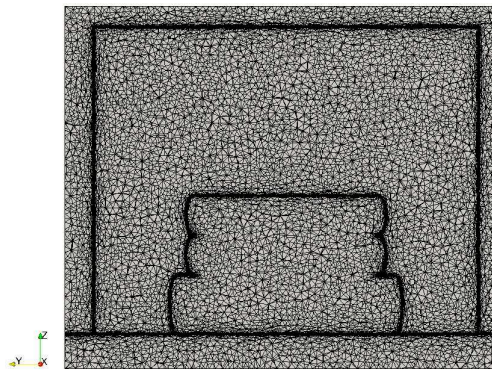
FIGURE 3.12: Cross section along the x axisFIGURE 3.13: Cross section along the y axis

FIGURE 3.14: Whole Facility: overview

FIGURE 3.15: Whole Facility: cross section along the xz planeFIGURE 3.16: Whole Facility: cross section along the xy planeFIGURE 3.17: Whole Facility: cross section along the yz plane

It is also possible to apply those mesh adaptation techniques on the computed fields such as temperature or velocity. In this case, the mesh adaptation and resolution of the equation become strongly coupled, in the sense that a solution is computed on a mesh, which is then adapted to the computed solution. This coupling is attained by iterating at a fixed point algorithm. Such an adaptation is illustrated on pictures below, on problems considered in the past chapter, namely the $2d$ natural convection in an empty cavity, and the $3d$ natural convection with an horizontal plate. The benefit of such a dynamic mesh adaptation can be substantial, particularly in terms of computational time.

Now that the tools for the construction of an appropriate mesh are introduced, the next section is dedicated to the method for dealing with multidomain problems.

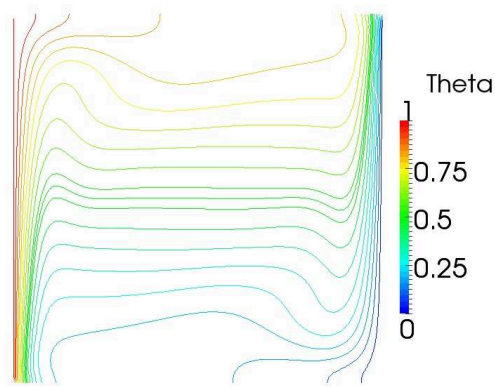


FIGURE 3.18: 2d Empty Cavity for $Ra = 10^6$: Temperature lines

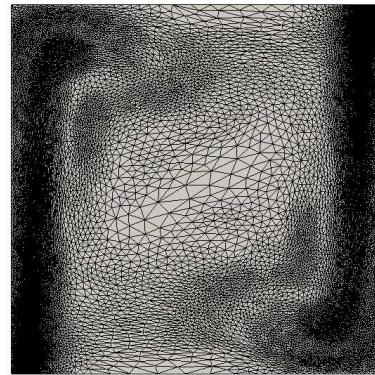


FIGURE 3.19: 2d Empty Cavity for $Ra = 10^6$: adapted mesh on temperature

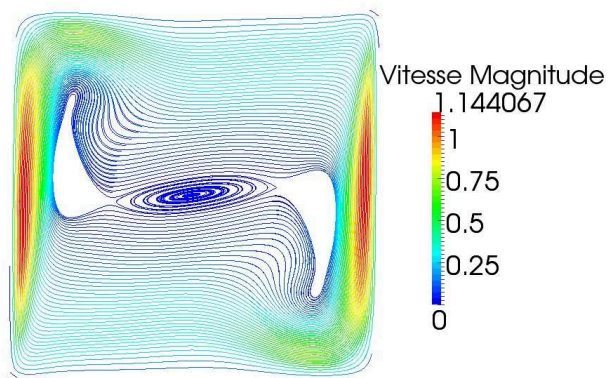


FIGURE 3.20: 2d Empty Cavity for $Ra = 10^6$: streamlines

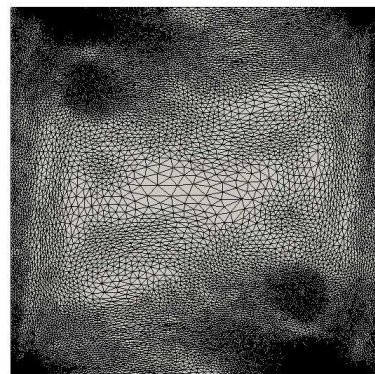


FIGURE 3.21: 2d Empty Cavity for $Ra = 10^6$: adapted mesh on velocity

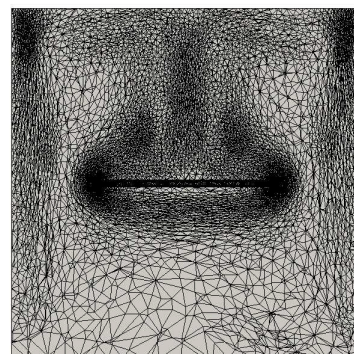
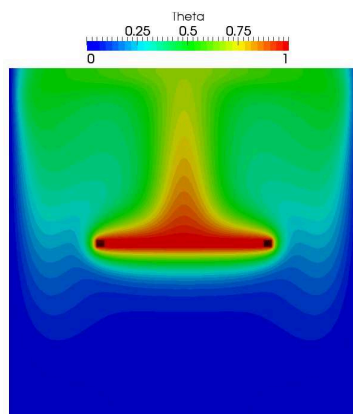


FIGURE 3.22: 3d Horizontal plate: adapted mesh on temperature

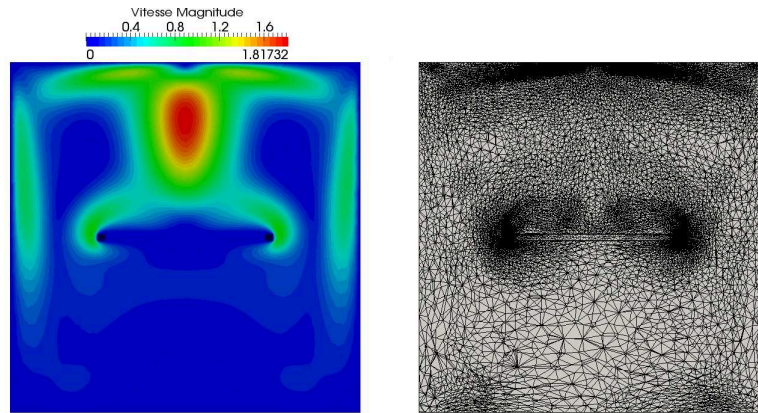


FIGURE 3.23: 3d Horizontal plate: adapted mesh on velocity

3.3 Multidomain problems

Let us recall that we want to perform monolithic simulations in the sense that both solids and fluids are represented on a single mesh leading to one single computation. However, fluids and solids are characterized by different thermophysical properties, so the question is now : how to assess physical properties to each "subdomain"? The most straightforward option would be to consider conform meshes, with nodes on the real interface, but on the one hand, the interface is only implicitly defined, and on the other hand, such a conform mesh is hard to construct for complex geometries. Another options is to make use of Generalized Finite Elements [110]: the idea is to enrich the Finite Element space with a suitable function, allowing to capture effects that a classical Finite Element fails to represent. It has been sucessfully applied to different problems with heterogeneous materials [111, 112] [113] and crack propagation [114]. However, the theoretical analysis is restricted to elliptic problems, and it was shown that the classical version lead to ill conditioned matrixes, even though improved versions can be considered [115]. Here, we are considering another approach based on "mixing laws". We illustrate it by taking the example of the density ρ : if we denote by ρ_f and ρ_s the densities of fluid and solid respectively, the "effective" density $\rho(\mathbf{x})$ is given by :

$$\rho(\mathbf{x}) = \rho_f H(\alpha(\mathbf{x})) + \rho_s (1 - H(\alpha(\mathbf{x}))) \quad (3.24)$$

where $H(\alpha(\mathbf{x}))$ is a Heaviside function, so that the density has the appropriate value in each region. However, this version produces a very sharp transition, and leads to inaccurate results. To circumvent this issue, we consider a smoothed Heavisde function by introducing an interface thickness ϵ , verifying $\epsilon = O(h)$. The Heaviside function will be smoothed on the thickness with respect to the following expression:

$$H(\alpha(\mathbf{x})) = \begin{cases} 1 & \text{if } \alpha(\mathbf{x}) > \epsilon \\ \frac{1}{2} \left(1 + \frac{\alpha(\mathbf{x})}{\epsilon} + \frac{1}{\pi} \sin\left(\frac{\pi\alpha(\mathbf{x})}{\epsilon}\right) \right) & \text{if } |\alpha(\mathbf{x})| \leq \epsilon \\ 0 & \text{if } \alpha(\mathbf{x}) < -\epsilon \end{cases} \quad (3.25)$$

All thermophysical properties will be computed in the same manner, referred to as *linear* mixing law at the exception of thermal conductivity, which has to be mixed using an *harmonic* mixing law to ensure conservation of conductive fluxes. It also can be understood by thinking of the way equivalent thermal resistances are obtained from assemblies in series.

$$\eta(\mathbf{x}) = \eta_f H(\alpha(\mathbf{x})) + \eta_s (1 - H(\alpha(\mathbf{x}))) \quad (3.26)$$

$$T(\mathbf{x}) = T_f H(\alpha(\mathbf{x})) + T_s (1 - H(\alpha(\mathbf{x}))) \quad (3.27)$$

$$\kappa(\mathbf{x}) = \kappa_f H(\alpha(\mathbf{x})) + \kappa_s (1 - H(\alpha(\mathbf{x}))) \quad (3.28)$$

$$\beta(\mathbf{x}) = \beta_f H(\alpha(\mathbf{x})) + \beta_s (1 - H(\alpha(\mathbf{x}))) \quad (3.29)$$

$$\rho c_p(\mathbf{x}) = \rho_f c_{p,f} H(\alpha(\mathbf{x})) + \rho_s c_{p,s} (1 - H(\alpha(\mathbf{x}))) \quad (3.30)$$

$$\lambda(\mathbf{x}) = \frac{1}{\frac{H(\alpha(\mathbf{x}))}{\lambda_f} + \frac{1-H(\alpha(\mathbf{x}))}{\lambda_s}} \quad (3.31)$$

Even though the temperature is one of the variables of the problem, such a mixing law will be useful to prescribe initial values in solid and fluid. For the viscosity, since there exists no definition of the viscosity for a solid, we will set a very important value (typically $\eta_s = 10^6$) in order to ensure a zero velocity inside the solid. This method, known as the penalty viscosity method, show satisfactory results to fit with classical body fitted results. For the case of moving objects, an augmented formulation can be considered [116], the constraint being to have a solid body (rigid or elastic) velocity in the solid obstacle. Regarding the thermal behaviour, a solid boundary with a Dirichlet boundary condition in temperature can easily be modelled in a monolithic context, by setting an important value of the thermal conductivity. To illustrate the use of such mixing laws, we come back to the case of the facility, where we display the effective heat capacity and viscosity.

It is interesting to note that the computation is driven by those spatially dependent properties: the velocity field, due to the high value of the viscosity at solid boundaries, coupled to appropriate physical properties of each component, properly mimics the convective transfer naturally, with no supplementary effort. The method allows to consider

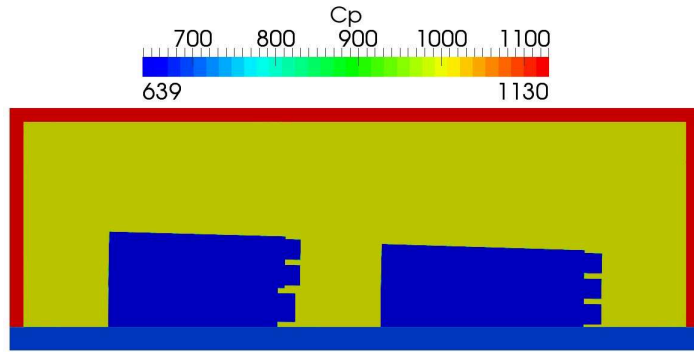


FIGURE 3.24: Industrial Facility: effective heat capacity

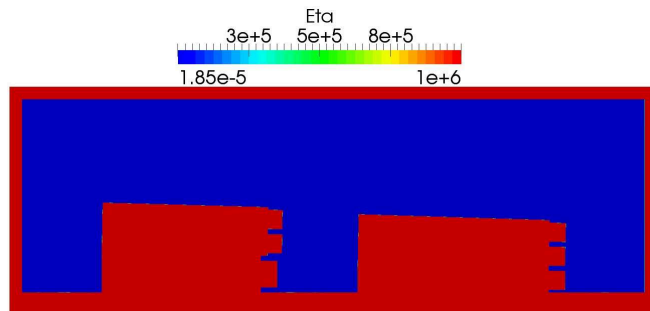


FIGURE 3.25: Industrial Facility: effective viscosity

various industrial configurations, the price to pay being the fact that the construction of the mesh can be time consuming, but, as stated previously, the construction of the mesh is an "offline" operation. Once the mesh has been constructed, the overall method has a computational cost similar to more classical methods, but allows to perform simulations that would be difficult to set up using a body fitted approach, as the results of chapter 6 will show.

Before moving to the numerical experiments regarding the immersed volume method, it is important to recall that the three features of this monolithic approach are strongly coupled: there might be several iterations to find a good couple between a well adapted mesh, properly represented interfaces and well assessed physical properties, due mostly in the choice of ϵ : a too small value of interface thickness would consume too many elements to represent the interface and a too large value would lead to an oversized interface that would modify the physical output of the system, leading to non-relevant results. The next section is dedicated to numerical experiments to demonstrate the consistency of the monolithic approach.

3.4 Numerical experiments

When a novel approach such as the IVM described upper is developed, the first validation step consists in the comparison of the obtained results with the ones obtained using a classical (body-fitted here) approach. Since the BF results were compared to results from literature in the last chapter, they will be considered as a reference here. We will see that the convergence of both results is essentially related to the construction of an appropriate mesh. In fact, it is not an easy task to construct a "monolithic" mesh that is comparable with a classical one; on the one hand, it is difficult to properly control the number of elements necessary to represent the interface over the total number of elements, and on the other hand, in the case of unstructured anisotropic meshes, what stands for the characteristic mesh size? To validate the approach we will make use of the problems presented in the previous part, in $2d$ as well in $3d$.

3.4.1 Natural convection in an empty cavity

For the $2d$ version, we will enlarge the domain model with slabs of a very highly conductive solid body (in order to replace the thermal boundary conditions) of length $l = 0.25m$, so that the computational domain that was $[0; 1] * [0; 1]$ will finally be $\Omega = [-0.25; 1.25] \times [0; 1]$. Adiabatic boundary conditions are imposed on lower and upper walls, and slip boundary conditions are imposed on all the boundaries for the velocity. We set here $Pr = 0.71$ and $Ra = 10^6$ for the $2d$ and $3d$ validation. Since an error analysis similar to the one in [44] will be performed in $2d$, we chose the same values for the temperature which are $T_h = 960K$, $T_c = 240K$ and $T_0 = 600K$.

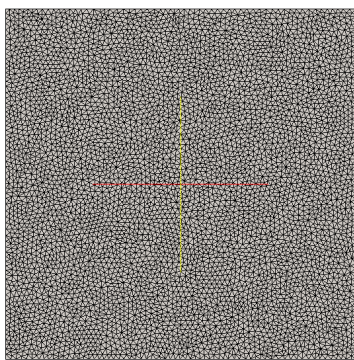


FIGURE 3.26: $2d$ Empty cavity: mesh for the body-fitted approach

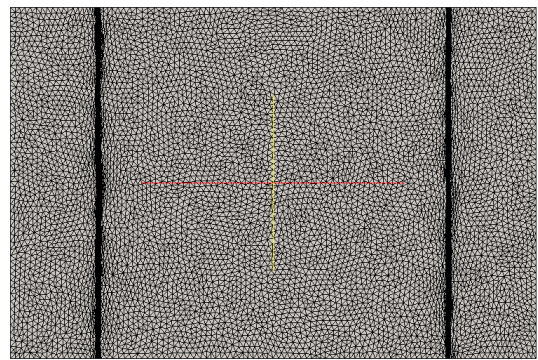


FIGURE 3.27: $2d$ Empty cavity: mesh for the immersed volume method

The meshes used for the computations highlight the extension of the domain and the obtained anisotropic mesh at the interface. Note that the same background mesh size was used elsewhere. Patterns of the temperature and the velocity are presented in figures 3.28 and 3.29 and compared to results obtained with a classical body-fitted approach.

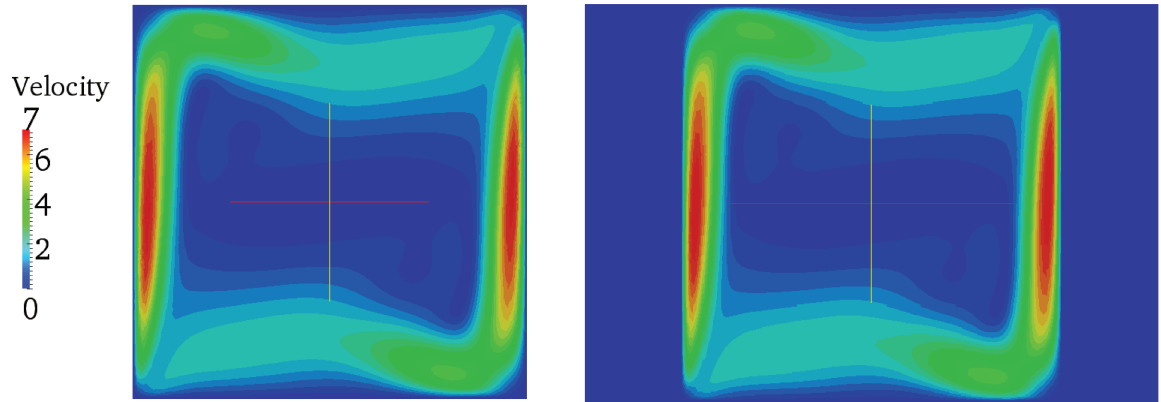


FIGURE 3.28: 2d Empty cavity: velocity profile using the body-fitted approach (left) and the immersed approach (right)

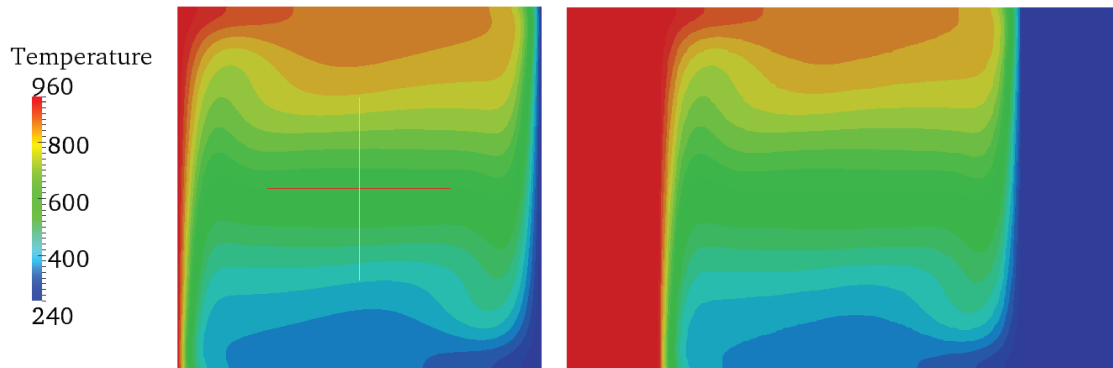


FIGURE 3.29: 2d Empty cavity: temperature distribution using the body-fitted approach (left) and the immersed approach (right)

The convergence of results with respect to the characteristic mesh size are illustrated of figures below, by plotting relevant quantities along the line $y = 0.5$, like the temperature or the x component of the velocity, on four different meshes of decreasing mesh sizes. The expected tendency is observed, that is to say, for an appropriately refined mesh, the monolithic approach tends to reproduce the body fitted results.

It is also relevant, for the most refined mesh M_1 , to plot quantities along the line $x = 0.5$, in order to quantify how the refined interfaces perform to represent the boundary layers. Here, thanks to the high values chosen for both viscosity and conductivity, the temperature and velocity remain constant and equal to zero, respectively, in the solid boundary.

Finally, we investigated the L^2 error with respect to the number of elements was performed using the four meshes used above. A linear convergence is observed, as it can be expected from the Finite Element theory.

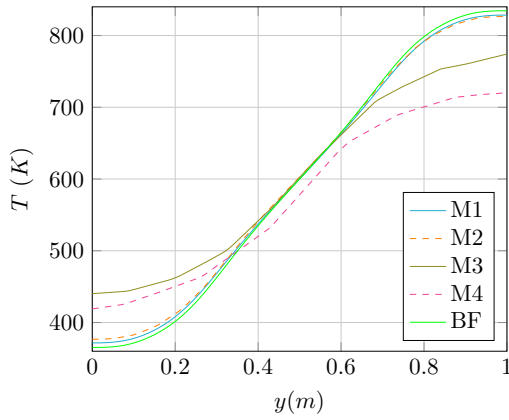
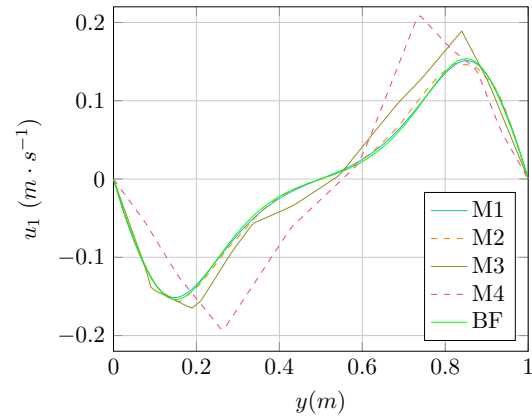
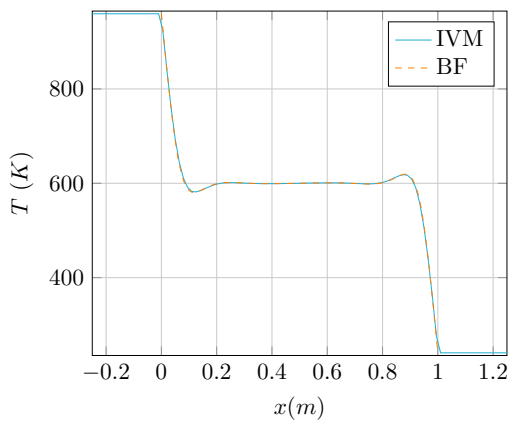
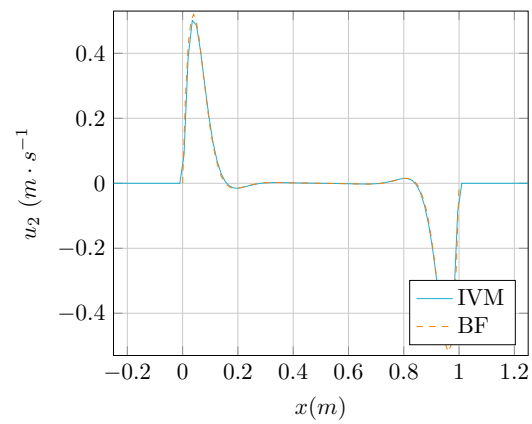
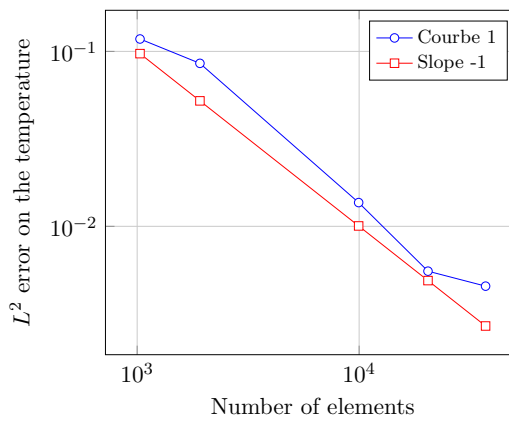
FIGURE 3.30: 2d Empty cavity: T for several meshesFIGURE 3.31: 2d Empty cavity: u_2 for several meshesFIGURE 3.32: 2d Empty cavity: T along $x = 0.5$ FIGURE 3.33: 2d Empty cavity: u_2 along $x = 0.5$ 

FIGURE 3.34: 2d Empty cavity: error analysis on the temperature

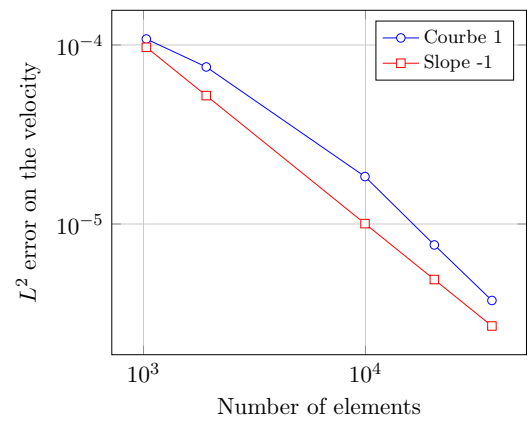


FIGURE 3.35: 2d Empty cavity: error analysis on the velocity

An 3d extension of this case was proposed, the volumic boundaries being represented in the same manner than in the 2d case with no difficulties, since the problem is invariant with respect to the third coordinate. The adapted meshes are presented below. Note that if the "edge-based" metric was used for the 2d computations, the 3d case was adapted by

means of the "Hessian-based" metric, showing both metrics lead to approximately the same results. The temperature and velocity profiles are exhibited as well, demonstrating the same coincidence between BF and IVM results than in $2d$, but a rigorous analysis of this coincidence requires to investigate the agreement between local quantities, likewise in the $2d$ case.

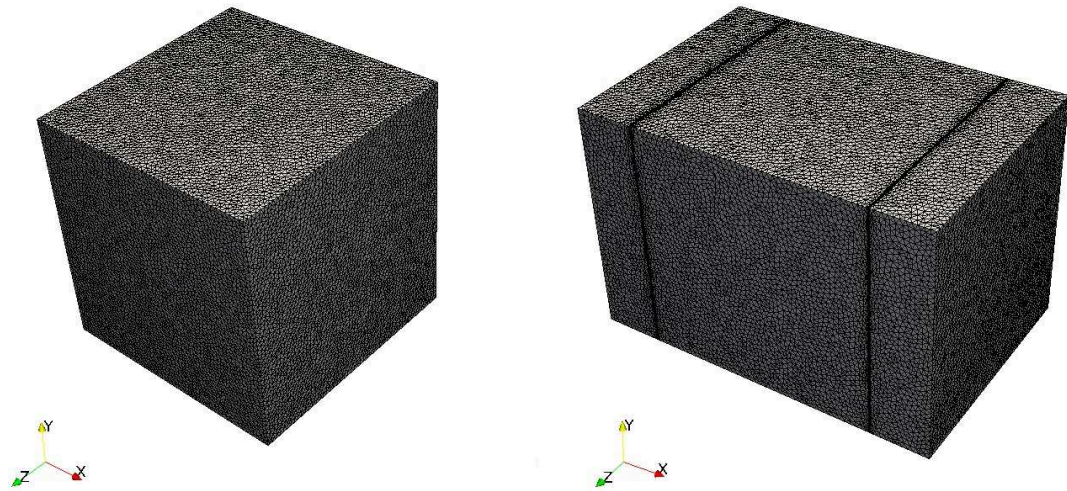


FIGURE 3.36: $3d$ Empty cavity: meshes used for the "BF" (left) and "IVM" (right) simulations

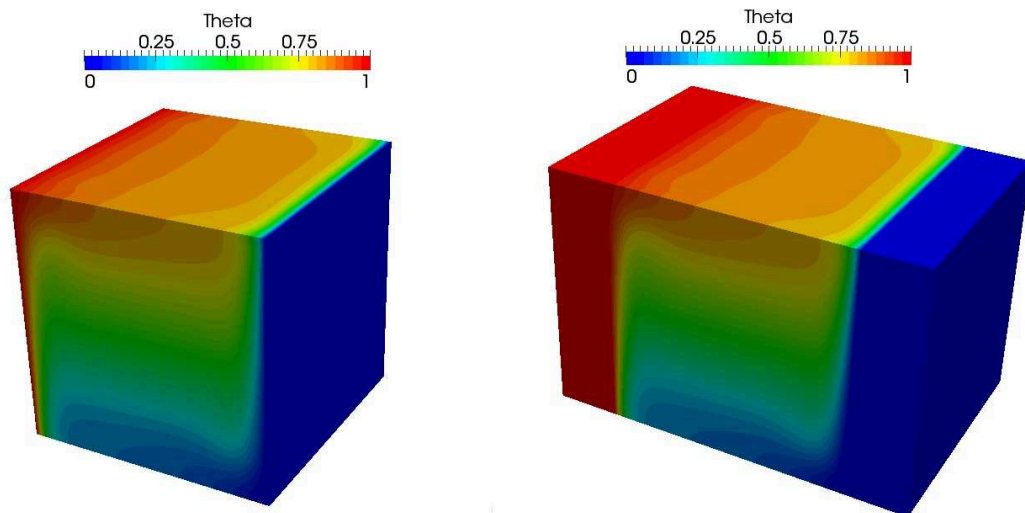


FIGURE 3.37: $3d$ Empty cavity: temperature profiles for "BF" (left) and "IVM" (right) simulations

First of all, we study the quantities which are the equivalent of the ones studied for the $2d$ case, that is to say the lines corresponding to the intersection of two planes $l_1 = \{y = 0.5 \cap z = 0.5\}$, $l_2 = \{x = 0.5 \cap z = 0.5\}$ and $l_3 = \{y = 0.5 \cap x = 0.5\}$. The pattern of the third component of the velocity is also presented.

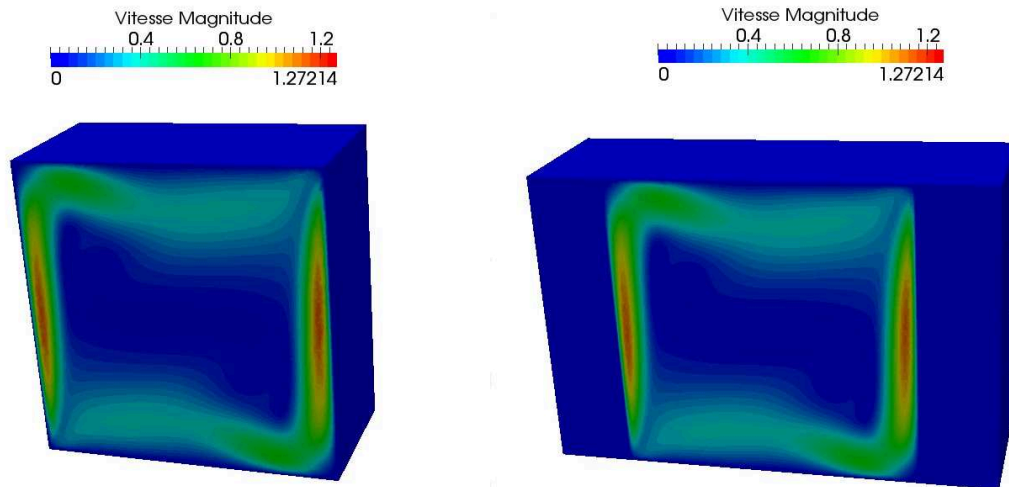


FIGURE 3.38: 3d Empty cavity: velocity profile for "BF" (left) and "IVM" (right) simulations

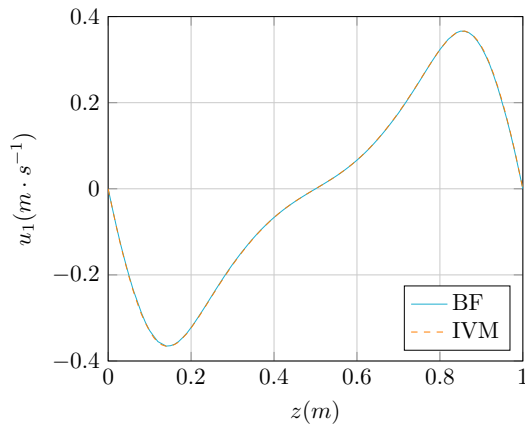


FIGURE 3.39: 3d Empty cavity: u_1 along l_1

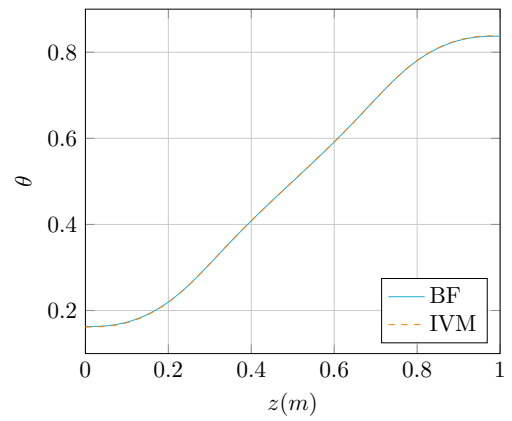


FIGURE 3.40: 3d Empty cavity: θ along l_1

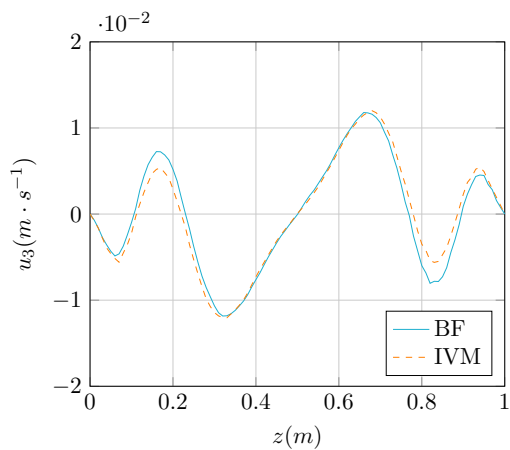


FIGURE 3.41: 3d Empty cavity: u_3 along l_1

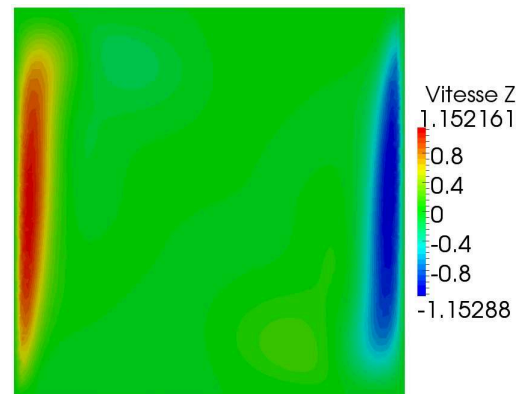


FIGURE 3.42: 3d Empty cavity: profile of u_3 for the considered line

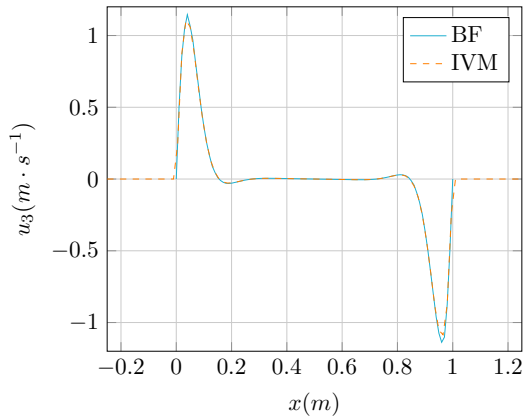


FIGURE 3.43: 3d Empty cavity: u_3 along l_2

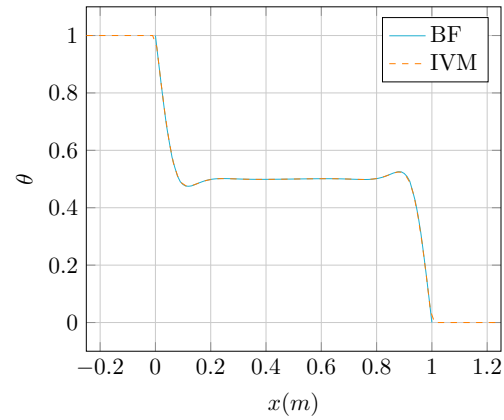


FIGURE 3.44: 3d Empty cavity: θ along l_2

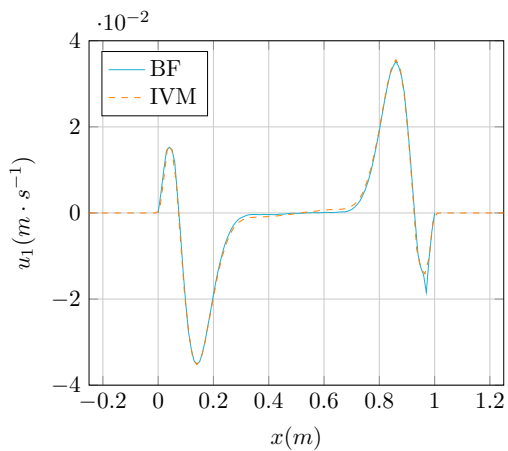


FIGURE 3.45: 3d Empty cavity: u_1 along l_2

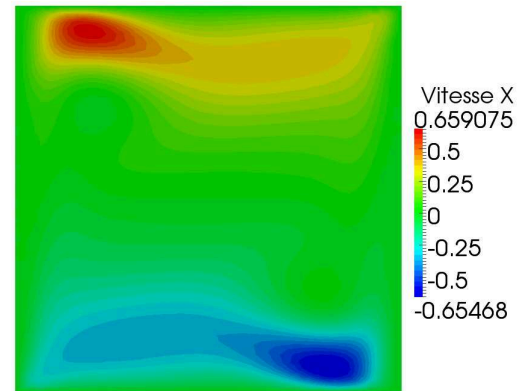


FIGURE 3.46: 3d Empty cavity: profile of u_1 for the considered line

3.4.2 Natural convection in a cavity containing a plate

Recall that, the "immersed" versions were considered naturally by introducing a levelset Function for the heated plate. For the duration of study, we keep $Ra = 10^6$ and $Pr = 0.71$. An interesting feature of our immersed method is that the set up for the vertical and horizontal cases are exactly the same, except for the definition of the levelset function. The meshes used for the computations are displayed below. Note that there are very few elements inside the plate, which makes sense since the quantities are expected to remain constant inside. Controlling the number of elements inside and outside is possible with our implementation of the "edge-based" metric. As in the previous case, we used body fitted meshes with approximately the same background mesh size than the ones displayed.

However, the validation would not be complete without a quantitative study, so we chose to study some relevant quantities along some lines at $y = cst$. We want to verify the

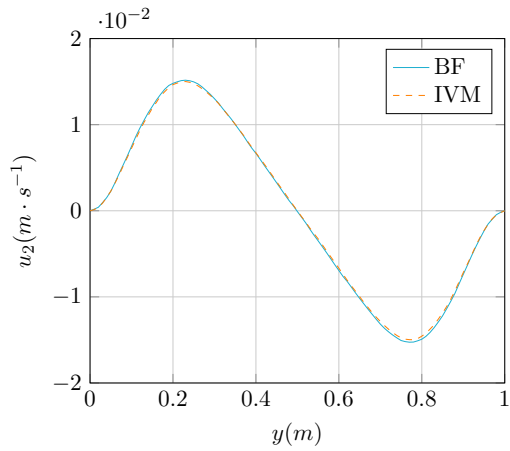


FIGURE 3.47: 3d Empty cavity: u_2 along l_3

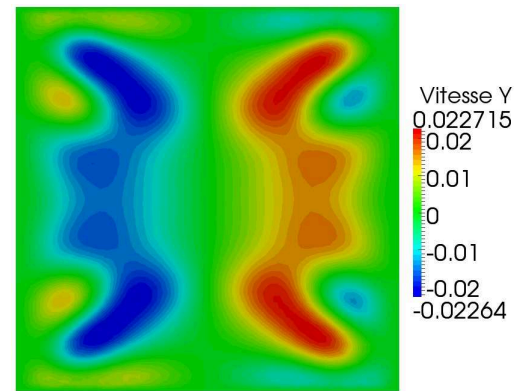


FIGURE 3.48: 3d Empty cavity: profile of u_2 for the considered line

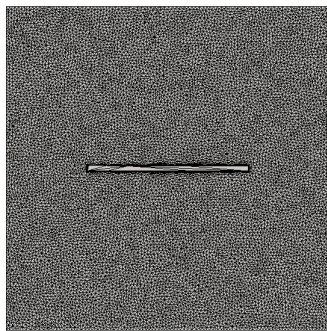


FIGURE 3.49: Mesh for the 2d horizontal case

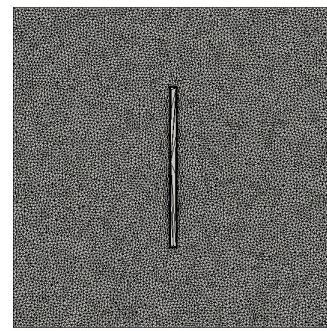


FIGURE 3.50: Mesh for the 2d vertical case

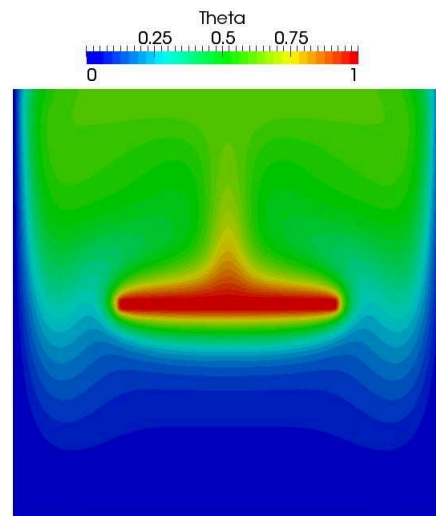
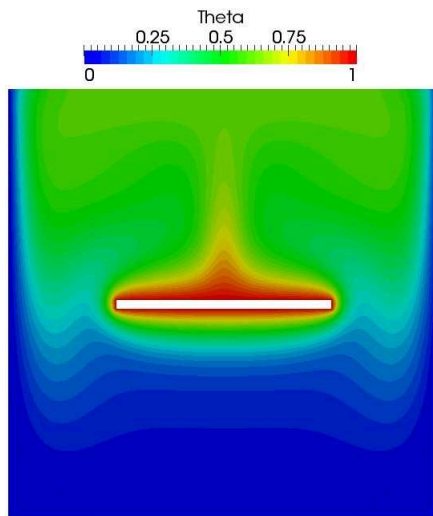
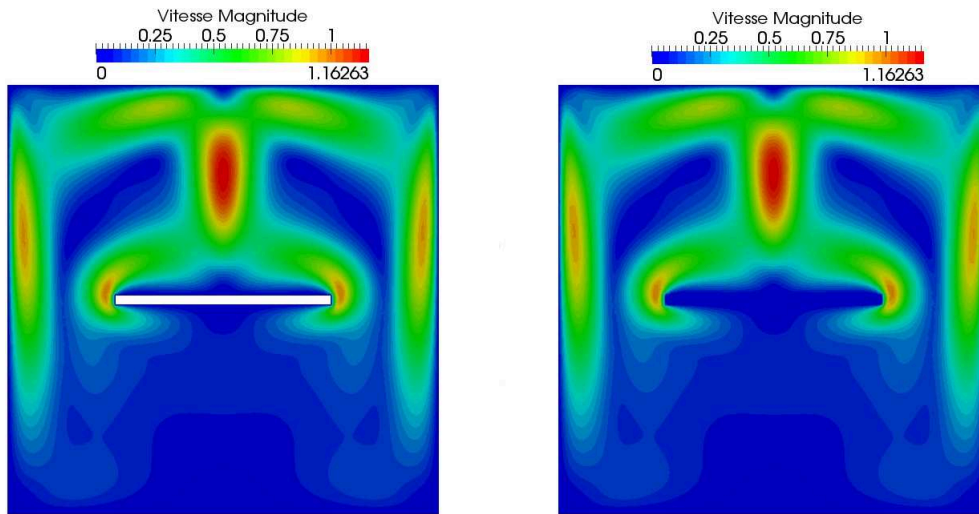
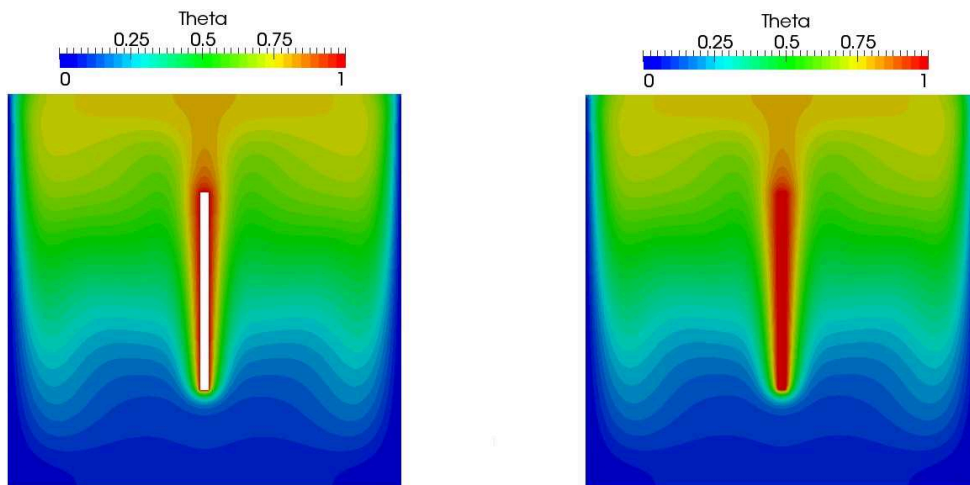
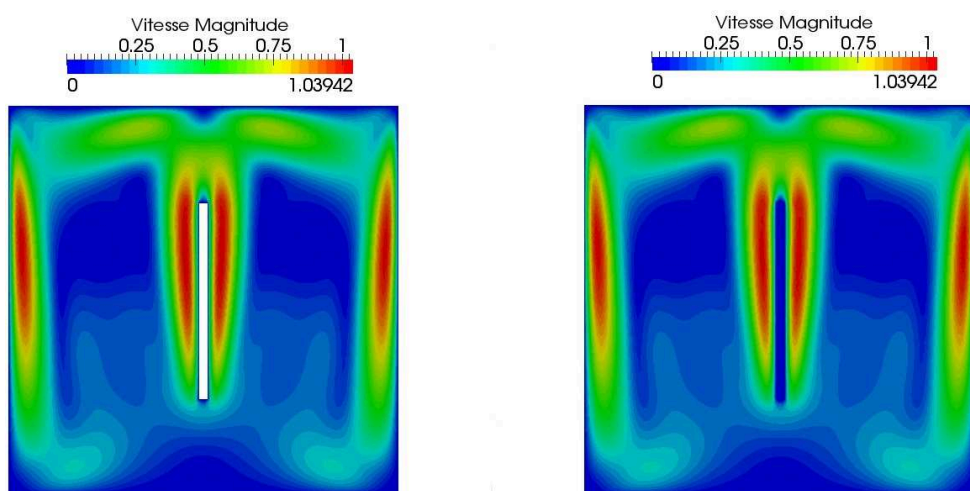
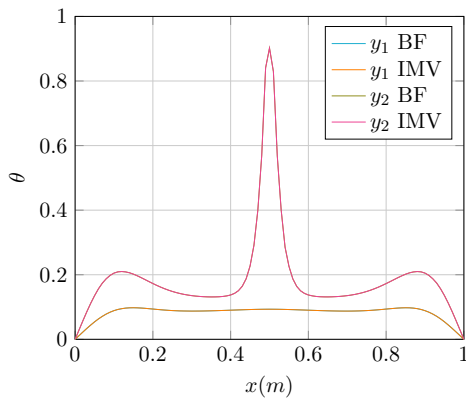
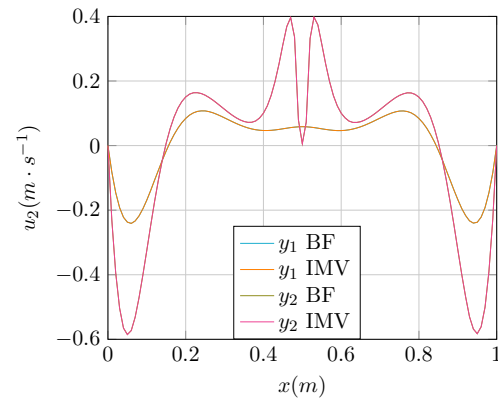
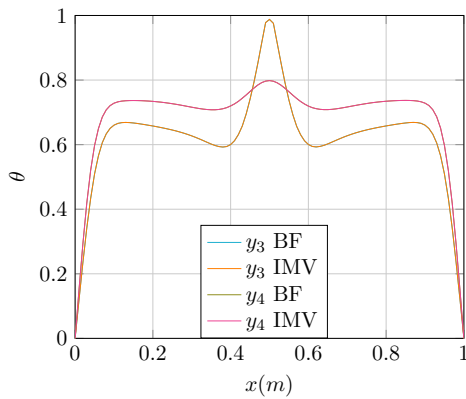
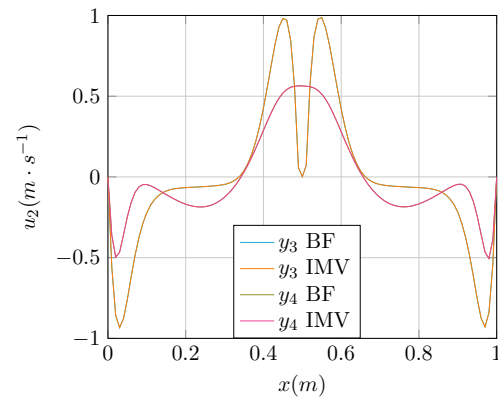


FIGURE 3.51: 2d Horizontal plate: θ for IVM and BF

results close to the surface of the plate in order to check if the interface behaviour is properly captured. To this end we chose four lines for each case, listed in the table below:

FIGURE 3.52: $2d$ Horizontal plate: velocity for IVM and BFFIGURE 3.53: $2d$ Vertical plate: θ for IVM and BFFIGURE 3.54: $2d$ Vertical plate: velocity for IVM and BF

y	Horizontal	Vertical
y_1	0.3	0.1
y_2	0.4875	0.2475
y_3	0.5125	0.7525
y_4	0.65	0.9

TABLE 3.2: 2d plates: y for the chosen linesFIGURE 3.55: 2d Vertical obstacle: θ along considered lines 1/2FIGURE 3.56: 2d Vertical obstacle: u_2 along considered lines 1/2FIGURE 3.57: 2d Vertical obstacle: θ along considered lines 2/2FIGURE 3.58: 2d Vertical obstacle: u_2 along considered lines 2/2

As it can be seen on the patterns, for the horizontal case, the results between y_2 and y_3 are almost symmetric, with a zone where the quantities are constant ($u_2 = 0$ and $\theta = 1$), as it can be expected in the vicinity of the heated plate. It should be pointed out that during previous computations, it was observed that a gap between BF and IMV values can be observed if the mesh is not well adapted at the interface, even though the results appear to be the same "to the eye".

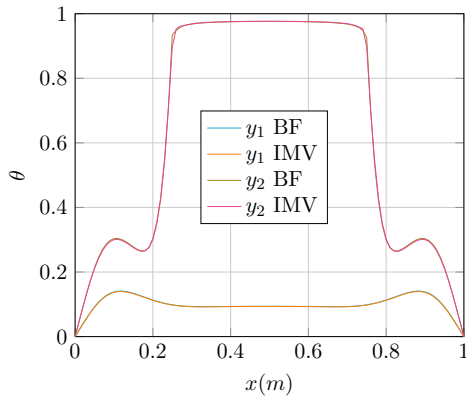


FIGURE 3.59: 2d Horizontal obstacle: θ along considered lines 1/2

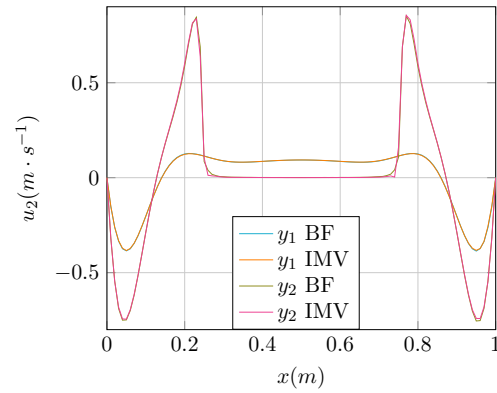


FIGURE 3.60: 2d Horizontal obstacle: u_2 along considered lines 1/2

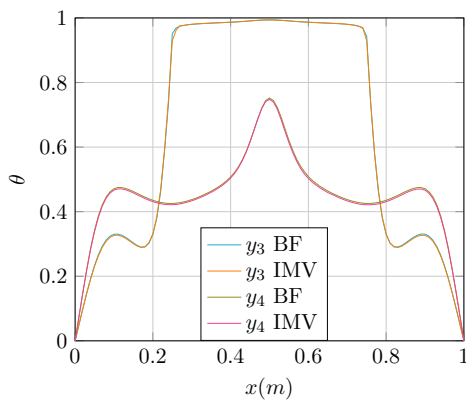


FIGURE 3.61: 2d Horizontal obstacle: θ along considered lines 2/2

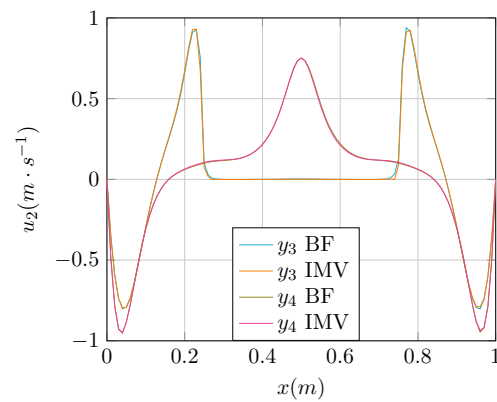


FIGURE 3.62: 2d Horizontal obstacle: u_2 along considered lines 2/2

The 3d extension for those cases were performed similarly to the 3d BF cases. We display three cutting planes for each mesh, showing that the interface is properly captured in all directions

One can see that the obtained results in the plane $z = 0.5$ are, for both cases, the same results that the ones obtained for the 2d cases. The results in the plate plane are presented as well, showing once again a good agreement for both problems.

Here again, we will verify that we obtain the same results quantitatively. As for the 2d, we will verify the consistency on quantities at middle locations between the plate and the boundaries and close to the interface. To this end, we chose different locations in the cavity. The chosen locations are listed in the table below. We considered the two directions, in order to verify the quantities at the interfaces in the two directions.

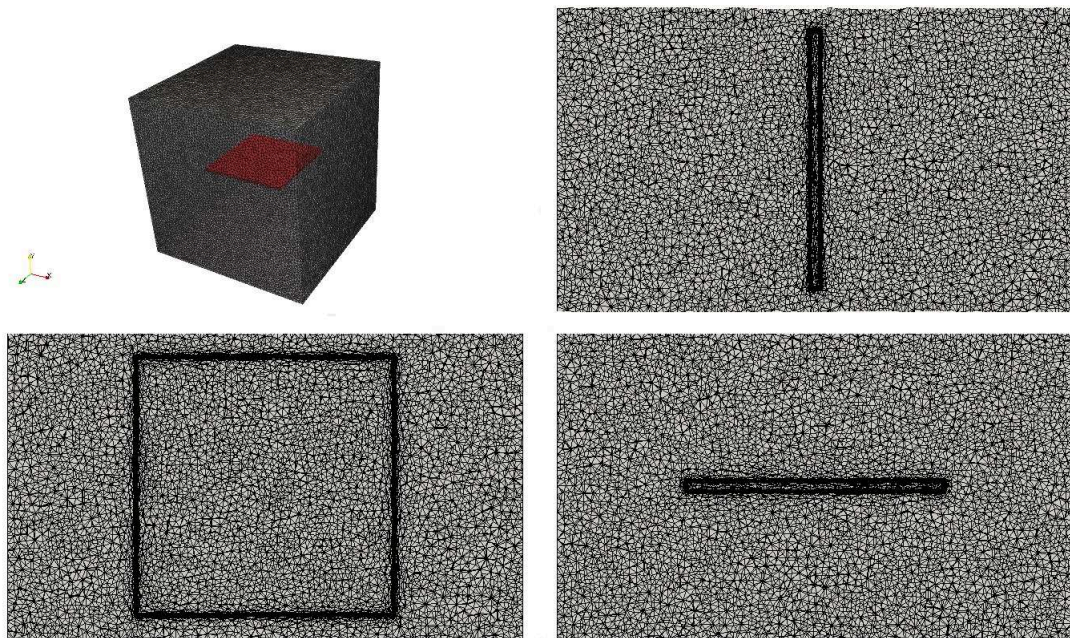


FIGURE 3.63: 3d Horizontal plate: IVM mesh

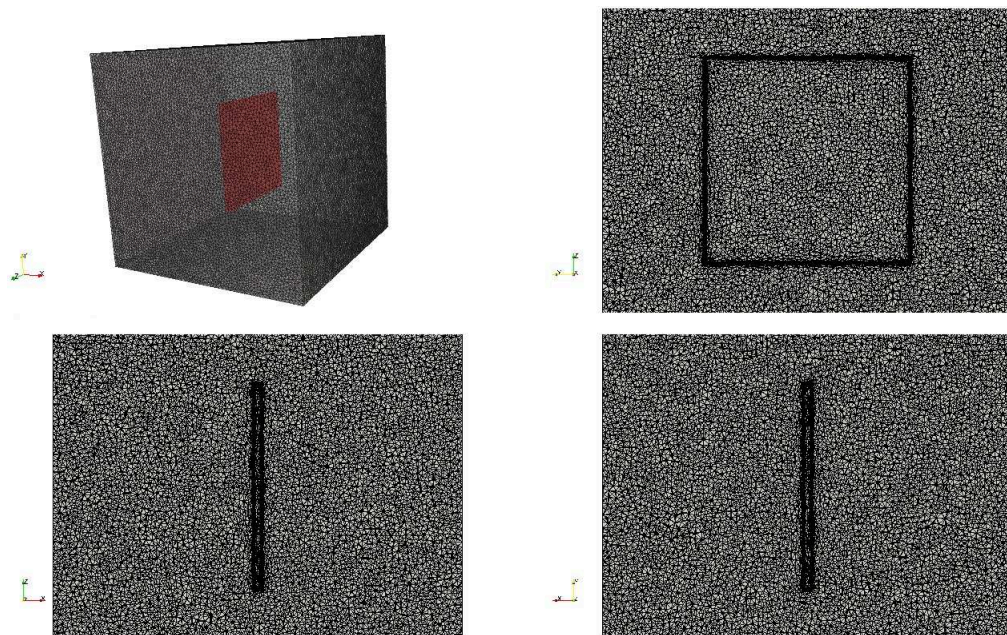
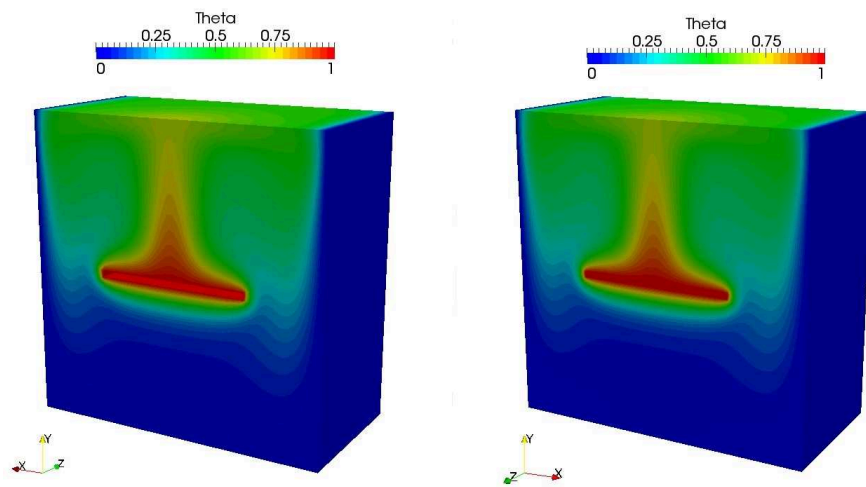
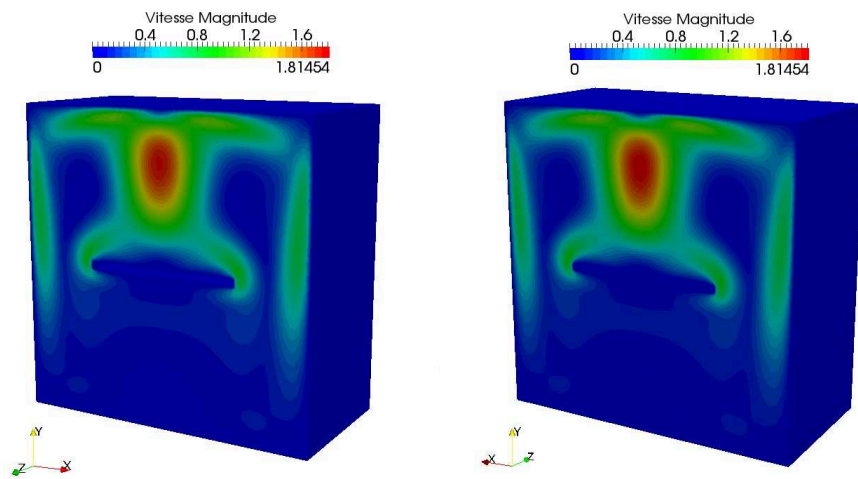
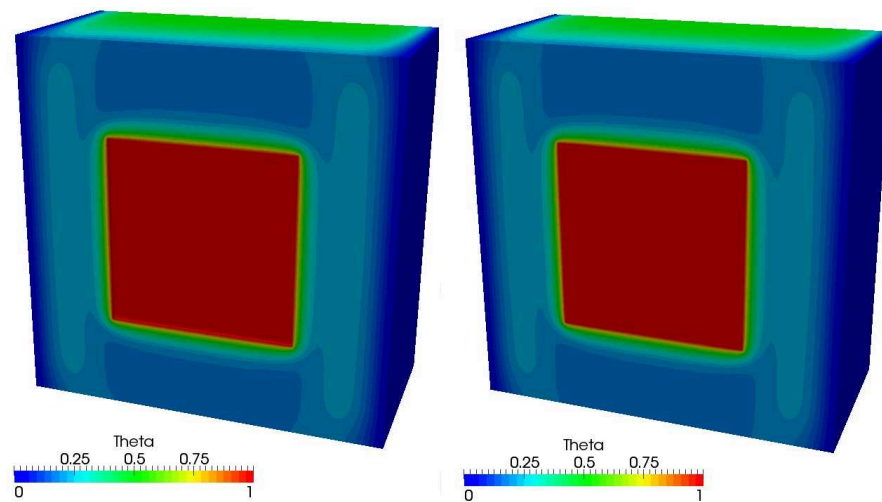
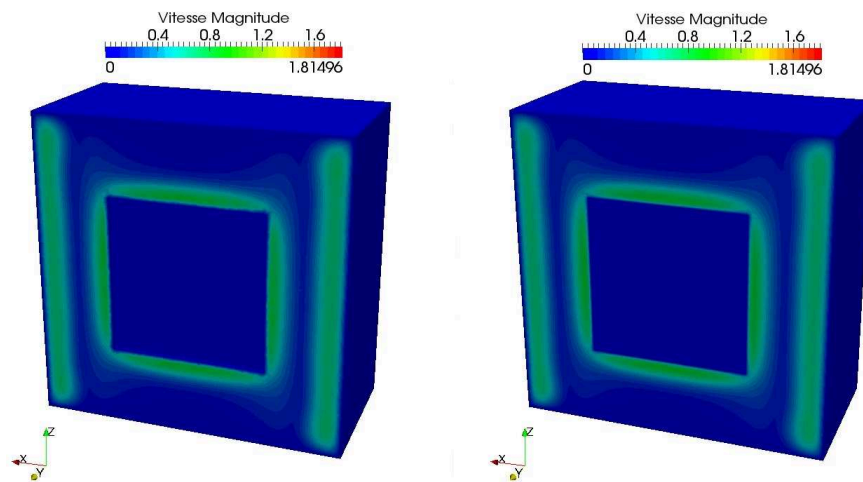
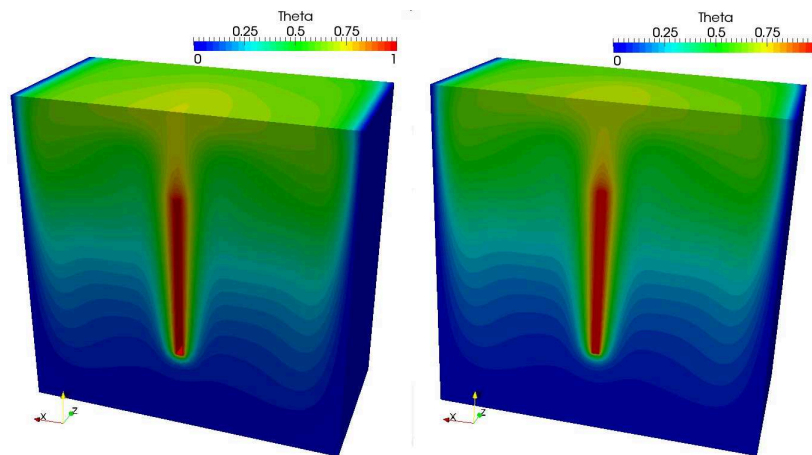
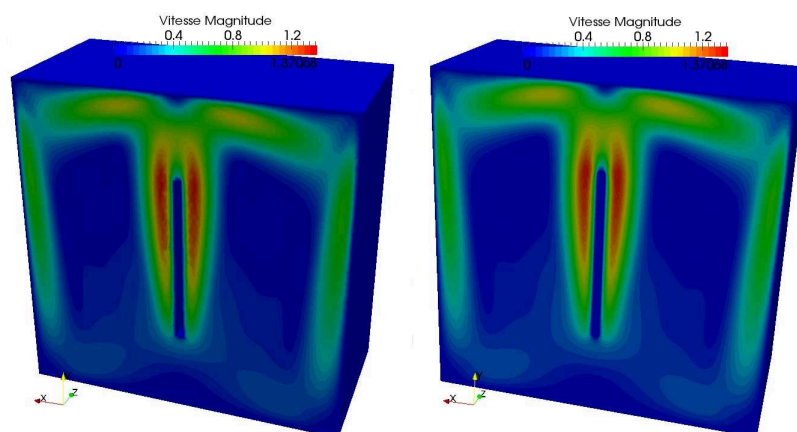


FIGURE 3.64: 3d Vertical plate: IVM

l	coordinate 1	coordinate 2
l_4	$y = 0.75$	$x = 0.5$
l_5	$y = 0.75$	$z = 0.5$
l_6	$y = 0.9$	$x = 0.5$
l_7	$y = 0.9$	$z = 0.5$

TABLE 3.3: 3d plates: coordinates of the chosen lines

FIGURE 3.65: 3d Horizontal plate: θ in the $z = 0.5$ planeFIGURE 3.66: 3d Horizontal plate: velocity in the $z = 0.5$ planeFIGURE 3.67: 3d Horizontal plate: θ in the $y = 0.5$ plane

FIGURE 3.68: 3d Horizontal plate: velocity in the $y = 0.5$ planeFIGURE 3.69: 3d Vertical plate: θ in the $z = 0.5$ planeFIGURE 3.70: 3d Vertical plate: velocity in the $z = 0.5$ plane

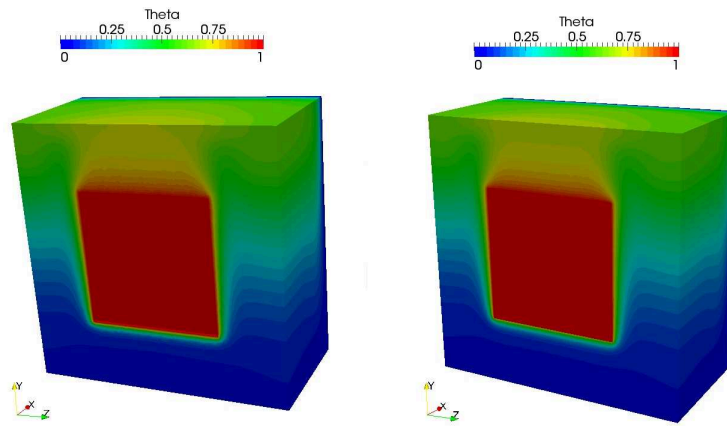


FIGURE 3.71: 3d Vertical plate: θ in the $y = 0.5$ plane

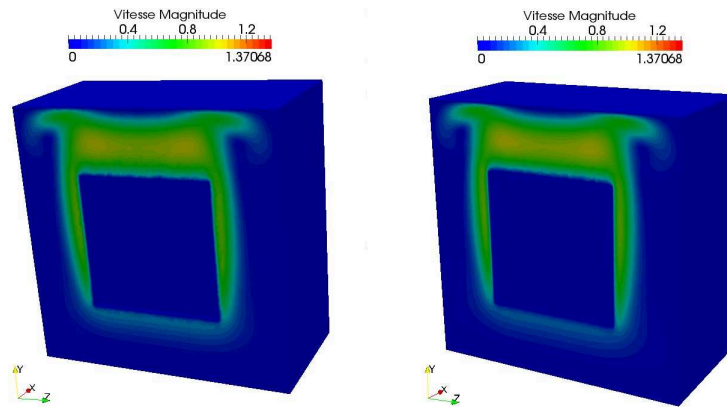


FIGURE 3.72: 3d Vertical plate: velocity in the $y = 0.5$ plane

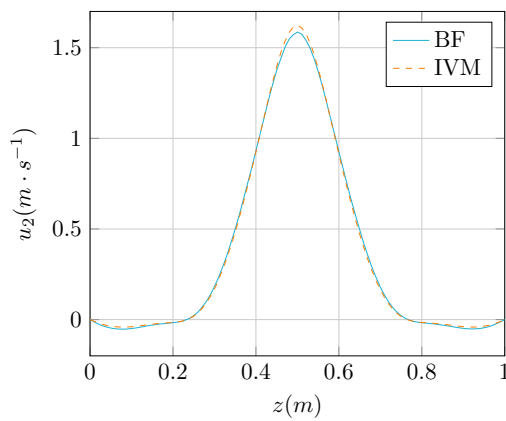


FIGURE 3.73: 3d Horizontal plate: u_2 along l_4

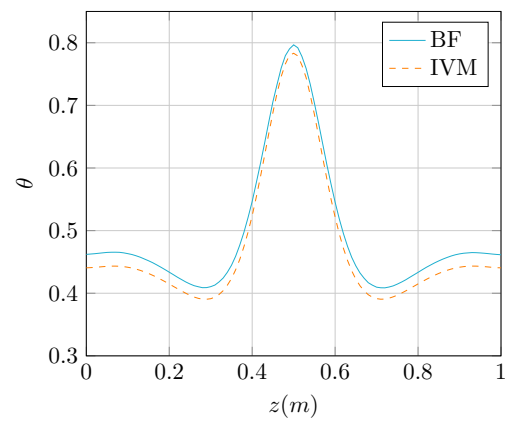


FIGURE 3.74: 3d Horizontal plate: θ along l_4

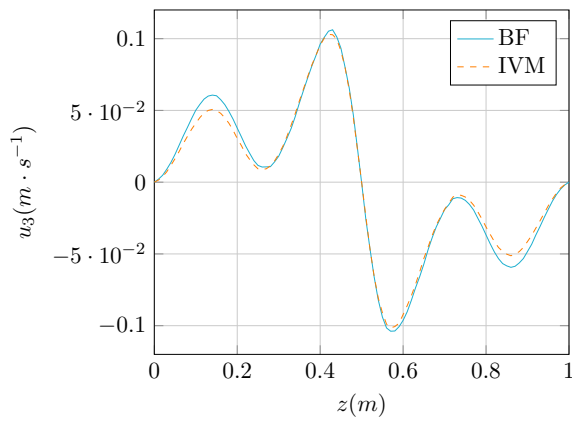


FIGURE 3.75: 3d Horizontal plate: u_3 along l_4

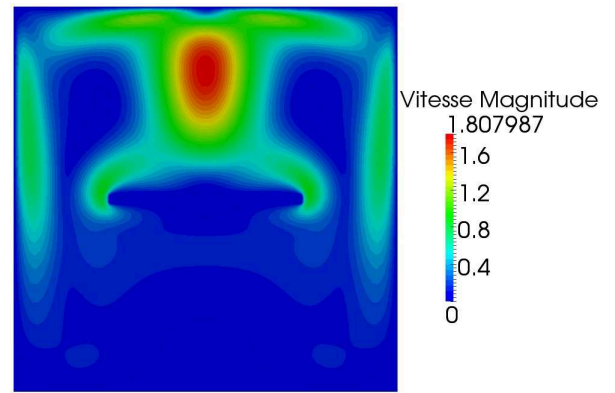


FIGURE 3.76: 3d Horizontal plate: corresponding velocity profile

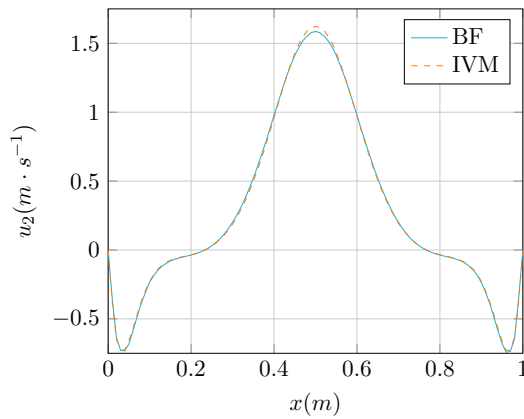


FIGURE 3.77: 3d Horizontal plate: u_2 along l_5

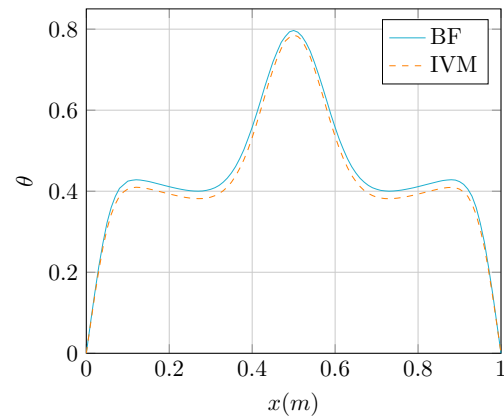


FIGURE 3.78: 3d Horizontal plate: θ along l_5

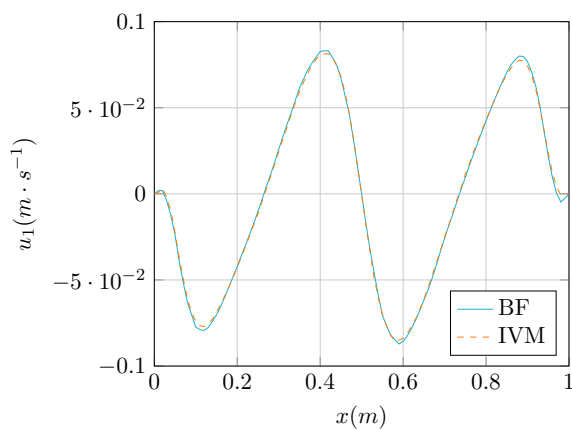


FIGURE 3.79: 3d Horizontal plate: u_1 along l_5

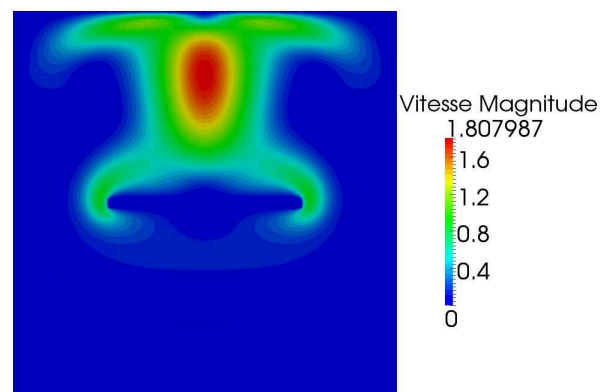


FIGURE 3.80: 3d Horizontal plate: corresponding velocity profile

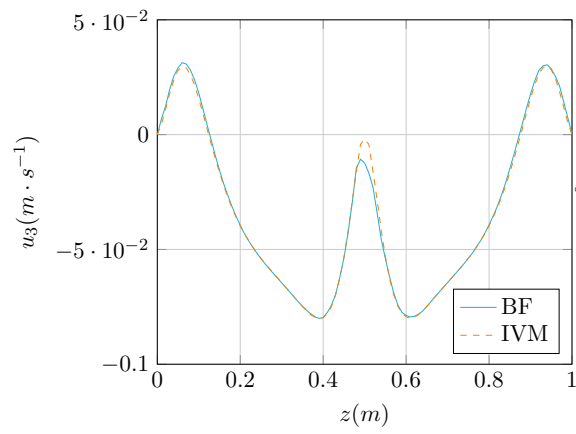


FIGURE 3.81: 3d Vertical plate: u_3 along l_6

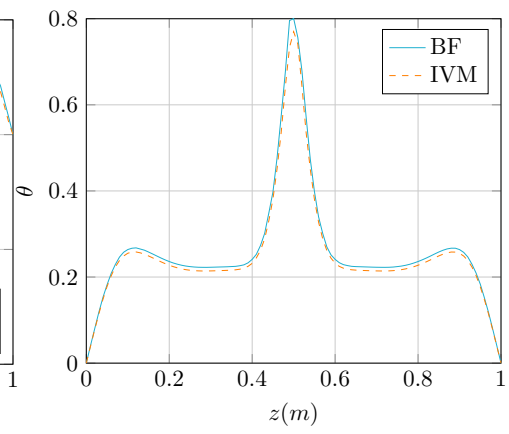


FIGURE 3.82: 3d Vertical plate: θ along l_6

3.4.3 Mixed convection of a group of ingots

This example is to demonstrate the ability of the immersed volume method to deal with a problem involving different components in interaction. On the left side of the computational domain, hot air at temperature T_h is injected with an inlet velocity U_{in} . An outflow boundary condition is prescribed on the left part of the domain, and no slip boundary conditions are prescribed elsewhere. Three rectangular pieces of different geometry (see pictures below) are present in the domain to be heated by the hot fluid coming from the inlet. We made use here of multi-criteria mesh adaptation, to adapt simultaneously on the levelset of ingots, the velocity and the temperature. One can see here the effects of the ingots that block the flow. This case is to demonstrate how this framework can be used for the optimization of real situations: if an user wants to analyse the position of ingots that minimizes the time of heating, or the one that ensures a homogeneous heating in all pieces, it is possible to change the position and/or the size of ingot only by modification of geometric parameters (size, position) and remeshing increments.

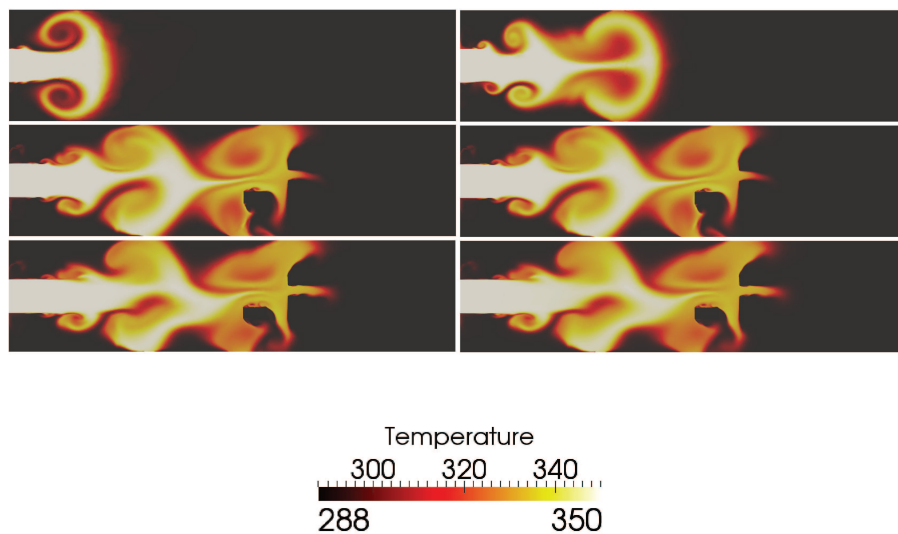
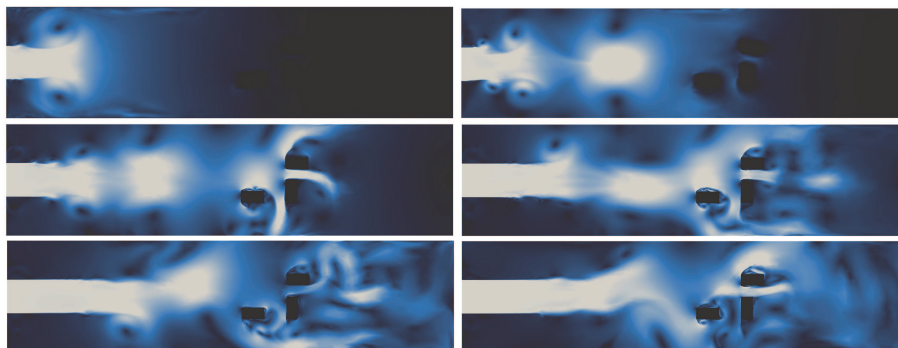


FIGURE 3.85: 2d Mixed convection: velocity at several time steps



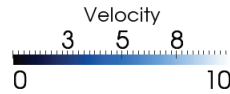


FIGURE 3.86: *2d* Mixed convection: velocity at several time steps

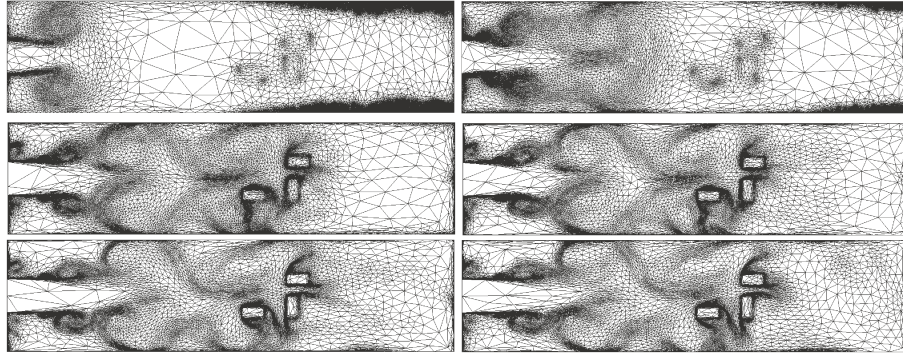


FIGURE 3.87: *2d* Mixed convection: mesh at several time steps

Conclusions

The numerical experiments have demonstrated the ability of the method to be consistent with a classical BF approach on the one hand, and on the other hand the flexibility of the method to deal with different geometric configurations. We would like to point out that the empty cavity case shows the possibility of modelling volume boundaries, which are important in the global thermal balance of an industrial furnace, whereas the cases with the plate demonstrate the potential of the method to properly represent the thermal performance of a multidomain problem, which was the most desired feature of the method. However, some slight differences can be observed between IVM and BF results, particularly for the *3d* plate cases. Those discrepancies can be explained by the following reasons:

- As it was stated before, the key point of the problem set up is the mesh adaptation process: even though the results could appear to match "at the eye", an extensive analysis of the results shows that a bias remain. This rise the question of the grid independency in a monolithic context: since an finer mesh means more elements concentrated at the interface, it is difficult to control the "background" mesh size which ensures the asymptotic regime for the FE solutions is reached in the fluid. An extensive reflection about those questions is ongoing.
- The velocity component presenting bias are some small magnitude components. Hence, one can expect the observed difference not to have a significative influence on global quantities (heat transfer rate, cooling time,...) that are of interest for engineers.

- Regarding the results in temperature, the small discrepancy might come from the stabilization technique: one of the stabilization term implies the thermal diffusivity $\frac{\lambda}{\rho c_p}$, and since important values were prescribed inside the plate to ensure a constant temperature, the gap for this stabilization parameter across the interface could be significant. It shows that the "tuning" of stabilization parameters is not yet perfect, and could be improved.

Nevertheless, a curious fact was observed during comparisons between BF and IVM simulations, particularly on the case of the vertical plate: sometimes the results looked "better" with the immersed volume method, even when a similar number of elements was used. This can be explained by the fact that, in the case of the immersed volume method, the elements are more "intelligently" located, where one can expect to encounter the thermal boundary layers. This is another argument in favor of the immersed volume method, when one knows the difficulty to construct a mesh before any computation.

We recall that this study regarding the consistency of the IVM is to be linked with the ones previously done in [41, 117].

Résumé français

Ce chapitre présente les méthodes utilisées pour le traitement de problèmes multi-domaines tels que les fours industriels ou les procédés de trempe. La géométrie des différents composants est représentée par le biais de fonctions levelset, qui peuvent être calculées de manière systématique à partir d'un modèle CAO de l'objet considéré. On décrit ensuite les outils nécessaires à la construction d'un maillage approprié à la représentation des interfaces. On introduit les notions d'erreur d'approximation et d'interpolation ainsi que celle de métrique, dont on détaille les deux exemples qui sont utilisés dans ce travail. On précise ensuite les lois de mélange utilisées pour déduire des propriétés physiques effectives à partir de celles des différents composants. Ces trois éléments constituent la méthode dite d'"immersion de volume", qualifiée de monolithique au sens où tous les composants sont traités sur une même maillage. Ces méthodes sont ensuite illustrées sur les problèmes illustratifs traités dans le chapitre 2, et l'on vérifie que l'approche présentée est consistante avec l'approche classique.

Chapter 4

Monolithic Surface Radiation: The "Immersed-Surface-to- Immersed-Surface" (IS2IS) method

Now that the retained approach has been presented and illustrated on several examples, we turn to the major contribution of this work, the numerical modelling of the radiation. In many engineering situations, such as glass treatment [118], nuclear engineering [119], combustion and flame modelling [120–122] and industrial furnaces [123–125], thermal radiation is the dominant mode of heat transfer. However, at the contrary of other physics presented in chapter 2, that can be stated as *macroscopic* physics, in the sense that, even if the phenomena can be related to the action of *particles* (atoms, molecules), the constitutive equations are, in some sense, averaged. This approach is not valid for the radiation, the considered particles being photons, and the point of view of the statistical physics have to be considered, when the particles are not directly considered, but only density of probability of their presence. This leads to an equation of Boltzmann type, the Radiative Transfer Equation, for which the numerical tools usually employed in the "Engineer" physics are not well suited, for many reasons that will be detailed in this chapter, but the main one being the complexity of the RTE. Therefore, some simplifications have to be made in order to be able to obtain a numerical solution. The main one being based on the fact that radiative effects can be split in two contributions:

- Surface radiation: when the medium separating the surfaces that define the enclosure does not affect the exchanges between surfaces, the medium is said to be

transparent. This assumption is valid for vacuum, and for air at low and moderate temperature. Those exchanges constitute the major part of interest, and the method exposed in this chapter aims to take these effects in account.

- Volume radiation: when the medium cannot be considered as transparent, one has to take in account the interaction with the surrounding medium, by means of emission, absorption and deflection of photons. Methods to deal with this type of transfer will be described in this chapter, but the specific method we developed will be detailed in a following chapter.

Before turning to the method we designed, we will briefly recall the basics of radiative transfer and give an overview of the existing methods.

4.1 The Radiative Transfer Equation

4.1.1 Equation and boundary conditions

Let Ω be the computational domain and $\partial\Omega$ its boundary. The considered time interval is $[0, T]$. A direction of the space $\boldsymbol{\omega}$ can be parametrized by two angles (φ, θ) , so that we can write the direction vector as

$$\boldsymbol{\omega} = \begin{bmatrix} \cos(\theta) \sin(\varphi) \\ \sin(\theta) \sin(\varphi) \\ \cos(\varphi) \end{bmatrix} \quad (4.1)$$

Let \mathcal{S} denote the unit sphere. In what follows, the symbol $\int_{\mathcal{S}}$ means that the integration is performed over all the directions, i.e., for all $\boldsymbol{\omega} \in \mathcal{S}$, which is equivalent to say that $\varphi \in [0, 2\pi]$ and $\theta \in [0, \pi]$.

The grey medium assumption is considered, and this yields to equations integrated all over the frequency range, therefore all the considered quantities will be frequency independent. The RTE permits to determine the specific radiative intensity $I(\boldsymbol{x}, t, \boldsymbol{\omega})$, which describes the density of photons at a given position, time and in a given direction. By considering an isotropic scattering to simplify the exposition, the full RTE reads:

$$\frac{1}{c} \frac{\partial I}{\partial t} + \boldsymbol{\omega} \cdot \nabla I = \frac{\sigma_r}{\pi} \kappa T^4 - (\kappa + \sigma) I + \frac{\sigma}{4\pi} \int_{\mathcal{S}} I(\boldsymbol{\omega}') d\boldsymbol{\omega}' \quad (4.2)$$

Here, $\kappa \geq 0$ is the absorption coefficient, $\sigma \geq 0$ the scattering coefficient, σ_r the Stefan-Boltzmann constant, c the light speed and T the (given) temperature field, acting as a right hand side in this case.

As boundary condition, different choices are possible. The most simple is to prescribe I at inflows to a given function I^0 , i.e.,

$$I(\mathbf{x}, t, \boldsymbol{\omega}) = I^0 \quad \text{for } \mathbf{x} \in \partial\Omega \text{ such that } \boldsymbol{\omega} \cdot \mathbf{n} < 0 \quad (4.3)$$

However, this kind of boundary condition is a bit simplistic, and a more realistic boundary condition would be to consider a reflected part (related to the solution) and an emitted part (related to the Planck distribution)

$$I(\mathbf{x}, t, \boldsymbol{\omega}) = \frac{(1 - \varepsilon)}{\pi} \int_{\boldsymbol{\omega}' \cdot \mathbf{n} < 0} I(\mathbf{x}, t, \boldsymbol{\omega}') |\boldsymbol{\omega}' \cdot \mathbf{n}| d\boldsymbol{\omega}' + \frac{\varepsilon \sigma_r}{\pi} T_w^4 \quad \text{for } \mathbf{x} \in \partial\Omega \text{ such that } \boldsymbol{\omega} \cdot \mathbf{n} < 0 \quad (4.4)$$

4.1.2 Physical meaning of the different terms

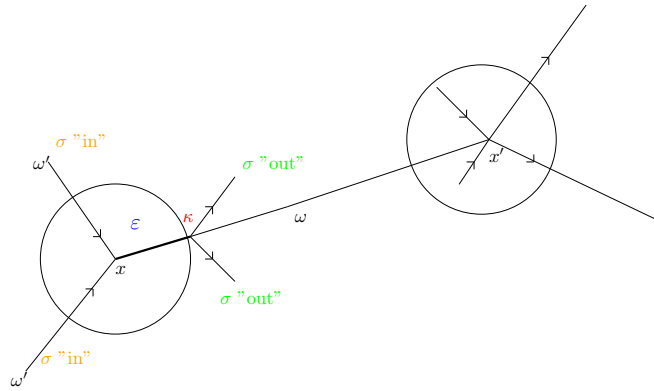


FIGURE 4.1: Illustration of the photon balance on an elementary volume

Equation (4.2) is obtained by a photon balance over an elementary volume, as illustrated in 4.1. We detail now the contributions of the different terms:

- the term $\frac{1}{c} \frac{\partial I}{\partial t} + \boldsymbol{\omega} \cdot \nabla I$ corresponds to the space-time variations of photons in the considered volume.
- $-(\kappa + \sigma)I$ designs the transmitted part to the outer, coming from two contributions: what is absorbed by the matter during interaction with photons, related to the absorption opacity κ , and what is deflected by the matter (*out* scattering), corresponding to the scattering opacity σ . Those opacities are homogeneous to the inverse of a length, and can be understood as the inverse of the mean-free-path of the absorption (for κ) of the deflection (for σ) of a photon.

- the term $\frac{\sigma_r}{\pi} \kappa T^4$ stands for what is emitted inside the volume. The term $\frac{\sigma_r}{\pi} T^4$ is the black-body intensity integrated over the frequency range (we have $\frac{\sigma_r}{\pi} T^4 = \int_0^\infty \frac{2h\nu^3}{c^2} \frac{1}{\exp(-\frac{h\nu}{kT})-1} d\nu$). The difference from a blackbody to a real body is contained in κ , which can be related to the emissive properties thanks to the Kirchoff law, even though κ is used as a volume property, whereas the emissivity ε is preferred for surface description.
- Finally, $\frac{\sigma}{4\pi} \int_{\mathcal{S}} I(\boldsymbol{\omega}') d\omega'$ represents the radiative energy deflected from all the directions of the space through the considered volume (*in scattering*). Even though isotropic scattering was considered, anisotropic effects could be taken into account by means of a phase function $\phi(\omega \rightarrow \omega')$ (we have $\phi(\omega \rightarrow \omega') = \frac{1}{4\pi}$ for isotropic scattering), so that this term become $\int_{\mathcal{S}} \phi(\omega \rightarrow \omega') I(\boldsymbol{\omega}') d\omega'$.

4.1.3 Numerical difficulties

There are at least two main reasons which make this equation difficult to solve :

- The presence of the scattering term $\frac{\sigma}{4\pi} \int_{\mathcal{S}} I(\boldsymbol{\omega}') d\omega'$, so that we have to deal with an integro differential equation, and things get even worse with anisotropic phase functions. However, this is not the most important in the situations we will consider, and, in first approximation, this term can be neglected.
- The major difficulty lies in the term $\boldsymbol{\omega} \cdot \nabla I$, and, more generally the fact that I is a function of the direction $\boldsymbol{\omega}$. On the one hand, it is not a common thing, so that conventional discretization methods are difficult to apply to such an equation, and on the other hand, it introduces a supplementary dimension to discretize, followed by an increase in the computational cost.

We will see in the following sections, that, all discretizations methods differ in the way that the angular dependency is treated. An approach is to consider an averaged version of the RTE, leading to model such as the P_1 model evoked in the chapter 2, or the M_1 model [126], but this will be detailed in the next chapter. We now turn to the methods of discretization of the radiative transfer equation, for which a good review can be found in [127].

4.2 Numerical formulations for the RTE

4.2.1 Monte Carlo Method

This approach, introduced by [128], is an application of the well-known Monte Carlo Method to radiative transfer. It is based on sampling a random walks of photons, introducing probability laws for the travelling of photons without interaction. This approach is mentioned in order to demonstrate a complete study, but due to its computational cost, it is unaffordable in situations coupled with other physics that are considered in this work, and as such, it will not be detailed here. A good summary of the principles can be found in [129].

4.2.2 Finite Element Methods

Here, the angular dependency is treated by means of angular shape functions. A variable separation can be performed to separate the contributions of classical spatial shape functions and angular shape functions. This leads us to consider inner products and decompositions of the solution of the following forms

$$(u, v)_{\Omega * \mathcal{S}} = \int_{\Omega} \int_{\mathcal{S}} u v d\mathbf{x} d\boldsymbol{\omega} \quad (4.5)$$

$$I_h(\mathbf{x}, \boldsymbol{\omega}) = \sum_{i=1}^{N_x} \sum_{k=1}^{N_{\omega}} \alpha_{i,k} \varphi_i(\mathbf{x}) \psi_k(\boldsymbol{\omega}) \quad (4.6)$$

Since, for a given $\boldsymbol{\omega}$, the RTE can be viewed as an advection-reaction equation, so it is natural to consider stabilized formulations, with SUPG stabilization for instance. We can quote several contributions, [130] for a "sparse tensor product" formulation of spatial and angular shape functions and with an extensive theoretical analysis, [131] in a domain decomposition context, [132, 133] for a formulation coupled with a diffusion approximation that will be detailed later on, [134, 135] for stabilized formulations using the VMS approach and [136] for a discontinuous Galerkin formulation.

4.2.3 S_N : Discrete Ordinates Method

A more straightforward idea, initially introduced by Chandrasekhar [137] in the context of astrophysics, would be to consider discrete directions in a collocation fashion, that is to say, exhibit couples $(w_i, \boldsymbol{\omega}_i)_{i \in [1; N]}$, $\boldsymbol{\omega}_i$ being discrete directions and w_i being some

weight to approximate the scattering term. Hence the DOM RTE reads, I_i being the intensity on the i th ordinate:

$$\forall i \in [1; N], \quad \frac{1}{c} \frac{\partial I_i}{\partial t} + \boldsymbol{\omega}_i \cdot \nabla I_i + (\kappa + \sigma) I_i = 4\sigma_r \kappa T^4 + \sigma \sum_{j \in I, j \neq i} w_j \Phi(\boldsymbol{\omega}_j - \boldsymbol{\omega}_i) I_j \quad (4.7)$$

This leads to a system of "ordinary" partial differential equations, coupled by the scattering term. However, even though the angular dependency is addressed this manner, a spatial discretization has to be performed, and there exists several approaches to do so: by means of finite volume [138] in the context of furnaces (see [139] for a complete review about Finite Volume and DOM), [140] with a discontinuous galerkin method, [141] using a classical finite element method in space, [142, 143] for matrix implementations. Recently, studies regarding the high performance computing aspects (Preconditioning, Krylov acceleration, fast resolution) can be quoted [144–146].

4.2.4 P_N : Spherical Harmonics

This approach, originally proposed by Jeans [147] in the context of the study of gaseous stars, consists in eliminating the angular dependency of the radiative intensity by expanding it in terms of a generalized Fourier series. Formally, it reads:

$$I = \sum_{l=0}^{\infty} \sum_{m=-l}^l I_l^m Y_l^m(\theta, \varphi) \approx \sum_{l=0}^N \sum_{m=-l}^l I_l^m Y_l^m(\theta, \varphi) \quad (4.8)$$

where θ and φ are according to (4.1), and $I_l^m(\mathbf{x})$ are the unknowns of the problem. $Y_l^m(\theta, \varphi)$ is the spherical mode, given by

$$Y_l^m(\theta, \varphi) = \begin{cases} \cos(m\varphi) P_l^m(\cos(\theta)) & \text{if } m \geq 0 \\ \sin(m\varphi) P_l^m(\cos(\theta)) & \text{if } m < 0 \end{cases} \quad (4.9)$$

$P_l^m(x)$ being the associated Legendre polynomial, defined by

$$P_n^m(x) = (-1)^m \frac{(1-x^2)^{\frac{|m|}{2}}}{2^n n!} \frac{d^{n+|m|}(x^2-1)^n}{dx^{n+|m|}} \quad (4.10)$$

This leads to a set of coupled partial differential equations, the integer N giving the order of the approximation. It is known that even order approximation gives irrelevant results

(the obtained intensity can be negative), so that only odd order approximations are used, even though it can be improved by a filtering operation [23]. It can be shown [26] that the spherical harmonics are equivalent to the DOM when a gaussian quadrature is chosen for For $N = 1$, one recovers the P_1 approximation of chapter 2. However, the complexity of those equations greatly increases for high order N , particularly for multidimensional problems [22], leading to the use of so called simplified approximations SP_N , which has driven the interest of many researchers in the past years. One can see [25] for a derivation of time-dependant SP_N equations, [148] which addresses the structure of matrixes obtained from the discretization of such equations, [149] for rigorous derivation of boundary conditions, [150] which introduces a corrected approximation to account diffusive effects, [151] with adaptive finite elements and [152] for an multidimensional formulation using tensor products. A detailed construction, when the time dependance is neglected, using a different method, is available in [24] or [153], but the main ideas are to perform an asymptotic development with respect to opacities and the use of formal Neumann series, the order of the approximation being related to the index at which the truncation of the formal series is operated. We give the first members of this family below, the unknown φ_r being related to the radiative energy and $\epsilon = \frac{1}{(\kappa+\sigma)L}$:

SP_1 Approximation

$$-\epsilon^2 \nabla \cdot \left(\frac{1}{3(\kappa + \sigma)} \nabla \varphi_r \right) + \kappa \varphi_r = \kappa (4\sigma_r T^4) \quad (4.11)$$

SP_2 Approximation

$$-\epsilon^2 \nabla \cdot \left(\frac{1}{3(\kappa + \sigma)} \nabla \left(\varphi_r - \frac{4}{5} (\varphi_r - 4\sigma_r T^4) \right) \right) + \kappa \varphi_r = \kappa (4\sigma_r T^4) \quad (4.12)$$

SP_3 Approximation

φ_r is here a linear combination of ψ_1 et ψ_2 , solutions of the following equations

$$-\epsilon^2 \nabla \cdot \left(\frac{\mu_1}{(\kappa + \sigma)} \nabla \psi_1 \right) + \kappa \psi_1 = \kappa (4\sigma_r T^4) \quad (4.13)$$

$$-\epsilon^2 \nabla \cdot \left(\frac{\mu_2}{(\kappa + \sigma)} \nabla \psi_2 \right) + \kappa \psi_2 = \kappa (4\sigma_r T^4) \quad (4.14)$$

$$\varphi_r = \frac{1}{30} (5 - 3\sqrt{\frac{5}{6}}) \psi_1 + \frac{1}{30} (5 + 3\sqrt{\frac{5}{6}}) \psi_2 \quad (4.15)$$

where

$$\mu_{1,2} = \sqrt{\frac{3}{7} \pm \frac{2}{7} \sqrt{\frac{6}{5}}} \quad (4.16)$$

One can note the SP_1 approximation is nothing but the P_1 approximation, obtained by a different approach. We will see in the next chapter that there exists a third way to derive these equations.

Now that a short overview of the existing method for the numerical resolution has been given, one can note that, since we are only interested here in surface radiation effects, it is not necessary to consider a full version of (4.2); in fact, for a transparent medium, we have $\kappa = 0$ and $\sigma = 0$, so that the right-hand side of the RTE vanishes. Moreover, the characteristic speed of the radiative phenomenon is very large compared to other phenomena, so that the transient term can be dropped as well. It leads us to consider a simplified model, where only the boundary of the domain $\partial\Omega$ is to be considered, and involves only geometric quantities. In the next part, we will give a state of the art explanation about this method, called the radiosity method, net radiative exchange or surface-to-surface method, and we will detail the extension we propose within our monolithic framework.

4.3 The Surface-to-Surface Method: state of the art

4.3.1 The view factor: a geometric function

As stated before, we are working in situations where the medium that separates the surfaces does not affect the energy exchange between them. Hence, the influent quantities here are the surface temperatures, its physical parameters (area and emissivity ε mostly), and the most important, its geometric characteristics. The geometric characteristics have to be taken into account, not for a surface alone, but for couples of surfaces, that is to say, the relative orientation and distance are of importance. To introduce this notion, let us consider to infinitesimal surfaces dS_i and dS_j .

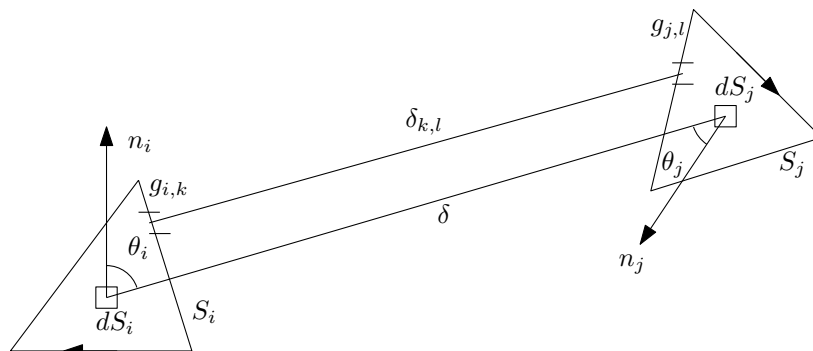


FIGURE 4.2: Geometric characteristics of the two surfaces

The *view factor* (sometimes referred to as *configuration factor*, *angle factor* or *shape factor*) is defined as the part of energy leaving the surface dS_i that directly strikes dS_j . It is given by, according to notations of figure 4.2:

$$dF_{dS_i \rightarrow dS_j} = (\cos(\theta_i) dS_i) d\Omega_i = \frac{\cos(\theta_i) \cos(\theta_j) dS_i dS_j}{\delta^2} \quad (4.17)$$

The view factor between those two surfaces is then obtained by performing integration over surfaces S_i and S_j .

$$F_{S_i \rightarrow S_j} = F_{ij} = \frac{1}{S_i} \int_{S_i} \int_{S_j} \frac{\cos(\theta_i) \cos(\theta_j)}{\delta^2} dS_i dS_j \quad (4.18)$$

It can be proved that the view factor verifies the following relations:

Reciprocity law:

$$F_{ij} S_i = F_{ji} S_j \quad (4.19)$$

This relation is useful to save computation time, because it allows the computation of a view factor from the knowledge of the other.

Summation law

$$\sum_{j=1}^{N_F} F_{ij} = 1 \quad (4.20)$$

(4.20) is only a consequence of the energy conservation principle: all the radiation leaving the surface i is entirely intercepted by other surfaces of the enclosure. This relation will be useful for code verification. The view factors are usually stored in a matrix $\mathbb{F} = (F_{ij})_{1 \leq i, j \leq N_F}$. Here, we made the assumption of *diffuse* view factors, in the sense that the energy absorbed by the surface is then re-emitted isotropically in all directions. This assumption is valid for many considered surfaces, but become less appropriate for polished surfaces; in this case, one has to compute *specular* view factors [154]. For simple geometric configurations, the view factor can be determined analytically (catalogue for well-known configurations are available in [155]), but the calculation of a view factor for a particular configuration can serve as a publication on itself [156–158]. However, as we will see in the following, we intend to perform surface calculation using some faces of the finite element mesh, so we will have to deal with arbitrary configurations. Hence, a general approach is necessary to numerically compute the view factor. One can see [159] for a review of existing methods, but here we detail a few the most common methods:

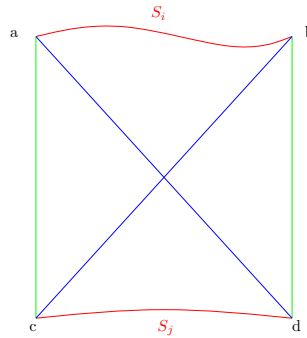


FIGURE 4.3: Illustration of the crossed strings method

- Area integration: the most straightforward approach, consists in computing numerically the two surface integrals by using a quadrature rule. However, since the integrand is non polynomial, high order integration might be required.
- Analytic integration: where the considered surfaces are polygons, analytic formulas can be obtained, but it implies using complex functions such as dilogarithm [160], which have to be evaluated numerically. Another analytic expression has been proposed for polygons [161], but at the price of a complicated analysis.
- Statistical determination: the view factor can be calculated by statistical sampling, using the Monte-Carlo method depicted earlier. The computation is expensive, but it often serves as a benchmark to assess the accuracy of new methods.
- Alternative methods: view factors can be determined by using basic properties and relations (4.19) and (4.20), but is only valid for a limited number of surfaces. The unit sphere method, making use of geometric projection can be quoted as well, as an interesting alternative [162],[163].

We want now to detail two particular approaches that will be used in this work: for $2d$ calculations, an interesting approach, developed by Hottel and Sarofilm [164] is the crossed string method. Using this, the view factor can be written, using notations according to fig (4.3)

$$F_{ij} = \frac{ac + db - (ad + bc)}{2ab} \quad (4.21)$$

Even though this formula is really simple and easy to implement, on the one hand, it does not involve any orientation of the surface, and, on the other hand, remains limited to $2d$ geometries. For $3d$ cases, eq (4.18) can be transformed into a double line integration [165] using the Stokes theorem, leading to the following relation, using notations of fig (4.2).

$$F_{i,j} = \frac{1}{4\pi A_i} \sum_{k=1}^3 \sum_{l=1}^3 \int_{g_k^i} \int_{g_l^j} \ln(\delta_{k,l}) g_k^i g_l^j dg_k^i dg_l^j \quad (4.22)$$

This method has gained popularity over the past years [166],[167], since it reduces to two simple integrals. However, since the integrand involves a logarithm function, the integral might be singular for surfaces sharing one edge. An analytical treatment of this singularity has been proposed in [168]. An interesting implementation, available in [169], is used here, and some details about the implementation are given in appendix B.

4.3.2 Visibility and obstructions

As mentioned above, the expressions (4.21) and (4.22) do not involve the relative orientation of surfaces. However, for some situations, depending on the relative orientation, there might be no radiative exchange between certain surfaces, because the two surfaces do not "see" each other or because the view can be obstructed by a third surface. Therefore, some view factors will not be calculated, because it would lead to a wrong contribution to the thermal balance on the one hand, and it permits to save computational time on the other hand. More details about this questions can be found in [170],[171] for visibility and [159], [171] for obstructions.

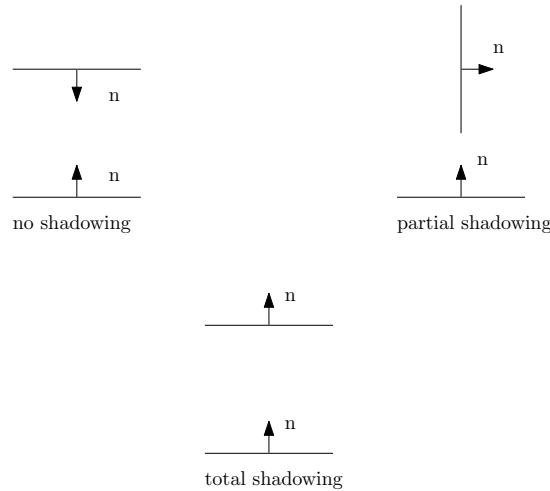


FIGURE 4.4: Different possibility for surfaces relative orientations

4.3.2.1 Visibility

It is actually easy to determine if two surfaces can see each other: one just needs to compute surface normals $\mathbf{n}_i, \mathbf{n}_j$ and a distance between faces centroids \mathbf{d}_{ij} . The visibility test will be related to the sign of $psI = \mathbf{d}_{ij} \cdot \mathbf{n}_i$ and $psJ = \mathbf{d}_{ij} \cdot \mathbf{n}_j$.

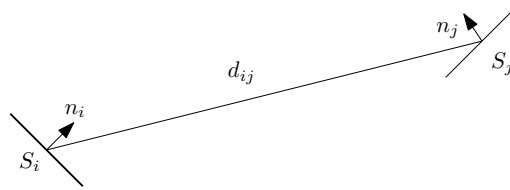


FIGURE 4.5: Notations for visibility test

For implementation considerations, we will define a boolean *NOVISIB*, which is false when faces can "see" each other. Formally we have

$$NOVISIB1 = (psI == 0) \text{ AND } (psJ == 0) \quad (4.23)$$

$$NOVISIB2 = (psI > 0) \text{ AND } (psJ > 0) \quad (4.24)$$

$$NOVISIB3 = (psA \cdot psB < 0) \quad (4.25)$$

$$NOVISIB4 = (psI == 0) \text{ AND } (psJ > 0) \quad (4.26)$$

$$NOVISIB = NOVISIB1 \text{ OR } NOVISIB2 \text{ OR } NOVISIB3 \text{ OR } NOVISIB4 \quad (4.27)$$

4.3.2.2 Obstruction

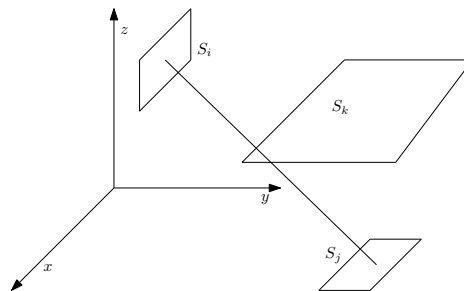


FIGURE 4.6: Two surfaces obstructed by a third

Obstruction calculation are different of visibility in the sense that obstruction between surfaces S_i and S_j involves a third surface S_k . The approach retained for obstruction calculation is the following: given the points of surfaces S_i and S_j , one can compute face

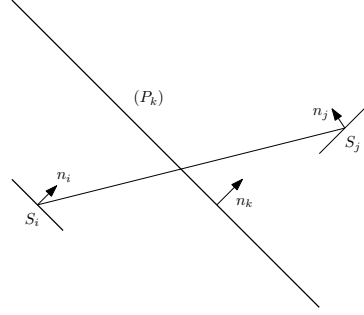


FIGURE 4.7: Notations for obstruction test

"centroids" (with a barycenter for example) $\mathbf{C}_i = (x_{0,p}^i)_{(1 \leq p \leq d)}$ and $\mathbf{C}_j = (x_{0,p}^j)_{(1 \leq p \leq d)}$ and the distance between those centroids $\mathbf{d}_{ij} = (d_p^{ij})_{(1 \leq p \leq d)}$. For surface S_k , given a centroid $\mathbf{C}_k = (x_{0,p}^k)_{(1 \leq p \leq d)}$ and the normal $\mathbf{n}_k = (n_p^k)_{(1 \leq p \leq d)}$, one equation of the plane defined by S_k is , with $\mathbf{X} = (x_p)_{(1 \leq p \leq d)}$ being the current point:

$$(\mathbf{X} - \mathbf{C}_K) \cdot \mathbf{n}_K = 0 \quad (4.28)$$

$$\sum_{p=1}^d n_p^k \cdot x_p - \sum_{p=1}^d n_p^k \cdot x_{0,p}^k = 0 \quad (P_k) \quad (4.29)$$

with this equation, one easily gets the distance between the current point and the plane K , with the help of an orthogonal projection.

$$\delta = \frac{\sum_{p=1}^d n_p^k \cdot x_p - \sum_{p=1}^d n_p^k \cdot x_{0,p}^k}{\sqrt{\sum_{p=1}^d (n_p^k)^2}} \quad (4.30)$$

We now want to check if the intersection point between P_k and \mathbf{d}_{ij} belongs to the triangle S_k . To this end, we use a parametric representation for \mathbf{d}_{ij} .

$$\mathbf{d}_p^{ij} = x_{0,p}^i + t(x_{0,p}^j - x_{0,p}^i) \quad t \in [0; 1] \quad (4.31)$$

making $\delta = 0$ and replacing the coordinates using (4.31), one can get the parameter corresponding to the intersection point t_I

$$t_I = \frac{\sum_{p=1}^d n_p^k \cdot x_{0,p}^i - \sum_{p=1}^d n_p^k \cdot x_{0,p}^k}{\sum_{p=1}^d n_p^k \cdot (x_{0,p}^j - x_{0,p}^i)} \quad (4.32)$$

substituting (4.32) in (4.31) gives the coordinates of the intersection point $\mathbf{X}_I = (x_{I,p})_{(1 \leq p \leq d)}$. The final step is to check if the intersection point belongs to S_k . This is achieved by

defining a parametric representation of S_k similar to (4.31), find the parameter t_K corresponding to \mathbf{X}_I , and check if $0 \leq t_K \leq 1$. A brutal approach for obstruction calculation would be to perform a loop over all surfaces for all pairs of surfaces (S_i, S_j) to check if, in the set of surfaces, there exists a surface that obstructs the view between S_i and S_j . However, this method was observed to be prohibitive in terms of computational time, even when used on relatively "light" meshes. To circumvent this issue, we will perform obstruction calculation at the level of the obstacle in the enclosure, since most obstructions encountered are between objects inside the enclosure and border faces. To this end, we extract the faces corresponding to the object interface, and we identify the minimum and maximum coordinates in each direction $\mathbf{X}_{min} = (X_{min,i})_{(1 \leq i \leq d)}$ and $\mathbf{X}_{max} = (X_{max,i})_{(1 \leq i \leq d)}$. Those minimum and maximum coordinates are then used to build an "encompassing" box defining lines in $2d$ and planes in $3d$ that will be used for the obstruction calculations.

4.3.3 Total exchange area, real surfaces and coupling with thermal balance

The notion of view factor as it was discussed in the beginning of this chapter holds for black surfaces, that absorb all the incoming radiation. However, for real surface (characterized by an emissivity ε , $0 \leq \varepsilon \leq 1$, there exists a fraction of the incoming radiation (corresponding to $\rho = 1 - \varepsilon$) that is reflected, and thus emitted through other surfaces. On the other hand, the computation of the radiative flux requires the solution of a non sparse linear system (the considered matrix being related to \mathbb{F}), which can be computationally demanding. Hence, an interesting approach, based on the idea of [172] or [173], consists in introducing another view factor, the total view factor (or total exchange area) that takes into account both the mutlireflections and the non-gray surfaces. We recall here the basic features by setting up the equations for the surface radiation problem.

If we denote by H_i the incoming flux density on the surface zone i and W_i the outgoing flux density, one has the following equations:

$$H_i A_i = \sum_{j=1}^{N_F} F_{ij} W_j \quad \forall i \in \llbracket 1; N_F \rrbracket \quad (4.33)$$

$$W_i = \varepsilon_i \sigma_r T_i^4 + (1 - \varepsilon_i) H_i \quad \forall i \in \llbracket 1; N_F \rrbracket \quad (4.34)$$

$$Q_{r,i} = A_i(W_i - H_i) \quad \forall i \in \llbracket 1; N_F \rrbracket \quad (4.35)$$

Using a matrix notation, it gives, using the following notations:

- $\mathbb{I} = (\delta_{ij})_{1 \leq i, j \leq N_F}$
- $\mathbf{W} = (W_i)_{1 \leq i \leq N_F}$
- $\mathbf{H} = (H_i)_{1 \leq i \leq N_F}$
- $\mathbf{E} = (\varepsilon_i \sigma_r T_i^4)_{1 \leq i \leq N_F}$
- $\mathbf{Q}_r = (Q_i)_{1 \leq i \leq N_F}$
- $\underline{\underline{\varepsilon}} = (\text{diag}(\varepsilon_i))_{1 \leq i \leq N_F}$
- $\underline{\underline{\rho}} = (\text{diag}((1 - \varepsilon_i)))_{1 \leq i \leq N_F}$
- $\mathbb{A} = (\text{diag}(A_i))_{1 \leq i \leq N_F}$

$$\mathbb{A}\mathbf{H} = \mathbb{F}\mathbf{W} \quad (4.36)$$

$$\mathbf{W} = \underline{\underline{\varepsilon}}\mathbf{E} + \underline{\underline{\rho}}\mathbf{H} \quad (4.37)$$

$$\mathbf{Q}_r = \mathbb{A}(\mathbf{W} - \mathbf{H}) \quad (4.38)$$

One can see that, to get the appropriate radiative flux to prescribe as a boundary condition, it is necessary to solve a non sparse $N_F * N_F$ system with temperature as input, which is not very convenient, since all the solvers for linear systems we have at hand are designed for sparse matrixes rising from finite element formulations. To circumvent this issue, we follow the lines described in [172], by using some total exchange area, that can be readily used to compute the needed radiative flux \mathbf{Q}_r . The matrix of total exchange areas $\underline{\underline{\mathcal{F}}}$ is defined by:

$$\mathbf{Q}_r = \underline{\underline{\varepsilon}}\mathbb{A}\mathbf{E} - \underline{\underline{\mathcal{F}}}\mathbf{E} \quad (4.39)$$

$\underline{\underline{\mathcal{F}}}$ can be explicitly determined by a general elimination procedure. Substituting (4.37) in (4.36) leads to

$$\underbrace{(\underline{\mathbb{A}} - \underline{\rho}\underline{\mathbb{F}})}_{=\underline{\mathbb{R}}} \mathbf{H} = \underline{\underline{\varepsilon}}\underline{\mathbb{F}}\mathbf{E} \implies \mathbf{H} = \underline{\mathbb{R}}^{-1}\underline{\underline{\varepsilon}}\underline{\mathbb{F}}\mathbf{E} \quad (4.40)$$

one finally gets

$$\underline{\underline{\mathcal{F}}} = \underline{\mathbb{A}}\underline{\underline{\varepsilon}}\underline{\mathbb{R}}^{-1}\underline{\underline{\varepsilon}}\underline{\mathbb{F}} \quad (4.41)$$

and the associated radiative boundary flux on the face i is given by

$$\mathbf{Q}_{r,i} = \frac{\sigma_r}{A_i} \sum_{j=1}^N A_j \mathcal{F}_{ij} (T_i^4 - T_j^4) \quad (4.42)$$

A "naive" approach to compute the total exchange factors would need to invert the matrix $\underline{\mathbb{R}}$. However it can be shown [173] that the total exchange factors can be obtained from the view factors and surfaces characteristics (ε_k, ρ_k) using the following algorithm

Given $(\underline{\mathbb{F}}, \underline{\mathcal{A}}, \underline{\underline{\varepsilon}}, \underline{\rho})$;

```

for  $i=1..N$  do
  for  $j=1..N$  do
    for  $k=1..N$  do
       $\mathcal{F}_{kk} = \frac{\varepsilon_k^2 F_{kk}}{1.0 - \rho_k F_{kk}} ;$ 
       $\mathcal{F}_{ik} = \frac{\varepsilon_k F_{ik}}{1.0 - \rho_k F_{kk}} ;$ 
       $\mathcal{F}_{kj} = \frac{\varepsilon_k F_{kj}}{1.0 - \rho_k F_{kk}} ;$ 
       $\mathcal{F}_{ij} = F_{ij} + \frac{\rho_k F_{ik} F_{kj}}{1.0 - \rho_k F_{kk}} ;$ 
    end
  end
end

```

Algorithm 1: Plating algorithm

The *S2S* method, or its extension to radiation in participative media, the zonal method, has been successfully applied in different contexts: furnaces [174, 175], urban canyons [176], combustion and fire modelling [177, 178], human modelling [165], electronic cooling [158][179] and solar reflectors [180] among others.

4.4 The *IS2IS* method

4.4.1 Motivations and features

Our goal is to design a computational framework based on the same principles as the *S2S* method, but adapted to the immersed volume method. Here, the main difficulty relies in the representation of the interfaces, since the interfaces between fluids and solids are implicitly defined by the zero iso-value of the levelset. Hence, one needs to reconstruct an approximation of the interface before performing a surface-to-surface calculation. This interface approximation will be reconstructed in terms of finite element mesh: in fact, the set of faces, that can be viewed as a submanifold of the one defined by the elements, gives a natural approximation of the interface, particularly in the framework depicted in the previous chapter, with a mesh appropriately refined around the interface. The next subsection is devoted to the description of the procedure used for the selection of suitable faces for the radiation calculation. We will see that a such approximation of the interface will permit to naturally handle complex geometries, in the sense that, as demonstrated in the previous chapter, our method is able to automatically generate a mesh for a given levelset, regardless of its geometric complexity.

4.4.2 Interface reconstruction

Our starting point is to come back to the finite element triangulation Ω_h . We recall some useful notations for the interface reconstruction procedure:

Notations	Definitions
d	dimension of space
D	topological dimension
\mathcal{K}	set of elements
\mathcal{N}	set of nodes
$K \in \mathcal{K}$	mesh element
$\mathcal{N}(K) = (\mathcal{N}_i(K))_{i \in \llbracket 1:D \rrbracket}$	nodes of a mesh element K
$\mathcal{F}(K) = (\mathcal{F}_i(K))_{i \in \llbracket 1:D \rrbracket}$	"faces" of a mesh element K
$\mathcal{N}(\mathcal{F}(K)) = (\mathcal{N}_i(\mathcal{F}(K)))_{i \in \llbracket 1:D-1 \rrbracket}$	nodes of a "face" $\mathcal{F}(K)$ of a mesh element K
$\mathbf{X}^i, i \in \mathcal{N}$	vector of coordinates for the i th node

TABLE 4.1: Notations for the mesh.

Numerical treatment of interfaces has received a growing interest in the recent years, together with the research conducted about immersed methods, and more generally, the research conducted on levelset methods: we can quote work for numerical modelling

of multiphase flows [81, 85, 181, 182]. However, in all previously quoted references, the interface remains implicitly defined only as the zero isovalue of a levelset function. But some physical situations require a more explicit description of the interface, for volume fraction modelling [183] or interfacial flows [80]. The approach proposed in [80] is interesting in the sense that auxiliary levelset isovalues are introduced to improve interface representation on certain elements. In the method presented in this chapter, those "auxiliary interfaces" will appear naturally.

Formally, the fluid-solid interface is defined as the zero isovalue of the levelset, in agreement with the notations of the previous chapter, we have

$$\Gamma_i = \{\mathbf{x} \in \Omega, \alpha(\mathbf{x}) = 0\} \quad (4.43)$$

its discrete equivalent can be defined by

$$\Gamma_{i,h} = \{K \in \mathcal{K}, \exists \mathbf{X}^i, \mathbf{X}^j \in \mathcal{N}(K), \alpha(\mathbf{X}^i) \cdot \alpha(\mathbf{X}^j) \leq 0\} \quad (4.44)$$

Γ_i is a line in $2d$, and a surface in $3d$. The first step of the interface reconstruction procedure is to detect the elements crossed by Γ_i . To this end, we follow the lines described in [83], of which we recall the main features: considering all the possible cases in $2d$ and $3d$, as illustrated below, elements of different types can be classified by the number of nodes where $\alpha(\mathbf{x}) > 0$, $\alpha(\mathbf{x}) < 0$ or $\alpha(\mathbf{x}) = 0$.

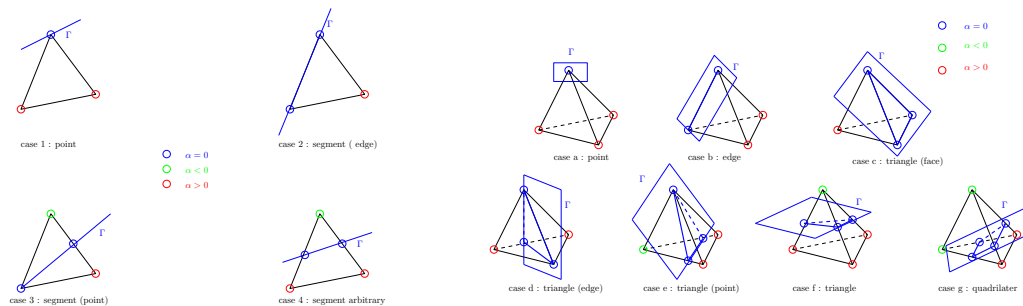


FIGURE 4.8: $2d$ Situations

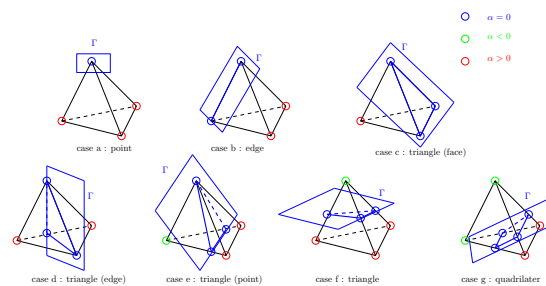


FIGURE 4.9: $3d$ Situations

By performing this test in a loop for all the elements, one can check if an element is crossed by the levelset zero isovalue or not. The procedure is illustrated below on several geometric forms already presented in chapter 3. The crossed elements are marked in red.

Once this procedure is performed, one gets a set of connected elements, that we call $E(\Gamma_i)$, which defines a volume. Therefore, the next step consists in, roughly speaking, eliminating what is "inside" the volume defined by $E(\Gamma_i)$. More formally, if we define

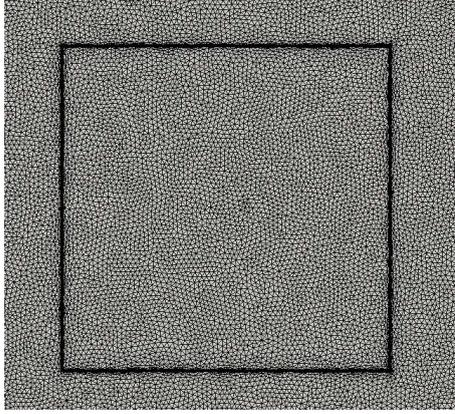


FIGURE 4.10: Test on a square brick: mesh

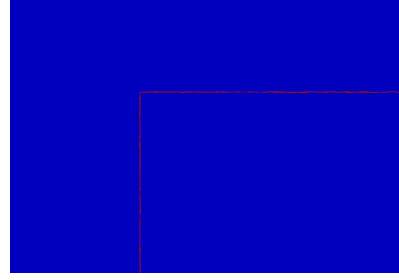


FIGURE 4.11: Test on a square brick: elements crossed (zoom on the corner)

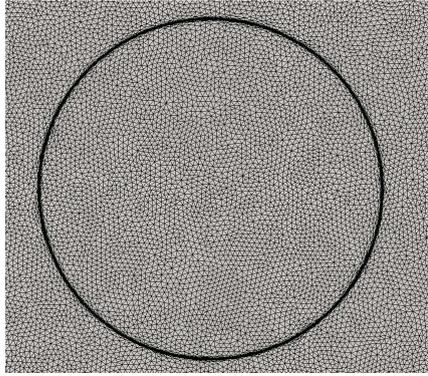


FIGURE 4.12: Test on a rectangular circle: mesh

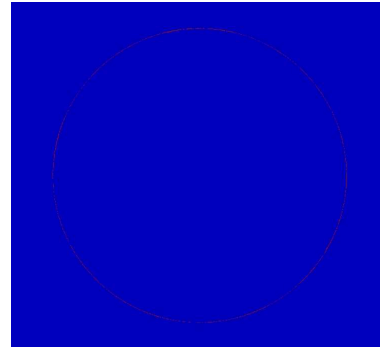


FIGURE 4.13: Test on a rectangular circle: elements crossed

$$\Gamma_i^+ = \{\mathbf{x} \in \Omega, \alpha(\mathbf{x}) > 0\} \quad (4.45)$$

$$\Gamma_i^- = \{\mathbf{x} \in \Omega, \alpha(\mathbf{x}) < 0\} \quad (4.46)$$

and if $V(\Gamma_i)$ stands for the counterpart of $\Gamma_i^+ \cup \Gamma_i^-$ in $E(\Gamma_i)$, we want to only retain the element of $E(\Gamma_i)$ belonging to Γ_i^+ or Γ_i^- , or, in other words, eliminate elements of $V(\Gamma_i)$. At the discrete level, since we want to reconstruct an approximation of Γ_i , it seems interesting to define $\Gamma_{i,h}^+$ and $\Gamma_{i,h}^-$ (discrete equivalent of Γ_i^+ and Γ_i^-) in terms of element "faces".

$$\Gamma_{i,h}^+ = \{\mathcal{F}(K), K \in \Gamma_{i,h}, \forall \mathbf{X} \in \mathcal{N}(\mathcal{F}(K)), \alpha(\mathbf{X}) < 0\} \quad (4.47)$$

$$\Gamma_{i,h}^- = \{\mathcal{F}(K), K \in \Gamma_{i,h}, \forall \mathbf{X} \in \mathcal{N}(\mathcal{F}(K)), \alpha(\mathbf{X}) > 0\} \quad (4.48)$$

Elements of $\Gamma_{i,h}^+$ and $\Gamma_{i,h}^-$ will be referred to as "Face Sup" and "Faces Inf" in the following. It is also useful to define $E(\Gamma_i)$ as a collection of faces of connected elements previously identified, which reads

$$E(\Gamma_{i,h}) = \left\{ \bigcup_{K \in \Gamma_{i,h}} \mathcal{F}(K) \right\} \quad (4.49)$$

Having such a vision of $E(\Gamma_{i,h})$, eliminating the interior faces becomes quite simple, knowing that since the interior faces are shared by two elements, they appear twice in the set $E(\Gamma_{i,h})$. Hence, retaining only the none repeated element of $E(\Gamma_{i,h})$, one gets the set $\Gamma_{i,h}^- \cup \Gamma_{i,h}^+$, that can be easily sorted in $\Gamma_{i,h}^-$ and $\Gamma_{i,h}^+$ by evaluating α at the face nodes. To check the efficiency of the approach described here, we chose to test the procedure on a very simple mesh where the considered object (a square here) is aligned on the mesh.

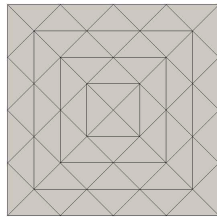


FIGURE 4.14: 2d Example:Mesh

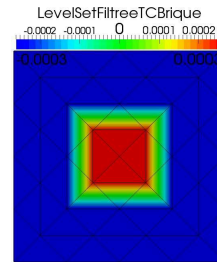


FIGURE 4.15: 2d Example: levelset of the square

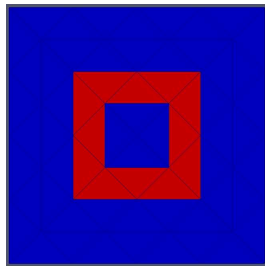


FIGURE 4.16: 2d Example: Element crossed by The levelset zero iso-value

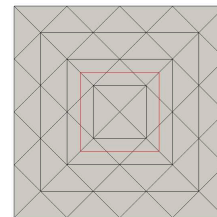


FIGURE 4.17: 2d Example: levelset zero iso-value

A similar mesh was used for 3d verifications; it was constructed as an extrusion of a mesh similar to the previous one in the xy plane (see 4.18, left), with one "layer" of elements in the z direction.

Regarding the border faces, since they are considered apart due to the specific treatment for boundary conditions, they are readily available without any supplementary work.

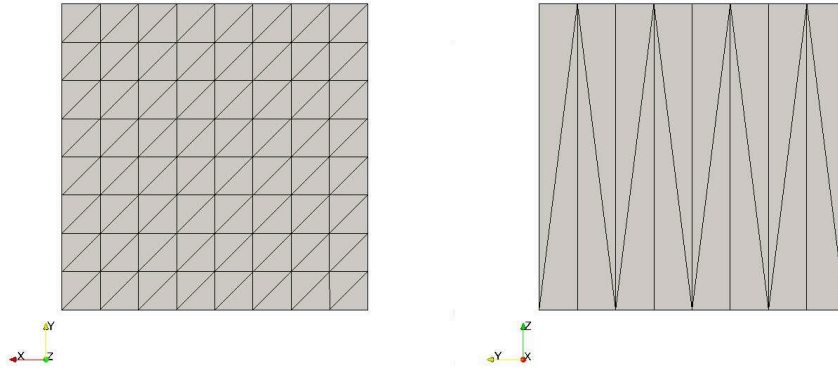


FIGURE 4.18: 3d Example: Mesh

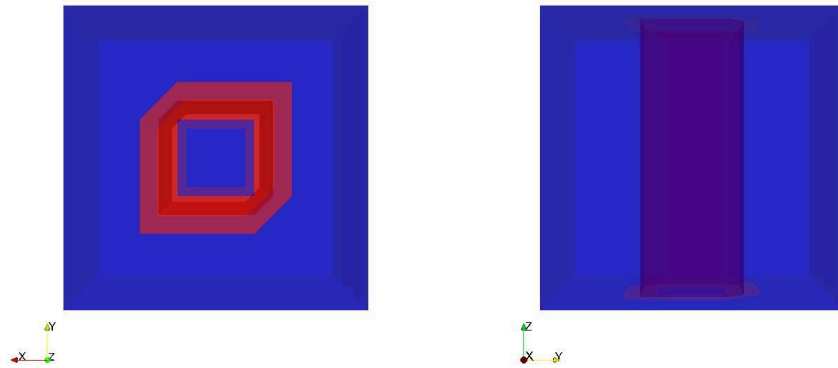


FIGURE 4.19: 3d Example: levelset Zero isovalue and Flag field

4.4.3 Computational aspects

At this point, in order to estimate the computational resources to be dedicated to the further view factor computation, it would be interesting to know what part of the total mesh is of interest for the calculations. Hence, we conducted a study on several meshes to at least get a tendency on this behaviour.

TABLE 4.2: Notations for faces numbers.

Notations	Definitions
N_{elts}	number of elements of the mesh
N_b	number of border faces
N_{is}	number of "Faces Sup"
N_{ii}	number of "Faces Inf"
$N_F = D * N_{elts}$	total number of faces
$d_{si} = N_{is} - N_{ii} $	difference between "Faces Sup" and "Faces Inf"

Two kind of meshes were used for this study: unadapted meshes, classically constructed using GMSH, and adapted meshes as explained in the previous chapter. We used here the metric described in [106] because the implementation we dispose of, permits to

control the maximum stretching factor, referred to as s_{max} in [106]. Unadapted meshes were the two already quoted above and another for $2d$, obtained by refining the one shown. Several adapted meshes are considered: four considering the same geometry for the unadapted mesh, for different value of the maximum stretching factor, and the circle presented above. In $3d$, we used the meshes presented in the previous chapter to illustrate the mesh adaptation, displayed again here for sake of clarity. The results are available on the following tables. One can see that, for all meshes considered, the number of faces involved in the surface computation does not exceed 5% of the total number of faces. It is interesting to note that the number of involved faces decreases as s_{max} increases. It can be explained in the following way: the higher the stretching factor is, the taller the elements are in the direction parallel to the interface and therefore less elements are needed to cover the whole interface. The conclusions of this study can be summarized as the following: the proposed approach naturally defines two approximated interfaces $\Gamma_{i,h}^+$ and $\Gamma_{i,h}^-$, quantitatively different on a arbitrary mesh, but along the mesh adaptation procedure, those two interfaces tend to get closer to each other, leading to an accurate description of the interface. The numerical results will confirm this tendency, by showing that this interface approximation is able to reproduce results obtained by a classical BF approach, where the interface is part the domain boundary.

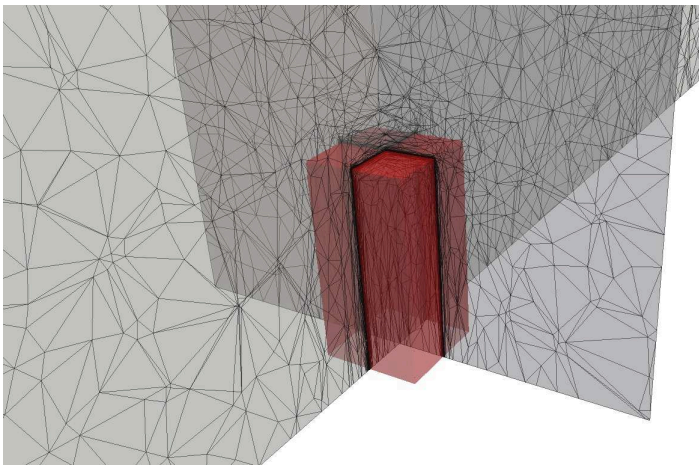


FIGURE 4.20: 3d Adapted mesh: brick

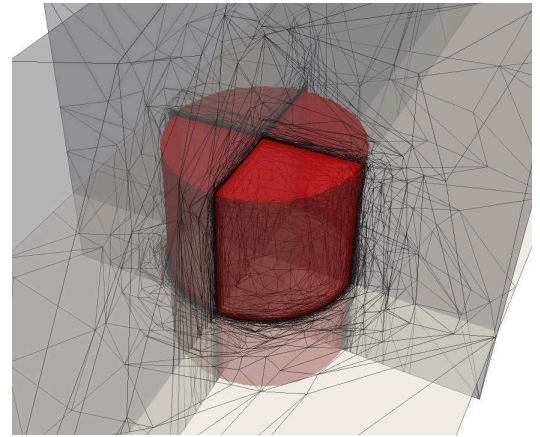


FIGURE 4.21: 3d Adapted mesh: cylinder

Case	N_b	N_{is}	N_{ii}	N_F	d_{si}	N_{elts}
adapted square $s = 8$	65	4.564	4.725	4.790	161	152.748
adapted square $s = 20$	51	3.798	3.965	4.016	167	162.356
adapted square $s = 30$	68	1.483	1.480	1.551	3	197.202
adapted square $s = 50$	74	1.025	996	1.099	29	194.718
adapted circle $s = 8$	1.550	1.802	1.805	3.335	3	489.150

TABLE 4.3: 2d Meshes

Case	N_b	N_{is}	N_{ii}	N_F	d_{si}	N_{elts}
adapted brick $s = 8$	4.730	3.330	26.964	31.424	23.364	300.753
adapted cylinder $s = 8$	2.652	4.343	33.827	36.479	29.484	369.193

TABLE 4.4: 3d Meshes

4.4.4 "Immersed" features of the *IS2IS* method

As stated before, the method we are describing can be understood as an "immersed" version of the *S2S* method. Hence, some of the features have to be adapted, for implementation purposes mostly:

It is sometimes common to perform a partitioning of the face set depending on certain characteristics, as seen in [172] for black and non-black surfaces, or it could be done for temperature-prescribed and flux-prescribed boundary faces. Here, the natural partitioning is between border faces and intern faces. Hence, since we know that $N_F = N_b + N_i$ we introduce the following notations to ease the discussion:

$$\mathbb{F} = \begin{bmatrix} \mathbb{F}_{ii} & \mathbb{F}_{ib} \\ \mathbb{F}_{ib}^T & \mathbb{F}_{bb} \end{bmatrix} \quad (4.50)$$

For a classical surface-to-surface calculation, only \mathbb{F}_{bb} exists, and will govern the radiative exchange between boundaries of the domain. \mathbb{F}_{ib} drives the radiative exchange between boundaries and the immersed object, and \mathbb{F}_{ii} represents radiative exchanges of the object onto itself a, phenomenon known as "self-radiation".

If the computation of a boundary flux $\mathbf{Q}_{r,i}$ is classical in the *S2S* method, the novelty is we have to prescribe a similar quantity at the fluid-solid interface, *ie* on internal faces. Those effects will be taken into account by means of a source term $\mathbf{S}_{r,i}$ localized on the interface.

For visibility and obstruction calculations, it is mandatory to have a consistent orientation for all faces, that is to say, the normals should be pointing outward. If it is naturally the case for the border faces, due to their specific treatment for boundary conditions, additional work has to be done for the interior faces. This is achieved by a first computation of the normal, and a checking test to be consistent with the gradient of the levelset function of the object.

For the plating algorithm described earlier, since all the blocks or \mathbb{F} are computed separately, one have to concatenate all the blocks in one single list, perform the plating operation, and de-concatenate, since we implemented in a way which compute the different contributions separately.

4.4.5 Parallel processing aspects

It is worth mentioning that the surface computation is not well fitted for the parallel processing framework implemented in our library: in fact, for classical resolutions (Navier-Stokes, Convection-diffusion-reaction equations), the computational domain is partitioned into subdomains, so that each processor only compute on one subdomain, and one has to deal with communication between processors in order to render the original problem. Unfortunately, this approach does not work for a view factor computation, since view factor have to be computed from one surface to all others. So that a special treatment is needed to perform a view factor computation on multiple processors. A possible strategy consists in, once the surfaces liable to participate to the surface radiation calculation have been identified, to duplicate these informations to all processors, and to balance the load of the view factor computation between all processors. It is also important to make sure that all processors are well synchronized during all the computation.

4.5 Numerical experiments

Before we try to assess the consistency of the new method, it is necessary to make sure our implementation is valid for a classical "surface-to-surface" calculation, that is to say when only the boundary faces are considered. The simulations we are going to use are the ones presented in the previous chapter, enhanced by taking into account radiative effects. As done in the previous chapter, the *IS2IS* method will be tested on the "immersed version" on each case, to assess the consistency of the method. To validate the radiative code, the obtained results were compared to the ones available in the references in terms of Nusselt number as defined in the chapter 2, and its radiative equivalent, defined as follows:

$$\overline{Nu}_{rad} = \frac{L}{\lambda(T_h - T_c)} \int_0^1 q_r(0, y) dy \quad (4.51)$$

4.5.1 Natural convection in a square empty cavity

Here, radiation is taken into account, by prescribing a net radiative flux, computed as depicted in previous sections, imposed as a Neumann boundary condition on the horizontal walls. The obtained results, in terms of iso temperature and streamlines, are in good agreement with [184] and [185]. We plot the adimensional temperature θ , along the line $y = 0.5$. One can note that, at the contrary of volumic radiation,

surface radiation preserves the centro-symmetry of the problem. The results shows the effect of radiation on the overall temperature distribution: the obtained radiative flux on horizontal walls is symmetric (negative on the upper wall, positive on the lower wall). Those radiative fluxes modify the thermal boundary layer by "moving away" the extremal values of the temperature inside the cavity, at the difference with the case $\varepsilon = 0$, where the maximal values of the vertical profile are located on the horizontal walls, as it can be seen on the temperature plot.

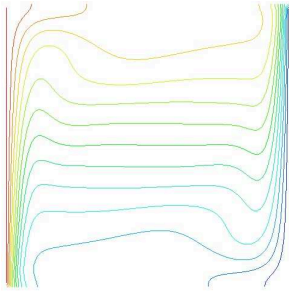


FIGURE 4.22: 2d Empty cavity: iso temperature and streamlines: $\varepsilon = 0$

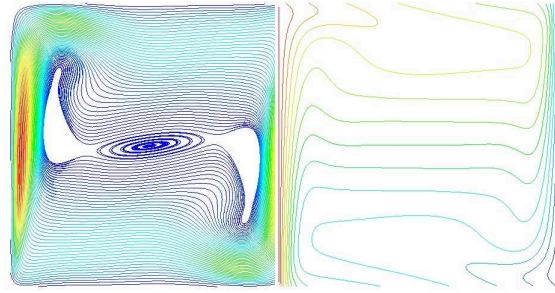


FIGURE 4.23: 2d Empty cavity: iso temperature and streamlines: $\varepsilon = 1$

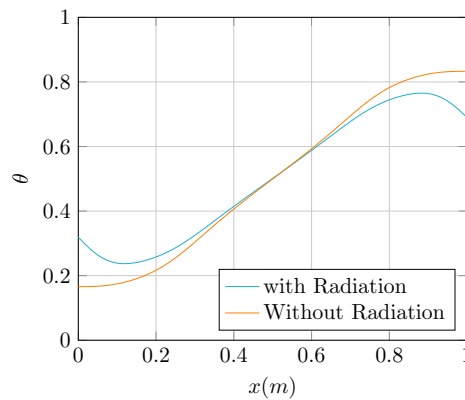


FIGURE 4.24: 2d Empty cavity: θ along $y = 0.5$

For the immersed version of this case, additional work is necessary to select the "radiative" faces, since not all the border faces will be involved in the radiation computation (only the ones corresponding to the horizontal walls in the BF case). In order to sort those faces among others, we make use of a "Flag" field naturally generated in our code, valued at one on the considered boundary, and zero elsewhere, so that sorting faces is done by evaluating the value of the Flag on the faces nodes. The meshes used are the ones displayed in the previous chapter. Quantitative comparisons, performed in the same manner as before, show an excellent agreement.

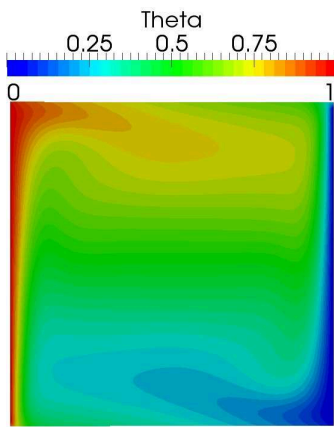


FIGURE 4.25: 2d Empty cavity: temperature profile BF $\varepsilon = 1$

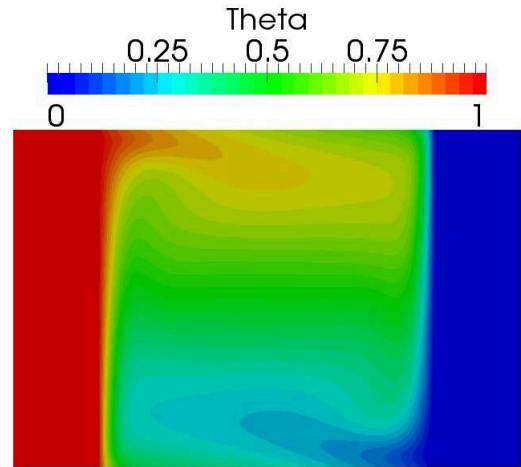


FIGURE 4.26: 2d Empty cavity: temperature profile IMV $\varepsilon = 1$

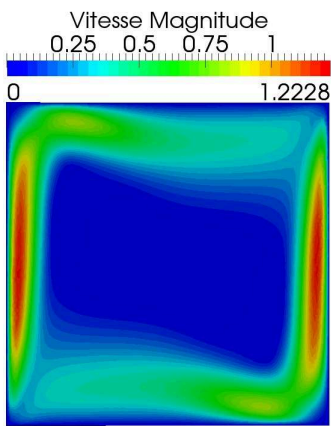


FIGURE 4.27: 2d Empty cavity: velocity profile BF $\varepsilon = 1$

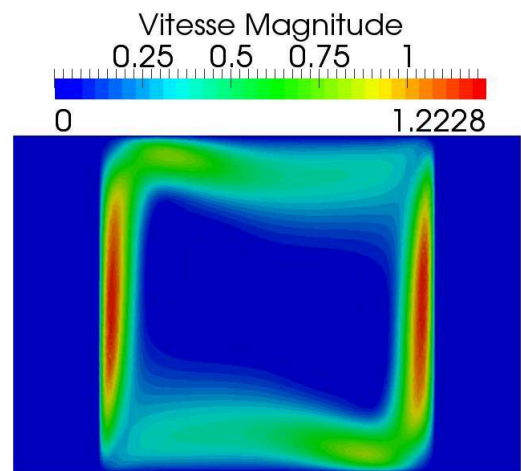


FIGURE 4.28: 2d Empty cavity: velocity profile IMV $\varepsilon = 1$

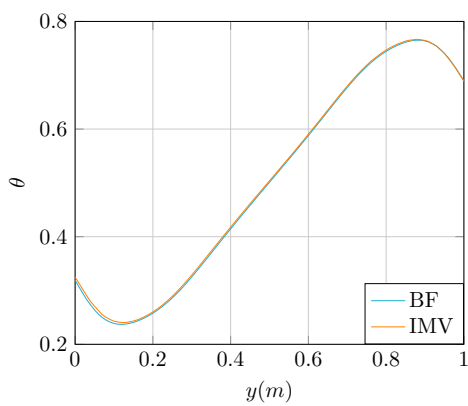


FIGURE 4.29: 2d Empty cavity: θ along $y = 0.5$

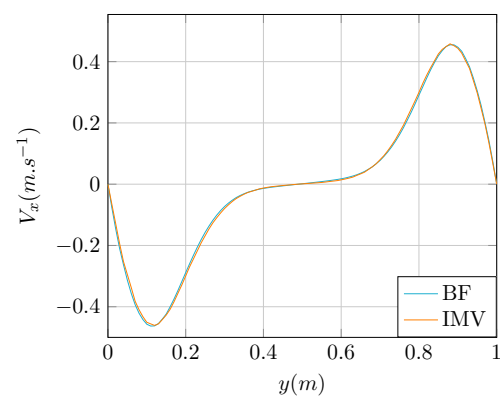


FIGURE 4.30: 2d Empty cavity: u_1 along $y = 0.5$

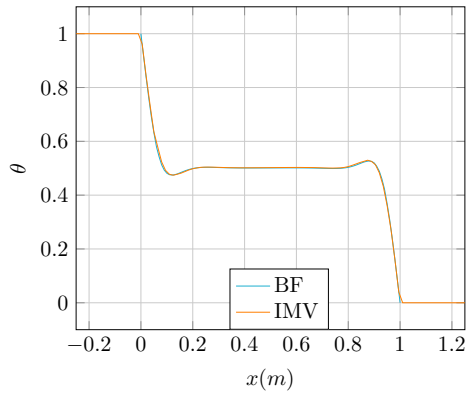


FIGURE 4.31: 2d Empty cavity: θ along $x = 0.5$

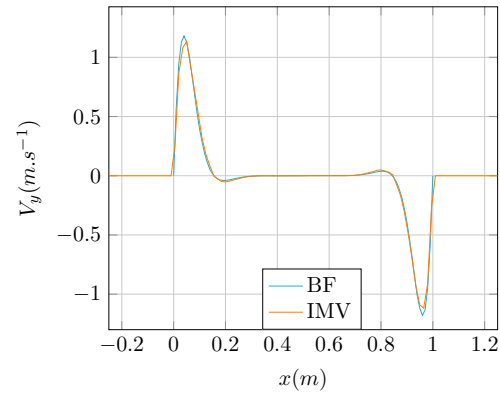


FIGURE 4.32: 2d Empty cavity: u_2 along $x = 0.5$

We used the developed method on the 3d version of the case that was already presented in the previous chapter. The iso temperature and streamlines are compared with the case without radiation for $Ra = 10^6$. One can see that the radiative fluxes applied on the top and bottom boundaries gives a "bathtub" like shape to the iso temperature lines, that are also more curved near the corner of the cavity. One can see a good agreement with the results presented in [185]. As a consequence, the shape of the streamlines is modified, with bigger recirculations zone close to the corners of the cavity.

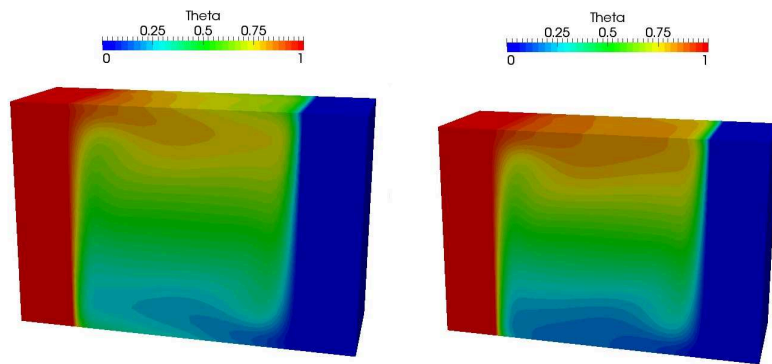


FIGURE 4.33: 3d Empty cavity: iso Temperature: $\varepsilon = 1$ (left) and $\varepsilon = 0$ (right)

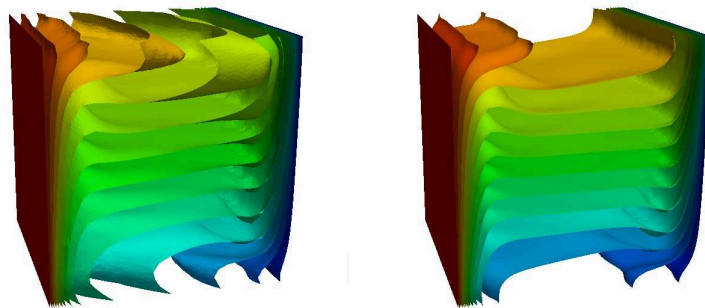


FIGURE 4.34: 3d Empty cavity: iso Temperature: $\varepsilon = 1$ (left) and $\varepsilon = 0$ (right)

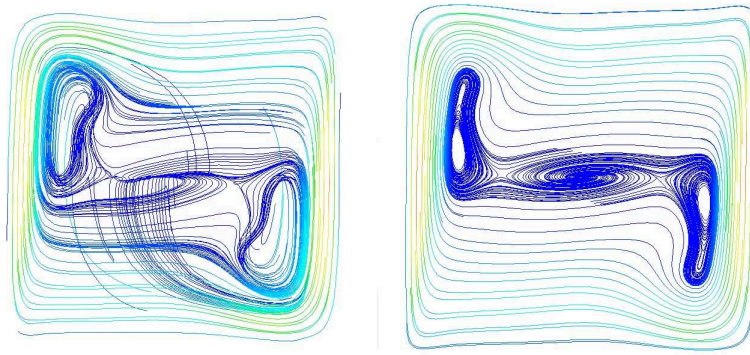


FIGURE 4.35: 3d Empty cavity: streamlines along x : $\varepsilon = 1$ (left) and $\varepsilon = 0$ (right)

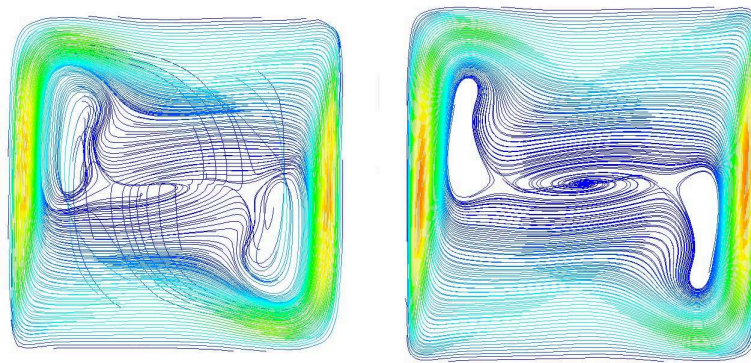


FIGURE 4.36: 3d Empty cavity: streamlines along z : $\varepsilon = 1$ (left) and $\varepsilon = 0$ (right)

The obtained results, in terms of radiative and convective Nusselt numbers, are displayed below and compared with the results available in [185]. One can see that the discrepancy does not exceed 3.5%.

	\overline{Nu}	\overline{Nu}_{conv}	\overline{Nu}_{rad}	$\overline{Nu} = \overline{Nu}_{conv} + \overline{Nu}_{rad}$
reference				
Colomer [185]		8.102	3.568	11.670
present work		8.122	3.712	11.834

TABLE 4.5: 3d Empty cavity: comparisons with benchmark solution

Similarly to the 2d case, the immersed version of the case was simulated, and results were compared to the ones obtained by a classical body fitted approach, in terms of velocity and normalized temperature. Here again, a good agreement is observed.

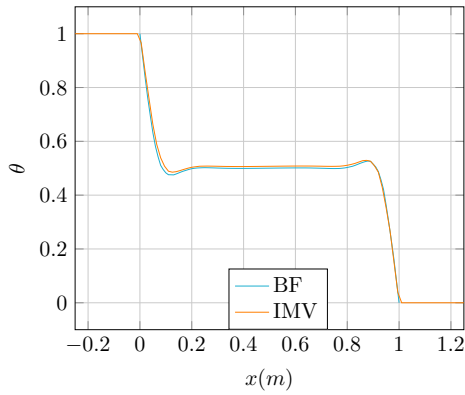


FIGURE 4.37: 3d Empty cavity: θ along l_1

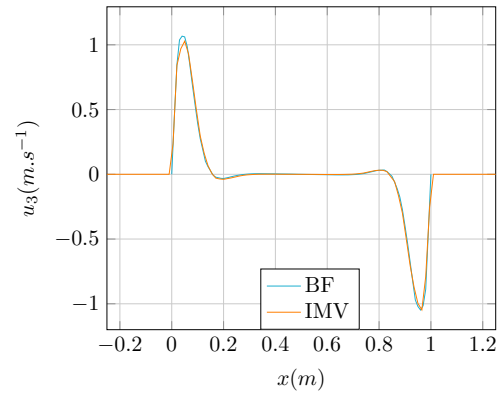


FIGURE 4.38: 3d Empty cavity: u_3 along l_1

4.5.2 Natural Convection in a cavity containing a plate

Here again, radiative flux are prescribed on horizontal walls as in the previous case. One could think that in this case, the plate inside the cavity may cause obstruction and visibility issues between border faces, but it was observed that taking into account the visibility and obstruction in the viewfactor computation does not have a significant influence. To represent the results, we make use of the symmetry around the line $x = 0.5$. The following pictures represent the iso-temperature lines on the left, and the streamlines on the right. The results, in terms of iso temperature and streamlines, correspond well with [65]. As in the previous case, radiative fluxes on horizontal walls generates temperature gradients that move away the iso temperature curves and modify the shape of the recirculation cells. As it can be seen on the curves, the supplementary amount of energy provided by radiative fluxes slightly increases the values of temperature inside the cavity, leading to a slight increase of velocity values by means of the Boussinesq term. The influence of the obstacle can also be observed, more pronounced in the case of the horizontal plate.

	\overline{Nu}	\overline{Nu}_{conv}	\overline{Nu}_{rad}	$\overline{Nu} = \overline{Nu}_{conv} + \overline{Nu}_{rad}$
reference				
Saravanan and al. [65]		5.8533	6.9885	12.8418
present work		5.8109	7.0928	12.9037

TABLE 4.6: 2d Horizontal plate: comparisons with benchmark solution

One can see that, on both cases, the discrepancy between the obtained results and the benchmark do not exceed 1.8%.

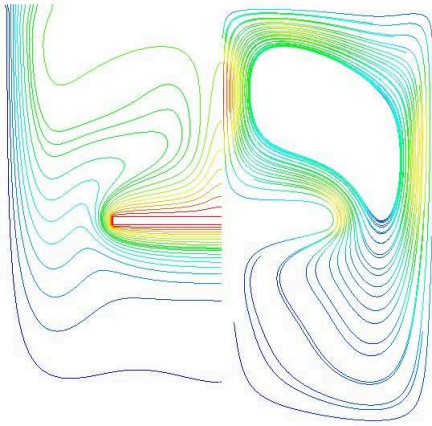


FIGURE 4.39: 2d Horizontal plate: iso temperature and streamlines: $\varepsilon = 0$

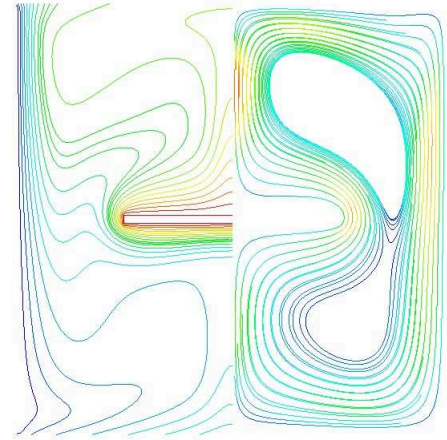


FIGURE 4.40: 2d Horizontal plate: iso temperature and streamlines: $\varepsilon = 1$

	\overline{Nu}	\overline{Nu}_{conv}	\overline{Nu}_{rad}	$\overline{Nu} = \overline{Nu}_{conv} + \overline{Nu}_{rad}$
reference				
Saravanan and al. [65]		6.6731	10.1914	16.8645
present work		6.7955	10.1144	16.9099

TABLE 4.7: 2d Vertical plate: comparisons with benchmark solution

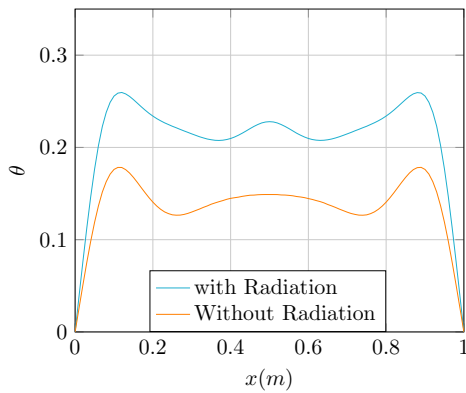


FIGURE 4.41: 2d Horizontal plate: θ along $y = 0.15$

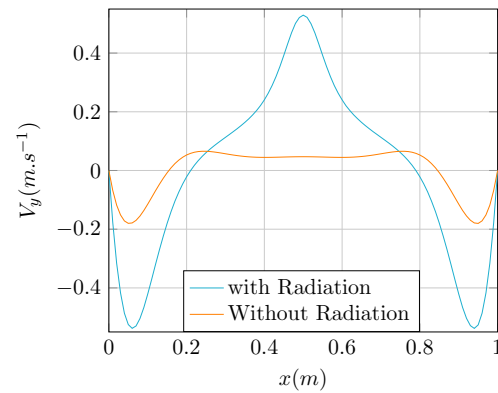


FIGURE 4.42: 2d Horizontal plate: V_y along $y = 0.15$

As observed in the previous case, the *IS2IS* method show results that seem to correspond well with the classical ones, in terms of temperature as well in terms of velocity. For the quantitative analysis, we will display plot along lines at $y = cst$, which is natural considering the symmetry of the problem. It also interesting to plot quantities along lines close to the solid obstacle, since it could be expected to encounter the steepest gradients at this location. The philosophy of the immersed volume method used here demonstrates its efficiency, since most elements of the mesh are around the interface in order to properly represent the sharp gradients. For the vertical case we chose the lines $y = 0.225$, $y = 0.5$, $y = 0.775$. For the body fitted case, all values go to zero inside the

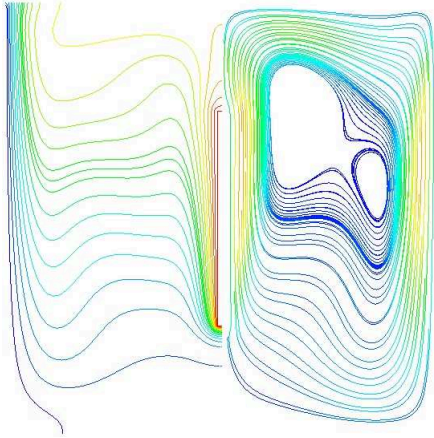


FIGURE 4.43: 2d Vertical plate: iso temperature and streamlines: $\varepsilon = 0$

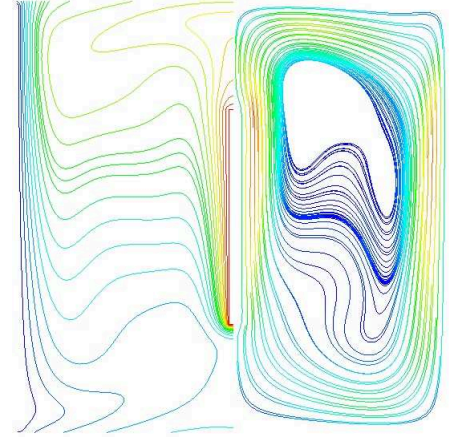


FIGURE 4.44: 2d Vertical plate: iso temperature and streamlines: $\varepsilon = 1$

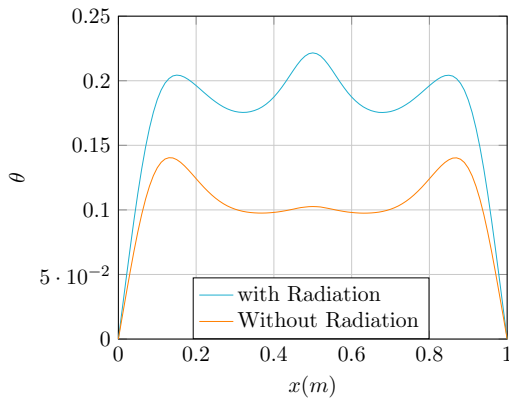


FIGURE 4.45: 2d Vertical plate: θ along $y = 0.15$

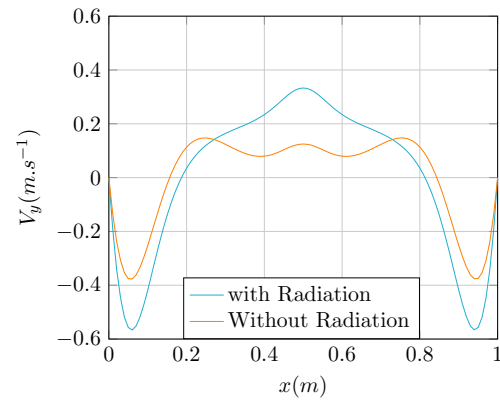


FIGURE 4.46: 2d Vertical plate: u_2 along $y = 0.15$

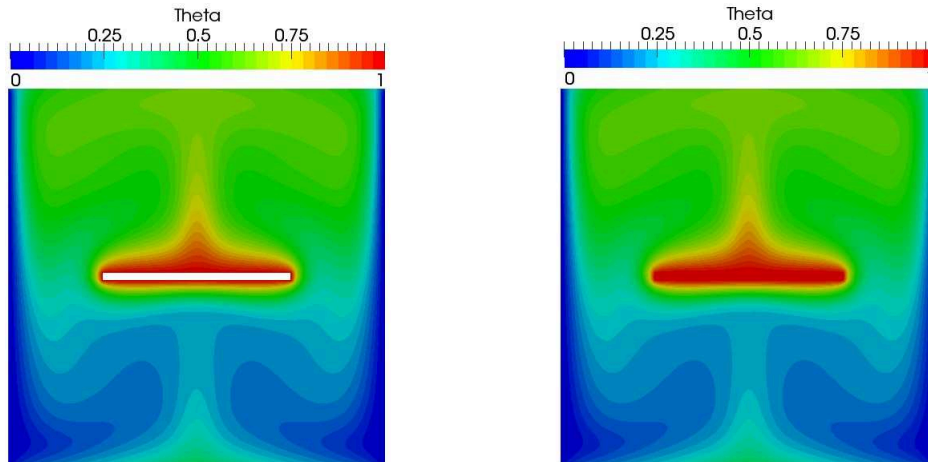
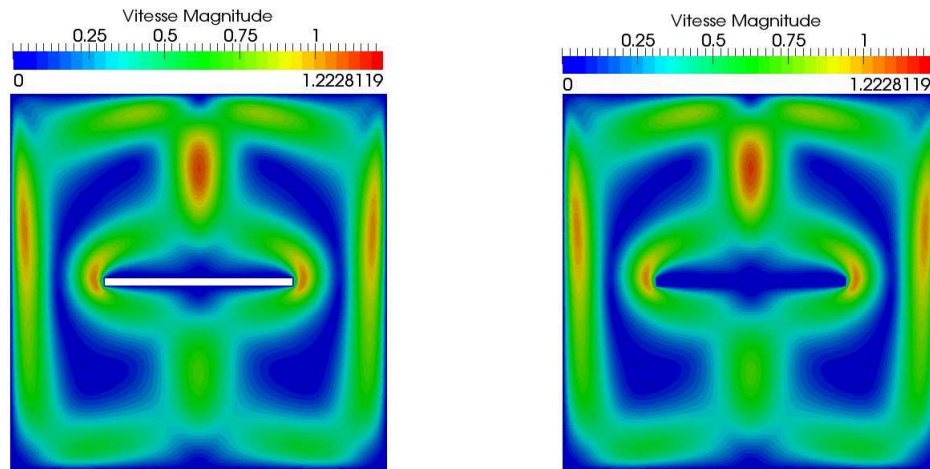
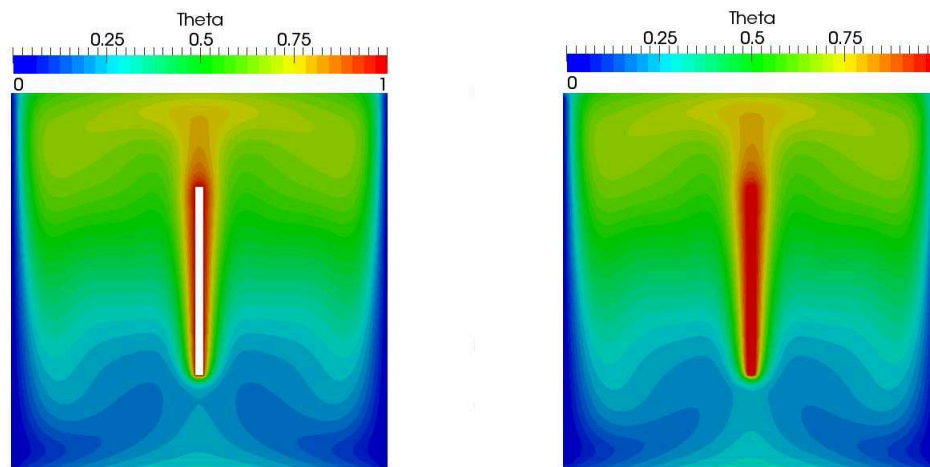
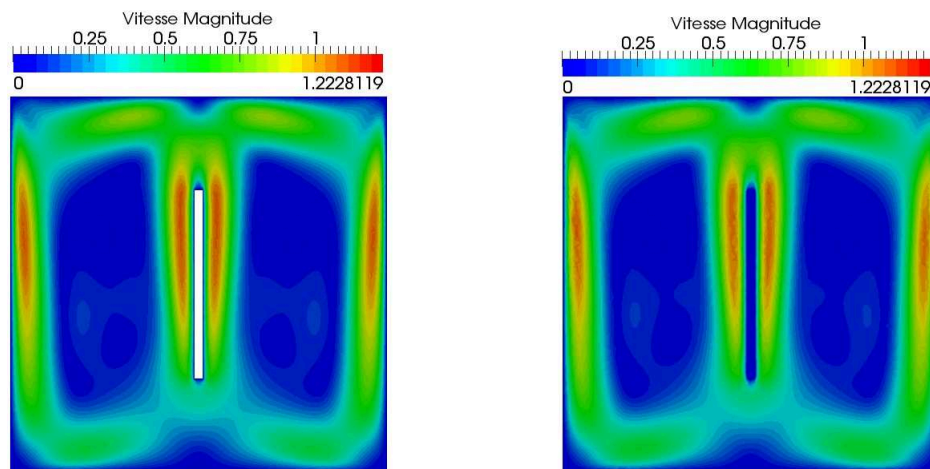


FIGURE 4.47: 2d Horizontal obstacle: iso temperature $\varepsilon = 1$

object because those points are not defined in the domain, but it is straightforward to see that a simple extension by continuity would lead the curves to fit perfectly. For the horizontal case, we chose four lines at $y = 0.15$, $y = 0.475$, $y = 0.525$, $y = 0.9$.

FIGURE 4.48: 2d Horizontal obstacle: streamlines $\varepsilon = 1$ FIGURE 4.49: 2d Horizontal obstacle: iso temperature $\varepsilon = 1$ FIGURE 4.50: 2d Horizontal obstacle: streamlines $\varepsilon = 1$

Likewise the previous chapters, we used our method on the 3d versions of these two cases. We notify that, since these cases are not presented in the literature, there is no way to compare the results with a reference. First we compare with the case without

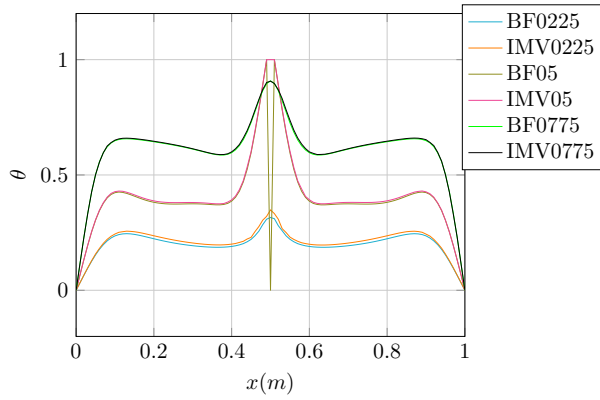


FIGURE 4.51: 2d Vertical obstacle: θ along considered lines

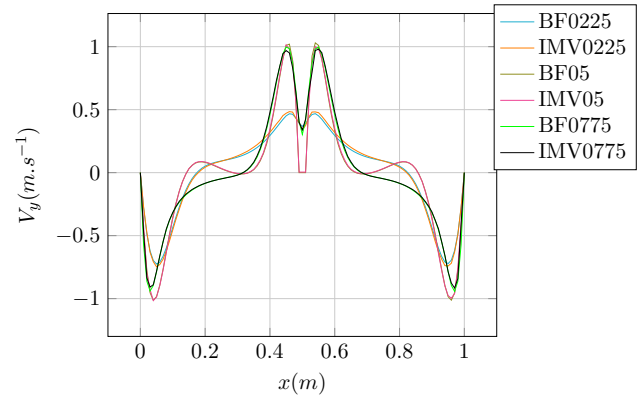


FIGURE 4.52: 2d Vertical obstacle: u_2 along considered lines

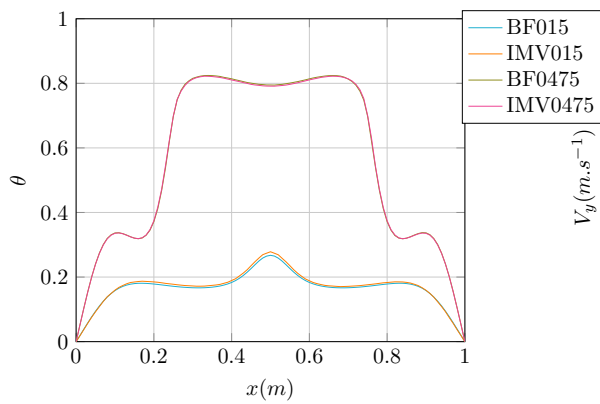


FIGURE 4.53: 2d Horizontal obstacle: θ along considered lower lines

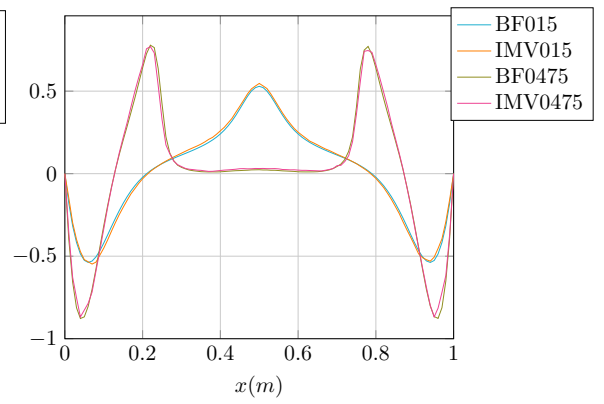


FIGURE 4.54: 2d Horizontal obstacle: u_2 along considered lower lines

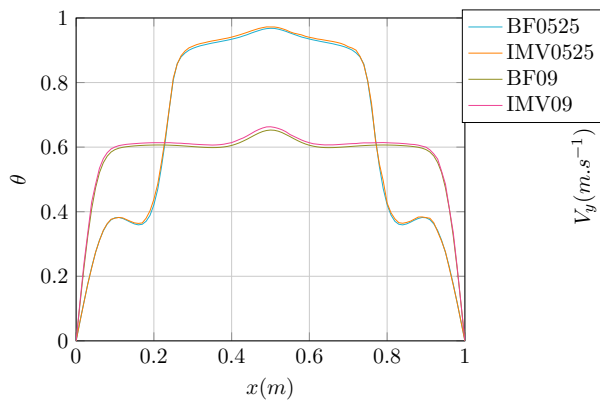


FIGURE 4.55: 2d Horizontal obstacle: θ along considered upper lines

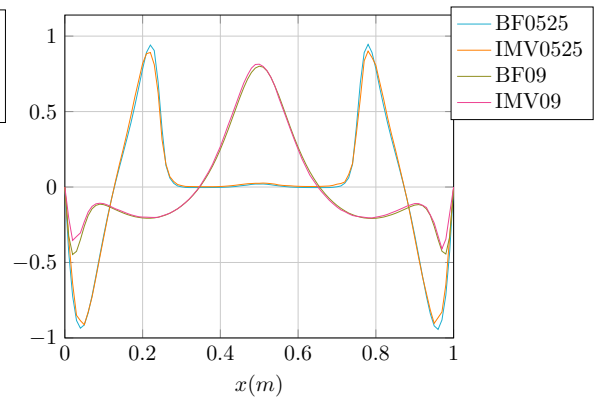


FIGURE 4.56: 2d Horizontal obstacle: u_2 along considered upper lines

radiation, and one can note the symmetry of the problem regarding the plane $x = 0.5$. Regarding the flow, the problem is also symmetric around the plane $z = 0.5$.

For both cases, one can see that, similarly to the 2d cases, due to the radiative fluxes on the horizontal boundaries, some convection is observed in the bottom part of the

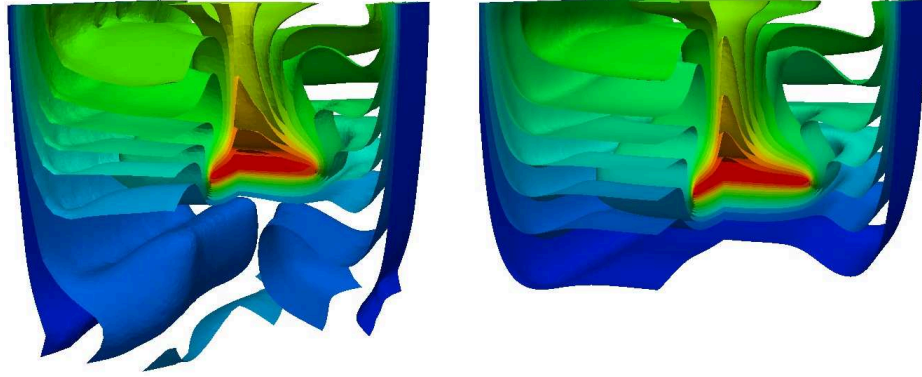


FIGURE 4.57: 3d Horizontal obstacle: iso-temperature : $\varepsilon = 1$ (left) and $\varepsilon = 0$ (right)

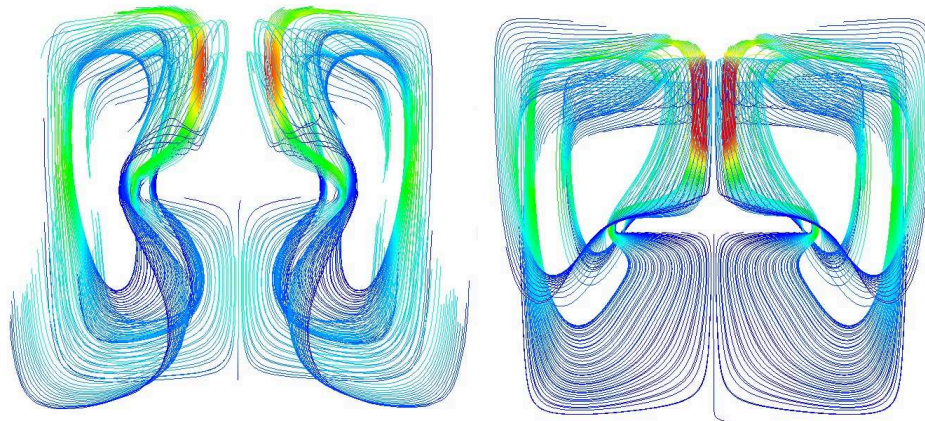


FIGURE 4.58: 3d Horizontal obstacle: streamlines: $\varepsilon = 1$ (left) and $\varepsilon = 0$ (right)

cavity, with curved iso temperature lines appearing below the plate. This can be seen on the streamlines as well, with a significant modification of their shapes. As for the 2d case, one can see that the impact of the plate on the flow is more pronounced in the horizontal case that in the vertical one, with a central iso line perturbed by the plate. One can also see the modification of thermal boundary layers for the horizontal case, with tighten lines compared to the no radiation case.

Conclusions

In this chapter, a method to model surface radiation in a monolithic context was developed. The key point is the definition of an interface approximation relying on the finite element mesh and the levelset isovalue zero, then used to perform a surface-to-surface computation with the classical features of the *S2S* approach. The approximation of the interface in terms of faces of the finite element mesh is an important feature, in the sense that the method provides radiative fluxes and source terms that naturally fits on the mesh, avoiding the problem of transport from a mesh to another one, and the coupling

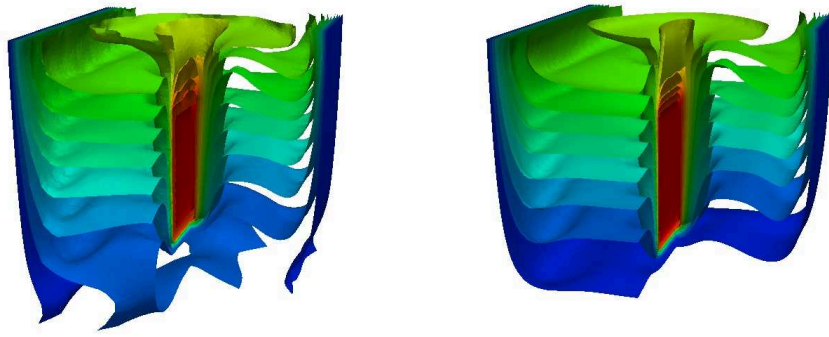


FIGURE 4.59: 3d Vertical obstacle: iso-temperature : $\varepsilon = 1$ (left) and $\varepsilon = 0$ (right)

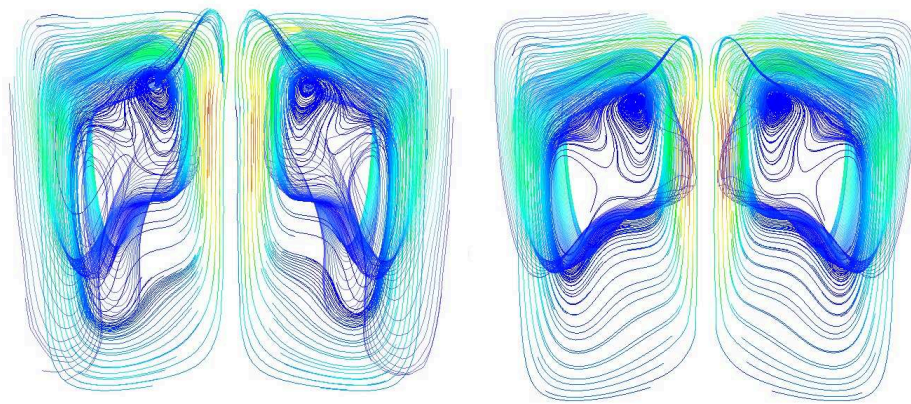


FIGURE 4.60: 3d Vertical obstacle: streamlines: $\varepsilon = 1$ (left) and $\varepsilon = 0$ (right)

can be done without any supplementary effort. The method was proven to be consistent with the classical approach, that is to say, for an appropriately refined mesh, the *IS2IS* approach give the same results that the classical *S2S* approach, for $2d$ problems as well for $3d$ problems. The problems of computational time and ressources are significant only in $3d$, but it was observed that the number of intern faces involved in the surface radiation computation remains reasonable, as expected from the results of the study conducted earlier in this chapter.

Résumé français

Dans ce chapitre, on présente une méthode pour modéliser le rayonnement surfacique dans le contexte de la méthode d'immersion de volume décrite au chapitre précédent, l'approche *IS2IS* pour "Immerse-surface-to-Immerse-surface". La difficulté majeure réside dans le fait que la description des interfaces y est implicite, uniquement définie par l'iso valeur zéro de fonctions levelset. On décrit le principe utilisé pour reconstruire

un interface en termes de faces du maillage éléments finis: on détecte les éléments traversés par la fonction levelset, donnant un bande d'éléments dont les faces intérieures sont éliminées. On procède ensuite à un calcul surfacique classique reposant sur la notion de facteur de forme, dont les éléments principaux sont rappelés dans ce chapitre. La méthode est ensuite illustrée sur les exemples présentés dans les chapitre précédent, ou l'on analyse l'influence du rayonnement surfacique sur la convection naturelle. Enfin, on vérifie que l'approche développée ici est consistante par rapport à une approche classique, avec un démarche similaire à celle du chapitre précédent.

Chapter 5

Monolithic Volume Radiation: Stabilized Finite Element Method for the Minimum Entropy closure M_1 radiation model

The last chapter was dedicated to the modelling of surface radiation effects, responsible for most radiative effects for the considered problems. Still, when temperature become very high, when dissociation and ionization of molecules can occur, or for furnaces, in the presence of combustion products (CO_2 , H_2O or soot) can be *radiatively active*, that is to say, the absorption and scattering by the medium cannot be neglected anymore. Taking into account those volumic effects implies a resolution of the RTE but, as explained in the previous chapter, the numerical methods to tackle this equation are not common in the engineering community and can be very computationally demanding. On the other hand, one can remark that, within this framework, since the purpose is the coupling of the radiation with the thermal balance, the quantity to be inserted in the energy equation (as a source term) has to be direction independent. Therefore, instead of considering the "full" radiative transfer equation, a promising lead is to consider approximate forms of the RTE (see [186] or [26] for good reviews on this topic), where the angular dependency has been eliminated, as done with the Spherical Harmonics or the DOM depicted in the previous chapter, but, in both cases, if one wants a good numerical approximation, it means dealing with an important number of equations (related to the order of the Legendre polynomial or the number of discrete ordinates), which increases substantially the computational cost and the complexity of the problem to be solved. It would be desirable to deal with a fixed number of equations, of a "classical" type if

possible (ie only dependant on space and time). Those requirements are fulfilled by the so-called moment models, where the RTE is averaged over the unit sphere, resulting in a coupled system of PDE, but with supplementary equations needed to close the system, the "essence" of the obtained model being the closure relation. Two main closures will be considered, one leading to the P_1 model briefly presented in chapter 2, and a more sophisticated one, namely the M_1 model.

Moreover, in many situations, the radiative disequilibrium is caused by spatially heterogeneous radiative properties. To treat such situations, the IVM appears as a natural tool, and so the developed method will be tested on multidomain problems.

The outline of this chapter will be as follows: first, we will introduce the concepts necessary for moment models, we will derive the two aforementioned models and a few others, secondly we will provide an overview of the existing methods for such models, and finally, we will describe the formulation we propose for the M_1 model.

5.1 Introduction to moment models

For the sake of clarity, we recall here the full RTE, the notations remaining the same

$$\frac{1}{c} \frac{\partial I}{\partial t} + \boldsymbol{\omega} \cdot \nabla I = \frac{\sigma_r}{\pi} \kappa T^4 - (\kappa + \sigma) I + \frac{\sigma}{4\pi} \int_{\mathcal{S}} I(\boldsymbol{\omega}') d\boldsymbol{\omega}' \quad (5.1)$$

At this stage, we would like to add that this equation presents different predominant regimes, depending on the values of the opacities κ and σ :

- when κ and σ values are low, the photons travel free in the medium without significant interactions with the medium. The interactions are therefore mainly long distance: this is the *transport limit*.
- when κ and σ values are high, the photons strongly interact with the medium, rendering the interaction close to isotropy (even close to the Planck distribution): this is the *diffusion limit*.

If those two limits are naturally obtained with the full RTE, this is not guaranteed for the approximate models that will be considered in this work, and the respect of this asymptotic behaviour is a desirable property for an approximate model.

The first step is the definition of the moments of the radiative intensity, the radiative energy E_r , radiative flux \mathbf{F}_r , and radiative pressure tensor \mathbb{P}_r (a less common quantity

than the first two, but interpretations and comments about it can be found in [187] or in [188]), are defined as the zeroth (sometimes called the incident radiation G , and can be expressed including the factor $\frac{1}{c}$), first and second order angular moments of the specific radiative intensity, respectively, i.e.,

$$E_r = \int_S I d\omega \quad (5.2)$$

$$\mathbf{F}_r = \int_S \boldsymbol{\omega} I d\omega \quad (5.3)$$

$$\mathbb{P}_r = \int_S (\boldsymbol{\omega} \otimes \boldsymbol{\omega}) I d\omega \quad (5.4)$$

\otimes being the dyadic product. It is also possible to define a n order moment as follows

$$\mathcal{M}^n(I) = \int_S \boldsymbol{\omega}^n I d\omega \quad (5.5)$$

$$\text{with } \boldsymbol{\omega}^n = \underbrace{\boldsymbol{\omega} \otimes \dots \otimes \boldsymbol{\omega}}_{n \otimes} \quad (5.6)$$

We notify that, thanks to the Cauchy-Schwarz inequality, (5.2) and (5.3) implies the two following so-called realizability conditions:

$$E_r \geq 0 \text{ since } I \geq 0 \quad (5.7)$$

and

$$\|\mathbf{F}_r\|_2 \leq E_r \text{ since } \|\boldsymbol{\omega}\|_2 \leq 1 \quad (5.8)$$

It can be demonstrated that all the couples (E_r, \mathbf{F}_r) that fulfill those realizability conditions, the set of admissible states, defined by

$$\mathcal{C} = \{(E_r, \mathbf{F}_r) \in \mathbb{R} * \mathbb{R}^d \text{ such } E_r \geq 0 \text{ and } \|\mathbf{F}_r\|_2 \leq E_r\} \quad (5.9)$$

is a closed convex cone. At this level, it is useful to define the reduced flux $\mathbf{f} = \frac{\mathbf{F}_r}{E_r}$ and $f = \|\mathbf{f}\|_2$. The realizability conditions implies that $0 \leq f \leq 1$. We will see that, depending on the chosen closure, those requirements are not necessarily fulfilled. A general family of moment models is obtained by integrating (5.1) and (5.1) multiplied

by $\boldsymbol{\omega}$ over all \mathcal{S} leads to

$$\frac{1}{c} \frac{\partial E_r}{\partial t} + \nabla \cdot \mathbf{F}_r + \kappa E_r = 4\kappa\sigma_r T^4 \quad (5.10)$$

$$\frac{1}{c} \frac{\partial \mathbf{F}_r}{\partial t} + \nabla \cdot \mathbb{P}_r + (\kappa + \sigma) \mathbf{F}_r = \mathbf{0} \quad (5.11)$$

One can note that the present system is not closed: we have 10 unknowns (E_r , 3 components for \mathbf{F}_r , 6 components for \mathbb{P}_r) for only four equations. We could be tempted to introduce angular moment of higher order, but because of the term $\boldsymbol{\omega} \cdot \nabla I$, the equation for the n th order moment will involve the moment of order $n + 1$. Hence, we need to introduce more equations to close the system. Two closures will be presented and compared in the following. An analogy of this system, involving the three quantities ($E_r, \mathbf{F}_r, \mathbb{P}_r$) can be done with the one encountered in the Navier Stokes equations, which involves $(\rho, \mathbf{u}, \underline{\sigma})$. Actually, the way which the NS equations are obtained from the Boltzmann equation [189, 190] is very similar to the approach presented here, $(\rho, \mathbf{u}, \underline{\sigma})$ being the moments of the distribution function of particles. Knowing this, the closure, which expresses the higher order moment in terms of lower order moments, can be seen as a constitutive relation.

5.2 Different closures

Three different models will be presented in this section, but a difference can be made between the first two, where a closed system is obtained by means of simplifying assumptions, and the third, where the closure relationship is obtained through a rigorous analysis. It is necessary to mention that, the source term to be inserted in the thermal balance is given by

$$S_{rad} = -\nabla \cdot \mathbf{q}_r = \kappa(4\sigma_r T^4 - E_r) \quad (5.12)$$

5.2.1 Rosseland approximation

The idea here is to express the radiative effects as a non-linear diffusion term. We assume a stationary phenomenon, an optically thick medium (high values of κ and σ). In such situations, the radiative energy is a Planckian of the temperature and, one gets

$$\mathbf{q}_r = -\frac{4\sigma_r}{3(\kappa + \sigma)} \nabla(T^4) = -\underbrace{\frac{16\sigma_r T^3}{3(\kappa + \sigma)}}_{=\lambda_{rad}(T)} \nabla(T) \quad (5.13)$$

This model is really easy to include in the thermal balance, just by adding a non-linear conductivity $\lambda_{rad}(T)$ which is available in many commercial softwares. Nonetheless, the model is adapted for optically thick media only, therefore is not well suited for transparent media.

5.2.2 P_1 model

This model remains interesting in the sense that it can be obtained using the spherical harmonics (the lowest order possible), and the SP_N approximation (asymptotic development with respect to opacities). We present here a way to derive it from the general moment equations, and it will provide a comparison tool to see the improvements thanks to the M_1 model that will be presented later. The closure is obtained starting from (5.11) assuming an isotropic radiative pressure $\mathbb{P}_r = \frac{1}{3}E_r\mathbb{I}$ and a stationary radiative flux so that one gets

$$\mathbf{F}_r = -\frac{1}{3(\kappa + \sigma)}\nabla E_r \quad (5.14)$$

Introducing (5.14) into (5.10) leads to the following linear diffusion-reaction time dependant type equation (the radiative energy is usually denoted as G in this context) :

$$\frac{1}{c}\frac{\partial G}{\partial t} - \nabla \cdot \left(\frac{1}{3(\kappa + \sigma)}\nabla G \right) + \kappa G = 4\sigma_r\kappa T^4 \quad (5.15)$$

As we will see after, equation (5.15) will correspond to the diffusion limit of the M_1 model.

Those two models have some well identified drawbacks: anisotropic effects cannot be rendered by such approximations (due to the isotropic radiative pressure). Moreover, the realizabilty conditions (5.7) and (5.8) can be violated: in (5.14), one can see that the \mathbf{F}_r is colinear to ∇E_r , leading to a possible violation of (5.8). This can be partially cured using the notion of "flux limiter" as described in [191], by modifying (5.14) up to a multiplicative factor, but no satisfactory compromise has been found for the transport limit yet. This justifies the use of a more sophisticated model, described in the next subsection.

5.2.3 Minimum entropy closure: the M_1 model

A section will be dedicated to a new formulation for this model, so we detail its derivation and its mathematical properties. Here the closure relationship is obtained using a maximum entropy principle. This idea has been successfully applied in other contexts, as kinetic theory [192],[193],[194] or Fokker-Planck equation [195]. Other work can be noted as well; [196] for the same approach in an abstract form, [197] for a detailed $1d$ analysis and [198] for the same results obtained with a different methodology. The idea can be described as follows: we are looking for the specific intensities that minimize a radiative entropy, under a realizability constraint, that is to say, the two first moments of the specific intensity are the ones that appear in (5.2) and (5.3). This procedure can be performed for a moment model of arbitrary high order, namely M_n models, but on the one hand, an analytic closure is only known for M_1 model, and on the other hand, a n order model involve an $n + 1$ order tensor, so such models are not convenient to implement within classic data structures, and only one dimensional applications are available in the literature for $n > 1$: we can quote [199] with the introduction of perturbed closure, [200] using adaptive closure, [201] for a special focus on the optimization problem, [202] for an exemple with a three moment model and [203] for application to slab geometries. Other non published work [204][205] can be evoked for the sake of a complete analysis. We detail only for $n = 1$, where the problem can be written as a convex optimization problem, with help from the following Lagrangian:

$$I = \arg \left(\min_{I_\nu^*, \alpha, \beta} \mathcal{J}(I_\nu^*) = \mathcal{I}(I_\nu^*) + \alpha \left(\int_0^\infty \int_S I_\nu^* d\omega d\nu - E_r \right) + \beta \cdot \left(\int_0^\infty \int_S I_\nu^* \boldsymbol{\omega} d\omega - \mathbf{F}_r \right) \right) \quad (5.16)$$

$$\mathcal{I}(I_\nu^*) = \int_0^\infty \int_S (n \log(n) - (n+1) \log(n+1)) \frac{2k\nu^2}{c^3} d\nu d\omega \quad (5.17)$$

where $n = \frac{c^2}{2h\nu^3} I_\nu^*$.

The saddle point of this Lagrangian is obtained for the following form [126] of the radiative intensity

$$I_\nu^* = \frac{2h\nu^3}{c^2} \frac{1}{\exp\left(\frac{h\nu}{kT}(\alpha + \beta \cdot \boldsymbol{\omega})\right) - 1} \quad (5.18)$$

The Lagrange multipliers α and β are then determined using realizabilty constraints. An integration over all frequencies gives

$$I^* = \frac{2\pi^4 k^4 T^4}{15c^2 h^3} \frac{1}{\left(1 - \frac{2 - \sqrt{4 - 3f^2}}{f^2}\right)^4} \quad (5.19)$$

We now want to emphasize the fact that the model to be obtained through this procedure can produce anisotropic effects : the goal is now to express a constitutive relation, under the form $\mathbb{P}_r = \mathbb{D}(f)E_r$, where $\mathbb{D}(f)$ is called the Eddington Tensor. Following Levermore's approach [191], we introduce normalized intensity and flux, defined by :

$$I = E_r \varphi, \mathbf{F}_r = E_r \mathbf{f} \quad (5.20)$$

where φ is the normalized radiative intensity, and \mathbf{f} is the reduced flux as previously defined. Using those quantities, the definition of the moments (5.2) can be recast as:

$$1 = \int_{\mathcal{S}} \varphi d\omega \quad (5.21)$$

$$\mathbf{f} = \int_{\mathcal{S}} \boldsymbol{\omega} \varphi d\omega \quad (5.22)$$

$$\mathbb{D} = \int_{\mathcal{S}} (\boldsymbol{\omega} \otimes \boldsymbol{\omega}) \varphi d\omega \quad (5.23)$$

Since φ is a non-negative density defined on the unit sphere, and \mathbf{f} and \mathbb{D} are its first and second order angular moment, respectively, they must satisfy the constraints:

$$\text{tr}(\mathbb{D}) = 1 \quad (5.24)$$

$$\mathbb{D} - \mathbf{f} \otimes \mathbf{f} \geq 0 \quad (5.25)$$

(5.24) tells us that the sum of the eigenvalues of the tensor \mathbb{D} are equal to one and (5.25) is to be understood in the sense that $\mathbb{D} - \mathbf{f} \otimes \mathbf{f}$ is a positive symmetric tensor (*ie* all its eigenvalues are non-negative). Now, let us consider the case when the intensity is symmetric about a preferred direction, denoted \mathbf{n} : it implies, thanks to equations (5.21) and (5.22), that φ , \mathbf{f} and \mathbb{D} should remain invariant under rotations that fix \mathbf{n} . It follows that :

$$\mathbf{f} = f\mathbf{n} \quad (5.26)$$

$$\mathbb{D}\mathbf{n} = \chi\mathbf{n} \quad (5.27)$$

Due to well-known arguments about real symmetric matrices, the plane orthogonal to \mathbf{n} must be an eigenspace of \mathbb{D} with an eigenvalue λ_{\perp} different of χ . Using (5.24), we obtain:

$$\lambda_{\perp} = \frac{1 - \chi}{2} \quad (5.28)$$

Thus, \mathbb{D} may be written in the form:

$$\mathbb{D} = \frac{1 - \chi}{2}(\mathbb{I} - \mathbf{n} \otimes \mathbf{n}) + \chi\mathbf{n} \otimes \mathbf{n} \quad (5.29)$$

$$\mathbb{D} = \frac{1 - \chi}{2}\mathbb{I} + \frac{3\chi - 1}{2}\mathbf{n} \otimes \mathbf{n} \quad (5.30)$$

Finally, thanks to the relations $\varphi = \frac{I}{cE_r}$ and $\mathbf{f} = f\mathbf{n}$, we can come back to the radiative pressure tensor:

$$\mathbb{P}_r = \underbrace{\left(\underbrace{\frac{1 - \chi}{2}\mathbb{I}}_{(1)} + \underbrace{\frac{3\chi - 1}{2}\frac{\mathbf{f} \otimes \mathbf{f}}{f^2}}_{(2)} \right)}_{=\mathbb{D}(\mathbf{f})} E_r \quad (5.31)$$

The expression for χ is still to be defined. We determine it using the relation:

$$\chi(f) = \int_{\mathcal{S}} (\boldsymbol{\omega} \cdot \mathbf{n})^2 \varphi d\boldsymbol{\omega} \quad (5.32)$$

The result of the calculation depends on the form of the radiative entropy, but the most common is the Maxwell Boltzmann entropy, used in the Lagrangian defined by (5.16). More details about the calculations and other alternatives are available in [206],[207],[191] linked to the flux limited diffusion models described earlier, [208] with the point of view of the thermodynamic, [209] for a derivation using entropy, and [210] for a geometric determination. Finally, for the Maxwell-Boltzmann entropy, one gets

$$\chi(f) = \frac{3 + 4f^2}{5 + 2\sqrt{4 - 3f^2}} \quad (5.33)$$

We note that all the non-linearity of the M_1 model is in (5.31) and (5.33). Some comments about the physical insight of the two contributions of the Eddington tensor can be given: term (1) can be viewed as an isotropic part of the radiative pressure, whereas term (2) is an anisotropic contribution in the direction of the normalized radiative flux \mathbf{f} . Those two terms are balanced by the Eddington factor $\chi(f)$, which is controlled by f , that can be viewed as a measure of the anisotropy of the radiation field. Moreover, this closure ensures the positivity of the energy and limitation of the radiative flux. The M_1 system renders the appropriate limits with respect to f : one can see that for $f = 0$, corresponding to the diffusion limit (isotropy), one gets

$$\chi(0) = \frac{1}{3} \quad (5.34)$$

$$\mathbb{D}(\mathbf{f}, 0) = \frac{1}{3} \mathbb{I}_d \quad (5.35)$$

and for the transport limit (anisotropy in one direction), corresponding to $f = 1$, reads

$$\chi(1) = 1 \quad (5.36)$$

$$\mathbb{D}(\mathbf{f}, 1) = \frac{\mathbf{f} \otimes \mathbf{f}}{f^2} \quad (5.37)$$

We would like to point out that it is not straightforward to derive boundary conditions for the M_1 model from the ones used for the full Radiative Transfer Equation: in (5.1), the specific intensity is prescribed for the incoming flux only, whereas in the moment model, the full moment values must be assigned, even if the notion of "partial" moment

brings an answer to this question. Nevertheless, in most of the cases [211],[212], the following boundary conditions are used

$$E_{r|\partial\Omega} = 4\pi\sigma_r T_w^4 \quad (5.38)$$

Where T_w is the temperature of the considered wall. We also consider that no radiative flux is transmitted through the wall of the enclosure, which writes

$$\mathbf{F}_{r,|\partial\Omega} = \mathbf{0} \quad (5.39)$$

Some studies about derivation of boundary conditions for general moment models (going beyond the context of radiative transfer) are available in [213],[214] or [215].

This model has been widely used in Radiation Hydrodynamics, since it offers a natural coupling with the other physics [216],[217],[218, 219],[220],[221], and the more advanced research codes for radiation hydrodynamics are based on these approaches: HERACLES [222], HADES [223] or KORAL [224]. Some applications dedicated to low Mach flows are also available [211, 225].

5.2.4 Extensions of the M_1 model

5.2.4.1 Method of partial moments

It is known that the M_1 model can produce non-physical solutions, notably in the $1d$ case of two opposed beams, where a non-physical shock is observed compared to the solution of the full RTE [226]. The reasons not to use higher order minimum entropy closure were depicted above, but an alternative is to define "partial" moments, not defined on the entire unit sphere \mathcal{S} but on a non overlapping subset forming a partition of \mathcal{S} (denoted here \mathcal{A} , with a current element $A \in \mathcal{A}$), for which we define a reduced flux f_A and an Eddington factor χ_A , but the closure (5.33) cannot be determined analytically anymore for general partial moments models. The first trace of this idea is given by [227] but without the notion of moment. Dubroca and coworkers impulsed this lead [228] with a half-moment approximation in $1d$, generalized by Ripoll [229] for multidimensional problems. A rigorous analysis for any partition and multidimensional problems is credited to Frank [205, 226]. One can also note an application to non-gray radiation [230], the subject of the next part.

5.2.4.2 Non-gray radiative transfer

In situations like astrophysics and flame modelling, the gray medium assumption is sometimes not sufficient. If full descriptions of the spectrum are available by means of databases, this is in practise out of range for situations of interest. Another option is to divide the spectrum in intervals on which radiative properties can be considered constant. One can speak of frequency groups or bands, the bands being thinner than groups. See [231] for multigroup model and [232] for a 3d multiband model, or [233] for a hybrid (coupled M_1 and full RTE) model.

5.3 State of the art: existing schemes for the M_1 model

Most of the numerical schemes for the M_1 model are of Harten-Lax-van Leer (HLL) type [234], a finite volume method taking advantage of the hyperbolic eigenstructure of the system, which can be viewed as a non-linear conservation law, and an interpretation using Riemann problems [235],[236][237],[238] between cells. The work of Berthon and coworkers, that designed a series of “asymptotic preserving” schemes [212, 239–247], is to be noted, since most of the schemes in literature are of this type. The work of Buet is also notable [248, 249] and [250], with an extension to radiation hydrodynamics, with the possibility of taking into account relativistic effects. Two other approaches can also be quoted, namely, one based on a discontinuous Galerkin approach credited to [251], and another one based on a modified system of moments proposed in [252]. In both cases, applications remain restricted to one-dimensional situations. We want to propose a multidimensional finite element method for the M_1 system: it will be a mixed formulation due to the coupled nature of the system, a stabilized formulation since we want to avoid the use of inf-sup compatible pairs, so we restrain ourselves to equal order interpolation spaces. The non-linearity of the equations will require a specific treatment as well.

5.4 Mixed Finite Element formulation for the M_1 radiation model

5.4.1 Weak formulation

We now turn to the weak formulation for the M_1 model, defined by equations (5.10), (5.11), (5.31) and (5.33). Let Q be the space where E_r belongs for each time t and W the space where \mathbf{F}_r belongs, i.e., $E_r(\cdot, t) \in Q$, $\mathbf{F}_r(\cdot, t) \in W$ for all $t > 0$. The spaces

for the test functions will be denoted by Q_0 and W_0 , so that functions in these spaces will be zero where functions in the corresponding trial spaces will be prescribed with Dirichlet boundary conditions. To avoid technical details, appropriate regularity in both space and time will be assumed.

The weak formulation of the problem is obtained by multiplying (5.10) by $q \in Q_0$ and (5.11) by $\mathbf{w} \in W_0$, integrating over the computational domain and using integration by parts on the term involving \mathbb{P}_r . This leads to the following problem:

$$\text{Find } (\mathbf{F}_r, E_r) \in W \times Q \text{ such that for all } (\mathbf{w}, q) \in W_0 \times Q_0$$

$$\frac{1}{c} \left\langle \frac{\partial \mathbf{F}_r}{\partial t}, \mathbf{w} \right\rangle + \langle (\kappa + \sigma) \mathbf{F}_r, \mathbf{w} \rangle - \langle \mathbb{P}_r, \nabla \mathbf{w} \rangle = 0 \quad (5.40)$$

$$\frac{1}{c} \left\langle \frac{\partial E_r}{\partial t}, q \right\rangle + \langle \kappa E_r, q \rangle + \langle \nabla \cdot \mathbf{F}_r, q \rangle = \langle 4\pi\kappa\sigma_r T^4, q \rangle \quad (5.41)$$

Here and in the following, $\langle f, g \rangle = \int_{\Omega} fg$ for any functions f and g , vector or scalar valued.

5.4.1.1 Time discretization and treatment of the non-linear term

Let us consider a uniform partition of the time interval $[0, T]$, so that $0 = t^0 < t^1 < \dots < t^N = T$, with $\delta t := t^{n+1} - t^n$ constant, $n = 0, \dots, N-1$. The time discretization will be performed using standard finite difference schemes. Using for example backward differences, for a generic time dependent function $g(t)$, the time derivative at t^n can be approximated by an appropriate incremental quotient $\frac{\delta g^n}{\delta t}$, with δg^n depending on g^{n-k} , $k = 0, 1, \dots$, and g^n being an approximation to $g(t^n)$. In particular, in the numerical examples we will use the simplest backward Euler scheme, in which $\delta g^n = g^n - g^{n-1}$ and all terms in the equation are evaluated at t^n . Since there is no possibility of confusion, the superscript with the time step level will be omitted.

As previously mentioned, all the non-linearity of the M_1 model is contained in \mathbb{P}_r . Hence, this term has to be treated in an appropriate manner, by performing non-linear iterations within each time step. Introducing a superscript counter i for these iterations, we can consider the following expansion of the radiative pressure tensor:

$$\mathbb{P}_r^{i+1} \approx \mathbb{P}_r^i + \mathbb{J}_E^i (E_r^{i+1} - E_r^i) + \underline{\mathbb{J}}_F^i (\mathbf{F}_r^{i+1} - \mathbf{F}_r^i) \quad (5.42)$$

where \mathbb{J}_E^i and $\underline{\mathbb{J}}_F^i$ (a third order tensor) are the Jacobian matrices of \mathbb{P}_r with respect to E_r and \mathbf{F}_r , respectively. The calculation of those matrices is detailed in the appendix

C. Introducing (5.42) into (5.40) and (5.41), one gets

$$\begin{aligned} & \frac{1}{c} \left\langle \frac{\delta \mathbf{F}_r^{i+1}}{\delta t}, \mathbf{w} \right\rangle + \langle (\kappa + \sigma) \mathbf{F}_r^{i+1}, \mathbf{w} \rangle - \langle \underline{\mathbb{J}}_F^i \mathbf{F}_r^{i+1}, \nabla \mathbf{w} \rangle - \langle \mathbb{J}_E^i E_r^{i+1}, \nabla \mathbf{w} \rangle \\ & = \langle \mathbb{P}_r^i, \nabla \mathbf{w} \rangle - \langle \underline{\mathbb{J}}_F^i \mathbf{F}_r^i, \nabla \mathbf{w} \rangle - \langle \mathbb{J}_E^i E_r^i, \nabla \mathbf{w} \rangle \end{aligned} \quad (5.43)$$

$$\frac{1}{c} \left\langle \frac{\delta E_r^{i+1}}{\delta t}, q \right\rangle + \langle \kappa E_r^{i+1}, q \rangle + \langle \nabla \cdot \mathbf{F}_r^{i+1}, q \rangle = \langle 4\pi\kappa\sigma_r T^4, q \rangle \quad (5.44)$$

More implementation details can be found in the appendix C. During numerical experiments, no significant difference was observed by using the classical Newton method and a linearization performed over a time step. However, further investigation about these questions have to be conducted, and will be the subject of future work.

5.4.1.2 Galerkin finite element approximation

Let us consider a finite element partition $\mathcal{T}_h = \{K\}$ of the computational domain of diameter h . From this we may construct finite element spaces $W_h \subset W$, $W_{h,0} \subset W_0$, $Q_h \subset Q$ and $Q_{h,0} \subset Q_0$ in the usual way.

The Galerkin finite element approximation to problem (5.43)-(5.44) reads: for each iteration $i + 1$ of each time step, find $\mathbf{F}_{r,h}^{i+1} \in W_h$, $E_{r,h}^{i+1} \in Q_h$ such that

$$\begin{aligned} & \frac{1}{c} \left\langle \frac{\delta \mathbf{F}_{r,h}^{i+1}}{\delta t}, \mathbf{w}_h \right\rangle + \langle (\kappa + \sigma) \mathbf{F}_{r,h}^{i+1}, \mathbf{w}_h \rangle - \langle \underline{\mathbb{J}}_F^i \mathbf{F}_{r,h}^{i+1}, \nabla \mathbf{w}_h \rangle - \langle \mathbb{J}_E^i E_{r,h}^{i+1}, \nabla \mathbf{w}_h \rangle \\ & = \langle \mathbb{P}_r^i, \nabla \mathbf{w}_h \rangle - \langle \underline{\mathbb{J}}_F^i \mathbf{F}_{r,h}^i, \nabla \mathbf{w}_h \rangle - \langle \mathbb{J}_E^i E_{r,h}^i, \nabla \mathbf{w}_h \rangle \end{aligned} \quad (5.45)$$

$$\frac{1}{c} \left\langle \frac{\delta E_{r,h}^{i+1}}{\delta t}, q_h \right\rangle + \langle \kappa E_{r,h}^{i+1}, q_h \rangle + \langle \nabla \cdot \mathbf{F}_{r,h}^{i+1}, q_h \rangle = \langle 4\pi\kappa\sigma_r T^4, q_h \rangle \quad (5.46)$$

for all $\mathbf{w}_h \in W_{h,0}$ and $q_h \in Q_{h,0}$. It is understood that the Jacobians and the pressure radiation tensor are computed with the finite element unknowns.

This is the classical Galerkin finite element method for the M_1 radiation model. To the best of the author's knowledge, there is no other finite element method available in literature for this model. Still, it was observed that the solution of the proposed formulation (5.45)-(5.46) suffers from numerical oscillations when it is used in the way we presented it above. Before turning to the stabilized approach, we propose coming back on the VMS approach.

5.4.2 The VMS as an abstract tool

The Variational MultiScale method presented and applied to NS and CDR problems was first introduced in the context of fluid dynamics, with the natural interpretation of fine and coarse scales as small structures and large structures. But, after all, if one analyzes the problem from an abstract point of view, the VMS method can be seen as a formal decomposition of functional spaces into a direct sum, implying a splitting of unknowns and test functions to be inserted in the weak formulation. Hence, if one has at hand the tools for a finite element method (the weak formulation and the functional setting), the VMS framework can be used to stabilize the formulation of any problem. This has been achieved for a large class of problems: strain localization in solid mechanics [253], inelasticity [254], diffusion in random media [255], Boussinesq equations [256], crack propagation [257], non-linear solid mechanics [258], Lagrangian Hydrodynamics [259] or plasma flows [260]. But the problem that inspired the most is the problem of waves, since the mixed form of the wave equation permits to handle situations that are out of reach with the full form of the wave equation [261], even though the VMS was applied before to the Helmholtz equation [262]. The first work on this problem is in [263], followed by [264–269]. Knowing this, the VMS appears as a natural tool to stabilize the presented formulation.

5.4.3 Stabilization for the proposed formulation

For ease the notation in the analysis to come, the following notations are introduced:

$$\mathbb{F}_f = \mathbb{P}_r^i - \mathbb{J}_F^i \mathbf{F}_{r,h}^i - \mathbb{J}_E^i E_{r,h}^i \quad (5.47)$$

$$f_E = 4\pi\kappa\sigma_r T^4 \quad (5.48)$$

5.4.3.1 Scale splitting within the VMS framework

Once the equations to be solved are written in variational form, a VMS decomposition is applied and the radiative flux and energy are split into a coarse-scale/fine-scale decomposition, and likewise for the associated test functions. Thus, the corresponding spaces can be written as $W = W_h \oplus W'$ and $Q = Q_h \oplus Q'$, and the functions belonging to them as

$$\begin{aligned} \mathbf{F}_r &= \mathbf{F}_{r,h} + \mathbf{F}'_r, & E_r &= E_{r,h} + E'_r \\ \mathbf{w} &= \mathbf{w}_h + \mathbf{w}', & q &= q_h + q' \end{aligned}$$

with the obvious identification of unknowns and test functions.

At each iteration we have to solve a linear problem. Since there is no possibility of confusion, superscripts are omitted in the following. Introducing the previous decompositions into the weak formulation leads to a coarse-scale and a fine scale problem for each unknown, which reads:

- Radiative flux equation

$$\begin{aligned} \frac{1}{c} \left\langle \frac{\delta(\mathbf{F}_{r,h} + \mathbf{F}'_r)}{\delta t}, \mathbf{w}_h \right\rangle + \langle (\kappa + \sigma)(\mathbf{F}_{r,h} + \mathbf{F}'_r), \mathbf{w}_h \rangle - \langle \mathbb{J}_F(\mathbf{F}_{r,h} + \mathbf{F}'_r), \nabla \mathbf{w}_h \rangle \\ - \langle \mathbb{J}_E(E_{r,h} + E'_r), \nabla \mathbf{w}_h \rangle = \langle \mathbb{F}_f, \nabla \mathbf{w}_h \rangle \end{aligned} \quad (5.49)$$

$$\begin{aligned} \frac{1}{c} \left\langle \frac{\delta(\mathbf{F}_{r,h} + \mathbf{F}'_r)}{\delta t}, \mathbf{w}' \right\rangle + \langle (\kappa + \sigma)(\mathbf{F}_{r,h} + \mathbf{F}'_r), \mathbf{w}' \rangle - \langle \mathbb{J}_F(\mathbf{F}_{r,h} + \mathbf{F}'_r), \nabla \mathbf{w}' \rangle \\ - \langle \mathbb{J}_E(E_{r,h} + E'_r), \nabla \mathbf{w}' \rangle = \langle \mathbb{F}_f, \nabla \mathbf{w}' \rangle \end{aligned} \quad (5.50)$$

- Radiative energy equation

$$\frac{1}{c} \left\langle \frac{\delta(E_{r,h} + E'_r)}{\delta t}, q_h \right\rangle + \langle \nabla \cdot (\mathbf{F}_{r,h} + \mathbf{F}'_r), q_h \rangle + \langle \kappa(E_{r,h} + E'_r), q_h \rangle = \langle f_E, q_h \rangle \quad (5.51)$$

$$\frac{1}{c} \left\langle \frac{\delta(E_{r,h} + E'_r)}{\delta t}, q' \right\rangle + \langle \nabla \cdot (\mathbf{F}_{r,h} + \mathbf{F}'_r), q' \rangle + \langle \kappa(E_{r,h} + E'_r), q' \rangle = \langle f_E, q' \rangle \quad (5.52)$$

5.4.3.2 Approximation for the Fine-scale problem

To approximate the fine scale problem, we will work under the assumptions presented in chapter 2. Nonetheless, some uncommon difficulties arise here due to the presence of tensors in the fine scale problem that require a specific treatment

Let us introduce the following notation:

$$\mathfrak{R}_{F,1} = -(\kappa + \sigma) \mathbf{F}_{r,h} - \frac{1}{c} \frac{\delta \mathbf{F}_{r,h}}{\delta t} \quad (5.53)$$

$$\mathbb{R}_{F,2} = \mathbb{F}_f + \mathbb{J}_F \mathbf{F}_{r,h} + \mathbb{J}_E E_{r,h} \quad (5.54)$$

$$\mathfrak{R}_E = f_E - \frac{1}{c} \frac{\delta E_{r,h}}{\delta t} - \nabla \cdot \mathbf{F}_{r,h} - \kappa E_{r,h} \quad (5.55)$$

$$\mathbb{A} = \mathbb{J}_F \mathbf{F}'_r + \mathbb{J}_E E'_r \quad (5.56)$$

With our working assumptions, the fine scale problem (5.50)-(5.52) then reads:

$$\langle (\kappa + \sigma) \mathbf{F}'_r, \mathbf{w}' \rangle - \langle \mathbb{A}, \nabla \mathbf{w}' \rangle = \langle \mathfrak{R}_{F,1}, \mathbf{w}' \rangle + \langle \mathbb{R}_{F,2}, \nabla \mathbf{w}' \rangle \quad (5.57)$$

$$\langle \nabla \cdot \mathbf{F}'_r, q' \rangle + \langle \kappa E'_r, q' \rangle = \langle \mathfrak{R}_E, q' \rangle \quad (5.58)$$

as stated before, the fine scale problem does not really need to be solved in an accurate way, it just has to be approximated in order to capture the effect of the fine scales on the large scales.

Since the fine scales vanish on inter-element boundaries, we can write

$$\begin{aligned}\langle \mathbb{A}, \nabla \mathbf{w}' \rangle &= -\langle \nabla \cdot \mathbb{A}, \mathbf{w}' \rangle \\ \langle \mathbb{R}_{F,2}, \nabla \mathbf{w}' \rangle &= -\langle \nabla \cdot \mathbb{R}_{F,2}, \mathbf{w}' \rangle\end{aligned}$$

We can now define

$$\mathfrak{R}_F = \mathfrak{R}_{F,1} - \nabla \cdot \mathbb{R}_{F,2}$$

The term $\nabla \cdot \mathbb{A}$ requires to make more assumptions. Since only the steady state is of interest, spatial variations of the Jacobian matrices in the left-hand side can be neglected without compromising the accuracy of the scheme. Hence, by denoting $\mathbb{J}_F = (\mathbb{J}_F^p)_{p \in \{1, \dots, d\}}$, we can write

$$\nabla \cdot \mathbb{A} = \mathbb{J}_E \nabla E'_r + \sum_{p=1}^d \mathbb{J}_F^p \nabla F'_{r,p} \quad (5.59)$$

Using this, the fine-scale problem can be written as

$$\langle (\kappa + \sigma) \mathbf{F}'_r + \mathbb{J}_E \nabla E'_r + \sum_{p=1}^d \mathbb{J}_F^p \nabla F'_{r,p}, \mathbf{w}' \rangle = \langle \mathfrak{R}_F, \mathbf{w}' \rangle \quad (5.60)$$

$$\langle \nabla \cdot \mathbf{F}'_r + \kappa E'_r, q' \rangle = \langle \mathfrak{R}_E, q' \rangle \quad (5.61)$$

for all test functions \mathbf{w}' and q' . This problem can be cast in the following abstract form

$$P'(\mathcal{L}(U)) = P'(\mathfrak{R}) \quad (5.62)$$

with

$$U = \begin{bmatrix} \mathbf{F}'_r \\ E'_r \end{bmatrix}, \quad \mathfrak{R} = \begin{bmatrix} \mathfrak{R}_F \\ \mathfrak{R}_E \end{bmatrix}$$

\mathcal{L} is the differential operator appearing in the left-hand-side of (5.60)-(5.61) and P' is the projection onto the space of subscales. In essence, the two common choices for this operator are to take either the projection orthogonal to the finite element space (OSS method) or the identity when applied to finite element residuals (ASGS method); see [37]. As mentioned before, the ASGS formulation will be used in this work.

The idea is now to approximate the operator \mathcal{L} by an operator easy to invert. A straightforward solution is to take $\mathcal{L}^{-1} \approx \mathbb{T}$, where \mathbb{T} is a diagonal matrix. Thus, we take

$$\mathbb{T} = \begin{bmatrix} \tau_F \mathbb{I}_d & 0 \\ 0 & \tau_E \end{bmatrix}$$

The values are obtained thanks to the Fourier analysis presented in chapter 2. Applying this transform to (5.62) gives:

$$(\kappa + \sigma) \widehat{\mathbf{F}}'_r - \mathbb{J}_E \frac{i\mathbf{k}}{h} \widehat{E}'_r - \sum_{p=1}^d \mathbb{J}_F^p \frac{i\mathbf{k}}{h} \widehat{F}'_{r,p} = \widehat{\mathfrak{R}}_F \quad (5.63)$$

$$-\frac{i\mathbf{k}}{h} \cdot \widehat{\mathbf{F}}'_r + \kappa \widehat{E}'_r = \widehat{\mathfrak{R}}_E \quad (5.64)$$

where we have assumed again that subscales vanish on the element boundaries.

At this stage, we would like to point out that the governing equations of the M_1 model are similar to a system of damped waves in mixed form, as addressed in [270]. This leads us to make an analogy with the approach proposed in [263] or [269] for undamped waves, and choose the stabilization parameters as

$$\tau_F = \frac{1}{\sqrt{\left(\frac{c_1(\rho(\mathbb{J}_E) + \sum_{i=1}^d \rho(\mathbb{J}_F^i))}{h} \right)^2 + (\kappa + \sigma)^2}} \quad (5.65)$$

$$\tau_E = \frac{1}{\sqrt{\left(\frac{c_2}{h} \right)^2 + \kappa^2}} \quad (5.66)$$

where $\rho(\cdot)$ stands for the spectral radius of a matrix and c_1 and c_2 are algorithmic constants defined earlier. We finally get

$$\mathbf{F}'_r = \tau_F \mathfrak{R}_F, \quad E'_r = \tau_E \mathfrak{R}_E \quad (5.67)$$

Then, one just needs to introduce (5.67) in (5.49) and (5.51) after integrating by parts the terms involving the subscales, leading to new terms in the previous formulation that provide the desired extra control. We now turn to numerical experiments.

5.5 Numerical results

This section is devoted to the testing of the formulation on four benchmark problems available in literature, in order to assess the implementation of the new mixed stabilized finite element method. The first example considers one single domain, whereas the three

other problems deal with multidomains to illustrate the use of the immersed volume method for such situations.

5.5.1 Transparent media in a square enclosure

For our first example, we consider radiative transfer in a static non-participating media contained in the unit square. This test case is close to the ones presented in [271] and [272] or [211], with the difference that we set here $\kappa = 0 \text{ m}^{-1}$. We want to make a comparison with the P_1 model, so we also perform the computation with $\kappa = 10^{-4} \text{ m}^{-1}$. We work with non-dimensional quantities, so that we have $c = 1$. We use Dirichlet boundary conditions with a bottom wall at a fixed $E_{r,in} = 7.13 \cdot 10^5 \text{ W}$ and the other walls are at $E_{r,b} = 5800 \text{ W}$, and a zero value is fixed for the normal component of \mathbf{F}_r . The initial radiative energy is $E_{r,0} = 5800 \text{ W}$. For both simulations, the time step is $\delta t = 0.05$, and we use a mesh of approximately 11 200 elements.

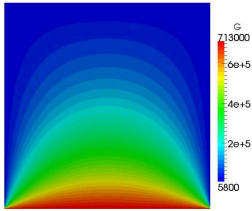


FIGURE 5.1: Radiative Energy for P_1 model (left) and M_1 model (right): $t = 5\delta t$

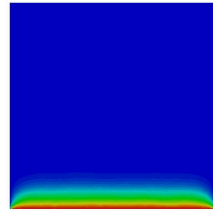


FIGURE 5.2: Radiative Energy for P_1 model (left) and M_1 model (right): $t = 25\delta t$

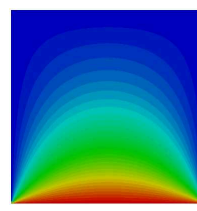


FIGURE 5.3: Radiative Energy for P_1 model (left) and M_1 model (right): $t = 400\delta t$

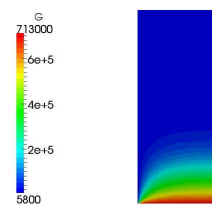


FIGURE 5.4: Radiative Energy for P_1 model (left) and M_1 model (right): steady state

The results show the ability of the M_1 model to reproduce the transient behavior of the phenomenon represented. It is observed that for the P_1 model, the equilibrium state is reached after only one time step, and using a smaller time step does not make any difference. This example demonstrates that the obtained solution is free of oscillations, justifying the coupled formulation and the stabilization developed here.

An important question is the accuracy of the formulation; to the best of our knowledge, there exists no analytical solution for the radiative transfer equation in two dimensions (for one-dimension, see [273], but a two dimensional extension is not straightforward).

We then propose to perform an error analysis by performing calculations on several meshes of different sizes. We will use a solution $E_{r,ref}$ computed on an unstructured mesh of 105 584 elements as our reference. The chosen norm is

$$\varepsilon(u_h) = \left(\int_{\Omega} (u_h - u_{ref})^2 d\Omega \right)^{\frac{1}{2}} \quad (5.68)$$

We considered four meshes $(\mathcal{M}_i)_{i=1..4}$. Their characteristics (number of elements, mesh size) are given in the table below. As it can be expected from the finite element theory, a linear convergence is observed.

Mesh	Number of elements N	mesh size h
\mathcal{M}_1	250	0.09006
\mathcal{M}_2	522	0,057556
\mathcal{M}_3	1036	0.040449
\mathcal{M}_4	4302	0.019711

TABLE 5.1: Meshes used for the error analysis

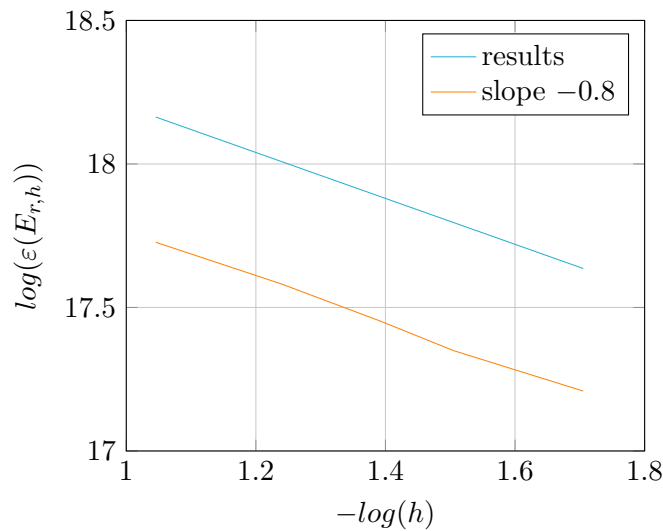


FIGURE 5.5: L^2 error with respect to the mesh size

5.5.2 Participating media with discontinuous coefficients: fixed temperature

This case is taken from [274], where solutions of different approximate models for radiation presented in this chapter and chapter 4 are compared to solutions obtained by

a direct resolution of Eq. (5.1), so it offers a reference to compare our results. We considered a fixed temperature, constant in two different subdomains, with a spatially dependent absorption coefficient κ . The computational domain is $\mathcal{D} = [0, 1] \times [0, 10]$, and we define $\mathcal{D}_0 = [0.45, 0.55] \times [4.5, 5.5]$, $\mathcal{D}_1 = \mathcal{D} \setminus \mathcal{D}_0$. We set $\sigma = 1$ and the temperature and absorption coefficients are taken as

$$T(\mathbf{x}) = \begin{cases} 1000 \text{ K} & \text{if } \mathbf{x} \in \mathcal{D}_0 \\ 1800 \text{ K} & \text{if } \mathbf{x} \in \mathcal{D}_1 \end{cases} \quad (5.69)$$

$$\kappa(\mathbf{x}) = \begin{cases} 3 \text{ m}^{-1} & \text{if } \mathbf{x} \in \mathcal{D}_0 \\ 1 \text{ m}^{-1} & \text{if } \mathbf{x} \in \mathcal{D}_1 \end{cases} \quad (5.70)$$

This temperature leads to a “manufactured” source term for Eq. (5.10), varying in space, but constant in time. The immersed volume method allows us to represent the spatial dependence of the absorption coefficient in a natural way.

The mesh used for the computations and the representation of the levelset function of the object are displayed in Fig. 5.6; this mesh is composed of 218 072 elements. We use homogeneous Neuman boundary conditions for E_r and a zero Dirichlet condition for the normal component of \mathbf{F}_r .

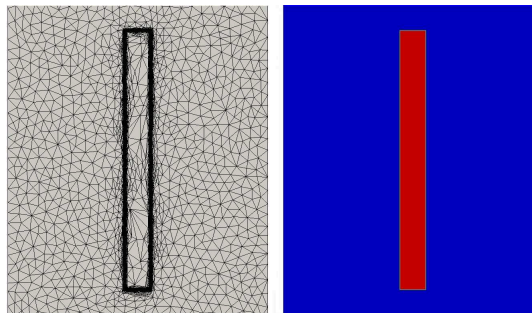


FIGURE 5.6: Adapted mesh and levelset of the center zone

Steady state results are presented in Fig. 5.7, where we display the patterns of the radiative energy for both the P_1 and M_1 models. In Figs. 5.8 and 5.9 we plot the values along $x = 0.5$ in order to compare with the reference solution.

The patterns show that both the P_1 and M_1 models overestimate the value of the radiative energy inside \mathcal{D}_0 , but whereas the P_1 model shows a qualitatively wrong profile, the correct profile is obtained with the M_1 model. Again, this numerical test demonstrates that the obtained solution is stable and free of oscillations, justifying the coupled formulation and the stabilization developed here.

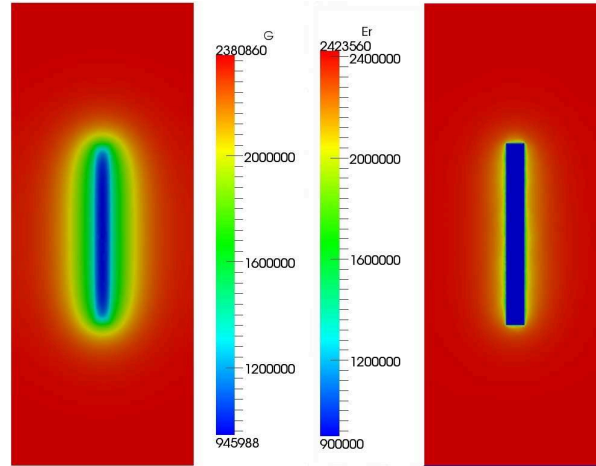


FIGURE 5.7: Patterns of the radiative energy obtained for P_1 (left) and M_1 (right) models

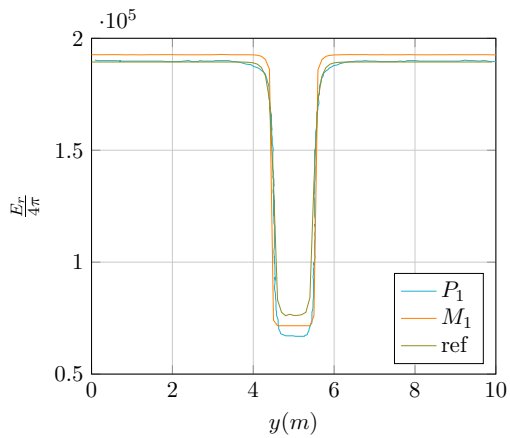


FIGURE 5.8: Radiative Energy along $x = 0.5$: present results

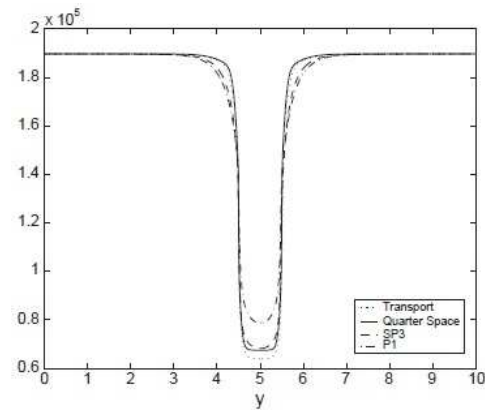


FIGURE 5.9: Radiative Energy along $x = 0.5$: reference from [274]

5.5.3 Radiation of an absorbing rod in a scattering media: the Mor-dant Test

The next example to be presented was introduced in [275, 276] and is also presented in [272]. The considered domain is a unit square. The test represents a purely absorbing region (a square rod of side 0.6) surrounded by a scattering region. Only steady state results are presented. The properties of the different zones are summarized in Table 5.2. Again, the central zone and the heterogeneous properties are represented by means of the immersed volume method. The adapted mesh (composed of 102 488 elements) and the levelset function used to adapt the mesh are presented in Fig. 5.10. In [272], results were compared with the results obtained by the discrete ordinates method, and it was shown that results from the M_1 model can differ for those obtained by the classical discrete ordinates method due to complex geometrical effects. The boundary conditions

are zero Neumann on the left and bottom boundaries, and a specular reflection on the top and right boundaries. For the M_1 , for a boundary Γ , with $\mathbf{F}_r = (F_{rn}, F_{rt})$ being respectively the normal and tangential components of the flux, those conditions read:

$$\begin{aligned} E_{r,\Gamma} &= E_{r,w} \\ F_{rn,\Gamma} &= -F_{rn,w} \\ F_{rt,\Gamma} &= F_{rt,w} \end{aligned}$$

where X_Γ refers to quantities imposed on the considered boundary, and X_w are those obtained from the calculations (hence, those boundary conditions are updated at each time step). It is not straightforward to derive this kind of boundary conditions, since in the P_1 model the flux is related to the gradient of E_r , and therefore imposing E_r and ∇E_r on the same boundary would lead to an ill-posed problem. However, we tried the two alternatives, which give similar results; these results are presented below.

Properties	Zone	
	Center zone	Outer zone
κ	100	0.05
σ	0	0,95
S_{rad}	0	1

TABLE 5.2: Thermodynamical properties of the considered case

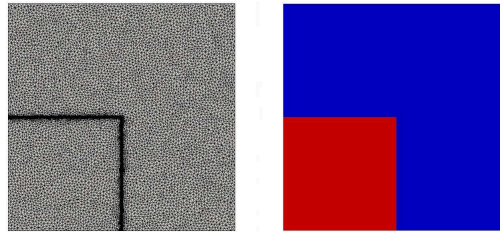


FIGURE 5.10: Adapted mesh and levelset of the center zone

The M_1 results obtained are correspondant with those obtained in the reference mentioned above. Since a flux limited diffusion was used in that reference, the pattern obtained differs a bit, but the same tendency is observed.

5.5.4 Radiative transfer behind an obstacle: the shadow test

The purpose of this test, inspired in the benchmark presented in [277] and [217], is to show the ability of the M_1 model to capture the anisotropy of the radiative field, contrary

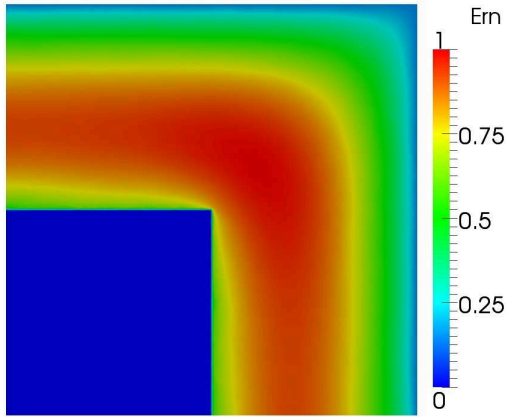


FIGURE 5.11: Patterns obtained for M_1 model

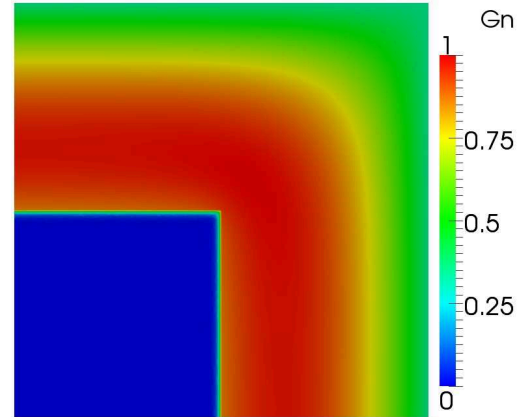


FIGURE 5.12: Patterns obtained for P_1 model

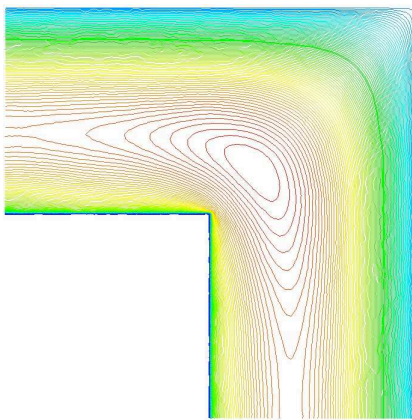


FIGURE 5.13: Iso-lines obtained for M_1 model

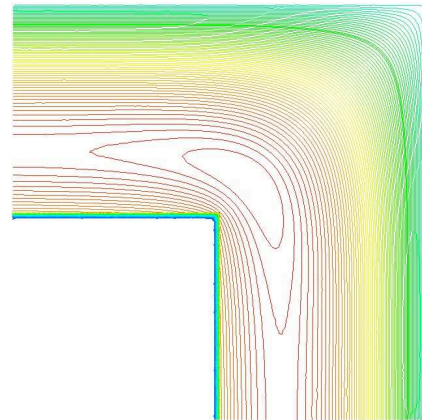


FIGURE 5.14: Iso-lines obtained for P_1 model

to the P_1 model. All cited references compute results on half of the computational domain for symmetry reasons, but we have chosen to compute the whole domain. The geometry represents a cylindrical domain of 1.0 m in length and 0.12 m in radius. An ellipsoidal obstacle, of semi-major and semi-minor axes (0.1, 0.06), respectively, is located in the domain. We have chosen values of absorption coefficient with a large difference between the obstacle and the surrounding media to produce a shadow effect ($\kappa_{\text{obstacle}} = 50000 \text{ m}^{-1}$, $\kappa_{\text{media}} = 0 \text{ m}^{-1}$). Contours of the obstacle are smoothed in [277], but this is replaced here by the anisotropic mesh adaptation to capture the interface of the obstacle properly. A radiative energy of $E_{r,in} = 6.5 \cdot 10^6 \text{ W}$ is imposed at the left boundary of the domain, and zero Neumann conditions are imposed elsewhere. On the whole boundary, a zero Dirichlet condition is imposed for the normal component of \mathbf{F}_r . The initial condition is $E_r(\mathbf{x}, 0) = E_{r,0} = 5.04 \cdot 10^2 \text{ W}$. The distributed absorption coefficient and the mesh used for the computations are presented in Fig. 5.15. We only look for steady state results. A mesh of 268 012 elements is used.

The results in Fig 5.16 show that whereas the P_1 model cannot reproduce disequilibrium

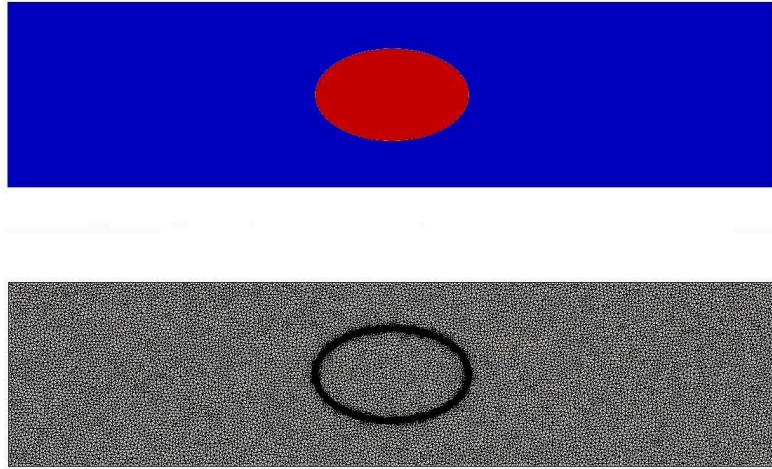
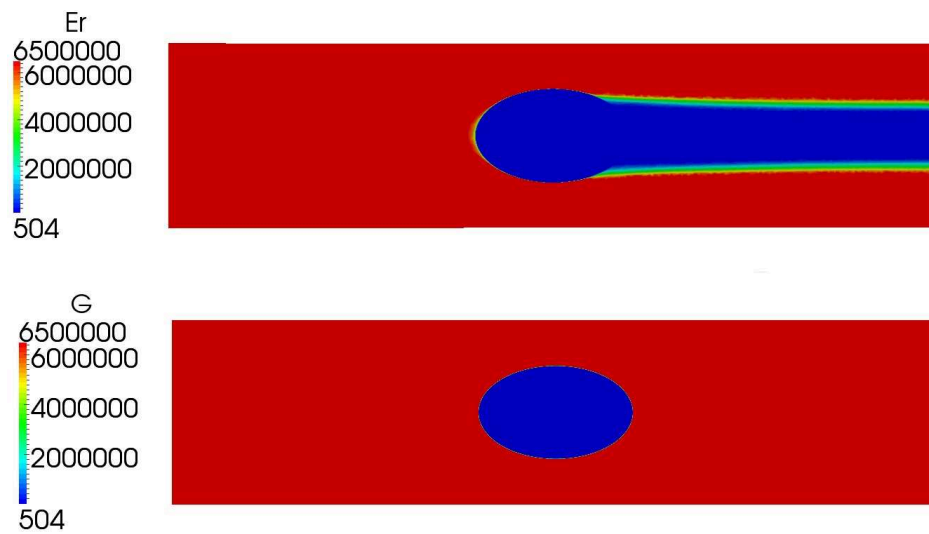


FIGURE 5.15: Distributed absorption and adapted mesh

FIGURE 5.16: Radiative Energy for the P_1 model (bottom) and for the M_1 model (top)

for the radiative energy, the M_1 model gives clearly a better approximation of the energy distribution. However, the shadow effect is not sharp as as presented in [277]. This can be explained by the principle of the stabilization method: the most important term is a “diffusion-like” one. On the other hand, the M_1 model aims to make a balance between a transport part and a diffusive part. Therefore, the extra diffusion added for the stabilization perturbs this balance. In fact, even if this balance is ensured at the continuous level (equation (5.31)), it is not guaranteed that it still holds for the discretized formulations.

Concluding remarks

In this chapter, a new stabilized finite element formulation for the M_1 radiation model has been developed and tested on some illustrative examples. The ability to represent multi-domain problems was also demonstrated. It is a first attempt, using a finite element framework, to deal with such a coupled non-linear system that solves both radiative energy and flux. Nevertheless, the formulation can be improved:

- Additional work should be done to ensure that the formulation preserves the admissible states: in a finite element context, this can be done by including the realizabilty constraints in the functional setting. However, since the set of realizable states is a convex set, it is not straightforward to exhibit such a space. An option would be to use the theorem of projection in an Hilbert space onto a convex [278],[279] iteratively, by finding the unique projection, consider its orthogonal complement and repeat the same operation. Another option would be to consider an augmented formulation, following the lines in [116], the constraint being related to the realizable states. This means to deal with variational inequations, as seen in the in the context of contact mechanics [280].
- Regarding the mixed finite element theory, all of the variational theory [29] assumes a symmetric formulation, which does not hold here. Therefore, it would be interesting to investigate the classical properties of the finite element formulation (order of convergence, regularity with respect to datas, existence of continuous weak solutions).
- An asymptotic analysis like the one presented in [246, 247] or more recently in [281] is difficult to transpose in a finite element context, on the one hand because the proposed formulation is fully implicit, so there is no CFL condition to work on, and on the other hand, there is no numerical reconstruction flux step or Riemann problem equivalent in a classical finite element context. An option would be to investigate the consequences of the realizabilty constraints on the jacobians \mathbb{J}_E and \mathbb{J}_F , since they appear to be the equivalent of the numerical fluxes in a finite element context.

Therefore, providing an asymptotic analysis on the proposed formulation represents a substantial work, and could serve as a mathematics PhD topic in itself, but the goal of this work was to propose a stabilized formulation for such systems of conservation laws, and it was demonstrated that our formulation is able to reproduce reference solutions on benchmarks problems.

Résumé français

Dans ce chapitre, on s'intéresse à la modélisation du rayonnement volumique. Pour ce faire, l'approche retenue consiste à utiliser des modèles aux moments, obtenus en moyennant l'équation du transfert radiatif sur l'espace des directions. On s'intéresse plus particulièrement au modèle dit M_1 , où la relation de fermeture est obtenue au travers d'un principe de maximum d'entropie. On décrit l'état de l'art sur les différents modèles aux moments, ainsi que les formulations existantes. Dans la mesure où la plupart des schémas pour ce modèle sont de type volumes finis HLL, on propose une formulation aux éléments finis pour ce système. Cette formulation, de type mixte, stabilisée par l'approche variationnelle multi-échelle, est détaillée au cours de ce chapitre. Elle est ensuite mise à l'épreuve et validée sur des problèmes illustratifs disponibles dans la littérature.

Chapter 6

Industrial Applications

This chapter is devoted to the numerical simulations of industrial applications rising from situations encountered by our industrial partners. The goal of this chapter is to demonstrate the ability of methods presented in the previous chapters to deal with "real" examples with a geometry and physical parameters representative of the reality. This study will show some specific problems that rise when dealing with such problems only, for the meshing as well for the solvers. When possible, the results will be compared with experimental results. The next section is related to the publication [42]:

6.1 Quenching of an hat shaped disk in various configurations

These problems are proposed by the industry to optimize the process of cooling for a particular shape. It consists in testing three different contexts and environments with ascending difficulty. We study first the free cooling of a solid in the air, then a forced convection using 12 jets inside an open cavity with supporting grid, and finally a natural convection inside a confined chamber with up to four different materials in contact. These problems highlight well the flexibility of the immersed methods, the necessity of applying anisotropic mesh adaptation and finally the inevitability of using full Eulerian stabilized solvers to handle abrupt changes in the temperature and in the material discontinuities across the interface. The geometry and the dimension of this disk are given in Figure 6.1. The material properties of the disk as well as the used physical parameter for the surrounding air are depicted in Table 6.1. Moreover, as shown in the consistency studies, setting the relative kinematic viscosity to a very high value in the solid region satisfies the zero velocity and hence the no-slip condition on the interface is also satisfied.

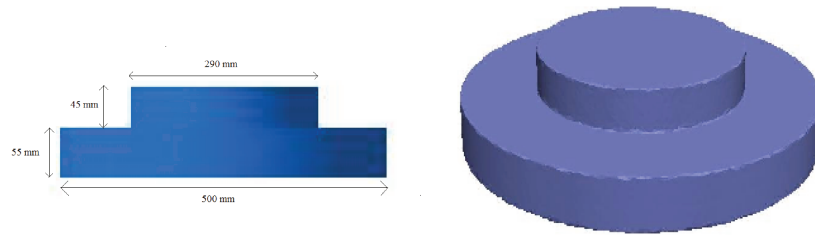


FIGURE 6.1: Geometry of the hat-shaped disk

TABLE 6.1: Properties of materials.

Properties	Air	Inconel 718
density ρ [kg/m ³]	1.25	7,800
heat capacity C_p [J/(kg K)]	1000	600
viscosity μ [kg/(m s)]	1.9e-5	–
conductivity λ [W/(m K)]	0.0262	37
emissivity ϵ	–	0.87

In the following, the features and the setups of the different experiments will be presented. The temperature measurements will be analyzed using sensors inserted in the disk at several critical positions. The results of the computations will be compared to experimental results. Note that at the beginning of all the tests, we consider the gas at rest at a temperature $T_{air,init} = 25C$. While the initial temperature of the disk is $T_{disk,init} = 1060C$. The emissivity of the walls is set to 0.9.

6.1.0.1 Cooling in open air

The first case consists of setting the disk in the open air and letting it cool down using a free natural convection. Here, the dominant mode of heat transfer will be the radiation and the free convection between the air at ambient temperature and the heated disk. The cooling process is simulated on a total time $T = 30 min$. All the computations were performed using 8 CPU. We place the disk at the center of an air-filled $2 \times 2 \times 1 m^3$ cavity and we use far-field boundary conditions. We apply the anisotropic mesh adaptation using the gradients of the levelset function. The mesh size ranges from 0.0005 to 0.1. Figures 6.2 and 6.3 present the obtained mesh along with the position of the sensors. It is clear that the geometry is very well captured which enables to deal accurately with the gradients across the interface.

This case is typically one case where radiation is the dominant mode of heat transfer: in fact, it was observed that, when radiation is neglected in our computations, the

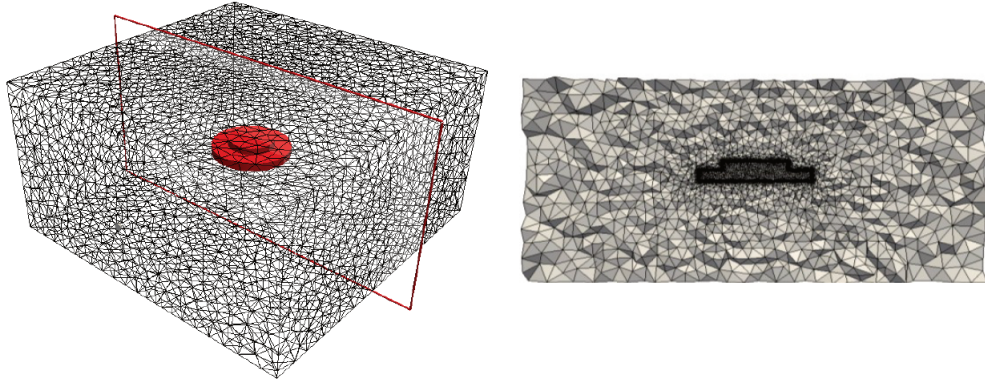


FIGURE 6.2: The obtained adapted mesh

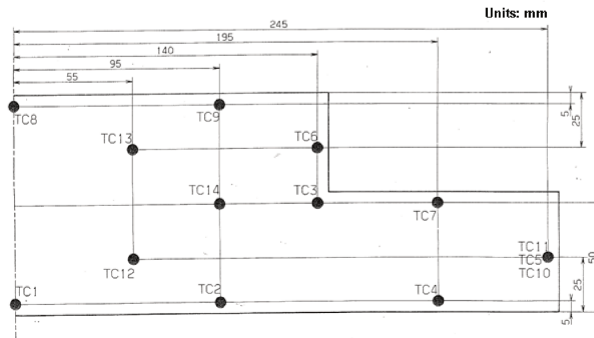


FIGURE 6.3: Position of the different sensors inside the disk

temperature of the disk only decreases by a few degrees, even after a long simulation time. Figure 6.4 to 6.9 show a very good agreement for the temperature evolution and the cooling speed compared to the experimental results. Note that to ease the presentation, we choose only three representative sensors. Furthermore, we generated two meshes using a fixed number of nodes equal to 100,000 and 200,000 respectively.

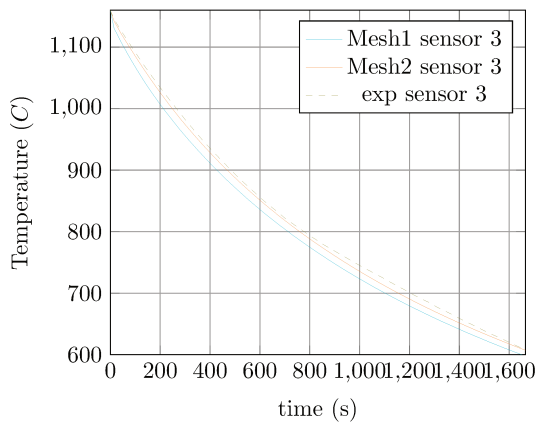


FIGURE 6.4: Comparisons of the temperature evolution in sensor 3

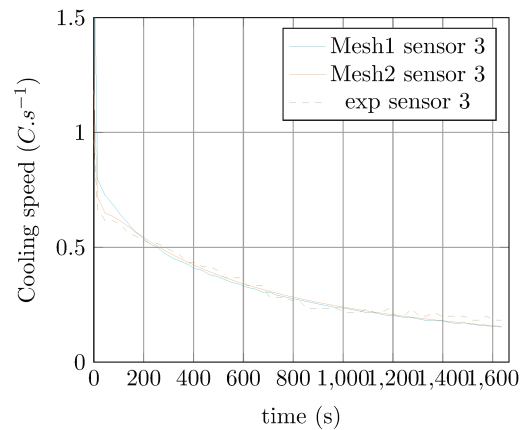


FIGURE 6.5: Comparisons of the cooling speed in sensor 3

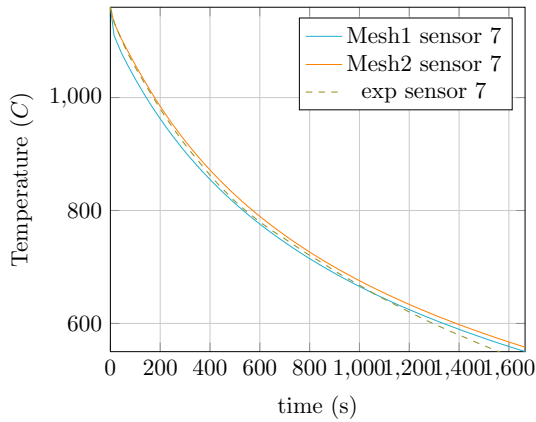


FIGURE 6.6: Comparisons of the temperature evolution in sensor 7

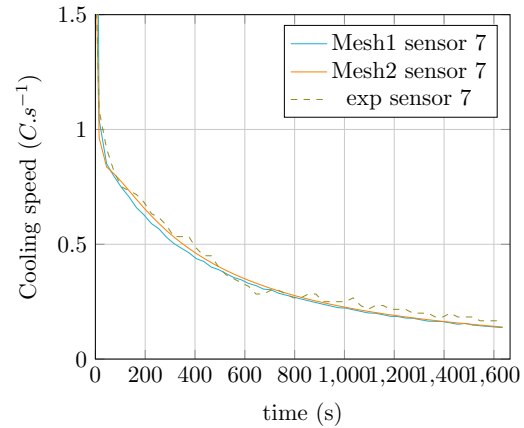


FIGURE 6.7: Comparisons of the cooling speed in sensor 7

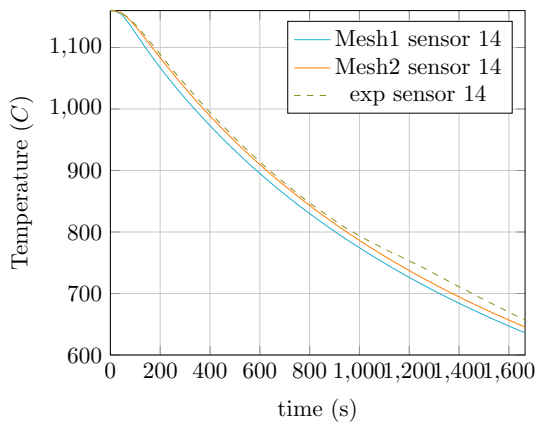


FIGURE 6.8: Comparisons of the temperature evolution in sensor 14

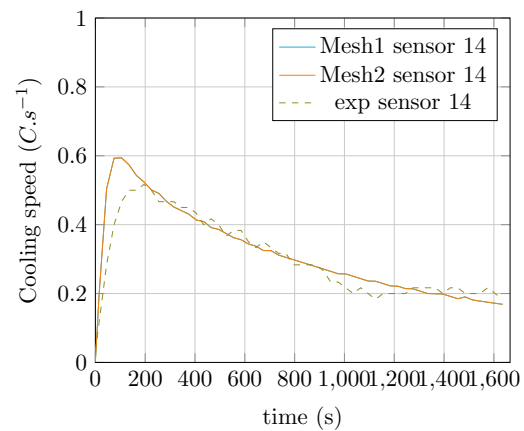


FIGURE 6.9: Comparisons of the cooling speed in sensor 14

6.1.0.2 Forced convection using air blast cooler

In this case, we place the disk on a grid inside an open chamber. It contains 12 jets with inflow condition of $\mathbf{v}_{in} = 25m.s^{-1}$ and $T_{in} = 20C$, blowing directly to the surface of the disk. The duration of the process is 15 min. Indeed, the dominant mode in this case is the convection and therefore, accurate resolution of Navier-Stokes is required. The case is very challenging in both the geometry representation (the very fine supporting grid, the heated disk, as well as the injectors), but also in the physical phenomena occurring close to the surface of the disk (turbulent gas-solid interactions).

Figure 6.10 gives a clear idea on the experimental setup and the position of the disk inside a $2.25 \times 2.25 \times 3m^3$ chamber while Figure 6.11 highlights the positions of the sensors.

We apply the anisotropic mesh adaptation taking into account at the same time the levelset of the fine supporting grid, the immersed disk as well as the injectors. The total

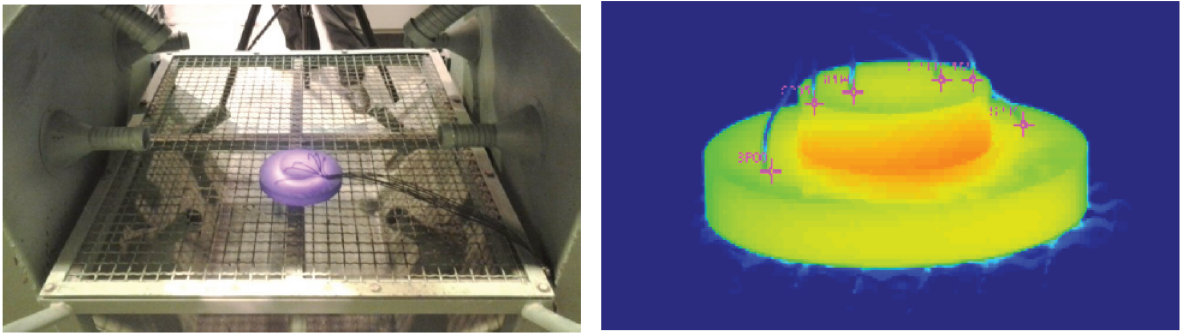


FIGURE 6.10: The experimental setup

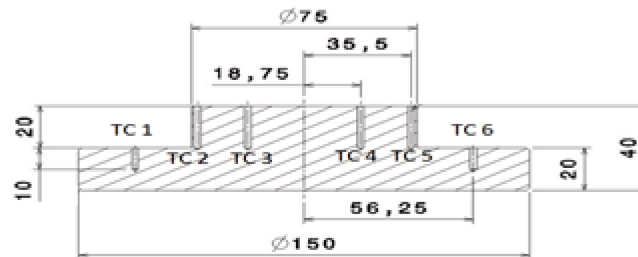


FIGURE 6.11: Position of the sensors

number of elements is 3,100,000 with a mesh size ranging from 0.0001 to 0.2. Figures 6.12 and 6.13 present the obtained adapted mesh. It reflects well the anisotropy of the elements caused by the discontinuity of the interface. Taking a closer look at the mesh near the interfaces, we can detect the good orientation of the elements with the stretching in the right direction. This demonstrates the ability of the algorithm to work under the constraint of a fixed number of nodes and to effectively control the elements sizes, orientations and locations.

The elements far from the immersed solid, the supporting grid and the injectors are mostly isotropic. Again, this reflects and explains why, for a controlled number of nodes, the mesh is naturally and automatically coarsened in that region with the goal of reducing the mesh size around the interfaces.

It is also worth mentioning that the design of the chamber is interesting (see Figure 6.12). It contains 12 injectors disposed all around the disk. We can distinguish three categories: the first ones are at the same level of the disk, the two others are above and below ensuring a homogenous air distribution.

As in the previous case, we plot the temperature and the cooling speed evolution from the 5 different sensors. Figure 6.14 to 6.23 shows a very good agreement of the solution compared to the experimental results. Again, this highlights the capability of the

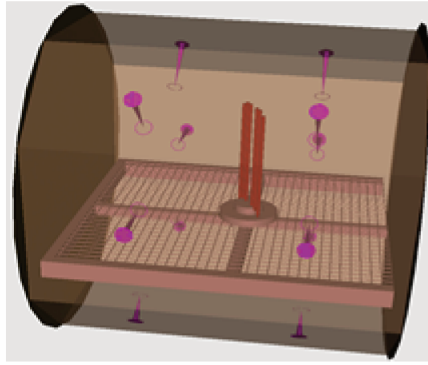


FIGURE 6.12: Position of the different injectors

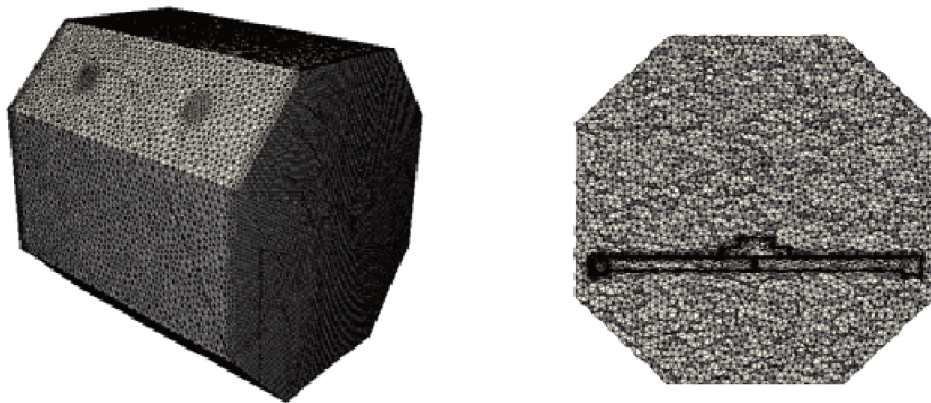


FIGURE 6.13: The obtained adapted mesh

approach to render accurate solutions for turbulent gas-solid interaction in a complex industrial configuration.

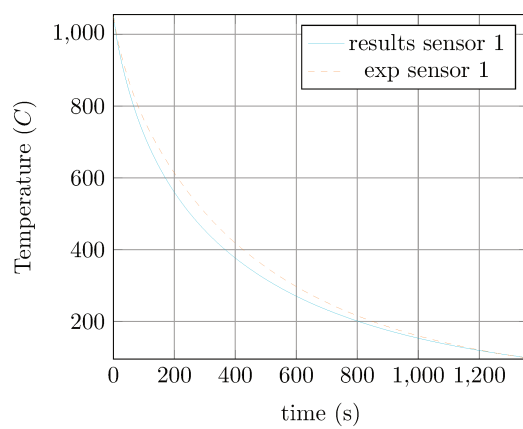


FIGURE 6.14: Comparisons of the temperature evolution in sensor 1

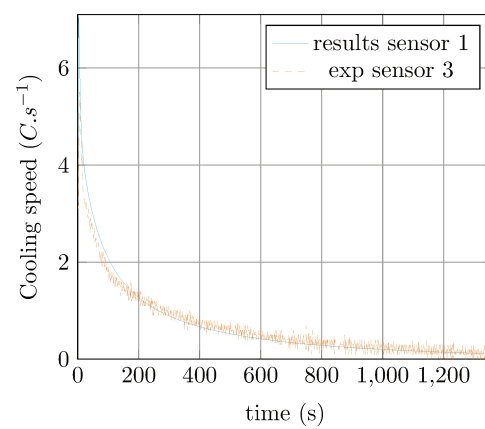


FIGURE 6.15: Comparisons of the cooling speed in sensor 1

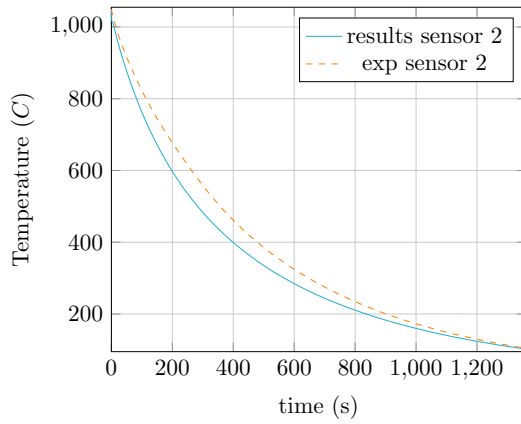


FIGURE 6.16: Comparisons of the temperature evolution in sensor 2

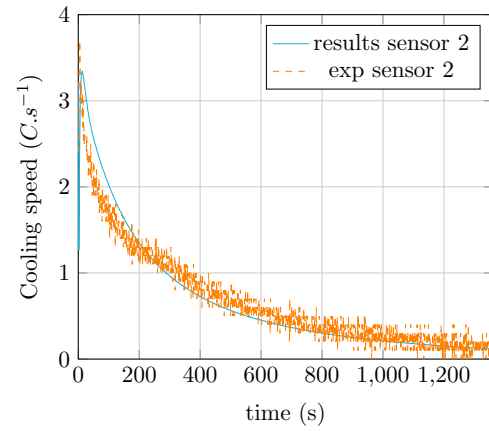


FIGURE 6.17: Comparisons of the cooling speed in sensor 2

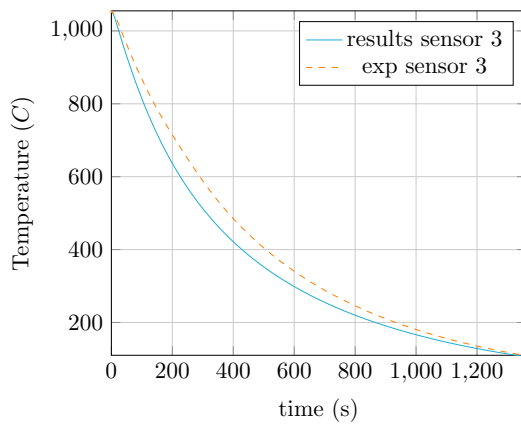


FIGURE 6.18: Comparisons of the temperature evolution in sensor 3

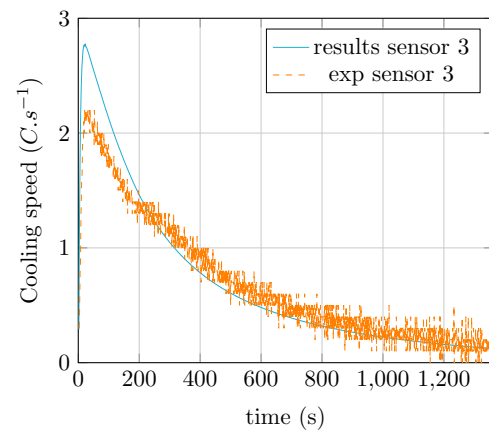


FIGURE 6.19: Comparisons of the cooling speed in sensor 3

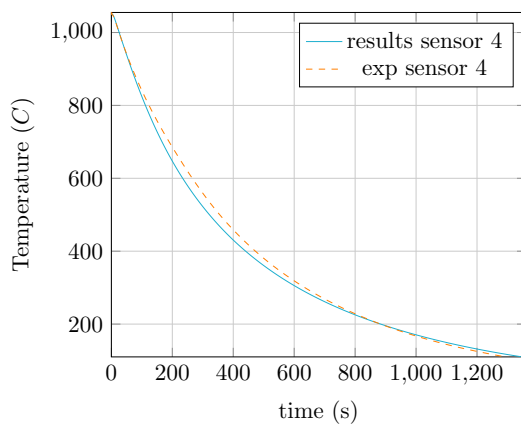


FIGURE 6.20: Comparisons of the temperature evolution in sensor 4

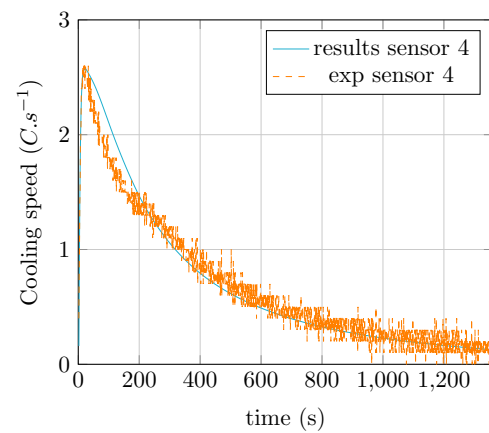


FIGURE 6.21: Comparisons of the cooling speed in sensor 4

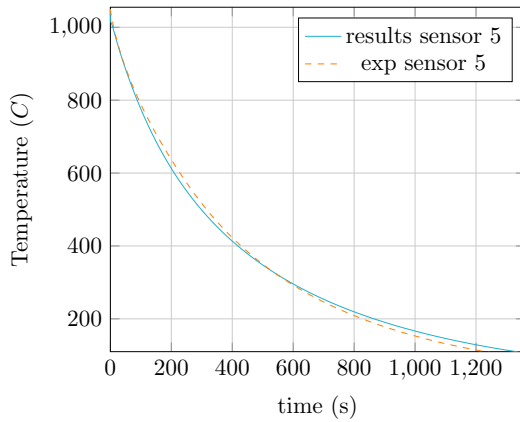


FIGURE 6.22: Comparisons of the temperature evolution in sensor 5

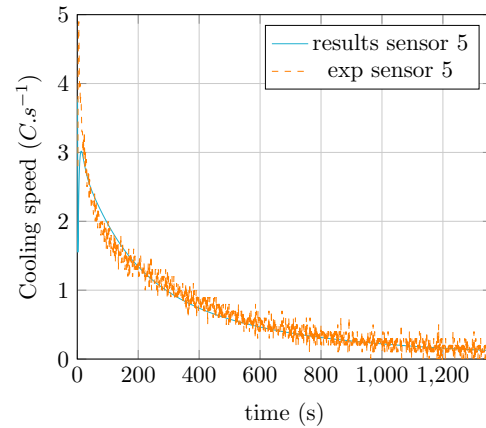


FIGURE 6.23: Comparisons of the cooling speed in sensor 5

6.1.0.3 Natural convection with multi-material

In this last case, we propose a natural convection inside a confined chamber of $1 \times 2 \times 3m^3$ with up to four different materials in contact. Note that due to the complexity of the geometry and the given material, the classical use of heat transfer coefficients may fail if no a priori experimental tests are executed and inverse analysis are applied. Figure 6.24 shows both the experimental and the numerical setup of the test case. We can clearly highlight the fidelity of this approach to reproduce the facility using the levelset of each material: the disk with three small supports (Titanium TA6V), the hexagonal supports (steel) as well as the different layers at the walls (refractory bricks).

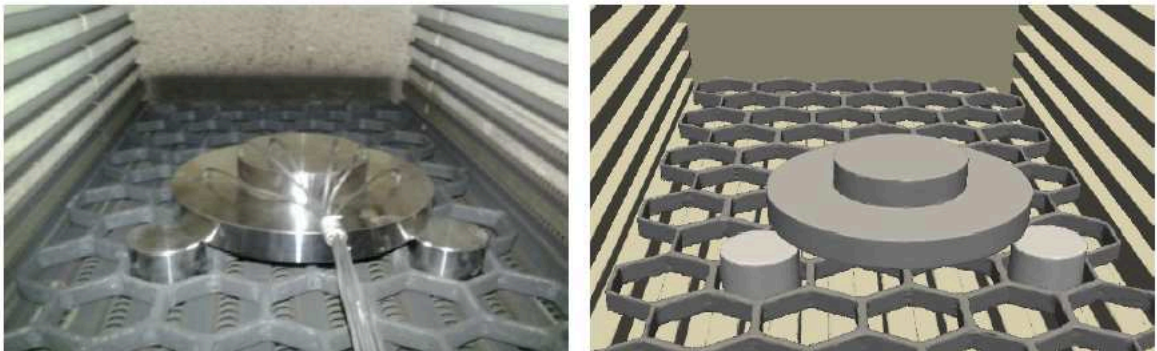


FIGURE 6.24: The immersed disk inside the chamber: experimental (left) and numerical (right)

Figure 6.25 presents two cuts in the plan reflecting again the flexibility of the anisotropic mesh adaptation to tackle different interfaces and to render a well adapted mesh. Taking again a closer look at the interfaces, we can detect the good orientation of the elements with the stretching in the gradient direction.

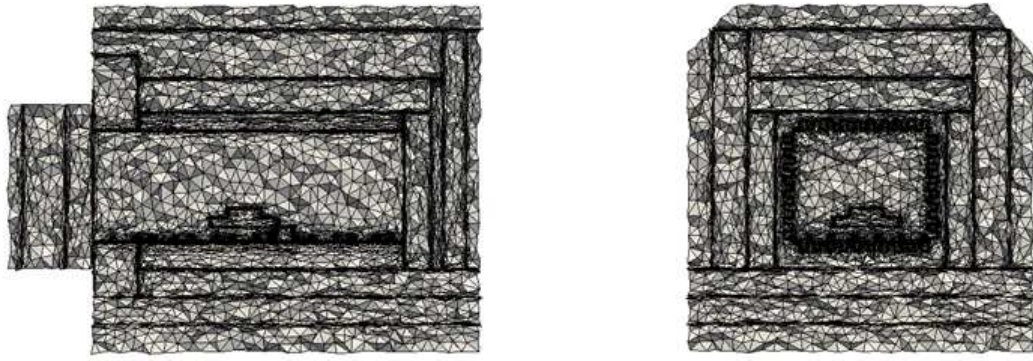


FIGURE 6.25: The adapted obtained mesh

Finally, Figure 6.26 shows the typical pattern of the streamline obtained due to the resolved natural convection inside the chamber. As in the previous case, results in Figure 6.27 to 6.36 are quantified in terms of temperature and cooling speed and compared to the experimental data showing very good agreement.

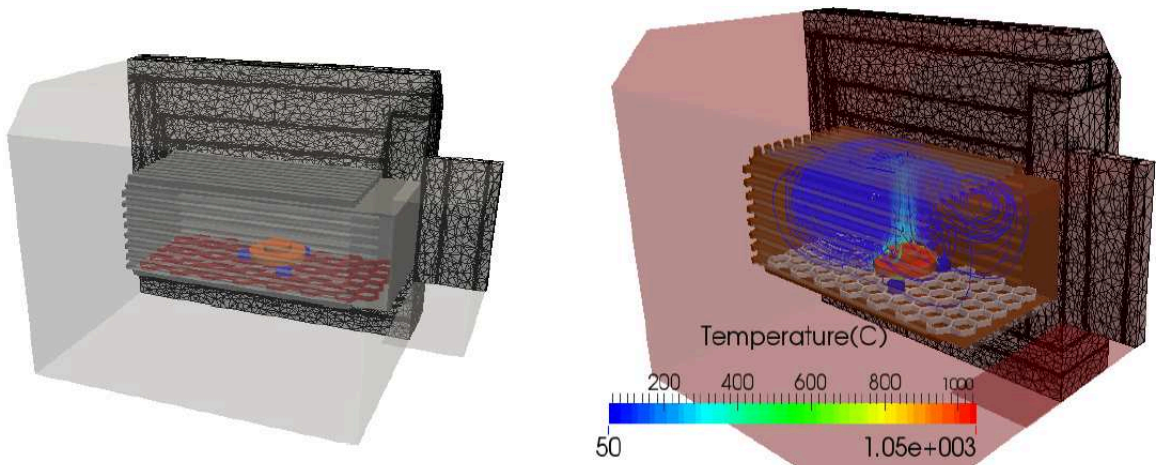


FIGURE 6.26: A snapshot of the streamline solution

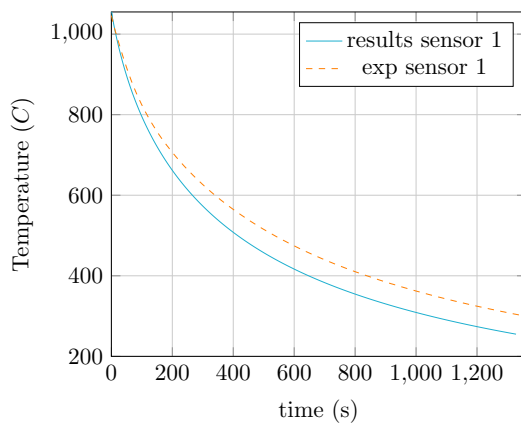


FIGURE 6.27: Comparisons of the temperature evolution in sensor 1

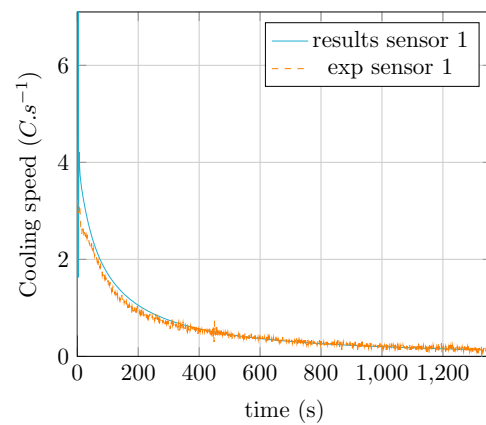


FIGURE 6.28: Comparisons of the cooling speed in sensor 1

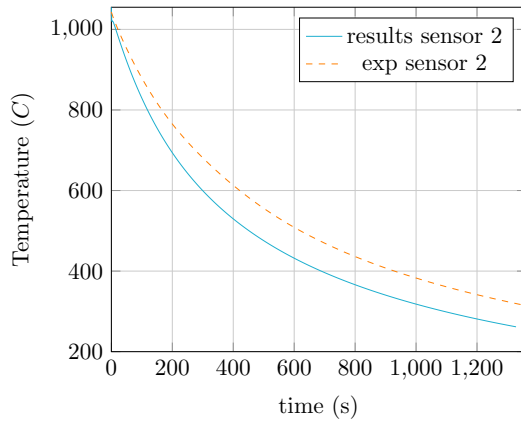


FIGURE 6.29: Comparisons of the temperature evolution in sensor 2

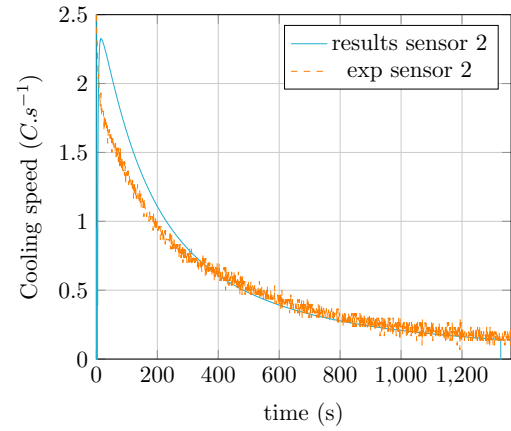


FIGURE 6.30: Comparisons of the cooling speed in sensor 2

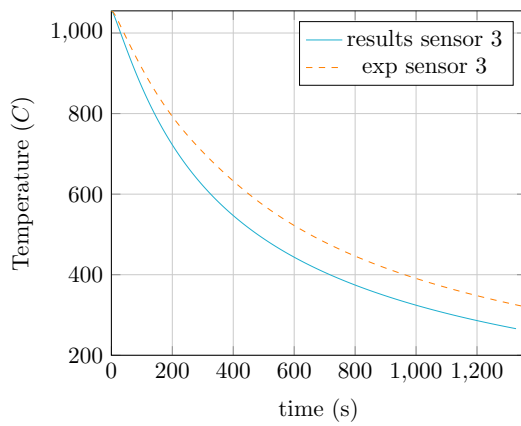


FIGURE 6.31: Comparisons of the temperature evolution in sensor 3

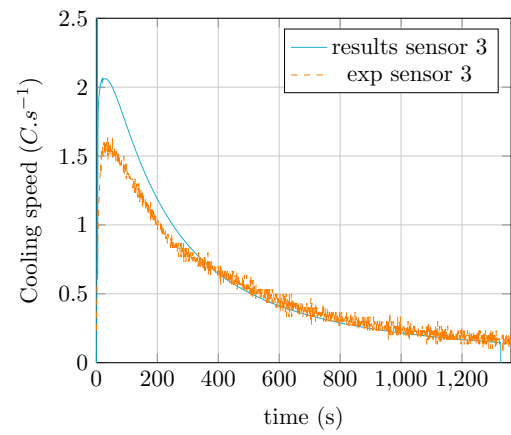


FIGURE 6.32: Comparisons of the cooling speed in sensor 3

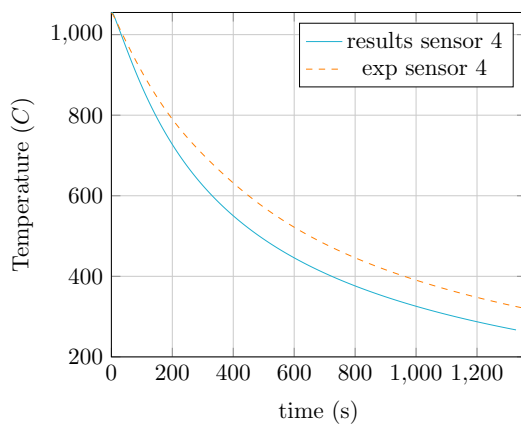


FIGURE 6.33: Comparisons of the temperature evolution in sensor 4

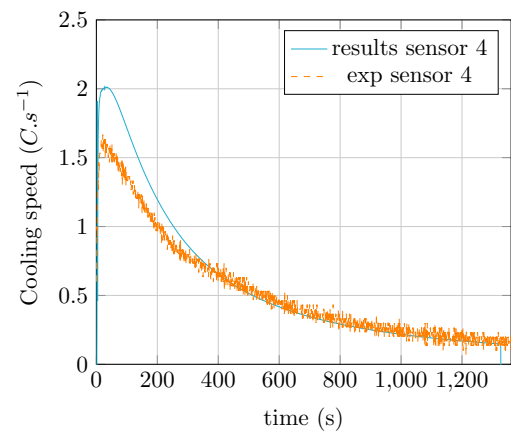


FIGURE 6.34: Comparisons of the cooling speed in sensor 4

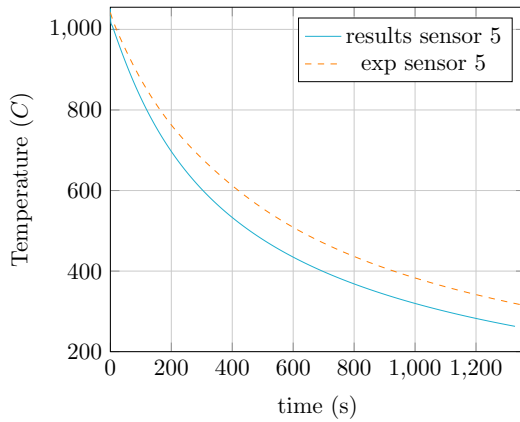


FIGURE 6.35: Comparisons of the temperature evolution in sensor 5

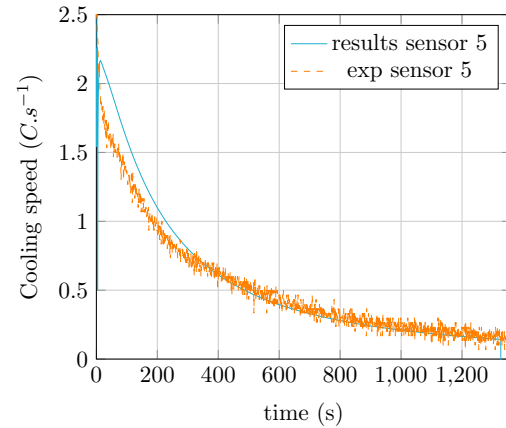


FIGURE 6.36: Comparisons of the cooling speed in sensor 5

6.1.1 Conclusions about the study

These three examples demonstrate the features of our immersed volume method, and assess its performances. The method can be interpreted as an unified Eulerian formulation for solving conjugate heat transfer problems. The corresponding stabilized finite element methods to compute the velocities, the pressure and the temperature were to work in unison with the multidomain framework, improving computational stability.

It was shown that the variational multiscale method allows an accurate simulation of high Reynolds number flows and that the streamline upwind method gives oscillation-free solution, even when used in a monolithic context. The three *3d* real industrial problems to demonstrate the ability of the method to handle problems arising from real industrial situations.

These test cases highlight the benefits of the immersed Eulerian method that can simultaneously model and solve for solutions in both the fluid and solid regions, as well as to compute the temperatures along the fluid-solid interface directly.

However, for radiation modelling, The P_1 model was used but is not adapted for those situations. There results were satisfactory here because of the relatively limited size of the enclosure and the fact that both device and ingots does not produce anisotropic effects. However, the next example that will be displayed will exhibit the limitations of the use of the P_1 model in a such context.

6.2 Quenching of two ingots in an enclosure

Another problem, proposed by one of our industrial partners, is similar the three last problem treated in the last part, with the difference that two ingots are present in the enclosure, so that some radiative exchange can be expected between the two pieces.

Furthermore, the two considered ingots are in fact composed of three smaller pieces in contact, with thermal contact neglected, so that different part of a piece are treated as a whole piece, that can exchange radiation with itself. These two ingots are lying on a sand layer, and the enclosure is delimited by an isolating material. The isolating material is actually composed of three layers of different materials, but a simplification assumption was made to consider an homogenized isolant, because on the one hand a full description of the three layers would require an important number of elements to capture interfaces, and on the other hand, since only conduction is occurring in the isolant, this approximation is not so rough. All physical properties will be considered temperature-dependent.

6.2.1 Mesh Generation

In this problem, several components are in contact (sand with ingots, sand with isolant), so that an appropriate treatment is to be performed to adapt the mesh on these interfaces. Two options are possible:

- The first option is to build a metric field for each component, and to compute the intersection of these different metrics, in the sense detailed in [4] and references therein.
- The other option is to perform multi-component adaptation, following the lines in [39]: instead of building a metric for each component, one can build a metric with contributions of all different component weighted by coefficients between 0 and 1.

In our implementation, it is more simple to make use of metric intersection with the hessian based metric, and to use the multi-component adaptation with the edge based metric. One can see here the three different cross sections of the mesh of the facility, obtained by the two different aforementioned methods.

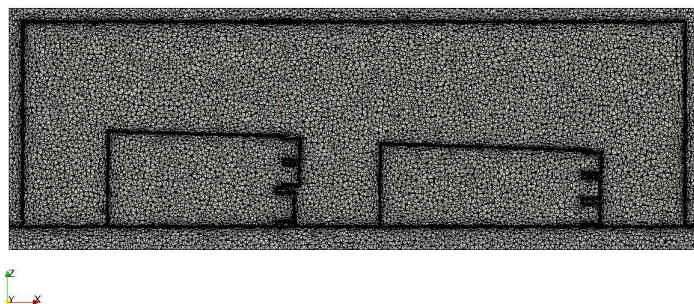
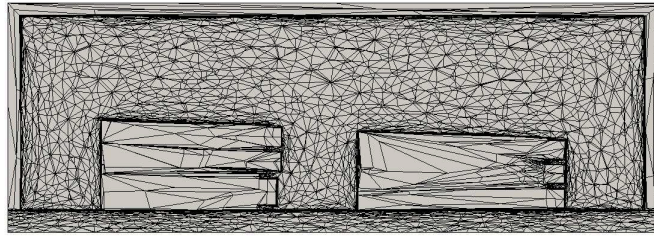
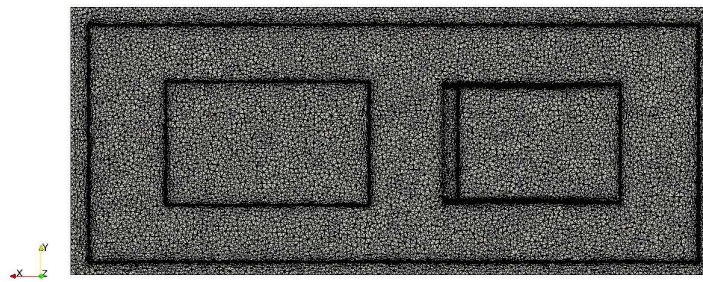
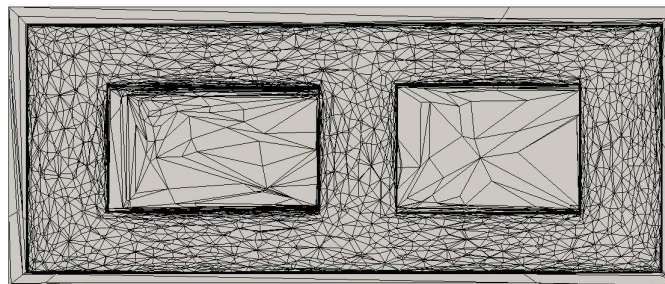
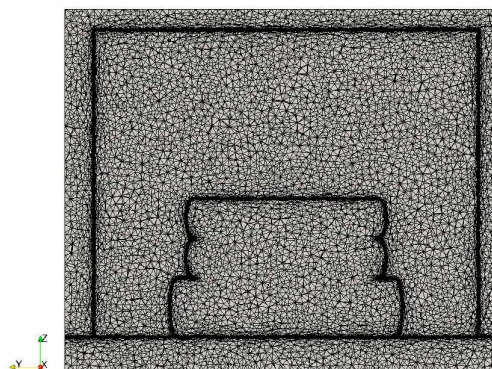


FIGURE 6.37: Cross section along the xz plane with hessian metric

Each approach have its own advantages and drawbacks: the implementation of the edge based metric allows to control the number of elements in each component, but a

FIGURE 6.38: Cross section along the xz plane with edge based metricFIGURE 6.39: Cross section along the xy plane with hessian metricFIGURE 6.40: Cross section along the xy plane with edge based metricFIGURE 6.41: Cross section along the yz plane with hessian metric

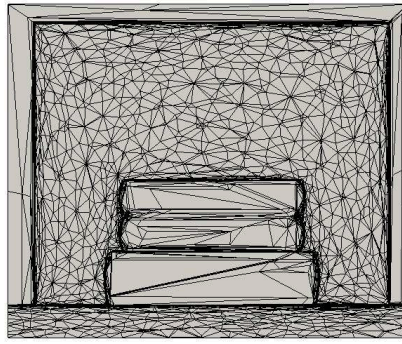


FIGURE 6.42: Cross section along the yz plane with edge based metric

satisfactory mesh can only be obtained after a tricky adjustment of weights and others computational parameters. The intersection approach naturally produce a more "homogeneous" repartition of elements far from the interfaces, but, in the hessian implementation, if the prescribed target number of elements is well respected for one single metric, it was observed that this property is not as well respected for metric intersection. Finally, the more appropriate choice of metric for a given problem remains, to the author's point of view, an open question.

6.2.2 First computations and simplifying assumptions

First, we performed simulations with modelling convection and conduction only. The pattern of the streamlines is displayed below, but this case was a first test, with a smaller temperature difference, just to verify the set up of the whole simulation.

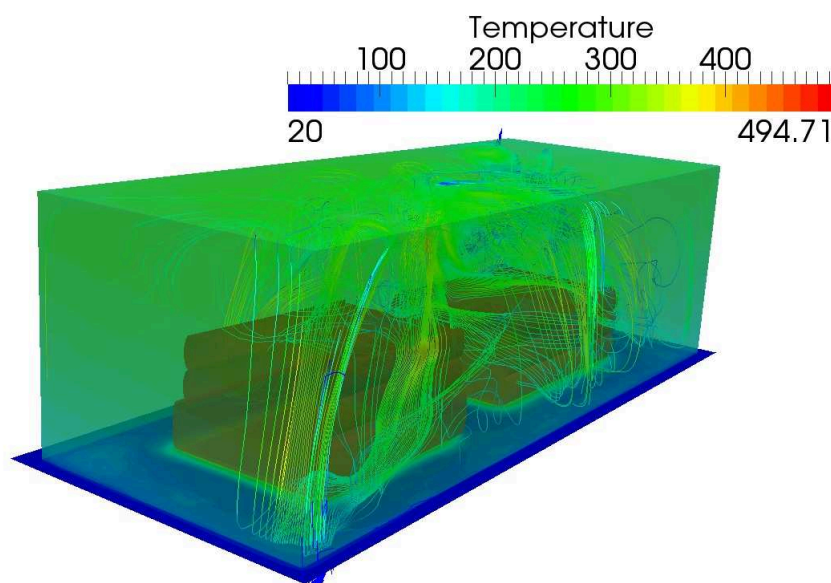


FIGURE 6.43: patterns of streamlines obtained for the facility

It was observed that, since a relatively fine meshe is required to represent the interface, the resolution of Navier-Stokes equations require a very important time and computational resources. To be consistent with the study performed in the last section, we started by performing a computation with the P_1 radiation model, with convection neglected. Here, one can see, the cross section of temperature in the xz at different time steps. Here, we took a time step $\Delta t = 2.5s$.

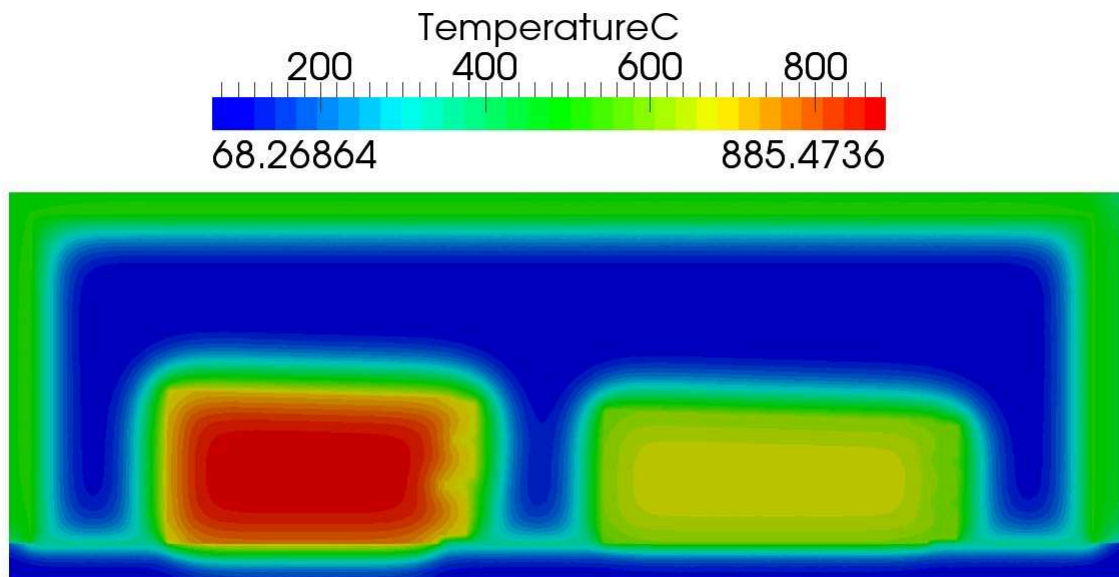


FIGURE 6.44: Conduction-radiation: temperature cross section at $t = 500s$

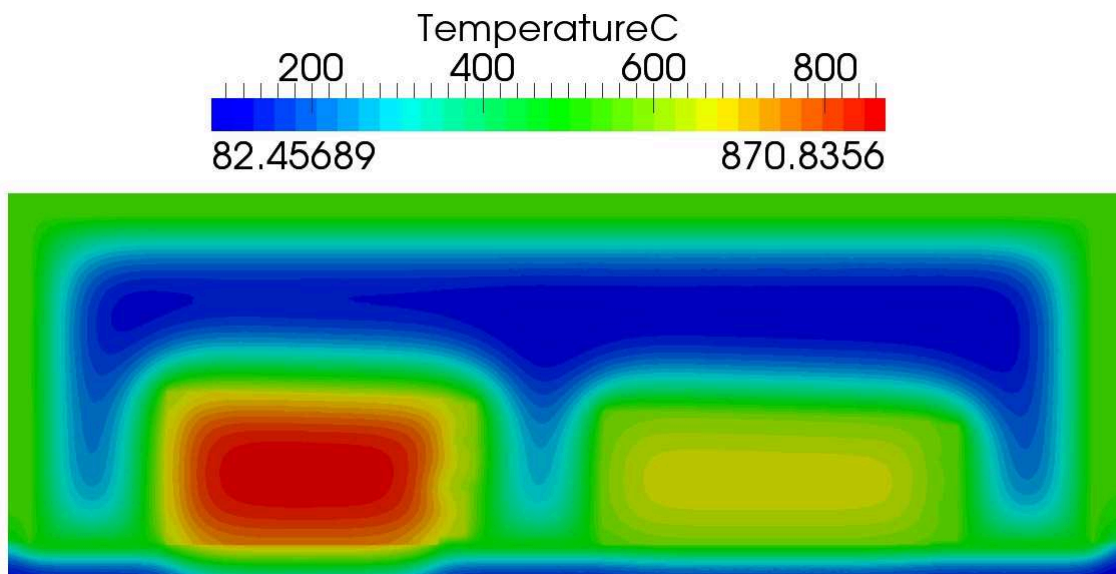
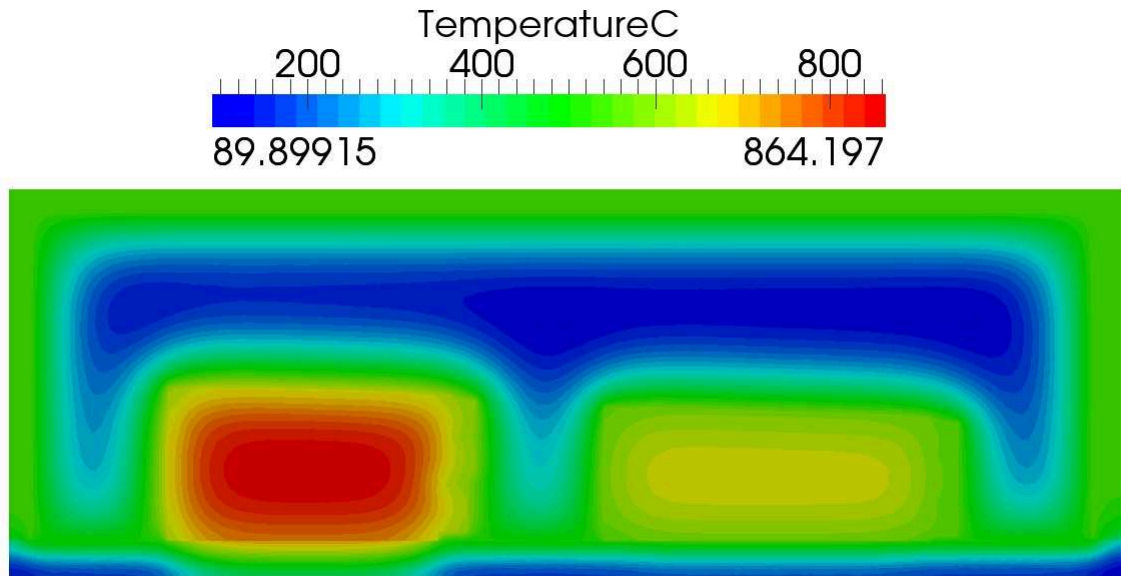
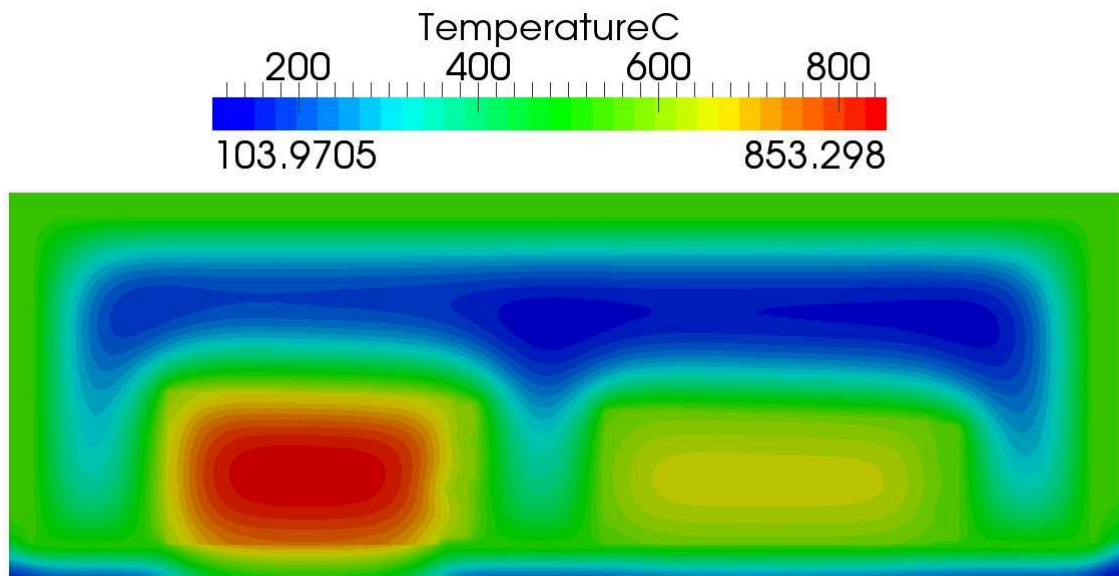


FIGURE 6.45: Conduction-radiation: temperature cross section at $t = 812.5s$

We also performed a computation with convection and P_1 radiation, of which a typical profile of streamlines and iso temperature are displayed below.

FIGURE 6.46: Conduction-radiation: temperature cross section at $t = 1312.5s$ FIGURE 6.47: Conduction-radiation: temperature cross section at $t = 2125s$

Conclusions

In this chapter, the methods developed were tested on some industrial problems. Some new problems, not present when dealing with benchmark problems, were encountered, like thermal shocks due to the large differences of temperature, the need of meshes composed of a large number of elements to properly capture the numerous interfaces, and, as a consequence, the computational resources, in terms of time and memory, to simulate such a facility. Regarding the *IS2IS* method, as explained, we are still working on the parallelization, and the computation using one single core is , in terms

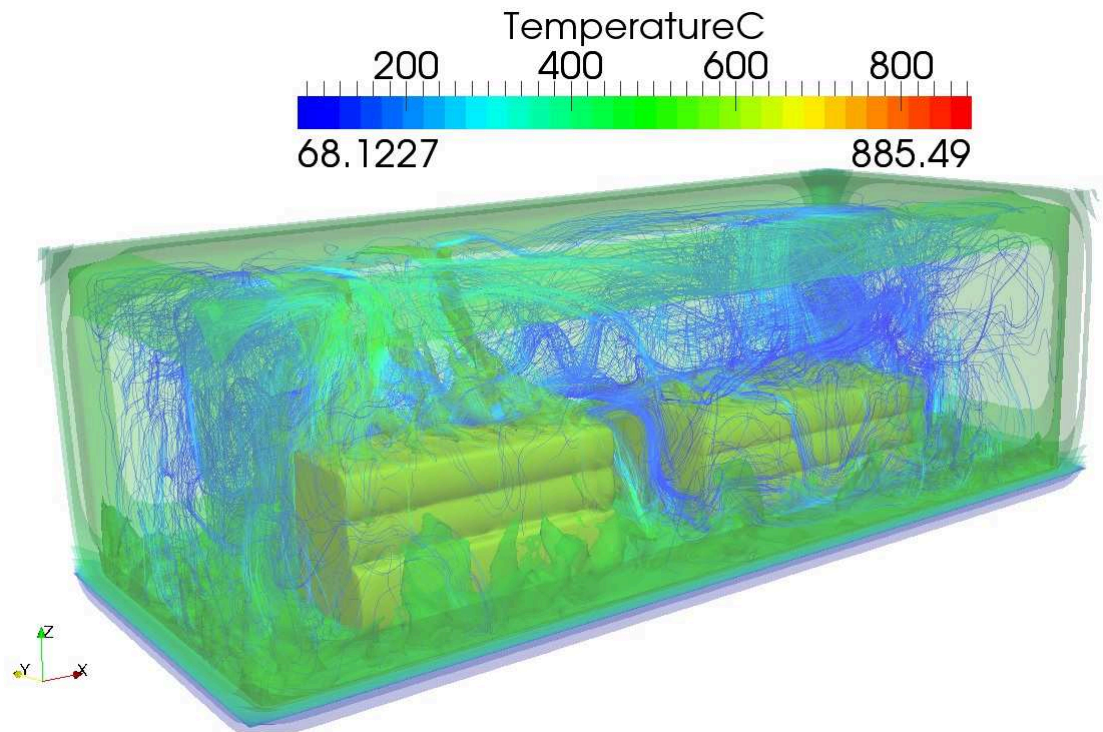


FIGURE 6.48: Conduction-radiation: pattern of streamlines and iso temperature surfaces

of computational time, prohibitive, but all the preparatory work for the set up of the simulation is ready, and we hope to be able to display results and perform a comparison with experimental results soon.

Résumé français

Dans ce chapitre, on s'est attaché à mettre en œuvre l'ensemble des outils présentés et développés dans cette thèse sur des problèmes fournis par nos partenaires industriels. On y a rencontré des problèmes non présents dans les cas des problèmes illustratifs des derniers chapitres, tels que les chocs thermiques liés aux écarts importants de température, la difficulté de capturer les nombreuses interfaces nécessitant des maillages relativement fins, impliquant des calculs longs et une importante mémoire CPU. Comme précisé dans le chapitre 4, nous travaillons actuellement sur une version parallèle de l'approche *IS2IS*, et son utilisation avec un seul cœur de calcul sur de tels maillages, est, du point de vue du temps de calcul, prohibitive. Toutefois, la préparation des simulations est, comme le démontre ce chapitre, finalisée, et nous avons bon espoir de pouvoir bientôt confronter les résultats obtenus aux données expérimentales.

Chapter 7

Conclusions and Outlook

7.1 Conclusions

The objective of this PhD was to improve, in a general manner, the modelling of thermal radiation. All the numerical developments will serve to improve the heat thermal software *Thost* and will be used by the industrial partners of this project. Based on an immersed volume method, the new developments must take into account such framework about how to deal with interfaces to represent complex geometries, how to deal with equations to ensure a direct fluid solid coupling, and how to ensure that these two *a priori* independent elements work in unison to achieve an accurate description of real systems that we intend to model. In this thesis, we took the time, in chapter 2 and chapter 3, to test these methods on some illustrative benchmarks and to prove the consistency of the approach. Regarding the main contributions of these thesis, described in chapters 4 and 5, the following comments can be made:

- The *IS2IS* approach, depicted in chapter 4, is, from the author's point of view, more interesting with regard to the interface reconstruction than the surface radiation. Indeed, regarding the surface radiation physics, we tried to gather all the advantages of existing approaches, but no major novelty about any one of these points was discovered. The innovative part of the approach lies in the way the interface is reconstructed in a topologic manner, that is to say, the only information required is the global node numbering. We think that this approach is an open door to an enhanced treatment of interface phenomena using immersed methods, when some quantities have to be localized on interfaces like surface tension, phase change, or, in solid mechanics with contact forces. Another approach for interface localization, based on regularized Dirac functions, was explored in [182], showing

that there are many alternatives to deal with implicit interfaces, despite of their implicit description, and we believe that this topic will draw the attention of engineers and researchers in the years to come. However, a drawback of this approach is the fact that it raises parallelization issues, even though all the functionalities have been validated. Future work will be dedicated to the optimization of the program for parallelization, "clustering" of faces to not compute useless viewfactors, and improvements about the visibility and the obstructions treatment.

- The stabilized formulation designed for the M_1 radiation model, described in chapter 5, is a contribution of a different kind: the idea to describe volume radiation effects by means of a fixed number of "classical" partial differential equations. Indeed it seems very interesting particularly in terms of computational time, when compared to other approaches available in literature. However, since most of available methods are based on a finite volume scheme, it remains therefore difficult to implement and to use within our data structures. Therefore, we proposed a novel finite element formulation suited for this system of equations. This groundbreaking and original formulation was very attractive, however we faced all along the developments numerous theoretical problems, for which, despite a relentless and meticulous investigation, we only found few answers in the published literature. Thanks to the VMS framework, we were able to reproduce the few benchmarks problems available in the references, but we then faced other problems, related to the fast radiation time scale, stabilization problems related to the importance of the source term or considerations about radiation in the monolithic framework, as much as outstanding question under investigation. But it should be recalled that after the pioneering work of Hugues and coworkers [30] about the stabilization techniques, it took almost 20 or 30 years for these concepts to be accepted by the community and to reach the maturity necessary to be used for industrial problems. Hence, this formulation is considered not as a "final product" but rather as a foundation stone for the future researchers interested in the VMS framework.

We would like to point out that, radiative effects represent a challenging problem inside industrial furnaces. Indeed, we count the wall refractions, radiations from the flame, auto-radiation between the treated solids. Therefore, all these effects cannot finally be treated by the proposed version of the M_1 model. We then limited ourselves to more classical models, for which we mobilized research effort to adapt such methods to our computational framework, which led us to design the *IS2IS* method. Hence, in this Phd work, a settlement between new fundamental research work and answering industrials needs must be considered and taken into account, in particular, for a three years program.

7.2 Outlook

The focus in this work is on a new concept for numerical methods to estimate the thermal radiation distributions at the same time in the furnace and within the workpieces under specified furnace geometry, thermal schedule, parts loading design, initial operation conditions, and performance requirements. Clearly, a number of other considerations have to be taken into account for more accurate predictions. Here is the list of several important steps towards enhanced simulation tools for more realistic problems. We can classify the possible improvements in three main categories: modelling issues, numerical issues and "experimental feedback" issues:

Modelling issues:

- Regarding combustion in burners: as stated in chapter 1, this phenomenon was neglected all along this work. Usually, some particular boundary conditions, in terms of velocity and temperature are obtained through empirical computations and measurements. This could be improved by considering a real combustion model, with the mixing of different species coupled by the chemistry. It would be useful for a better description of the volume radiation, since we know that the combustion products make the fluid inside the furnace become radiatively active.
- Regarding the boiling, as stated in chapter 1, a PhD [11] is actually ongoing in our laboratory: The preliminary results, about an implicit treatment of the surface tension, improvements concerning the convection of a levelset function for multiphase flow and numerical modelling of phase change, are promising, and a part of it is available in [182].
- The modelling of natural convection could be improved as well: until now, it was modelled under the Boussinesq approximation, so that the compressibility effects are only considered in the gravity terms. However, it is known that this approximation fails for large temperature differences. An improvement would be to consider a modified version of the Navier-Stokes equations with different mass conservation, supplemented by a state equation $\rho = \rho(p, T)$ as done in [282]. Note that an activity has started in our laboratory about these questions, as it can be seen in [27].

Numerical issues:

- For the duration of this work, we made of first order accurate scheme, in space as well in time. However, when industrial problems are treated, one often encounters

large temperature differences, so that solutions can exhibit nonphysical shocks. This would be cured by considering higher order formulations; if implementing P_2 or higher elements for the finite element formulations could result in an increase of computational time, implementing high order time marching scheme could be done easily, without a significant implementation effort, and appear as a promising lead for future work.

- The computational time to perform such simulations, remains, at a certain level, quite expensive: in fact, when the domain to model present different geometric details, the number of elements to properly capture all the interfaces can become important. For instance, on the last case presented in the previous chapter, simulating a few seconds of "real-time" takes a few hour of computations, which is prohibitive for an industrial user. To circumvent this issue, it could be interesting to resort to reduction model techniques, by constructing a reduced basis. To do so, for the type of equations (NS-CDR) considered in this work, two main alternatives are possible: an *a posteriori* approach, the proper orthogonal decomposition (POD) [283, 284], which relies on a first computation ("snapshot") to compute a reduced basis by means of a single value decomposition (SVD). This approach can be applied regardless of the considered physics, but the computed reduced basis is dependent on the snapshot. An *a priori* approach is also possible, based on the proper generalized decomposition (PGD) [285, 286], where the original problem is converted in a collection of $1d$ problems regarding each variable. This approach is promising, but theoretical properties can be proven only for simple elliptic problems. The model reduction will be investigated for the Thost consortium within the HECO project for moving ingots and meshes in [287].

Experimental feedback issues:

This category is different from the two previous in the sense that, there is no specific points on which we can improve, but it is more a global process that can be improved. As stated in chapter 1, the goal of implementing numerical methods for industrial applications is to compare the results with experimental data, to see where discrepancies remain, to validate the developed approach on the one hand, and to understand which phenomena are not well modelled on the other hand. It was covered in this PhD, but not as much as the author would have preferred. Actions have started from our industrial partners, by setting up quenching and heating chambers, not at an industrial scale, but more at a "laboratory" scale, which can be a valuable tool for researchers.

Résumé français

L'objectif de cette thèse était de proposer de nouveaux outils pour la modélisation du rayonnement thermique dans le contexte de la méthode d'immersion de volume sur laquelle est basé le logiciel Thost. Nous nous sommes attachés, dans la première partie de cette thèse, à décrire et tester les outils utilisés, tant pour la résolution numérique de problèmes physiques que pour les méthodes de description d'environnement complexes. Ensuite, les deux contributions principales de ce travail ont été décrites. Elles sont de natures différentes, l'une consistant en l'adaptation d'une méthode existant à notre contexte d'immersion, la nouveauté principale résidant dans la façon d'approximer l'interface, l'autre faisant appel à des notions avancées de la technologie des éléments finis stabilisés, appliqués à un modèle de rayonnement pour lequel il n'existait que des formulations aux volumes finis. Il subsiste toutefois un petit regret, celui de n'avoir pas pu passer beaucoup de temps à mettre les méthodes développées à l'épreuve "du feu" des simulations industrielles, dans la mesure où les développements ont démarré d'une feuille blanche. Toutefois, il y a eu le souci de laisser des outils pérennes, afin que les futurs chercheurs qui s'intéresseront à ces questions puissent faire progresser et améliorer les actions initiées par ce travail.

Appendix A

Parametrized Rayleigh and Prandtl numbers for natural convection

The purpose of this appendix is to describe how to set the physical parameters to obtain desired Prandtl and Rayleigh numbers for natural convection problems under the Boussinesq approximation. This approach is inspired by the one depicted in: Fluent v6.3 User's guide, September 2006.

It is assumed that the characteristic length of the cavity is $L = 1.0$. First, one has to fix the values of certain parameters, here $\eta = 1.0$, $c_p = 1.0$, $g = \|\mathbf{g}\|_2 = 1.0$, $\beta = 1.0$. Then, once the values of Ra and Pr are set, the density is computed as follows

$$\rho = \sqrt{\frac{Ra}{\Delta T Pr}} \quad (\text{A.1})$$

This value is used to compute the diffusivity $\alpha = \frac{\lambda}{\rho c_p}$

$$\alpha = \frac{\eta}{\rho Pr} \quad (\text{A.2})$$

Finally, we can deduce the value of the conductivity λ by

$$\lambda = \rho c_p \alpha \quad (\text{A.3})$$

The temperatures T_c and T_h remain as free parameters. Other sets of fixed parameters could be considered, but we kept this one since it gave satisfactory results. This way of

computing parameters will be used for all natural convection problem benchmarks, even though the obtained values are not representative of realistic simulations. The reader could use results as a comparison tool, since they are presented in terms of adimensional temperature.

Appendix B

Double line integral for the view Factor Calculation: 8 points quadrature rule

In the method we chose to compute the view factor, one has to deal with integrals of type:

$$I_1 = \int_{g_k^i} \int_{g_l^j} \ln(\delta_{k,l}) g_k^i g_l^j dg_k^i dg_l^j \quad (\text{B.1})$$

Using basic geometric arguments, the integrand $\ln(\delta_{k,l})$ can be expressed as an homogeneous second order polynomial of two variables of which the coefficients are related to the geometric characteristics of the two edges of the considered segment. Moreover, with help of an appropriate change of variables, both line integrals can be performed on $[0; 1]$. Finally, one has to deal with integrals of type:

$$I_2 = \int_0^1 \int_0^1 \ln(P(x, y)) dx dy \quad (\text{B.2})$$

$$\text{with } P(x, y) = \alpha_1 x^2 + \alpha_2 y^2 + \alpha_{12} xy + \beta_1 x + \beta_2 y + \gamma \quad (\text{B.3})$$

Such integral cannot be computed analytically in the general case, so one has to resort to numerical integration. To this end, we use a Gauss integration, but such quadrature are known to be exact only for polynoms (the order being related to the order of integration). It was observed that a 5 points quadrature rule is not exact for that kind

of function, so we made use of an 8 points quadrature rule, recalled in the table below since it is hard to find in literature. We use the notations

$$\int_{-1}^1 \int_{-1}^1 f(x, y) dx dy = \sum_{i=1}^8 \omega_i \omega_j f(x_i, x_j) \quad (\text{B.4})$$

i	ω_i	x_i
1	0.1012285362	-0.9602898564
2	0.2223810344	-0.7966664774
3	0.3137066458	-0.5255324099
4	0.3626837833	-0.1834346424
5	0.3626837833	0.1834346424
6	0.3137066458	0.5255324099
7	0.2223810344	0.7966664774
8	0.1012285362	0.9602898564

TABLE B.1: Weights and abscissas for the considered quadrature

This formula was verified on the following function $Q(x, y) = (x - y + 3)^2$, where the integral can be computed analytically

$$\int_0^1 \int_0^1 \ln(Q(x, y)) dx dy = 16\ln(4) - 18\ln(3) + 4\ln(2) - 3 \simeq 2.178277 \quad (\text{B.5})$$

Appendix C

Detailed calculations for the SFEM formulation

C.1 Calculation of the Jacobians

Let δ_{ij} be the Kronecker delta associated to indexes i and j . Let also $\{\mathbf{e}_i\}_{1 \leq i \leq d}$ be the canonical basis of \mathbb{R}^d . A third order tensor is denoted by $\underline{\mathbb{X}}$, and its component are written as $(X^{ijk})_{1 \leq i,j,k \leq d}$.

Let us recall the definitions

$$\mathbb{P}_r = \underbrace{\left(\frac{1-\chi}{2} \mathbb{I}_d + \frac{3\chi-1}{2} \frac{\mathbf{f} \otimes \mathbf{f}}{f^2} \right)}_{=\mathbb{D}(\mathbf{f})} E_r \quad (\text{C.1})$$

$$\chi(f) = \frac{3+4f^2}{5+2\sqrt{4-3f^2}} \quad (\text{C.2})$$

The Jacobian matrixes of \mathbb{P}_r are defined by

$$\underline{\mathbb{J}}_E = (\underline{\mathbb{J}}_E^{ij})_{1 \leq i,j \leq d} = \left(\frac{\partial \mathbb{P}_r^{ij}}{\partial E_r} \right)_{1 \leq i,j \leq d} = \frac{\partial \mathbb{P}_r}{\partial E_r} \quad (\text{C.3})$$

$$\underline{\mathbb{J}}_F = (\underline{\mathbb{J}}_F^{ijk})_{1 \leq i,j,k \leq d} = \left(\frac{\partial \mathbb{P}_r^{ij}}{\partial F_r^k} \right)_{1 \leq i,j,k \leq d} = \frac{\partial \mathbb{P}_r}{\partial \mathbf{F}_r} \quad (\text{C.4})$$

Using (C.1), one can write

$$\underline{\mathbb{J}}_E = \mathbb{D} + E_r \frac{\partial \mathbb{D}}{\partial E_r} \quad (\text{C.5})$$

$$\underline{\mathbb{J}}_F = E_r \frac{\partial \mathbb{D}}{\partial \mathbf{F}_r} \quad (\text{C.6})$$

At this step, one can see that the tedious part of the calculation consists in differentiating $\chi(f)$ with respect to E_r and \mathbf{F}_r . We detail this calculation as follows.

We know that

$$\chi(f) = \chi\left(\left\|\frac{\mathbf{F}_r}{cE_r}\right\|_2\right) \Rightarrow \begin{cases} \frac{\partial\chi}{\partial E_r} = \frac{\partial f}{\partial E_r} \frac{d\chi}{df} = -\frac{f}{E_r} \frac{d\chi}{df} \\ \frac{\partial\chi}{\partial F_r^k} = \frac{\partial f}{\partial F_r^k} \frac{d\chi}{df} = \frac{F_r^k}{cE_r\|\mathbf{F}_r\|} \frac{d\chi}{df} \end{cases} \quad (\text{C.7})$$

Moreover, one can easily show that

$$\frac{d\chi}{df} = \frac{2f}{\sqrt{4-3f^2}} \quad (\text{C.8})$$

Finally, we have

$$\begin{cases} \frac{\partial\chi}{\partial E_r} = -\frac{2f^2}{E_r\sqrt{4-3f^2}} \\ \frac{\partial\chi}{\partial F_r^k} = \frac{F_r^k}{cE_r\|\mathbf{F}_r\|} \frac{f}{\sqrt{4-3f^2}} \end{cases} \quad (\text{C.9})$$

Knowing this, the calculation of \mathbb{J}_E is straightforward:

$$\frac{\partial\mathbb{D}}{\partial E_r} = \frac{1}{2} \frac{\partial\chi}{\partial E_r} \left(3 \frac{\mathbf{F}_r \otimes \mathbf{F}_r}{\|\mathbf{F}_r\|^2} - \mathbb{I}_d\right) \quad (\text{C.10})$$

Then we have

$$\boxed{\mathbb{J}_E = \mathbb{D} - \frac{f^2}{\sqrt{4-3f^2}} \left(3 \frac{\mathbf{F}_r \otimes \mathbf{F}_r}{\|\mathbf{F}_r\|^2} - \mathbb{I}_d\right)} \quad (\text{C.11})$$

We now turn to $\frac{\partial\mathbb{D}}{\partial F_r^k}$. We choose to make the differentiation component-wise. We can write

$$\mathbb{P}_r^{ij} = \frac{1-\chi}{2} \delta_{ij} + \frac{3\chi-1}{2} \frac{F_r^i F_r^j}{\|\mathbf{F}_r\|^2} \quad (\text{C.12})$$

We now have

$$\begin{aligned} \frac{\partial\mathbb{P}_r^{ij}}{\partial F_r^k} &= \frac{1}{2} \frac{\partial\chi}{\partial F_r^k} \left(3 \frac{F_r^i F_r^j}{\|\mathbf{F}_r\|^2} - \delta_{ij}\right) + \frac{3\chi-1}{2} \left(\frac{\delta_{ik} F_r^j}{\|\mathbf{F}_r\|^2} + \frac{\delta_{kj} F_r^i}{\|\mathbf{F}_r\|^2} - \frac{2F_r^i F_r^j F_r^k}{\|\mathbf{F}_r\|^4}\right) \\ \frac{\partial\mathbb{P}_r^{ij}}{\partial F_r^k} &= \frac{f}{2cE_r\sqrt{4-3f^2}} \left(3 \frac{F_r^i F_r^j F_r^k}{\|\mathbf{F}_r\|^3} - \frac{\delta_{ij} F_r^k}{\|\mathbf{F}_r\|}\right) + \frac{3\chi-1}{2} \left(\frac{\delta_{ik} F_r^j}{\|\mathbf{F}_r\|^2} + \frac{\delta_{kj} F_r^i}{\|\mathbf{F}_r\|^2} - \frac{2F_r^i F_r^j F_r^k}{\|\mathbf{F}_r\|^4}\right) \end{aligned}$$

Re-arranging terms, we finally get

$$J_F^{ijk} = \left(\frac{3f}{2cE_r\sqrt{4-3f^2}} - \frac{3\chi-1}{\|\mathbf{F}_r\|} \right) \frac{F_r^i F_r^j F_r^k}{\|\mathbf{F}_r\|^3} + \frac{3\chi-1}{2} \left(\frac{F_r^j \delta_{ik}}{\|\mathbf{F}_r\|^2} + \frac{F_r^i \delta_{jk}}{\|\mathbf{F}_r\|^2} \right) - \frac{f}{2cE_r\sqrt{4-3f^2}} \frac{F_r^k \delta_{ij}}{\|\mathbf{F}_r\|} \quad (\text{C.13})$$

C.2 Calculation of spectral radii

The expressions of the stabilization parameters τ_F and τ_E involve the spectral radii of \mathbb{J}_E and \mathbb{J}_F^k , the second order tensor of components J_F^{ijk} for a fixed k . So we need to get an expression, or at least an approximation to these spectral radii. For \mathbb{J}_E , since we know that

$$\rho(\mathbb{D}) = \max \left(\chi, \frac{1-\chi}{2} \right)$$

it is necessary to calculate the spectral radius of

$$\mathbb{B} = 3 \frac{\mathbf{F}_r \otimes \mathbf{F}_r}{\|\mathbf{F}_r\|^2} - \mathbb{I}_d$$

Since $\mathbf{F}_r \otimes \mathbf{F}_r$ is a rank-one matrix and the trace of $\mathbf{F}_r \otimes \mathbf{F}_r$ is $\|\mathbf{F}_r\|^2$, we have

$$\rho \left(\frac{\mathbf{F}_r \otimes \mathbf{F}_r}{\|\mathbf{F}_r\|^2} \right) = 1 \Rightarrow \rho(\mathbb{B}) = 2$$

From this we obtain

$$\rho(\mathbb{J}_E) = \rho(\mathbb{D}) + \frac{2f^2}{\sqrt{4-3f^2}} \quad (\text{C.14})$$

Using similar arguments about rank-one matrixes, one can obtain

$$\rho(\mathbb{J}_F^k) = \frac{4\alpha|F_r^k|}{\|\mathbf{F}_r\|} \quad (\text{C.15})$$

$$\sum_{k=1}^d \rho(\mathbb{J}_F^k) = \frac{4\alpha\|\mathbf{F}_r\|_1}{\|\mathbf{F}_r\|_2} \quad (\text{C.16})$$

with

$$\alpha = \frac{f}{2cE_r\sqrt{4-3f^2}}$$

C.3 Algorithm for the proposed formulation

At this point, for the sake of clarity, we will make the difference with "time" right hand sides (coming from discretization of terms $\frac{\delta \mathbf{F}_{r,h}^{i+1}}{\delta t}$ and $\frac{\delta E_{r,h}^{i+1}}{\delta t}$) and " non linear" right hand sides . The superscripts are n and i , respectively. An algorithm for this formulation can be found in the table below:

Given (\mathbf{F}_r^n, E_r^n) ;

at the first non-linear iteration ($i = 0$) ,set $\mathbf{F}_r^0 = \mathbf{F}_r^n$ and $E_r^0 = E_r^n$;

compute the local "time" right hand sides ;

assemble a global "time" right hand side ;

while ($\|E_r^{i+1} - E_r^i\| \leq \varepsilon_E$ AND $\|\mathbf{F}_r^{i+1} - \mathbf{F}_r^i\| \leq \varepsilon_F$) **do**

 compute \mathbf{f}^i ;

 compute $\chi(\mathbf{f}^i)$;

 compute $\mathbb{D}(\mathbf{f}^i)$;

 compute $\mathbb{P}_r^i, \mathbb{J}_E^i$ and \mathbb{J}_F^i ;

 compute elementar matrix and "non linear" right hand side ;

 assemble a global matrix and a global "non linear" right hand side ;

 compute the global "total" right-hand side (with "time" and "non linear" contributions) ;

 solve the system $\rightarrow (\mathbf{F}_r^{i+1}, E_r^{i+1})$;

 update \mathbf{F}_r and E_r ;

end

at last non linear iteration i_{end} , $\mathbf{F}_r^{n+1} = \mathbf{F}_r^{i_{end}}$ and $E_r^{n+1} = E_r^{i_{end}}$;

Algorithm 2: algorithm for M_1 finite element method described above

C.4 Final Stabilized formulation

This section details all the stabilization terms appearing in the present formulation, for whoever may be interested to implement this formulation, even though the reader is invited to re-derive the formulation himself. For sake of clarity, let us write our problem in the following way, also valid for the previous formulation

$$\begin{cases} a_{FF}(\mathbf{F}_{r,h}, \mathbf{w}_h) + a_{FE}(E_{r,h}, \mathbf{w}_h) = s_F(\mathbf{w}_h) \\ a_{EF}(\mathbf{F}_{r,h}, q_h) + a_{EE}(E_{r,h}, q_h) = s_E(q_h) \end{cases} \quad (\text{C.17})$$

each of the bilinear linear forms written above can be cast in the form:

$$x_{y,stab} = x_{y,\text{Galerkin}} + x_{y,\text{F-Stab}} + x_{y,\text{E-Stab}} \quad (\text{C.18})$$

$$x \in [a; s] \quad (\text{C.19})$$

$$y \in [FF; FE; EF; EE] \quad (\text{C.20})$$

The Galerkin terms have already been calculated in a previous section, so we will not repeat it here. We separate contributions to the different terms coming from enrichment on \mathbf{F}_r and E_r .

- FF terms

$$a_{FF,F-stab}(\mathbf{F}_{r,h}, \mathbf{w}_h) = -\tau_F \left\langle \left(\frac{1}{c\Delta t} + (\kappa + \sigma) \right) (\kappa + \sigma) \mathbf{F}_{r,h}, \mathbf{w}_h \right\rangle + \tau_F \left\langle \left(\frac{1}{c\Delta t} + (\kappa + \sigma) \right) \underline{\mathbb{J}}_F \mathbf{F}_{r,h}, \nabla \mathbf{w}_h \right\rangle \quad (\text{C.21})$$

$$-\tau_F \left\langle (\kappa + \sigma) \sum_{i=1}^d \underline{\mathbb{J}}_F^i \nabla F_{r,h}^i, \mathbf{w}_h \right\rangle + \tau_F \left\langle \underline{\mathbb{J}}_F \left(\sum_{i=1}^d \underline{\mathbb{J}}_F^i \nabla F_{r,h}^i \right), \nabla \mathbf{w}_h \right\rangle \quad (\text{C.22})$$

$$a_{FF,E-stab}(\mathbf{F}_{r,h}, \mathbf{w}_h) = \tau_E \langle \underline{\mathbb{J}}_E \nabla \cdot \mathbf{F}_{r,h}, \nabla \mathbf{w}_h \rangle \quad (\text{C.23})$$

- FE terms

$$a_{FE,F-stab}(E_{r,h}, \mathbf{w}_h) = -\tau_F \langle (\kappa + \sigma) \underline{\mathbb{J}}_E \nabla E_{r,h}, \mathbf{w}_h \rangle + \tau_F \langle \underline{\mathbb{J}}_F (\underline{\mathbb{J}}_E \nabla E_{r,h}), \nabla \mathbf{w}_h \rangle \quad (\text{C.24})$$

$$a_{FE,E-stab}(E_{r,h}, \mathbf{w}_h) = \tau_E \left\langle \left(\frac{1}{c\Delta t} + \kappa \right) \underline{\mathbb{J}}_E E_{r,h}, \nabla \mathbf{w}_h \right\rangle \quad (\text{C.25})$$

- F right-hand-side terms

$$s_{F,F-stab}(\mathbf{w}_h) = -\tau_F \left\langle \frac{(\kappa + \sigma)}{c\Delta t} \mathbf{F}_{r,h}^n, \mathbf{w}_h \right\rangle + \tau_F \left\langle \frac{1}{c\Delta t} \mathbb{J}_F \mathbf{F}_{r,h}^n, \nabla \mathbf{w}_h \right\rangle \quad (\text{C.26})$$

$$-\tau_F \left\langle (\kappa + \sigma) \nabla \cdot \mathbb{R}_{F,2}, \mathbf{w}_h \right\rangle + \tau_F \left\langle \mathbb{J}_F \nabla \cdot \mathbb{R}_{F,2}, \nabla \mathbf{w}_h \right\rangle \quad (\text{C.27})$$

$$s_{F,E-stab}(\mathbf{w}_h) = \tau_E \left\langle \mathbb{J}_E \left(f_E + \frac{E_{r,h}^n}{c\Delta t} \right), \nabla \mathbf{w}_h \right\rangle \quad (\text{C.28})$$

- EF terms

$$a_{EF,F-stab}(E_{r,h}, q_h) = \tau_F \left\langle \left(\frac{1}{c\Delta t} + (\kappa + \sigma) \right) \mathbf{F}_{r,h}, \nabla q_h \right\rangle + \tau_F \left\langle \sum_{i=1}^d \mathbb{J}_F^i \nabla F_{r,h}^i, \nabla q_h \right\rangle \quad (\text{C.29})$$

$$a_{EF,E-stab}(E_{r,h}, q_h) = -\tau_E \left\langle \kappa \nabla \cdot \mathbf{F}_{r,h}, q_h \right\rangle \quad (\text{C.30})$$

- EE terms

$$a_{EE,F-stab}(E_{r,h}, q_h) = \tau_F \left\langle \mathbb{J}_E \nabla E_{r,h}, \nabla q_h \right\rangle \quad (\text{C.31})$$

$$a_{EE,E-stab}(E_{r,h}, q_h) = -\tau_E \left\langle \left(\frac{1}{c\Delta t} + \kappa \right) \kappa E_{r,h}, q_h \right\rangle \quad (\text{C.32})$$

- E right-hand-side

$$s_{E,F-stab}(q_h) = \tau_F \left\langle \frac{\mathbf{F}_{r,h}^n}{c\Delta t}, \nabla q_h \right\rangle + \tau_F \left\langle \nabla \cdot \mathbb{R}_{F,2}, \nabla q_h \right\rangle \quad (\text{C.33})$$

$$s_{E,E-stab}(q_h) = -\tau_E \left\langle \kappa \left(f_E + \frac{E_{r,h}^n}{c\Delta t} \right), q_h \right\rangle \quad (\text{C.34})$$

Bibliography

- [1] Elie Hachem. *Stabilized finite element method for heat transfer and turbulent flows inside industrial furnaces*. PhD thesis, Ecole Nationale Supérieure des mines de Paris, 2009.
- [2] Nadine El Kousseifi. *Numerical simulation of boiling for industrial quenching processes*. PhD thesis, Ecole Nationale Supérieure des Mines de Paris, 2012.
- [3] Stéphanie El Feghali. *Novel monolithic stabilized finite element method for fluid-structure interaction*. PhD thesis, Ecole Nationale Supérieure des Mines de Paris, 2012.
- [4] Ghina El Jannoun. *Space-Time accurate anisotropic adaptation and stabilized finite element methods for the resolution of unsteady CFD problems*. PhD thesis, Ecole Nationale Supérieure des Mines de Paris, 2014.
- [5] Jeremy Veysset. *Numerical modeling of large scales and long time*. PhD thesis, Ecole Nationale Supérieure des Mines de Paris, 2014.
- [6] Hugues Digonnet, Luisa Silva, and Thierry Coupez. Cimlib: a fully parallel application for numerical simulations based on components assembly. In *Materials processing and design; Modeling, Simulation and Applications; NUMIFORM'07; Proceedings of the 9th International Conference on Numerical Methods in Industrial Forming Processes*, volume 908, pages 269–274. AIP Publishing, 2007.
- [7] S Balay, S Abhyankar, M Adams, J Brown, P Brune, K Buschelman, V Eijkhout, W Gropp, D Kaushik, M Knepley, et al. *Petsc users manual revision 3.5*. Argonne National Laboratory (ANL), 2014.
- [8] William Gropp, Ewing Lusk, and Anthony Skjellum. *Using MPI: portable parallel programming with the message-passing interface*, volume 1. MIT press, 1999.
- [9] Thierry Coupez, Hugues Digonnet, and Richard Ducloux. Parallel meshing and remeshing. *Applied Mathematical Modelling*, 25(2):153–175, 2000.

- [10] Marc Bernacki, Héba Resk, Thierry Coupez, et al. Finite element model of primary recrystallization in polycrystalline aggregates using a level set framework. *Modelling and Simulation in Materials Science and Engineering*, 17(6):064006, 2009.
- [11] Mehdi Khalouffi. *Multiphase flows with phase change and turbulent boiling in quenching processes*. PhD thesis, Ecole Nationale Supérieure des Mines de Paris, 2017.
- [12] Stuart W Churchill and Humbert HS Chu. Correlating equations for laminar and turbulent free convection from a vertical plate. *International journal of heat and mass transfer*, 18(11):1323–1329, 1975.
- [13] Stephen Whitaker. Forced convection heat transfer correlations for flow in pipes, past flat plates, single cylinders, single spheres, and for flow in packed beds and tube bundles. *AIChE Journal*, 18(2):361–371, 1972.
- [14] Philip M Gresho. Some current cfd issues relevant to the incompressible navier-stokes equations. *Computer Methods in Applied Mechanics and Engineering*, 87(2):201–252, 1991.
- [15] Jan S Hesthaven and David Gottlieb. A stable penalty method for the compressible navier-stokes equations: I. open boundary conditions. *SIAM Journal on Scientific Computing*, 17(3):579–612, 1996.
- [16] Rolf Stenberg. On some techniques for approximating boundary conditions in the finite element method. *Journal of Computational and applied Mathematics*, 63(1):139–148, 1995.
- [17] Erik Burman and Miguel A Fernández. Stabilized explicit coupling for fluid–structure interaction using nitsche’s method. *Comptes Rendus Mathématique*, 345(8):467–472, 2007.
- [18] Mika Juntunen and Rolf Stenberg. Nitsche’s method for general boundary conditions. *Mathematics of computation*, 78(267):1353–1374, 2009.
- [19] Qinfu Hou and Zongshu Zou. Comparison between standard and renormalization group k - ϵ models in numerical simulation of swirling flow tundish. *ISIJ international*, 45(3):325–330, 2005.
- [20] Brian Edward Launder and DB Spalding. The numerical computation of turbulent flows. *Computer methods in applied mechanics and engineering*, 3(2):269–289, 1974.

-
- [21] Philippe R Spalart and Stephen R Allmaras. A one equation turbulence model for aerodynamic flows. *AIAA journal*, 94, 1992.
- [22] Szu-Cheng S Ou and Kuo-Nan Liou. Generalization of the spherical harmonic method to radiative transfer in multi-dimensional space. *Journal of Quantitative Spectroscopy and Radiative Transfer*, 28(4):271–288, 1982.
- [23] Ryan G McClarren and Cory D Hauck. Robust and accurate filtered spherical harmonics expansions for radiative transfer. *Journal of Computational Physics*, 229(16):5597–5614, 2010.
- [24] Edward W Larsen, Guido Thömmes, Axel Klar, Mohammed Seaid, and Thomas Götz. Simplified p_n approximations to the equations of radiative heat transfer and applications. *Journal of Computational Physics*, 183(2):652–675, 2002.
- [25] Edgar Olbrant, Edward W Larsen, Martin Frank, and Benjamin Seibold. Asymptotic derivation and numerical investigation of time-dependent simplified pn equations. *Journal of Computational Physics*, 238:315–336, 2013.
- [26] Martin Frank, A Klar, EW Larsen, and S Yasuda. Approximate models for radiative transfer. *Bulletin-Institut of Mathematics academia sinica*, 2(2):409, 2007.
- [27] E Hachem, M Khalloufi, J Bruchon, R Valette, and Y Mesri. Unified adaptive variational multiscale method for two phase compressible-incompressible flows. *Computer Methods in Applied Mechanics and Engineering*, 2016.
- [28] J Tinsley Oden. *A history of scientific computing*. ACM New York, NY, USA ©1990, 1996.
- [29] Pavel B Bochev and Max D Gunzburger. *Least-squares finite element methods*, volume 166. Springer Science & Business Media, 2009.
- [30] Thomas JR Hughes. Multiscale phenomena: Green’s functions, the dirichlet-to-neumann formulation, subgrid scale models, bubbles and the origins of stabilized methods. *Computer methods in applied mechanics and engineering*, 127(1):387–401, 1995.
- [31] Thomas JR Hughes, Gonzalo R Feijóo, Luca Mazzei, and Jean-Baptiste Quinicy. The variational multiscale method? a paradigm for computational mechanics. *Computer methods in applied mechanics and engineering*, 166(1):3–24, 1998.
- [32] Oriol Colomés, Santiago Badia, Ramon Codina, and Javier Principe. Assessment of variational multiscale models for the large eddy simulation of turbulent incompressible flows. *Computer Methods in Applied Mechanics and Engineering*, 285: 32–63, 2015.

- [33] Ramon Codina and Javier Principe. Dynamic subscales in the finite element approximation of thermally coupled incompressible flows. *International Journal for Numerical Methods in Fluids*, 54(6-8):707–730, 2007.
- [34] Ramon Codina, Javier Principe, Oriol Guasch, and Santiago Badia. Time dependent subscales in the stabilized finite element approximation of incompressible flow problems. *Computer Methods in Applied Mechanics and Engineering*, 196(21):2413–2430, 2007.
- [35] Peter Gamnitzer, Volker Gravemeier, and Wolfgang A Wall. Time-dependent subgrid scales in residual-based large eddy simulation of turbulent channel flow. *Computer Methods in Applied Mechanics and Engineering*, 199(13):819–827, 2010.
- [36] Ramon Codina, Javier Principe, and Joan Baiges. Subscales on the element boundaries in the variational two-scale finite element method. *Computer Methods in Applied Mechanics and Engineering*, 198(5):838–852, 2009.
- [37] Ramon Codina. Stabilized finite element approximation of transient incompressible flows using orthogonal subscales. *Computer Methods in Applied Mechanics and Engineering*, 191(39):4295–4321, 2002.
- [38] Elie Hachem, Benjamin Rivaux, Thibaud Kloczko, Hugues Digonnet, and Thierry Coupez. Stabilized finite element method for incompressible flows with high reynolds number. *Journal of Computational Physics*, 229(23):8643–8665, 2010.
- [39] Thierry Coupez and Elie Hachem. Solution of high-reynolds incompressible flow with stabilized finite element and adaptive anisotropic meshing. *Computer Methods in Applied Mechanics and Engineering*, 267:65–85, 2013.
- [40] Elie Hachem, Thibaud Kloczko, Hugues Digonnet, and Thierry Coupez. Stabilized finite element solution to handle complex heat and fluid flows in industrial furnaces using the immersed volume method. *International Journal for Numerical Methods in Fluids*, 68(1):99–121, 2012.
- [41] Elie Hachem, Ghina Jannoun, Jérémy Veysset, Marc Henri, Romuald Pierrot, Isabelle Poitrault, Elisabeth Massoni, and Thierry Coupez. Modeling of heat transfer and turbulent flows inside industrial furnaces. *Simulation Modelling Practice and Theory*, 30:35–53, 2013.
- [42] Q Schmid, E Marchal, JM Franchet, J Schwartz, Y Mesri, and E Hachem. Unified formulation for modeling heat and fluid flow in complex real industrial equipment. *Computers & Fluids*, 134:146–156, 2016.

- [43] Ramon Codina. A stabilized finite element method for generalized stationary incompressible flows. *Computer Methods in Applied Mechanics and Engineering*, 190(20):2681–2706, 2001.
- [44] Matias Avila, Javier Principe, and Ramon Codina. A finite element dynamical nonlinear subscale approximation for the low mach number flow equations. *Journal of Computational Physics*, 230(22):7988–8009, 2011.
- [45] Javier Principe, Ramon Codina, and Florian Henke. The dissipative structure of variational multiscale methods for incompressible flows. *Computer Methods in Applied Mechanics and Engineering*, 199(13):791–801, 2010.
- [46] Yu Jiang, Liquan Mei, and Huiming Wei. A finite element variational multiscale method for incompressible flow. *Applied Mathematics and Computation*, 266:374–384, 2015.
- [47] Volker Gravemeier. Scale-separating operators for variational multiscale large eddy simulation of turbulent flows. *Journal of Computational Physics*, 212(2):400–435, 2006.
- [48] Volker Gravemeier, Michael W Gee, Martin Kronbichler, and Wolfgang A Wall. An algebraic variational multiscale–multigrid method for large eddy simulation of turbulent flow. *Computer Methods in Applied Mechanics and Engineering*, 199(13):853–864, 2010.
- [49] Charbel Farhat, Ajaykumar Rajasekharan, and Bruno Koobus. A dynamic variational multiscale method for large eddy simulations on unstructured meshes. *Computer Methods in Applied Mechanics and Engineering*, 195(13):1667–1691, 2006.
- [50] Tomás Chacón Rebollo, Macarena Gómez Mármol, and Samuele Rubino. Numerical analysis of a finite element projection-based vms turbulence model with wall laws. *Computer Methods in Applied Mechanics and Engineering*, 285:379–405, 2015.
- [51] Fedderik van der Bos, Jaap JW van der Vegt, and Bernard J Geurts. A multi-scale formulation for compressible turbulent flows suitable for general variational discretization techniques. *Computer methods in applied mechanics and engineering*, 196(29):2863–2875, 2007.
- [52] Santiago Badia and Ramon Codina. On a multiscale approach to the transient stokes problem: Dynamic subscales and anisotropic space–time discretization. *Applied Mathematics and Computation*, 207(2):415–433, 2009.

- [53] Santiago Badia and Ramon Codina. Unified stabilized finite element formulations for the stokes and the darcy problems. *SIAM journal on Numerical Analysis*, 47(3):1971–2000, 2009.
- [54] Arif Masud and Thomas JR Hughes. A stabilized mixed finite element method for darcy flow. *Computer Methods in Applied Mechanics and Engineering*, 191(39):4341–4370, 2002.
- [55] Arif Masud. A stabilized mixed finite element method for darcy-stokes flow. *International journal for numerical methods in fluids*, 54(6-8):665–682, 2007.
- [56] KB Nakshatrala, DZ Turner, KD Hjelmstad, and Arif Masud. A stabilized mixed finite element method for darcy flow based on a multiscale decomposition of the solution. *Computer Methods in Applied Mechanics and Engineering*, 195(33):4036–4049, 2006.
- [57] Alexander N Brooks and Thomas JR Hughes. Streamline upwind/petrov-galerkin formulations for convection dominated flows with particular emphasis on the incompressible navier-stokes equations. *Computer methods in applied mechanics and engineering*, 32(1):199–259, 1982.
- [58] Augusto Cesar Galeão and Eduardo Gomes Dutra Do Carmo. A consistent approximate upwind petrov-galerkin method for convection-dominated problems. *Computer Methods in Applied Mechanics and Engineering*, 68(1):83–95, 1988.
- [59] Santiago Badia and Ramon Codina. Analysis of a stabilized finite element approximation of the transient convection-diffusion equation using an ale framework. *SIAM Journal on Numerical Analysis*, 44(5):2159–2197, 2006.
- [60] G de Vahl Davis. Natural convection of air in a square cavity: a bench mark numerical solution. *International journal for numerical methods in fluids*, 3(3):249–264, 1983.
- [61] Jiten C Kalita, DC Dalal, and Anoop K Dass. Fully compact higher-order computation of steady-state natural convection in a square cavity. *Physical Review E*, 64(6):066703, 2001.
- [62] HN Dixit and V Babu. Simulation of high rayleigh number natural convection in a square cavity using the lattice boltzmann method. *International journal of heat and mass transfer*, 49(3):727–739, 2006.
- [63] Shinichiro Wakashima and Takeo S Saitoh. Benchmark solutions for natural convection in a cubic cavity using the high-order time-space method. *International Journal of Heat and Mass Transfer*, 47(4):853–864, 2004.

- [64] E Tric, G Labrosse, and M Betrouni. A first incursion into the 3d structure of natural convection of air in a differentially heated cubic cavity, from accurate numerical solutions. *International Journal of Heat and Mass Transfer*, 43(21): 4043–4056, 2000.
- [65] S Saravanan and C Sivaraaj. Coupled thermal radiation and natural convection heat transfer in a cavity with a heated plate inside. *International Journal of Heat and Fluid Flow*, 40:54–64, 2013.
- [66] Slimane Adjerid, Nabil Chaabane, and Tao Lin. An immersed discontinuous finite element method for stokes interface problems. *Computer Methods in Applied Mechanics and Engineering*, 293:170–190, 2015.
- [67] Ruifeng Yuan, Chengwen Zhong, and He Zhang. An immersed-boundary method based on the gas kinetic bgk scheme for incompressible viscous flow. *Journal of Computational Physics*, 296:184–208, 2015.
- [68] CF Rowlatt and TN Phillips. A spectral element formulation of the immersed boundary method for newtonian fluids. *Computer Methods in Applied Mechanics and Engineering*, 298:29–57, 2016.
- [69] Chengjie Wang and Jeff D Eldredge. Strongly coupled dynamics of fluids and rigid-body systems with the immersed boundary projection method. *Journal of Computational Physics*, 295:87–113, 2015.
- [70] U?is Lācis, Kunihiko Taira, and Shervin Bagheri. A stable fluid–structure-interaction solver for low-density rigid bodies using the immersed boundary projection method. *Journal of Computational Physics*, 305:300–318, 2016.
- [71] Zhe Li, Julien Favier, Umberto D’Ortona, and Sébastien Poncet. An immersed boundary-lattice boltzmann method for single-and multi-component fluid flows. *Journal of Computational Physics*, 304:424–440, 2016.
- [72] Jeffrey K Wiens and John M Stockie. Simulating flexible fiber suspensions using a scalable immersed boundary algorithm. *Computer Methods in Applied Mechanics and Engineering*, 290:1–18, 2015.
- [73] MY Ge, KJ Chua, C Shu, and WM Yang. Analytical and numerical study of tissue cryofreezing via the immersed boundary method. *International Journal of Heat and Mass Transfer*, 83:1–10, 2015.
- [74] Junjie Xia, Kun Luo, and Jianren Fan. A ghost-cell based high-order immersed boundary method for inter-phase heat transfer simulation. *International Journal of Heat and Mass Transfer*, 75:302–312, 2014.

- [75] Stanley Osher and Ronald Fedkiw. *Level set methods and dynamic implicit surfaces*, volume 153. Springer Science & Business Media, 2006.
- [76] Zhan Kang, Yaguang Wang, and Yiqiang Wang. Structural topology optimization with minimum distance control of multiphase embedded components by level set method. *Computer Methods in Applied Mechanics and Engineering*, 306:299–318, 2016.
- [77] Julien Bruchon, Hugues Digonnet, and Thierry Coupez. Using a signed distance function for the simulation of metal forming processes: Formulation of the contact condition and mesh adaptation. from a lagrangian approach to an eulerian approach. *International journal for numerical methods in engineering*, 78(8):980–1008, 2009.
- [78] Tomasz Waclawczyk. A consistent solution of the re-initialization equation in the conservative level-set method. *Journal of Computational Physics*, 299:487–525, 2015.
- [79] Amin Mahmoudi Moghadam, Mehdi Shafieefar, and Roozbeh Panahi. Development of a high-order level set method: Compact conservative level set (ccls). *Computers & Fluids*, 129:79–90, 2016.
- [80] J Luo, XY Hu, and NA Adams. Efficient formulation of scale separation for multi-scale modeling of interfacial flows. *Journal of Computational Physics*, 308:411–420, 2016.
- [81] Xiaofeng Yang, Ashley J James, John Lowengrub, Xiaoming Zheng, and Vittorio Cristini. An adaptive coupled level-set/volume-of-fluid interface capturing method for unstructured triangular grids. *Journal of Computational Physics*, 217(2):364–394, 2006.
- [82] Matthieu Graveleau, Nicolas Chevaugeon, and Nicolas Moës. The inequality level-set approach to handle contact: membrane case. *Advanced Modeling and Simulation in Engineering Sciences*, 2(1):1–25, 2015.
- [83] D Pino Muñoz, Julien Bruchon, Sylvain Drapier, and François Valdivieso. A finite element-based level set method for fluid–elastic solid interaction with surface tension. *International Journal for Numerical Methods in Engineering*, 93(9):919–941, 2013.
- [84] Ursula Rasthofer. *Computational multiscale methods for turbulent single and two-phase flows*. Ph. D. thesis. München, Technische Universität München, Diss, 2015.

- [85] Seungwon Shin and Damir Juric. Modeling three-dimensional multiphase flow using a level contour reconstruction method for front tracking without connectivity. *Journal of Computational Physics*, 180(2):427–470, 2002.
- [86] Ivo Babuška and Werner C Rheinboldt. A-posteriori error estimates for the finite element method. *International Journal for Numerical Methods in Engineering*, 12(10):1597–1615, 1978.
- [87] Olgierd C Zienkiewicz and Jian Z Zhu. A simple error estimator and adaptive procedure for practical engineering analysis. *International Journal for Numerical Methods in Engineering*, 24(2):337–357, 1987.
- [88] Olgierd Cecil Zienkiewicz and Jian Zhong Zhu. The superconvergent patch recovery and a posteriori error estimates. part 1: The recovery technique. *International Journal for Numerical Methods in Engineering*, 33(7):1331–1364, 1992.
- [89] Olgierd Cecil Zienkiewicz and Jian Zhong Zhu. The superconvergent patch recovery and a posteriori error estimates. part 2: Error estimates and adaptivity. *International Journal for Numerical Methods in Engineering*, 33(7):1365–1382, 1992.
- [90] Pierre Ladeveze and D Leguillon. Error estimate procedure in the finite element method and applications. *SIAM Journal on Numerical Analysis*, 20(3):485–509, 1983.
- [91] Mark Ainsworth and J Tinsley Oden. A posteriori error estimation in finite element analysis. *Computer Methods in Applied Mechanics and Engineering*, 142(1):1–88, 1997.
- [92] Thomas Grätsch and Klaus-Jürgen Bathe. A posteriori error estimation techniques in practical finite element analysis. *Computers & structures*, 83(4):235–265, 2005.
- [93] Karel Segeth. A review of some a posteriori error estimates for adaptive finite element methods. *Mathematics and Computers in Simulation*, 80(8):1589–1600, 2010.
- [94] L Gallimard and D Ryckelynck. A posteriori global error estimator based on the error in the constitutive relation for reduced basis approximation of parametrized linear elastic problems. *Applied Mathematical Modelling*, 2015.
- [95] Tomás P Barrios, Edwin M Behrens, and María González. Low cost a posteriori error estimators for an augmented mixed fem in linear elasticity. *Applied Numerical Mathematics*, 84:46–65, 2014.

- [96] Guillermo Hauke and Diego Irisarri. Variational multiscale a posteriori error estimation for systems. application to linear elasticity. *Computer Methods in Applied Mechanics and Engineering*, 285:291–314, 2015.
- [97] Igor Mozolevski and Serge Prudhomme. Goal-oriented error estimation based on equilibrated-flux reconstruction for finite element approximations of elliptic problems. *Computer Methods in Applied Mechanics and Engineering*, 288:127–145, 2015.
- [98] Ludovic Chamoin and Laurent Desvillettes. Control of modeling errors in the coupling of linear transport and diffusion models. *Computer Methods in Applied Mechanics and Engineering*, 261:83–95, 2013.
- [99] Mark Ainsworth and Tomáš Vejchodský. Robust error bounds for finite element approximation of reaction–diffusion problems with non-constant reaction coefficient in arbitrary space dimension. *Computer Methods in Applied Mechanics and Engineering*, 281:184–199, 2014.
- [100] Jichun Li and Yanping Lin. A priori and posteriori error analysis for time-dependent maxwell’s equations. *Computer Methods in Applied Mechanics and Engineering*, 292:54–68, 2015.
- [101] J Tinsley Oden, Weihan Wu, and Mark Ainsworth. An a posteriori error estimate for finite element approximations of the navier-stokes equations. *Computer Methods in Applied Mechanics and Engineering*, 111(1):185–202, 1994.
- [102] Erik Burman. Robust error estimates for stabilized finite element approximations of the two dimensional navier–stokes’ equations at high reynolds number. *Computer Methods in Applied Mechanics and Engineering*, 288:2–23, 2015.
- [103] Abigail L Bowers, Sabine Le Borne, and Leo G Rebholz. Error analysis and iterative solvers for navier–stokes projection methods with standard and sparse grad-div stabilization. *Computer Methods in Applied Mechanics and Engineering*, 275:1–19, 2014.
- [104] Guillermo Hauke, Daniel Fuster, and Fernando Lizarraga. Variational multiscale a posteriori error estimation for systems: The euler and navier–stokes equations. *Computer Methods in Applied Mechanics and Engineering*, 283:1493–1524, 2015.
- [105] Weizhang Huang. Metric tensors for anisotropic mesh generation. *Journal of computational physics*, 204(2):633–665, 2005.
- [106] Thierry Coupez. Metric construction by length distribution tensor and edge based error for anisotropic adaptive meshing. *Journal of Computational Physics*, 230(7): 2391–2405, 2011.

- [107] Y Mesri, M Khalloufi, and E Hachem. On optimal simplicial 3d meshes for minimizing the hessian-based errors. *Applied Numerical Mathematics*, 109:235–249, 2016.
- [108] Cyril Gruau and Thierry Coupez. 3d tetrahedral, unstructured and anisotropic mesh generation with adaptation to natural and multidomain metric. *Computer Methods in Applied Mechanics and Engineering*, 194(48):4951–4976, 2005.
- [109] Ramzy Boussetta, Thierry Coupez, and Lionel Fourment. Adaptive remeshing based on a posteriori error estimation for forging simulation. *Computer methods in applied mechanics and engineering*, 195(48):6626–6645, 2006.
- [110] Theofanis Strouboulis, Kevin Copps, and Ivo Babuška. The generalized finite element method. *Computer methods in applied mechanics and engineering*, 190(32):4081–4193, 2001.
- [111] Soheil Soghrati. Hierarchical interface-enriched finite element method: An automated technique for mesh-independent simulations. *Journal of Computational Physics*, 275:41–52, 2014.
- [112] Soheil Soghrati and Hossein Ahmadian. 3d hierarchical interface-enriched finite element method: Implementation and applications. *Journal of Computational Physics*, 299:45–55, 2015.
- [113] Ahmad R Najafi, Masoud Safdari, Daniel A Tortorelli, and Philippe H Geubelle. A gradient-based shape optimization scheme using an interface-enriched generalized fem. *Computer Methods in Applied Mechanics and Engineering*, 296:1–17, 2015.
- [114] JOHN Dolbow and Ted Belytschko. A finite element method for crack growth without remeshing. *International journal for numerical methods in engineering*, 46(1):131–150, 1999.
- [115] Kenan Kergrene, Ivo Babuška, and Uday Banerjee. Stable generalized finite element method and associated iterative schemes; application to interface problems. *Computer Methods in Applied Mechanics and Engineering*, 305:1–36, 2016.
- [116] Elie Hachem, Stephanie Feghali, Ramon Codina, and Thierry Coupez. Immersed stress method for fluid–structure interaction using anisotropic mesh adaptation. *International Journal for Numerical Methods in Engineering*, 94(9):805–825, 2013.
- [117] Elie Hachem, Hugues Digonnet, Thierry Coupez, et al. Stabilized finite element solution to handle complex heat and turbulent flows in industrial furnaces. In *Proceedings V European Conference on Computational Fluid Dynamics*, 2010.

- [118] Frank-Thomas Lentès and Norbert Siedow. Three-dimensional radiative heat transfer in glass cooling processes. *Glastech. Ber. Glass Sci. Technol.*, 72(6):188–196, 1999.
- [119] Hyoung Tae Kim, Bo Wook Rhee, and Joo Hwan Park. Benchmark calculations of a radiation heat transfer for a candu fuel channel analysis using the cfd code. *Journal of Nuclear Science and Technology*, 43(11):1422–1430, 2006.
- [120] Raymond Viskanta and MP Mengüç. Radiation heat transfer in combustion systems. *Progress in Energy and Combustion Science*, 13(2):97–160, 1987.
- [121] Lionel Tessé, Francis Dupoirieux, and Jean Taine. Monte carlo modeling of radiative transfer in a turbulent sooty flame. *International journal of heat and mass transfer*, 47(3):555–572, 2004.
- [122] B Garten, F Hunger, D Messig, B Stelzner, D Trimis, and C Hasse. Detailed radiation modeling of a partial-oxidation flame. *International Journal of Thermal Sciences*, 87:68–84, 2015.
- [123] Jinwu Kang and Yiming Rong. Modeling and simulation of load heating in heat treatment furnaces. *Journal of materials processing technology*, 174(1):109–114, 2006.
- [124] EP Keramida, HH Liakos, MA Founti, AG Boudouvis, and NC Markatos. Radiative heat transfer in natural gas-fired furnaces. *International Journal of Heat and Mass Transfer*, 43(10):1801–1809, 2000.
- [125] A Habibi, Bart Merci, and Geraldine J Heynderickx. Impact of radiation models in cfd simulations of steam cracking furnaces. *Computers & Chemical Engineering*, 31(11):1389–1406, 2007.
- [126] Bruno Dubroca and Jean-Luc Feugeas. Etude théorique et numérique d’une hiérarchie de modèles aux moments pour le transfert radiatif. *Comptes Rendus de l’Académie des Sciences-Series I-Mathematics*, 329(10):915–920, 1999.
- [127] E Meinköhn, G Kanschat, R Rannacher, and R Wehrse. Numerical methods for multidimensional radiative transfer. In *Reactive Flows, Diffusion and Transport*, pages 485–526. Springer, 2007.
- [128] Joseph A Fleck Jr. The calculation of nonlinear radiation transport by a monte carlo method. Technical report, Lawrence Radiation Lab., Univ. of California, Livermore, 1961.

- [129] Barbara A Whitney. Monte carlo radiative transfer. *Fluid Flows to Black Holes: A Tribute to S Chandrasekhar on his Birth Centenary*. Edited by Saikia DJ et al. Published by World Scientific Publishing Co. Pte. Ltd., 2011. ISBN# 9789814374774, pp. 151-176, 1:151–176, 2011.
- [130] Gisela Widmer, Ralf Hiptmair, and Ch Schwab. Sparse adaptive finite elements for radiative transfer. *Journal of Computational Physics*, 227(12):6071–6105, 2008.
- [131] O Lehtikangas, Tanja Tarvainen, AD Kim, and Simon R Arridge. Finite element approximation of the radiative transport equation in a medium with piece-wise constant refractive index. *Journal of Computational Physics*, 282:345–359, 2015.
- [132] T Tarvainen, M Vauhkonen, V Kolehmainen, and JP Kaipio. Finite element model for the coupled radiative transfer equation and diffusion approximation. *International Journal for Numerical Methods in Engineering*, 65(3):383–405, 2006.
- [133] Dimitris Gorpas, Dido Yova, and Konstantinos Politopoulos. A three-dimensional finite elements approach for the coupled radiative transfer equation and diffusion approximation modeling in fluorescence imaging. *Journal of Quantitative Spectroscopy and Radiative Transfer*, 111(4):553–568, 2010.
- [134] Rafael O Castro and Juan Pablo Trelles. Spatial and angular finite element method for radiative transfer in participating media. *Journal of Quantitative Spectroscopy and Radiative Transfer*, 157:81–105, 2015.
- [135] Matias Avila, Ramon Codina, and Javier Principe. Spatial approximation of the radiation transport equation using a subgrid-scale finite element method. *Computer Methods in Applied Mechanics and Engineering*, 200(5):425–438, 2011.
- [136] Jean-Luc Guermond and Guido Kanschat. Asymptotic analysis of upwind discontinuous galerkin approximation of the radiative transport equation in the diffusive limit. *SIAM Journal on Numerical Analysis*, 48(1):53–78, 2010.
- [137] Subrahmanyam Chandrasekhar. *Radiative transfer*. Courier Corporation, 2013.
- [138] Nevin Selçuk and Nuray Kayakol. Evaluation of discrete ordinates method for radiative transfer in rectangular furnaces. *International Journal of Heat and Mass Transfer*, 40(2):213–222, 1997.
- [139] Pedro J Coelho. Advances in the discrete ordinates and finite volume methods for the solution of radiative heat transfer problems in participating media. *Journal of Quantitative Spectroscopy and Radiative Transfer*, 145:121–146, 2014.

- [140] Jean C Ragusa, J-L Guermond, and Guido Kanschat. A robust s n-dg-approximation for radiation transport in optically thick and diffusive regimes. *Journal of Computational Physics*, 231(4):1947–1962, 2012.
- [141] W An, LM Ruan, H Qi, and LH Liu. Finite element method for radiative heat transfer in absorbing and anisotropic scattering media. *Journal of Quantitative Spectroscopy and Radiative Transfer*, 96(3):409–422, 2005.
- [142] Barry D Ganapol. The response matrix discrete ordinates solution to the 1d radiative transfer equation. *Journal of Quantitative Spectroscopy and Radiative Transfer*, 154:72–90, 2015.
- [143] Knut Stamnes, S-Chee Tsay, Warren Wiscombe, and Kolf Jayaweera. Numerically stable algorithm for discrete-ordinate-method radiative transfer in multiple scattering and emitting layered media. *Applied optics*, 27(12):2502–2509, 1988.
- [144] Matthew T Calef, Erin D Fichtl, James S Warsa, Markus Berndt, and Neil N Carlson. Nonlinear krylov acceleration applied to a discrete ordinates formulation of the k-eigenvalue problem. *Journal of Computational Physics*, 238:188–209, 2013.
- [145] Don E Bruss, Jim E Morel, and Jean C Ragusa. S 2 sa preconditioning for the s n equations with strictly nonnegative spatial discretization. *Journal of Computational Physics*, 273:706–719, 2014.
- [146] Jingfei Jia, Hyun K Kim, and Andreas H Hielscher. Fast linear solver for radiative transport equation with multiple right hand sides in diffuse optical tomography. *Journal of Quantitative Spectroscopy and Radiative Transfer*, 167:10–22, 2015.
- [147] JH Jeans. The equations of radiative transfer of energy. *Monthly Notices of the Royal Astronomical Society*, 78(1):28–36, 1917.
- [148] Steven P Hamilton and Thomas M Evans. Efficient solution of the simplified pn equations. *Journal of Computational Physics*, 284:155–170, 2015.
- [149] Zekeriya Altaç. On radiative transfer using synthetic kernel and simplified spherical harmonics methods in linearly anisotropically scattering media. *Journal of Quantitative Spectroscopy and Radiative Transfer*, 147:8–23, 2014.
- [150] Matthias Schäfer, Martin Frank, and C David Levermore. Diffusive corrections to p_n approximations. *Multiscale Modeling & Simulation*, 9(1):1–28, 2011.
- [151] Martin Frank, Jens Lang, and Matthias Schäfer. Adaptive finite element simulation of the time-dependent simplified p_n equations. *Journal of Scientific Computing*, 49(3):332–350, 2011.

- [152] Konstantin Grella and Ch Schwab. Sparse tensor spherical harmonics approximation in radiative transfer. *Journal of Computational Physics*, 230(23):8452–8473, 2011.
- [153] Ioan Teleaga, Mohammed Seaïd, Ingenuin Gasser, Axel Klar, and Jens Struckmeier. Radiation models for thermal flows at low mach number. *Journal of Computational Physics*, 215(2):506–525, 2006.
- [154] ERG Eckert and EM Sparrow. Radiative heat exchange between surfaces with specular reflection. *International Journal of Heat and Mass Transfer*, 3(1):42–54, 1961.
- [155] Michael F Modest. *Radiative heat transfer*. Academic press, 2013.
- [156] Vladimir A Lebedev and Vladimir P Solovjov. View factors of cylindrical spiral surfaces. *Journal of Quantitative Spectroscopy and Radiative Transfer*, 171:1–3, 2016.
- [157] Santosh B Bopche and Arunkumar Sridharan. Determination of view factors by contour integral technique. *Annals of Nuclear Energy*, 36(11):1681–1688, 2009.
- [158] Yong Kang Khor, Yew Mun Hung, and Boon Kian Lim. On the role of radiation view factor in thermal performance of straight-fin heat sinks. *International Communications in Heat and Mass Transfer*, 37(8):1087–1095, 2010.
- [159] George N Walton. *Calculation of obstructed view factors by adaptive integration*. Citeseer, 2002.
- [160] Peter Schröder and Pat Hanrahan. *A closed form expression for the form factor between two polygons*. Princeton University, Department of Computer Science, 1993.
- [161] Arvind Narayanaswamy. An analytic expression for radiation view factor between two arbitrarily oriented planar polygons. *International Journal of Heat and Mass Transfer*, 91:841–847, 2015.
- [162] R Farrell. Determination of configuration factors of irregular shape. *Journal of Heat Transfer*, 98(2):311–313, 1976.
- [163] D Alciatore, S Lipp, and WS Janna. Closed form solution of the general three-dimensional radiation configuration factor problem with microcomputer solution. In *National Heat Transfer Conference*, pages 165–169, 1989.
- [164] ERG Eckert. Radiative transfer, hc hottel and af sarofim, mcgraw-hill book company, new york, 1967. 52 pages. *AIChE Journal*, 15(5):794–796, 1969.

- [165] Naoto Kakuta, Shintaro Yokoyama, Mitsuyoshi Nakamura, and Kunihiko Mabuchi. Estimation of radiative heat transfer using a geometric human model. *Biomedical Engineering, IEEE Transactions on*, 48(3):324–331, 2001.
- [166] Amrit Ambirajan and SP Venkateshan. Accurate determination of diffuse view factors between planar surfaces. *International journal of heat and mass transfer*, 36(8):2203–2208, 1993.
- [167] Mahesh Ravishankar, Sandip Mazumder, and Maathangi Sankar. Application of the modified differential approximation for radiative transfer to arbitrary geometry. *Journal of Quantitative Spectroscopy and Radiative Transfer*, 111(14):2052–2069, 2010.
- [168] V Rammohan Rao and VMK Sastri. Efficient evaluation of diffuse view factors for radiation. *International journal of heat and mass transfer*, 39(6):1281–1286, 1996.
- [169] Sandip Mazumder and Mahesh Ravishankar. General procedure for calculation of diffuse view factors between arbitrary planar polygons. *International Journal of Heat and Mass Transfer*, 55(23):7330–7335, 2012.
- [170] Daniel R Baum, Holly E Rushmeier, and James M Winget. Improving radiosity solutions through the use of analytically determined form-factors. *ACM Siggraph Computer Graphics*, 23(3):325–334, 1989.
- [171] Sara C Francisco, António M Raimundo, Adélio R Gaspar, A Virgílio M Oliveira, and Divo A Quintela. Calculation of view factors for complex geometries using stokes theorem. *Journal of Building Performance Simulation*, 7(3):203–216, 2014.
- [172] James J Noble. The zone method: explicit matrix relations for total exchange areas. *International Journal of Heat and Mass Transfer*, 18(2):261–269, 1975.
- [173] DK Edwards. The plating algorithm for radiation script-f transfer factor. *Journal of heat transfer*, 108(1):237–238, 1986.
- [174] TR Johnson and JM Beer. Radiative heat transfer in furnaces: further development of the zone method of analysis. In *Symposium (International) on Combustion*, volume 14, pages 639–649. Elsevier, 1973.
- [175] Shuaibu Ndache Mohammed. Numerical computation of net radiative heat transfer within a non absorbing furnace enclosure. *Leonardo Journal of Sciences*, 1(5):149–158, 2006.
- [176] Glenn T Johnson and Ian D Watson. The determination of view-factors in urban canyons. *Journal of Climate and Applied Meteorology*, 23(2):329–335, 1984.

- [177] Glenn P Forney. Computing radiative heat transfer occurring in a zone fire model. *Fire Science and Technology*, 14(1/2):31–47, 1994.
- [178] Haytham Sayah, Maroun Nemer, Wassim Nehmé, and Denis Clodic. Computational fluid dynamics modeling of a self-recuperative burner and development of a simplified equivalent radiative model. *Journal of Heat Transfer*, 134(12):121201, 2012.
- [179] TF Smith, ZF Shen, and JN Friedman. Evaluation of coefficients for the weighted sum of gray gases model. *J. Heat Transfer;(United States)*, 104(4), 1982.
- [180] KS Reddy and K Ravi Kumar. Estimation of convective and radiative heat losses from an inverted trapezoidal cavity receiver of solar linear fresnel reflector system. *International Journal of Thermal Sciences*, 80:48–57, 2014.
- [181] Mark Sussman and Emad Fatemi. An efficient, interface-preserving level set re-distancing algorithm and its application to interfacial incompressible fluid flow. *SIAM Journal on scientific computing*, 20(4):1165–1191, 1999.
- [182] M Khalloufi, Y Mesri, R Valette, E Massoni, and E Hachem. High fidelity anisotropic adaptive variational multiscale method for multiphase flows with surface tension. *Computer Methods in Applied Mechanics and Engineering*, 2016.
- [183] Steven Diot and Marianne M François. An interface reconstruction method based on an analytical formula for 3d arbitrary convex cells. *Journal of Computational Physics*, 305:63–74, 2016.
- [184] A Raji and M Hasnaoui. Combined mixed convection and radiation in ventilated cavities. *Engineering Computations*, 18(7):922–949, 2001.
- [185] Guillem Colomer Rey. *Numerical methods for radiative heat transfer*. Universitat Politècnica de Catalunya, 2007.
- [186] Thomas A Brunner. Forms of approximate radiation transport. *Sandia report*, 2002.
- [187] Xinzhong Chen and Edward A Spiegel. The radiative stress tensor. *The Astrophysical Journal*, 540(2):1069, 2000.
- [188] Raquel Domínguez-Cascante and Jordi Faraudo. Nonequilibrium corrections in the pressure tensor due to an energy flux. *Physical Review E*, 54(6):6933, 1996.
- [189] Claude Bardos, François Golse, and David Levermore. Fluid dynamic limits of kinetic equations. i. formal derivations. *Journal of statistical physics*, 63(1-2):323–344, 1991.

- [190] Dirk Helbing. Gas-kinetic derivation of navier-stokes-like traffic equations. *Physical Review E*, 53(3):2366, 1996.
- [191] CD Levermore. Relating eddington factors to flux limiters. *Journal of Quantitative Spectroscopy and Radiative Transfer*, 31(2):149–160, 1984.
- [192] Clinton PT Groth and James G McDonald. Towards physically realizable and hyperbolic moment closures for kinetic theory. *Continuum Mechanics and Thermodynamics*, 21(6):467–493, 2009.
- [193] José A Carrillo, Thierry Goudon, Pauline Lafitte, and Francesco Vecil. Numerical schemes of diffusion asymptotics and moment closures for kinetic equations. *Journal of Scientific Computing*, 36(1):113–149, 2008.
- [194] C David Levermore. Moment closure hierarchies for kinetic theories. *Journal of Statistical Physics*, 83(5-6):1021–1065, 1996.
- [195] B Dubroca, J-L Feugeas, and M Frank. Angular moment model for the fokker-planck equation. *The European Physical Journal D*, 60(2):301–307, 2010.
- [196] Michael Junk. Maximum entropy for reduced moment problems. *Mathematical Models and Methods in Applied Sciences*, 10(07):1001–1025, 2000.
- [197] Jose A Pons, J Ma Ibáñez, and Juan A Miralles. Hyperbolic character of the angular moment equations of radiative transfer and numerical methods. *Monthly Notices of the Royal Astronomical Society*, 317(3):550–562, 2000.
- [198] J Fort. Information-theoretical approach to radiative transfer. *Physica A: Statistical Mechanics and its Applications*, 243(3):275–303, 1997.
- [199] Cory D Hauck, Martin Frank, and Edgar Olbrant. Perturbed, entropy-based closure for radiative transfer. *SIAM Journal on Applied Mathematics*, 6(3), 2013.
- [200] Graham W Alldredge, Cory D Hauck, Dianne P O’Leary, and André L Tits. Adaptive change of basis in entropy-based moment closures for linear kinetic equations. *Journal of Computational Physics*, 258:489–508, 2014.
- [201] Graham W Alldredge, Cory D Hauck, and Andre L Tits. High-order entropy-based closures for linear transport in slab geometry ii: A computational study of the optimization problem. *SIAM Journal on Scientific Computing*, 34(4):B361–B391, 2012.
- [202] Zbigniew Banach and Wieslaw Larecki. One-dimensional maximum entropy radiation hydrodynamics: three-moment theory. *Journal of Physics A: Mathematical and Theoretical*, 45(38):385501, 2012.

- [203] Cory D Hauck. High-order entropy-based closures for linear transport in slab geometry. *Commun. Math. Sci*, 9:187–205, 2011.
- [204] Philipp Monreal and Martin Frank. Higher order minimum entropy approximations in radiative transfer. *arXiv preprint arXiv:0812.3063*, 2008.
- [205] Martin Frank and Benjamin Seibold. Optimal prediction for radiative transfer: A new perspective on moment closure. *arXiv preprint arXiv:0806.4707*, 2008.
- [206] Gerald N Minerbo. Maximum entropy eddington factors. *Journal of Quantitative Spectroscopy and Radiative Transfer*, 20(6):541–545, 1978.
- [207] GC Pomraning. Maximum entropy eddington factors and flux limited diffusion theory. *Journal of Quantitative Spectroscopy and Radiative Transfer*, 26(5):385–388, 1981.
- [208] AM Anile, S Pennisi, and M Sammartino. A thermodynamical approach to eddington factors. *Journal of mathematical physics*, 32(2):544–550, 1991.
- [209] Wieslaw Larecki and Zbigniew Banach. Entropic derivation of the spectral eddington factors. *Journal of Quantitative Spectroscopy and Radiative Transfer*, 112(15):2486–2506, 2011.
- [210] J Cartierf A Munnierl. Geometric eddington factor for radiative transfer problems. *Numerical Methods for Hyperbolic and Kinetic Problems: CEMRACS 2003, Summer Research Center in Mathematics and Advances in Scientific Computing, July 21-August 29, 2003, CIRM, Marseille, France*, 7:271, 2005.
- [211] Bruno Dubroca, Mohammed Seaïd, and Ioan Teleaga. A consistent approach for the coupling of radiation and hydrodynamics at low mach number. *Journal of Computational Physics*, 225(1):1039–1065, 2007.
- [212] Christophe Berthon, Pierre Charrier, and Bruno Dubroca. An hllc scheme to solve the m 1 model of radiative transfer in two space dimensions. *Journal of Scientific Computing*, 31(3):347–389, 2007.
- [213] Thomas A Brunner and James P Holloway. Two new boundary conditions for use with the maximum entropy closure and an approximate riemann solver. *Transport*, 10:3, 2000.
- [214] AV Latyshev and AA Yushkanov. Moment boundary conditions in rarefied gas slip-flow problems. *Fluid Dynamics*, 39(2):339–353, 2004.
- [215] Michael J Fryer and Henning Struchtrup. Moment model and boundary conditions for energy transport in the phonon gas. *Continuum Mechanics and Thermodynamics*, 26(5):593–618, 2014.

- [216] RB Lowrie and JE Morel. Issues with high-resolution godunov methods for radiation hydrodynamics. *Journal of Quantitative Spectroscopy and Radiative Transfer*, 69(4):475–489, 2001.
- [217] Matthias Gonzalez. *Contribution à l'étude numérique de l'hydrodynamique radiative: des expériences de chocs radiatifs aux jets astrophysiques*. PhD thesis, Université Paris Sud-Paris XI, 2006.
- [218] NMH Vaytet, Edouard Audit, Bruno Dubroca, and F Delahaye. A numerical model for multigroup radiation hydrodynamics. *Journal of Quantitative Spectroscopy and Radiative Transfer*, 112(8):1323–1335, 2011.
- [219] Neil Vaytet, Edouard Audit, Gilles Chabrier, Benoit Commercon, and Jacques Masson. Simulations of protostellar collapse using multigroup radiation hydrodynamics. i. the first collapse. *arXiv preprint arXiv:1205.5143*, 2012.
- [220] Samet Y Kadioglu, Dana A Knoll, Robert B Lowrie, and Rick M Rauenzahn. A second order self-consistent imex method for radiation hydrodynamics. *Journal of Computational Physics*, 229(22):8313–8332, 2010.
- [221] L Ibgui, C Stehlé, M González, J-P Chièze, L de Sá, T Lanz, and I Hubeny. Assessment of the gray m1 model in the case of a laboratory radiative shock simulation. *High Energy Density Physics*, 17:98–105, 2015.
- [222] M Gonzalez, E Audit, and P Huynh. Heracles: a three-dimensional radiation hydrodynamics code. *Astronomy & Astrophysics*, 464(2):429–435, 2007.
- [223] C Michaut, HC Nguyen, and L Di Menza. Computational radiation hydrodynamics. *Astrophysics and Space Science*, 336(1):175–181, 2011.
- [224] Aleksander Skadowski, Ramesh Narayan, Alexander Tchekhovskoy, and Yucong Zhu. Semi-implicit scheme for treating radiation under m1 closure in general relativistic conservative fluid dynamics codes. *Monthly Notices of the Royal Astronomical Society*, 429(4):3533–3550, 2013.
- [225] M Seaid, A Klar, and B Dubroca. Flux limiters in the coupling of radiation and hydrodynamic models. *Journal of computational and applied mathematics*, 168(1):425–435, 2004.
- [226] Martin Frank, Bruno Dubroca, and Axel Klar. Partial moment entropy approximation to radiative heat transfer. *Journal of Computational Physics*, 218(1):1–18, 2006.

- [227] WE Meador and WR Weaver. Two-stream approximations to radiative transfer in planetary atmospheres: A unified description of existing methods and a new improvement. *Journal of the atmospheric sciences*, 37(3):630–643, 1980.
- [228] B Dubroca and A Klar. Half-moment closure for radiative transfer equations. *Journal of Computational Physics*, 180(2):584–596, 2002.
- [229] J-F Ripoll and AA Wray. A half-moment model for radiative transfer in a 3d gray medium and its reduction to a moment model for hot, opaque sources. *Journal of Quantitative Spectroscopy and Radiative Transfer*, 93(4):473–519, 2005.
- [230] R Turpault, M Frank, B Dubroca, and A Klar. Multigroup half space moment approximations to the radiative heat transfer equations. *Journal of Computational Physics*, 198(1):363–371, 2004.
- [231] Rodolphe Turpault. A consistent multigroup model for radiative transfer and its underlying mean opacities. *Journal of Quantitative Spectroscopy and Radiative Transfer*, 94(3):357–371, 2005.
- [232] J-F Ripoll and AA Wray. A 3-d multiband closure for radiation and neutron transfer moment models. *Journal of Computational Physics*, 227(4):2212–2237, 2008.
- [233] Rodolphe Turpault. Properties and frequential hybridisation of the multigroup m1 model for radiative transfer. *Nonlinear Analysis: Real World Applications*, 11(4):2514–2528, 2010.
- [234] Amiram Harten, Peter D Lax, and Bram van Leer. On upstream differencing and godunov-type schemes for hyperbolic conservation laws. *SIAM review*, 25(1):35–61, 1983.
- [235] Alexander Kurganov and Eitan Tadmor. Solution of two-dimensional riemann problems for gas dynamics without riemann problem solvers. *Numerical Methods for Partial Differential Equations*, 18(5):584–608, 2002.
- [236] Thomas A Brunner and James Paul Holloway. One-dimensional riemann solvers and the maximum entropy closure. *Journal of Quantitative Spectroscopy and Radiative Transfer*, 69(5):543–566, 2001.
- [237] G Montecinos, Cristóbal E Castro, Michael Dumbser, and Eleuterio F Toro. Comparison of solvers for the generalized riemann problem for hyperbolic systems with source terms. *Journal of Computational Physics*, 231(19):6472–6494, 2012.

- [238] Dinshaw S Balsara and Michael Dumbser. Multidimensional riemann problem with self-similar internal structure. part ii—application to hyperbolic conservation laws on unstructured meshes. *Journal of Computational Physics*, 287:269–292, 2015.
- [239] Christophe Berthon. Inégalités d’entropie pour un schéma de relaxation. *Comptes Rendus Mathématique*, 340(1):63–68, 2005.
- [240] Christophe Berthon, Pierre Charrier, and Bruno Dubroca. An asymptotic preserving relaxation scheme for a moment model of radiative transfer. *Comptes Rendus Mathématique*, 344(7):467–472, 2007.
- [241] Christophe Berthon, Philippe G LeFloch, and Rodolphe Turpault. Late-time relaxation limits of nonlinear hyperbolic systems. a general framework. *Math. of Comp*, 2010.
- [242] C Berthon, J Dubois, B Dubroca, TH Nguyen-Bui, and R Turpault. A free streaming contact preserving scheme for the m1 model. *Adv. Appl. Math. Mech*, 3:259–285, 2010.
- [243] Christophe Berthon and Rodolphe Turpault. Asymptotic preserving hll schemes. *Numerical methods for partial differential equations*, 27(6):1396–1422, 2011.
- [244] Christophe Berthon and Rodolphe Turpault. A numerical correction of the m1-model in the diffusive limit. *Discrete and Continuous Dynamical Systems Series S*, 5:245–255, 2012.
- [245] Kai Krycki, Christophe Berthon, Martin Frank, and Rodolphe Turpault. Asymptotic preserving numerical schemes for a non-classical radiation transport model for atmospheric clouds. *Mathematical Methods in the Applied Sciences*, 36(16):2101–2116, 2013.
- [246] Christophe Berthon, Christophe Chalons, and Rodolphe Turpault. Asymptotic-preserving godunov-type numerical schemes for hyperbolic systems with stiff and nonstiff relaxation terms. *Numerical Methods for Partial Differential Equations*, 29(4):1149–1172, 2013.
- [247] Christophe Berthon, Philippe LeFloch, and Rodolphe Turpault. Late-time/stiff-relaxation asymptotic-preserving approximations of hyperbolic equations. *Mathematics of Computation*, 82(282):831–860, 2013.
- [248] Christophe Buet and Bruno Despres. Asymptotic preserving and positive schemes for radiation hydrodynamics. *Journal of Computational Physics*, 215(2):717–740, 2006.

- [249] Christophe Buet, Bruno Després, and Emmanuel Franck. An asymptotic preserving scheme with the maximum principle for the m1 model on distorted meshes. *Comptes Rendus Mathématique*, 350(11):633–638, 2012.
- [250] Emmanuel Franck, Christophe Buet, and Bruno Després. Asymptotic preserving finite volumes discretization for non-linear moment model on unstructured meshes. In *Finite Volumes for Complex Applications VI Problems & Perspectives*, pages 467–474. Springer, 2011.
- [251] Edgar Olbrant, Cory D Hauck, and Martin Frank. A realizability-preserving discontinuous galerkin method for the m1 model of radiative transfer. *Journal of Computational Physics*, 231(17):5612–5639, 2012.
- [252] V Vikas, CD Hauck, ZJ Wang, and RO Fox. Radiation transport modeling using extended quadrature method of moments. *Journal of Computational Physics*, 246: 221–241, 2013.
- [253] K Garikipati and TJR Hughes. A variational multiscale approach to strain localization—formulation for multidimensional problems. *Computer Methods in Applied Mechanics and Engineering*, 188(1):39–60, 2000.
- [254] Arif Masud and Kaiming Xia. A variational multiscale method for inelasticity: Application to superelasticity in shape memory alloys. *Computer methods in applied mechanics and engineering*, 195(33):4512–4531, 2006.
- [255] Baskar Ganapathysubramanian and Nicholas Zabaras. Modeling diffusion in random heterogeneous media: Data-driven models, stochastic collocation and the variational multiscale method. *Journal of Computational Physics*, 226(1):326–353, 2007.
- [256] Ramon Codina, José M González-Ondina, Gabriel Díaz-Hernández, and Javier Principe. Finite element approximation of the modified boussinesq equations using a stabilized formulation. *International Journal for Numerical Methods in Fluids*, 57(9):1249–1268, 2008.
- [257] J Mergheim. A variational multiscale method to model crack propagation at finite strains. *International journal for numerical methods in engineering*, 80(3):269–289, 2009.
- [258] M Cervera, M Chiumenti, and R Codina. Mixed stabilized finite element methods in nonlinear solid mechanics: Part ii: Strain localization. *Computer Methods in Applied Mechanics and Engineering*, 199(37):2571–2589, 2010.

- [259] Guglielmo Scovazzi. Lagrangian shock hydrodynamics on tetrahedral meshes: A stable and accurate variational multiscale approach. *Journal of Computational Physics*, 231(24):8029–8069, 2012.
- [260] Juan Pablo Trelles and S Mahnaz Modirkhazeni. Variational multiscale method for nonequilibrium plasma flows. *Computer Methods in Applied Mechanics and Engineering*, 282:87–131, 2014.
- [261] Oriol Guasch, Marc Arnela, Ramon Codina, and Hector Espinoza. A stabilized finite element method for the mixed wave equation in an ale framework with application to diphthong production. *Acta Acustica united with Acustica*, 102(1): 94–106, 2016.
- [262] Assad A Oberai and Peter M Pinsky. A multiscale finite element method for the helmholtz equation. *Computer Methods in Applied Mechanics and Engineering*, 154(3):281–297, 1998.
- [263] Ramon Codina. Finite element approximation of the hyperbolic wave equation in mixed form. *Computer Methods in Applied Mechanics and Engineering*, 197(13): 1305–1322, 2008.
- [264] G Scovazzi and B Carnes. Weak boundary conditions for wave propagation problems in confined domains: Formulation and implementation using a variational multiscale method. *Computer Methods in Applied Mechanics and Engineering*, 221:117–131, 2012.
- [265] O Guasch, M Arnela, R Codina, and H Espinoza. A stabilized finite element method for the mixed wave equation in an ale framework with application to diphthong production. *J. Comput. Phys.*, *Submitted*, 2014.
- [266] Santiago Badia, Ramon Codina, and Hector Espinoza. Stability, convergence, and accuracy of stabilized finite element methods for the wave equation in mixed form. *SIAM Journal on Numerical Analysis*, 52(4):1729–1752, 2014.
- [267] Hector Espinoza, Ramon Codina, and Santiago Badia. A sommerfeld non-reflecting boundary condition for the wave equation in mixed form. *Computer Methods in Applied Mechanics and Engineering*, 276:122–148, 2014.
- [268] Hector Espinoza, Ramon Codina, and Santiago Badia. On some time marching schemes for the stabilized finite element approximation of the mixed wave equation. *Computer Methods in Applied Mechanics and Engineering*, 296:295–326, 2015.
- [269] T Song and G Scovazzi. A nitsche method for wave propagation problems in time domain. *Computer Methods in Applied Mechanics and Engineering*, 293:481–521, 2015.

- [270] Amiya K Pani and Jin Yun Yuan. Mixed finite element method for a strongly damped wave equation. *Numerical Methods for Partial Differential Equations*, 17(2):105–119, 2001.
- [271] Subhash C Mishra, Prabal Talukdar, D Trimis, and Franz Durst. Computational efficiency improvements of the radiative transfer problems with or without conduction—a comparison of the collapsed dimension method and the discrete transfer method. *International journal of heat and mass transfer*, 46(16):3083–3095, 2003.
- [272] Matthias González, Carlos García-Fernández, and Pedro Velarde. 2d numerical comparison between sn and m1 radiation transport methods. *Annals of Nuclear Energy*, 36(7):886–895, 2009.
- [273] Bingjing Su and Gordon L Olson. An analytical benchmark for non-equilibrium radiative transfer in an isotropically scattering medium. *Annals of Nuclear Energy*, 24(13):1035–1055, 1997.
- [274] M Seaid, M Frank, A Klar, R Pinnau, and G Thömmes. Efficient numerical methods for radiation in gas turbines. *Journal of Computational and Applied Mathematics*, 170(1):217–239, 2004.
- [275] Maurice Mordant. Some efficient lagrangian mesh finite elements encoded in zephyr for two-dimensional transport calculations. *Annals of Nuclear Energy*, 8(11):657–675, 1981.
- [276] Pieter G Dykema, Richard I Klein, and John I Castor. A new scheme for multidimensional line transfer. iii. a two-dimensional lagrangian variable tensor method with discontinuous finite-element sn transport. *The Astrophysical Journal*, 457:892, 1996.
- [277] John C Hayes and Michael L Norman. Beyond flux-limited diffusion: parallel algorithms for multidimensional radiation hydrodynamics. *The Astrophysical Journal Supplement Series*, 147(1):197, 2003.
- [278] Heinz H Bauschke, Jonathan M Borwein, and Adrian S Lewis. The method of cyclic projections for closed convex sets in hilbert space. *Contemporary Mathematics*, 204:1–38, 1997.
- [279] Gilbert Crombez. Finding projections onto the intersection of convex sets in hilbert spaces. *Numerical Functional Analysis and Optimization*, 16(5-6):637–652, 1995.
- [280] Noboru Kikuchi and John Tinsley Oden. *Contact problems in elasticity: a study of variational inequalities and finite element methods*, volume 8. siam, 1988.

- [281] Florian Blachère and Rodolphe Turpault. An admissibility and asymptotic-preserving scheme for systems of conservation laws with source term on 2d unstructured meshes. *Journal of Computational Physics*, 315:98–123, 2016.
- [282] Sergey A Suslov and Samuel Paolucci. Stability of natural convection flow in a tall vertical enclosure under non-boussinesq conditions. *International Journal of Heat and Mass Transfer*, 38(12):2143–2157, 1995.
- [283] Gal Berkooz, Philip Holmes, and John L Lumley. The proper orthogonal decomposition in the analysis of turbulent flows. *Annual review of fluid mechanics*, 25(1):539–575, 1993.
- [284] Traian Iliescu and Zhu Wang. Variational multiscale proper orthogonal decomposition: Convection-dominated convection-diffusion-reaction equations. *Mathematics of Computation*, 82(283):1357–1378, 2013.
- [285] Francisco Chinesta, Amine Ammar, and Elías Cueto. Recent advances and new challenges in the use of the proper generalized decomposition for solving multi-dimensional models. *Archives of Computational methods in Engineering*, 17(4):327–350, 2010.
- [286] Antoine Dumon, Cyrille Allery, and Amine Ammar. Proper general decomposition (pgd) for the resolution of navier–stokes equations. *Journal of Computational Physics*, 230(4):1387–1407, 2011.
- [287] Wafa Daldoul. *Du chauffage au refroidissement : le suivi des charges pour le traitement thermique*. PhD thesis, Ecole Nationale Supérieure des Mines de Paris, 2019.

Résumé

Dans le cadre des procédés de chauffage et de trempe réalisés lors d'opération de mise en forme des matériaux, le rayonnement thermique joue un rôle prépondérant. Lors de l'élaboration de modèles numériques permettant la simulation de ces procédés, il est donc nécessaire de disposer d'outils performants pour simuler ce phénomène.

La simulation numérique de tels procédés soulèvent de nombreuses problématiques, comme la représentation d'un environnement complexe impliquant plusieurs composants (pièces, brûleurs, buses d'injection, parois), la gestion des divers phénomènes physiques couplés (écoulement, transfert thermiques, ébullition, rayonnement). Dans cette perspective, les méthodes dites « d'immersion », permettant un traitement généraliste de ces divers problèmes, rencontrent depuis quelques années un intérêt grandissant dans la communauté scientifique.

C'est dans ce contexte que s'inscrit le projet Thost, au sein duquel est réalisée cette thèse. L'objectif est donc de développer des outils pour la modélisation du rayonnement dans le contexte d'immersion de volume propre au logiciel Thost. Deux approches sont développées : l'une consistant en l'adaptation d'une méthode existante au contexte de l'immersion de volume, l'autre explorant l'élaboration d'une formulation pour un modèle particulier de rayonnement. Les outils développés sont ensuite mis à l'épreuve sur des simulations de cas industriels fournis par nos partenaires.

Mots Clés

Éléments Finis Stabilisés, approche LevelSet, adaptation de maillage anisotrope, Rayonnement thermique, applications industrielles

Abstract

For heating and quenching operations occurring during material forming processes, thermal radiation is the the predominant physical phenomenon. Hence, when one tries to simulate such processes, it is important to have at disposal powerful tools for the numerical modelling of thermal radiation.

The numerical simulation of these processes often rises numerous problems and questions, as the representation of a complex environment, involving several components (ingots, burners, nozzles, walls), to deal with different coupled physical phenomena (flow, heat transfer, boiling, thermal radiation). In this regard, some "immersed" numerical methods, allows a generalist treatment of these different problems, have gained popularity and drag interest of the scientific community in the recent years.

The Thost project, aiming to produce a software for heat transfer during material forming processes, fits in the framework, and this PhD is part of this project. The goal is therefore to design tools for numerical modelling of thermal radiation within the immersed volume method of the Thost software. Two approaches are presented: one consisting in the adaptation of an existing method to the context of the immersed volume method, another concerning the development of a formulation for a specific model of radiation. These methods are then tested on industrial applications provided by our partners.

Keywords

Stabilized Finite Element, LevelSet approach, anisotropic mesh adaptation, thermal radiation, industrial applications